



HAL
open science

Quantitative modeling of cell and tissue mechanics with agent-based models

Paul van Liedekerke

► **To cite this version:**

Paul van Liedekerke. Quantitative modeling of cell and tissue mechanics with agent-based models. Biological Physics [physics.bio-ph]. Inria Paris, Sorbonne Université, 2019. tel-02064216

HAL Id: tel-02064216

<https://inria.hal.science/tel-02064216v1>

Submitted on 28 Mar 2019

HAL is a multi-disciplinary open access archive for the deposit and dissemination of scientific research documents, whether they are published or not. The documents may come from teaching and research institutions in France or abroad, or from public or private research centers.

L'archive ouverte pluridisciplinaire **HAL**, est destinée au dépôt et à la diffusion de documents scientifiques de niveau recherche, publiés ou non, émanant des établissements d'enseignement et de recherche français ou étrangers, des laboratoires publics ou privés.



MÉMOIRE

d'habilitation à diriger des recherches de l'université Pierre et Marie Curie

Specialité: INGENIERIE

Quantitative modeling of cell and tissue mechanics with agent-based models

PAUL VAN LIEDEKERKE

LUIS ALMEIDA (Examineur)
MARIE DOUMIC-JAUFFRET (Examinatrice)
DIRK DRASDO (Examineur)
JOSE MANUEL GARCIA AZNAR (Rapporteur)
AMIT GEFEN (Rapporteur)
BERTRAND MAURY (Rapporteur)
PIERRE NASSOY (Examineur)
IRENE VIGNON-CLEMENTEL (Examinatrice)

Sorbonne Université
INRIA
INRIA
Universidad de Zaragoza
Tel Aviv University
Université Paris-Sud
Université de Bordeaux
INRIA

Defense date: March 26 2019

Acknowledgements

This work would have been difficult to achieve without the help of following people. I am very grateful to¹:

Margriet Palm, Herman Ramon, Andreas Buttenschoen, Bart Smeets, Irene Vignon-Clementel, Tim Johann, Tommy Heck, Dirk Drasdo, Kevin Bonny, Tim Odenthal, Noémie Boissier, Eugenio Lella, Géraldine Cellière, Francois Bertaux, Simon Vanmaercke, Hans Van Oosterwijck, Nick Jagiella, Nicole Moussa, Ismael Gonzales, Engelbert Tijskens, Nelly Maloisel, Marie Doumic-Jauffret, Pierre Nassoy, Nathalie Bonte, Kévin Alessandri, Yi Yin, Jan Hengstler, Jieling Zhao, Monika Turasjki, Sanjay Pant, Pieter Ghijsels, Johannes Neitsch, for their technical support.

I further would like to particularly thank Dr. Habil. Dirk Drasdo (INRIA) and Prof. H. Ramon (K.U.Leuven) for their moral and financial support over the past 7 years;

Jose Manuel Garcia Aznar, Amit Gefen, Bertrand Maury, for carefully reading this text, and Luis Almeida, Marie Doumic-Jauffret, Dirk Drasdo, Pierre Nassoy and Irene Vignon-Clemental for accepting to be a member of my jury: this is a great honor to me!

I am also very grateful to Aiko Dinale, Nora Aissiouene, Carola Kruse, Yi Yin, Sanjay Pant, Faisal Amlani, Eugenio Lella, Mikel Landajuela Larma, for the all great times we spent together in Paris (et la Province).

Finally, I am indebted to my parents and family. Without their support this adventure would not have been possible.

Merci à toutes et tous!

I dedicate this work to Alice, Ella, Emma, and Soetkin.

¹in pseudo random order.

Contents

Acknowledgements	iii
1 General Introduction	1
1.1 Biomechanics, mechanobiology, and agent-based models	1
1.2 Discrete or continuum approach ?	2
1.3 Models and Motivations	3
2 Agent-based models for tissue mechanics: basic idea's and new concepts	8
2.1 Introduction	8
2.2 Short overview and review of existing models	8
2.2.1 Lattice-based models	8
Cellular automaton type I and type II	8
Cellular Potts Models (CPM)	9
Lattice-Gas Cellular Automata (LGCA)	11
2.2.2 Lattice-free models	11
Center Based Models (CBM)	11
2.2.3 Deformable Cell Models	16
2.2.4 Hybrid models	16
2.3 New model developments and concepts	17
2.3.1 SPH as a method to model cellular tissues and ECM	17
SPH: equations of motion with extensions	17
Simulation of over-damped motion with SPH: NSPH	19
Simulation of viscoelastic extracellular matrix with NSPH	20
2.3.2 Deformable Cell Model: towards high resolution multi-cellular simulations	21
2.3.3 Models for cell migration and invasion in ECM	25
3 Modeling impact mechanics and bruising of parenchymal tissues: a multi-scale approach	31
3.1 Introduction	31
3.2 Model for parenchyma cells	31
3.3 Results	34
3.3.1 Model Initialization and mechanical consistency	34
3.3.2 Quasi-static loading of single cells and tissues	35
3.3.3 Dynamic loading and tissue damage	38
3.3.4 Concluding remarks	41
3.4 Micro-macro approach to achieve large scale tissue simulations	42
3.4.1 Multiple spatio-temporal scales and rescaled microscopic equations	42
3.4.2 Initialization of the micro-problem	44
3.4.3 Example simulation	46
3.5 Summary and discussion	48

4	Modeling of multi-cellular systems in high resolution in 3D	49
4.1	Introduction	49
4.2	Models	50
4.3	Results	50
4.3.1	Single cell experiments	50
4.4	Multi-cellular simulations	58
4.4.1	Monolayer and spheroid simulations	58
4.4.2	Regeneration of a liver lobule	60
4.5	Summary and conclusions	66
5	Quantitative hybrid modeling of mechanical stress response of growing tumor spheroids	68
5.1	Introduction	68
5.2	Experimental observations	69
5.3	Models and hypotheses	71
5.3.1	Hypotheses for growth and death of tumor cells	71
5.3.2	Establishment of the Agent-Based Model and its parameterization	74
5.4	Results	74
5.4.1	Simulation of cell deformation and pressure distribution during in a small compressed spheroid with DCM	74
5.4.2	Model for experiment I with thin capsule	76
	Validation of model for experiment I with thick capsule data	77
	Validation of model for experiment II	80
	Robustness of the proposed cell cycle progression function	82
5.5	Conclusion and discussion	83
6	Modeling of cell motion in fluid and matrix environment	85
6.1	Introduction	85
6.2	Modeling of red blood cells through capillaries in Stokes regime	86
6.3	Motion of cells in homogeneous degradable viscoelastic matrix	87
6.3.1	Matrix degradation model	87
6.3.2	Example: single cell motion in degradable matrix	88
6.4	Migration of cells through non-homogeneous matrix	89
7	Conclusion, outlook and challenges	92
7.1	Aftermath of the proposed agent-based models	92
7.2	Ongoing work and future directions	93
7.2.1	Mechano-transduction and developmental biology	93
7.2.2	Cell migration mechanics	95
7.2.3	Multi-scale modeling approaches	97
7.2.4	Software development	98
A		99
A.1	Fluid-boundary coupling consistency in the parenchyma cell model	99
A.2	Derivation of SPH Euler equations from a coarse-grained MD system	100
B	Modeling cell and tissue mechanics with high resolution models: model components and parameter calibration	102
B.1	Deformable Cell Model: forces	102
B.1.1	Internal forces	102
B.1.2	Maugis-Dugdale contact model	104
B.2	Deformable Cell Model: growth, division, and death	106
B.3	Optical stretcher: DCM parameter determination	107

B.4	DCM parameters and CBM contact force calibration	109
B.5	Estimation of the surface forces on a cell during the optical stretcher experiment . . .	109
B.6	Table with model parameters	111
C	Modeling stress response spheroids: model components and parameter calibration	113
C.1	Models	113
C.1.1	CBM volume and compressibility	113
C.1.2	CBM Measures for stress and pressure	114
C.1.3	CBM Cell growth, mitosis, and lysis	114
C.1.4	Elastic Capsule Model	114
C.1.5	Calibration of the CBM contact forces using DCM	115
C.2	Model setup and parameter determination	118
C.2.1	Cell-specific parameters $\{P_{C=j}\}$ to obtain the initial spheroid configuration and free growth	118
C.2.2	Experiment specific parameters $\{P_{EXP}\}$	119
C.2.3	Cell-specific parameters K and T_{lys} during stress conditions	119
C.3	Model parameter and algorithm sensitivity	123
C.3.1	Comparison of calibration methods	123
C.3.2	Influence of cell division algorithms	123
C.4	Possible ways to include extracellular matrix in the DCM	125
C.5	Table with model parameters and algorithm flow chart	126

“Those who can, do. Those who can’t, simulate.”

Unknown

Chapter 1

General Introduction

1.1 Biomechanics, mechanobiology, and agent-based models

Biological cells are constantly exposed to mechanical stress. In response to this stress they may change their shape, their fate, or start migrating. Overall, mechanics influences the cellular organization in an organism. Over the past decades, the majority of research has been focusing on the molecular processes and their impact on biological organization processes. Molecular biology was led by the expectation that unveiling the genome, identifying genes and their function, could be sufficient to understand functioning and failure of living organisms. Despite impressive insights triggered by molecular biology, these expectations were not fulfilled. Since then, mechanics and organization in tissues have been linked to the lower levels, arriving at gene expression, gene regulation, gene translation, post translational protein modifications, and signal transduction and metabolism. It is becoming increasingly obvious that molecular events can impact cell behavior and subsequently modify multi-cellular organization and mechanics, which in turn can feed back to the molecular control inside the cell [1, 2, 3].

Mathematical modeling and computer-based simulation of living matter is a non-trivial task due to the complexity, biological variability, and the various scales that are involved. Biomedical sciences have created plenty of challenges and endowed several new subjects for the biomechanics and mechanobiology modeling community. For example, a lot of mathematical models have emerged from communities contemplating bone modeling and cardiovascular modeling [4, 5]. Most of the modeling approaches regard the problem as a homogenized system which are solved by ordinary differential equations (ODEs) and partial differential equations (PDEs). These have become standard and widespread in mathematical biology literature [6].

Agent Based Models (ABM) or Individual Based Models (IBM) for cellular systems are a relatively new class of mathematical models that aim to simulate multicellular dynamics or tissues while identifying the behavior of every individual cell and capturing natural spatial inhomogeneities and variability between cells. ABMs allow to include behaviors and interactions of real biological components, embody them as computational agents, and run simulations to observe the emergent phenomena. They are thus well suited to answer questions about the dependence of emergent properties on specific agent behaviors or environmental factors. The nature of ABMs permits to include the individual variability observed in biological cells. This variability can be established on the level of physical and biomechanical properties (such as Young's Modulus, cell size, . . .) as well as on the level of gene expression or protein concentrations. In recent years, several ABM types have been developed to mimic and understand multicellular organization processes, ranging from disease progression to wound healing (e.g. [7, 8, 9, 10, 11, 12, 13, 14, 15]).

In this work, we contemplated both the developments and applications of agent-based modeling. While the central question is practically always a biological one, the path to that answer is seldom in *linea recta* and may require new developments and algorithms in order to answer the question.

1.2 Discrete or continuum approach ?

Since the introduction, development and popularization of computer based simulation of matter, in particular Finite Element Methods (FEM) [16] and Molecular Dynamics (MD) approaches [17] in the 60's, one has witnessed a tremendous expansion of the methods in various research fields (hydrodynamics, structural mechanics, biomechanics,...). The two above mentioned methods represent a different philosophy of modeling: the former one regards matter as a continuum, whereas the latter sees it as a discrete system of interacting particles (atoms).

As matter is a discrete system, a particle approach provides in principle a natural way of description. The dynamics of such a system can be expressed in two ways. Most simply, the movement of particles can be described as a hopping process on lattice sites governed by rule-based -usually a probabilistic- dynamics. This is the basic idea in a cellular automaton, as discussed in chapter 2. Alternatively, the dynamics can be described by equations of motion, the approach we have chosen in this work. Let us begin with an isolated system of atoms or molecules. Using the classic equations of motion, the position of any particle i in a system can be obtained by solving :

$$m_i \frac{d\mathbf{v}_i}{dt} = -\nabla_i U_e, (\mathbf{r}_1, \dots, \mathbf{r}_N), \quad (1.1)$$

where \mathbf{v}_i is the particle velocity, and U_e is the effective potential energy originating from the presence of other particles $j = 1..N$ which are positioned at \mathbf{r}_j . This dynamics represents a conservative system in equilibrium. The interaction potential is usually simplified to a pairwise one, i.e. $U_e = \sum_{j \neq i} U(\mathbf{r}_i, \mathbf{r}_j)$. Still, these potentials functions can be very complex and depend on the structure of the atom. Furthermore, if for instance the system is not in equilibrium due to presence of external forces, some degrees of freedom of the atoms may not be excited in the simulation and one may need to apply a "thermostat" correction to ensure the temperature of the system (which reflects the kinetic energy of the particles) does not rise artificially.

The number of particles for a system dramatically increases with its size, making the method unsuitable to simulate a problem with mesoscale dimensions in a feasible time. To still benefit from the generality of particle based approaches, one has developed *coarse graining* techniques, in which (large clusters of) molecules of interest are regarded as one particle that move in a "heat bath" of smaller molecules which are not explicitly taken into account. The motion of the particles of interest are described by the Langevin equation, in which they gain random forces and have their velocities lowered through friction forces, which work as a thermostat. The motion of such a particle reads:

$$m_i \frac{d\mathbf{v}_i}{dt} = -\nabla_i U_e + \mathbf{F}_i^D + \mathbf{F}_i^R, \quad (1.2)$$

with \mathbf{F}_D and \mathbf{F}_R the dissipative force and random force respectively. A particularly well-known method is called Dissipative Particle Dynamics (DPD) [18]. Herein, the dissipative force and random force fulfill the *Fluctuation-Dissipation* theorem in statistical physics. The method can be used to accurately simulate meso-scale systems (such as cell membranes or other subcellular structures), in which the erratic motion of the molecules is clearly noticeable. Inspired by the formalism for atoms and molecules, Galle et al. (2005) [19] used Langevin type equation to simulate the movement of cells. However, although indeed a similar random movement can be observed in cells, the magnitudes of the forces in Eq. 1.2 scale differently than for molecular systems.

Continuum methods on the other hand, are based on well-known macroscopic conservation laws described by PDEs which provide a realistic description of matter at scales much larger than the size of the molecular structure. The equivalent continuum hydrodynamic equations for the velocity field \mathbf{v} in Lagrangian form reads:

$$\frac{D\mathbf{v}}{Dt} = \frac{1}{\rho} \nabla \cdot \boldsymbol{\sigma}, \quad (1.3)$$

where ρ and σ represent the material density and the stress tensor. In a framework that is conceived on a continuum approach, cell-averaged effects for cell migration, cell adhesion, chemotaxis, etc.. must be incorporated by appropriate partial differential equations and constitutive equations [20, 21, 22, 23]. Numerical solution methods such as the Finite Element Method (FEM) are mathematically solidly founded and effective. However, continuum approaches leave open key questions on how the cellular scale is related to the tissue-scale. They may also suffer from representing insufficiently detail, inhomogeneities and variability, which arise from the inherently discrete nature of cell-cell interactions [7]. Conversely, continuum models offer a reliable and effective way to model macroscopic effects such as diffusion or flow phenomena. They generally require less parameters, allowing a quicker analysis of results. Furthermore they are generally suitable to rigorous mathematical analysis. They represent a *top-down* approach, where one seeks to find the "ideal" constitutive equations that can summarize the ensemble of microscopic effects. Discrete models frame in *bottom-up* approaches where one seeks average to out the microscopic effects and deduce macroscopic laws. More and more research is being devoted at the interface between the two approaches, endowing multi-scale models (e.g. [24, 25, 22, 26]) and hybrid models (e.g. [27, 28]).

An interesting evolution since the 1980's is the development of the method called Smoothed Particle Hydrodynamics (SPH) [29, 30]. SPH was originally derived as a numerical discretization of continuum hydrodynamic equations for astronomical applications. Being a mesh-free Lagrangian method, SPH is particularly advantageous because it can naturally deal with discontinuities, free surfaces and multi-physics problems without the need of re-meshing. Unlike any mesh-based solution method (e.g. Finite Elements), the dynamics is here governed by a set of interacting particles through a kernel function. SPH provides a link between continuum methods and discrete methods. For instance, the SPH Euler equations can be formally regarded as coarse-grained MD system where the SPH kernel function plays the role of a molecular dynamics potential [31] (see also Appendix A.2). Furthermore, DPD and the SPH formalism can be merged into thermodynamically consistent method (called SDPP) describing mesoscopic hydrodynamics in which thermal fluctuations are tangible [32, 18]. SPH has similar algorithms for collision detection of particles and similar numerical integrators for the equations of motion as in MD. Generally, SPH methods are also relatively easy to implement in established MD softwares (see e.g. "LAMMPS" software [Ganzenmüller et al., 2011]). We have exploited the features of SPH in chapter 3, where it is used to model the interior of cells, and in chapter 6, where it is used as model for the medium in which the cells can move.

1.3 Models and Motivations

Modeling of biological phenomena implies that one must take a large variety of phenomena into account. For example, an imaginary model that would us enable to simulate the overall behavior of one cell, would need to be able to address mechanics, hydraulics, electrostatics, gene regulatory networks, ODE models for molecular pathway modeling, and so on. All the algorithms of this model may need to talk to each other simultaneously.

The models that were conceived in this work are conceived in "particle-based" frameworks¹. I have chosen for this approach because of its versatility and flexibility to add physical and biological laws. Generally, the "particles" in such frameworks are an abstraction. I used the Discrete Element Methods (DEM) through my PhD work (K.U.Leuven, Belgium) to model granular flow in machines (see e.g. [Van Liedekerke et al., 2009]). Here the particles are inert objects. The jump from grains to cells as a modeling object involves many new algorithms and challenges. This is also true for models of humans crowds (e.g. [33]) or animal flocks. For particles which are allowed to express a complex individual behavior, one speaks of agent-based models. Typically, a basic working scheme for such a framework includes iterative loops over modules:

¹Mostly in-house codes.

1. Definition and construction of the discrete elements
2. Apply initial conditions
3. Model elements description of the motion dynamics (cfr. Eq. 1.2)
4. Model elements description of the internal state dynamics
5. Loop (time < T_{end}):
 - Check for contact between elements, compute mechanical forces
 - Update positions of elements
 - Update element internal state, function of position and forces

I have aimed to build models for cells for which the parameters are physically sound (meaning: they can be measured in an experiment) and can only vary in a physiological range. It is almost needless to say that experiments play a large role in model development. Experiments are needed to guide the model construction, to calibrate the model parameters, and to validate models. On the other hand, experiments may also serve to falsify model hypotheses. When experiments are not available, we can use the model to predict or to give insight. The relation between model and experiment is thus a dynamic feedback loop. An important remark is that a model cannot be developed as a static concept. Indeed, models may need to be adapted to new insights or new experimental techniques. As a consequence, their functionality will have to be constantly expanded or enriched with more detail. For example, recent developments of experimental imaging techniques facilitate validation of simulation models at histological scales. High resolution confocal microscopy and intra-vital imaging can now represent tissue micro-architecture accurately, allowing to study the interplay between cell shape, cell mechanics and cell environment [34]. This means that models in which cells are regarded as rigid homogeneous objects will gradually need to be replaced by models which account for deformability and subcellular structures. With the models that have been developed in this work, I hope to contribute to this evolution.

Below, the concepts and motivations for the models that have been developed are briefly summarized:

Chapter 2: Agent-based models for tissue mechanics: basic idea's and new concepts

Over the past decades, the modeling community in biology has expanded tremendously. Beginning scientists are often overwhelmed with a plethora of models which makes a optimal choice for a particular biological question difficult. As a response, in chapter 2, we first give a short introduction to the state-of-the-art of agent-based models and their applications (in more detail explained an invited review article and book chapters [Van Liedekerke et al., 2015, Van Liedekerke et al., 2017, Drasdo et al., 2017]). Upon this, we give an overview of the new models and concepts that have been introduced by my co-workers and me over the past 10 years of work. These model (components) are applied in the following chapters which each treat a more specific question.

Chapter 3: Modeling impact mechanics and bruising of parenchymal tissues: a multi-scale approach

The original work in chapter 2 was established during my post-doc period at K.U.Leuven (MeBioS lab). A collaboration between the research groups of Prof. H. Ramon (MeBios lab) and prof. D. Roose (NUMA research unit) framed in a project whose goal was to understand the mechanisms of

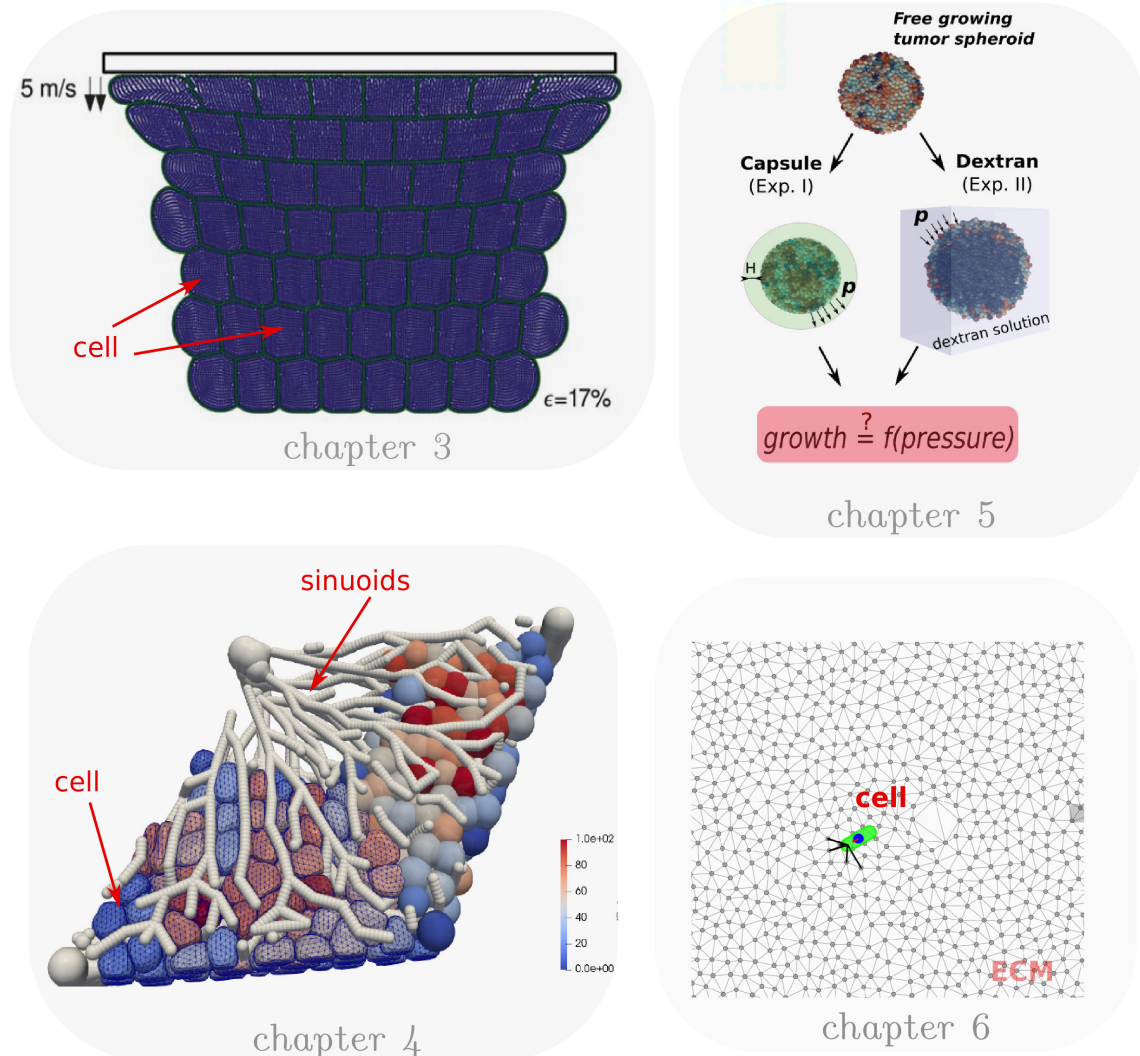


FIGURE 1.1: Simulation snapshots of the models presented in this work aiming to address a biomechanical or biological question. **Chapter 3:** Cellular response during impact of parenchyma tissues. **Chapter 4:** Towards organ modeling with high resolution models. **Chapter 5:** Influence of mechanical stress on tumor growth. **Chapter 6:** Mechanics of cell migration in extracellular matrix.

damage propagation in plant parenchyma tissue. Bruising of fruits during transport and handling brings significant financial losses to vendors [Van Zeebroeck et al., 2003].

Plant parenchyma cells represent the bulk of the soft parts of plants, including fruits. They are hierarchically structured and their apparent mechanical properties emerge from the features at (sub)cellular scales. The characteristics of these cells are important to food processing. To better understand the characteristics of foods, mathematical modeling in the food engineering community has shifted more and more towards multi-scale approaches [Ho et al., 2013].

Macroscopic physical parameters of the fruits or vegetables (shape, external forces, temperature), as well as microscopic parameters (cell parameters, tissue structure) can influence the probability of being damaged. The initial research questions were: (i) how do individual cells mechanically respond to a sudden stress and (ii) can we relate mechanical subcellular properties of individual cells to a macroscopic constitutive law ?

Microscopic model: For the first part of this work, we introduced the SPH method to build a cell model that captures the basic viscoelastic behavior of individual parenchyma cells or small cell aggregates of maximum ~ 100 cells [Van Liedekerke et al., 2010a, Van Liedekerke et al., 2010b, Van Liedekerke et al., 2011]. The cells are regarded as fluid-filled vessels with flexible elastic boundaries. We performed simulations to study the mechanical behavior during loading and damage. The models have been constructed guided by the requirement that model parameters are physically sound, which makes comparison of the simulation results with experiments without parameter tuning possible.

Macroscopic model: We elaborated on a multi-scale modeling framework to relate the ensemble microscopic behavior of cells to a continuum description. For this, we first performed a multi-scale analysis of the dynamics of the microscopic model. Using homogenization and Representative Volume Elements (RVEs) we show that simulations of large tissues can be performed with a FE model which uses *on-the-fly* runs of the microscopic model replacing a constitutive equation [Ghysels et al., 2009, Ghysels et al., 2010a, Ghysels et al., 2010b].

Chapter 4: Modeling of multi-cellular systems in high resolution in 3D

With the recent developments in imaging and microscopy (e.g. [35, 34]), there is a demand for models which can simulate with more cellular details. Indeed, in the past agent-based models have largely used rigid cell shapes ("center-based models"). In this chapter, we introduce a so-called "Deformable Cell Model" (DCM) which can handle arbitrary cell shapes [Odenthal et al., 2013]. We have enriched this model with a cell-cell adhesion model and with the capability to grow and divide [Van Liedekerke et al., 2018b]. The model can be fully parametrized by single cell experiments. As a proof on concept, we show that this model can be used in future simulations for liver regeneration. We compare the results of these simulations with those obtained with a center-based model. This model is the result of earlier work at K.U.Leuven (Prof. H. Ramon) and recent work at INRIA (Dr. Habil. D. Drasdo).

Chapter 5: Quantitative hybrid modeling of mechanical stress response of growing tumor spheroids

Chapter 3 has been devoted to the question of how cells respond to mechanical stress during growth. In collaboration with the Lab of Dr. Pierre Nassoy (Institut Optique, Bordeaux) and Dr. Habil. D. Drasdo (INRIA) I have studied and analyzed two different kinds of experiments for growing tumor spheroids under mechanical stress in order to find response functions for cell growth [Van Liedekerke et al., 2018a]. We have used a robust and general model strategy in which cells are represented by individual units parameterized by measurable biophysical and cell-biological parameters. We have used a hybrid modeling strategy combining a center-based model type and a deformable

cell model type. Cell cycle progression in our model is controlled by cell volumetric strain, the latter being derived from a bio-mechanical relation between applied pressure and cell compressibility. After parameter calibration from experiments with mouse colon carcinoma cells (CT26) growing against the resistance of an elastic alginate capsule, the model can adequately predict the growth curve in (i) soft and rigid capsules, (ii) in different experimental conditions where the mechanical stress is generated by osmosis via a high molecular weight dextran solution, and (iii) for other cell types with varying doubling times. Our simulations thus indicate that the response of growing cell populations on mechanical stress follows the same functional relationship and is predictable over different cell lines and growth conditions despite the response curves look largely different .

Chapter 6: Modeling of cell motion in fluid and matrix environment

In this chapter, we focus on the movement of cells in fluids and solid like media such as ECM. The mainly ongoing work is the result of a collaboration with Dr. Habil. D. Drasdo (INRIA), Dr. Andreas Buttenschoen (University of British Colombia), Dr. Magriet Palm (University of Leiden) on one project, and with Tommy Heck and Prof. H. Van Oosterwyck (K.U.Leuven) on another project. We distinguish two aspects:

(i) We introduce two ways of representing a medium: The first possibility is to regard it as a continuum. Here we have exploited the benefits of the SPH method. In collaboration with former co-workers at K.U.Leuven (MeBioS lab), I studied the abilities of SPH to represent fluid dynamics for low Reynolds numbers (chapter 2) [Van Liedekerke et al., 2013]. This new method (called NSPH) allows the use of larger timesteps in simulations. More recently, we have used the same methodology to model homogeneous solid-like media (in particular, a homogeneous Extracellular Matrix or hydrogels) [Heck et al., 2017] In the second approach, we have tried to model the porous structure of collagen Extracellular Matrix. Here we have mimicked the scaffolding structure of the fibers by a viscoelastic network of nodes, whereby the springs and inter-particle distance in the network reflect the stiffness and porosity of the ECM respectively. The cells embedded in a collagen-reinforced ECM need to negotiate space in order to migrate. This can be established by adapting its shape and deformation or degradation of the obstructions.

(ii) We propose models for cells moving in a medium: Red blood cells in the blood plasma are dragged so there is no active motion. Yet, the blood transport properties heavily depend on the mechanical properties of the RBCs. We coupled a 2D deformable RBC model with our low Reynolds particle fluid solver to show that this coupling effectively can be used to study transport phenomena. Next, we have started to study models for active cell migration in elastic medium (ECM). In a first, simplified approach, we represent the cell as a rigid boundary that can move in response to a global migration force and can local degradation of the matrix. In the second approach we propose a model type in which a cell is regarded as a rod which moves through an inhomogeneous matrix containing collagen fibers. Here, the cells can adapt their shape from spherical-like to elongated-like. The cells can move by expressing protrusions, which are modeled as contractile elements between the cell body and ECM nodes. The cells are also able to locally degrade matrix. This model should be able to handle large cell numbers easily and thus makes it suitable to multi-cellular simulations.

Chapter 2

Agent-based models for tissue mechanics: basic idea's and new concepts

2.1 Introduction

In recent years, numerous ABMs have been developed to mimic multicellular organization. In this chapter, I will in a first part briefly recapitulate the taxonomy of agent-based models, for which the extensive reviews have been published in recent works by my co-workers and me [Van Liedekerke et al., 2015, Drasdo et al., 2017, Van Liedekerke et al., 2017]. I focus mainly on the basic ingredients of lattice-free type models, as these have been used throughout this work. In the second part, I explain several new concepts that we have introduced over the past 10 years and that have been applied to biological problems issued in the next chapters.

2.2 Short overview and review of existing models

2.2.1 Lattice-based models

In lattice-based models the space is subdivided into space-fixed discrete compartments, and motion of the cells is possible only in discrete steps by shifts of the cell position from one to another space compartment. Common lattices based on the bounds of space compartments are the square lattice, the hexagonal lattice or the Voronoi tessellation that as a generalization of the former two regular lattice types can be irregular. Lattice-based models of multicellular systems are in literature often referred to as "Cellular Automaton models" (CA). Models where only the cell positions are recorded may further be sub-divided into three classes depending on their spatial resolution. The same construction point may either be occupied by exactly one cell (**Type I**), by many ($N > 1$) cells (**Type II**), or may simultaneously be associated with the same cell (**Cellular Potts Models**). The other model type recording besides the spatial position also the cell velocity, is called Lattice-Gas Cellular Automaton (**LGCA**) model (see Fig. 2.1). Each of these models defines a stochastic growth process in time.

Cellular automaton type I and type II

In the CA type I, the precise cell position is resolved in time and space. In CA type II, this is not the case anymore, as each compartment contains a certain number of cells that can change during the time course of the simulation (see Fig. 2.1). The dynamics in both types are described by a master equation. The advantage of formulating the master equation in combination with a lattice is that this gives a well defined framework to include cell creation, growth, division, movement of cells by "hopping", cell death, etc.

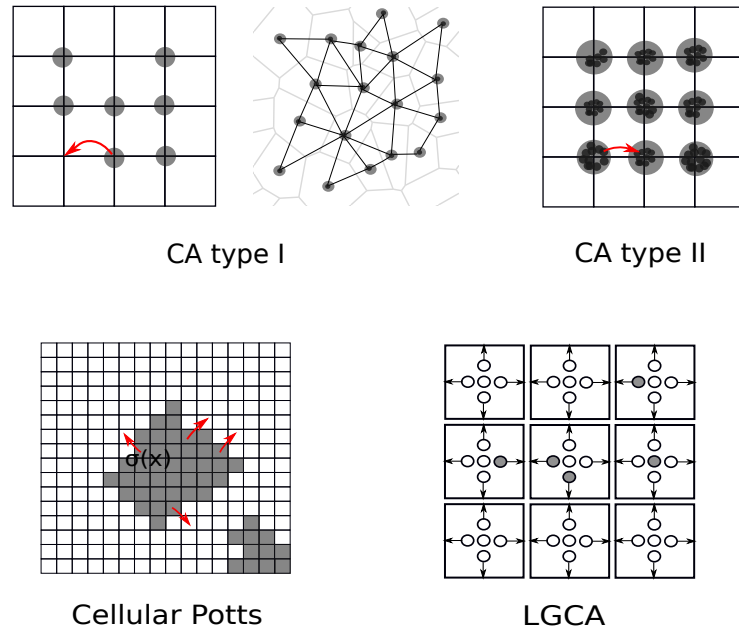


FIGURE 2.1: Lattice models type I (regular and irregular), type II, Cellular Potts Models, and LGCA. The gray areas represents a location occupied by cells. The arrows indicate a possible jumping process. In the LGCA, in each node the middle circle represents a rest channel, whereas the other circles represent velocity channels.

The master equation for the change of the multivariate probability \mathcal{P} to find the multicellular systems in a certain system state Z with time t reads:

$$\frac{\partial \mathcal{P}(Z, t)}{\partial t} = \sum_{Z'} W(Z' \rightarrow Z) \mathcal{P}(Z', t) - W(Z \rightarrow Z') \mathcal{P}(Z, t). \quad (2.1)$$

Here the first term denotes all transition from neighbor states Z' into the "current" state Z and the second term denotes all transitions from the current state Z into any accessible neighbor state Z' . A reasonable reference time scale may be the duration of the cell cycle. Standard ways of solving the master equation are either by a fixed time-step algorithm choosing the time step Δt so small that only a single event is likely to occur within $[t \dots t + \Delta t]$, or by the Gillespie algorithm [36, 37].

For both CA type I and II, requirements in terms of simulation time are modest. Because of the short simulation times, simulated parameter sensitivity analyses are feasible. The weak points are that the cell size and shape are fixed and a lattice property, the existence of the lattice spacing as a lower length scale, and that the stochastic processes play a key role in the simulation dynamics, which are all simulated by jump-type processes. The physics is represented by rules, that are hoped to cover the physical processes correctly, which can be a significant shortcoming compared to models that implement physical laws directly. The methods have been successfully used to model monolayer growth [38, 39] and tumor growth [40, 41].

Cellular Potts Models (CPM)

The Cellular Potts Model (CPM) is an "energy-based" modeling framework. It uses an energy functional generalized from the Potts model, originally derived for a ferromagnet, to evaluate a multicellular state. In a CPM, one cell occupies many lattice sites (positioned on a 2D or 3D lattices). Each lattice site \underline{x} is assigned an identifier $\sigma \in \mathbb{N}^0$ (see Fig. 2.1, bottom). Sites with the same

identifier $\sigma > 0$ belong to the same cell, and all remaining lattice sites, with $\sigma = 0$, belong to the extra-cellular medium.

The assignment of lattice sites to cells and extra-cellular medium are controlled by an effective energy functional on the lattice. The minimal standard effective energy functional of the CPM consists of three terms:

$$E = \sum_{(\underline{x}, \underline{x}')} J(\sigma(\underline{x}), \sigma(\underline{x}')) (1 - \delta(\sigma(\underline{x}), \sigma(\underline{x}'))) + \lambda_S \sum_{\sigma} (S_0(\sigma) - S(\sigma))^2 + \lambda_V \sum_{\sigma} (V_0(\sigma) - V(\sigma))^2. \quad (2.2)$$

The first term represents both cell-cell adhesion and cell-ECM adhesion that is computed for all sets of neighboring lattice sites $(\underline{x}, \underline{x}')$ where $J(\sigma(\underline{x}), \sigma(\underline{x}'))$ represents the energy cost of an interface between lattice sites belonging to two different cells. Because only interfaces at the cell membrane are associated with an energy costs, the Kronecker delta ($\delta(x, y) = \{1, x = y; 0, x \neq y\}$) is used such that the contact energy becomes zero for $\sigma(\underline{x}) = \sigma(\underline{x}')$. The second term denotes a surface constraint with actual surface S , target surface S_0 and penalty parameter λ_S , the third term a volume constraint, with cell volume $V(\sigma)$ and target volume $V_0(\sigma)$, and penalty parameter λ_V . In 2D simulations the volume is replaced with the area, the surface by the circumference. The magnitudes of shape constraints are not invariant with respect to the fineness of the lattice. This can be addressed by introducing relative shape constraint [42, 43, 44]. The penalty parameters λ_S and λ_V can be viewed as Lagrangian parameters which permit to add constraints and may be related to physical quantities. E.g., the Lagrangian parameter λ_V for the volume constraint can be related to the material properties of the cell. The CPM can also model cell growth, cell division and chemotaxis [45, 46, 47].

In principle the dynamics could again be modeled by a multivariate master equation mimicking the time development for the probability to find the multicellular system in a particular multicellular state. However, the neighbor states of a give state are so numerous that this way is usually not pursued. Instead, cell migration, cell growth and cell shape changes are modeled using a Markov chain Monte Carlo method. Here, the CPM iteratively attempts to change the state of a randomly chosen lattice site \underline{x} to that of a randomly chosen neighboring lattice site \underline{x}' (see Fig. 2.1). To determine whether such a move attempt is successful the change in effective energy (ΔE) between the two configurations is evaluated using the Metropolis algorithm. The underlying conceptual idea originating from Statistical Mechanics is that the energy functional ("Hamiltonian" in Statistical Mechanics) characterizes the equilibrium of the system hence permits calculation of the equilibrium probability distribution.

The CPM has been established as a standard simulation method used frequently for modeling biological phenomena. The CPM provides a flexible modeling framework called "CompuCell3D" [48], which is used and has been extended by numerous authors. It is straightforward to implement and computationally inexpensive in 2D. It is therefore possible to perform large scale parameter sweeps and carry out sensitivity analyses with CPM-based models [49, 50]. However, there are some notable disadvantages too. First, whereas the CPM performs well in 2D and quasi-3D, real 3D simulations take long and are therefore uncommon. Second, because the CPM minimizes the effective energy, cell behavior is highly linked to cell motility. Cell motility on the other hand links to material parameters of the cell. The physics is partially directly represented (e.g. mechanics, adhesion), but partially unphysical couplings of migration and physical properties can occur. Finally, all dynamics processes (migration, division, death, pushing) are modeled by a jump-type stochastic process. As a given multicellular configuration has usually a very large number of possible neighbor configurations, too large to be completely listed, the dynamics is by Monte-Carlo sampling, which can lead to unnatural distortions of the time scale. CPMs have been a popular tool to model morphogenic processes such as cell sorting [51, 52], cancer and tumor growth [53, 54, 55, 56, 57, 58, 59], and angiogenesis [60, 61, 62, 63, 64, 65, 66, 43].

Lattice-Gas Cellular Automata (LGCA)

In addition to the previous model types, LGCA models have further an explicit dynamical variable: the cell speed. LGCA models include velocity channels hence now the particles are characterized by their position and velocity, which are both discrete. The dynamics of the cells is dictated by a collision step and a propagation step. Frisch, Hasslacher and Pomeau demonstrated in 1986 that by defining a set of rules for the interaction (in their case collision) and propagation of particles on a regular lattice with discrete time steps and a small set of velocities, one can generate dynamics that on large scales reproduce the behavior of the incompressible Navier-Stokes equation [67, 68, 69]. Deutsch and co-workers extended the framework to model growth and migration of cells in multi-cellular environments [70, 71, 72, 73]. Each node contains rest channel(s) and velocity channels (see Fig. 2.1). The dynamics of an LGCA emerges from applying super-positions of local probabilistic interactions and deterministic transport steps. The first step involves a time-independent probability for transition from the pre-interaction to the post-interaction node state. In the deterministic propagation step, all particles (cells) are moved simultaneously to nodes in the direction of their assigned velocity. This results in a set of micro-dynamical equations for the occupation numbers at each node.

An excellent article introducing LGCA is the one by Hatzikirou and Deutsch in [74]. Advantages and disadvantages of LGCA are similar to those for Type A lattice models.

2.2.2 Lattice-free models

In lattice-free models, cells are represented by a single or a clusters of particles which can continuously move in space. As in lattice-based models, cells have the ability to grow, migrate, divide, and die. By using the term "lattice-free", we mean there is no fixed Eulerian underlying computational mesh to calculate the cells' position and movement. Among lattice-free models, one can roughly distinguish between **Center-Based Models (CBM)** and **Deformable Cell Models (DCM)**. In the center-based models, the interaction of cells is usually described by pairwise forces or energies functions defined between cell centers, while cell shape is not resolved precisely. Deformable cell models consider also the intracellular forces and permit a representation of complex cell shapes.

We will focus here on force based models, for which the cell's motion is described by an equation of motion. The dynamics of a system of cells can also be mimicked using energy-based methods using numerical procedures (similarly to the CPM). The advantages of force-based models is that they have a straightforward definition of time, and a intuitive way of taking complex interactions of cells with other cells or their environment into account. In the equation of motion, there is usually a well defined probabilistic and deterministic part. The level of stochasticity is tunable. For example, the motion of erythrocytes in blood plasma is influenced by both stochastic fluctuations and a deterministic flow component. At very small scales stochastic events are immanent and can be quantified by principles of statistical physics. These principles are also applied in ABMs although this is a priori not always physically or biologically justified.

Center Based Models (CBM)

Center-Based Models (CBM) have been used with remarkable success for several decades. With cell numbers starting from few and ranging to more than 10^6 on a single processor machine, their simulation scale range is "sub-tissue", i.e. monolayers, small tumors, and representative tissue units. Typical application fields are tumors [38, 75, 76, 76, 13], intestinal crypts and epithelial tissues [77, 78, 79, 80, 81, 82, 83], cell migration in ECM [84, 85, 86], wound healing [87, 88], bone tissue engineering applications [Geris et al., 2010], tissue regeneration [8], and even tissue rheology [89, 90]. Despite the fact that the mechanical information that can be extracted from these models is rather approximate, various biomechanical aspects in these problems have been explained

Equation of motion for cells: In center-based models, cells are represented by simple geometrical bodies (see e.g. Fig. 2.2). In formal analogy to physical particles, the assumption is that each trajectory of a cell in space can be described by an equation of motion. In microscopic biological systems, it is commonly supposed that inertia effects can be neglected as the Reynolds numbers are very small, meaning friction dominates the system [91]. The drop of acceleration terms in the equations of motion leads to a first order coupled system. In this over-damped limit, the basic equation considering forces between cells and between cells and substrate reads for cell i

$$\mathbf{\Gamma}_i^{cs} \mathbf{v}_i + \sum_j \mathbf{\Gamma}_{ij}^{cc} (\mathbf{v}_i - \mathbf{v}_j) = \sum_j \mathbf{F}_{ij}^{int} + \mathbf{F}_i^{sub} + \mathbf{F}_i^{mig} + \mathbf{F}_i^{chem}. \quad (2.3)$$

On the left side, we find the friction forces of cell with the substrate (1st term) and other cells (2nd term). On the right hand side, we have the forces on the cell emerging from repulsion or adhesion with other cells j and substrate, respectively \mathbf{F}_{ij}^{int} and \mathbf{F}_i^{sub} , as well as the cell migration forces \mathbf{F}_i^{mig} and chemotaxis forces \mathbf{F}_i^{chem} . These are discussed shortly below. The friction terms involve tensors for the cell-cell friction ($\mathbf{\Gamma}_{ij}^{cc}$) and cell-substrate friction ($\mathbf{\Gamma}_i^{cs}$), which can represent ECM, capillaries or membranes. If friction coefficients parallel and normal to the movement direction are different, the friction tensor becomes

$$\mathbf{\Gamma}_{ij} = \gamma_{\perp} (\mathbf{e}_{ij} \otimes \mathbf{e}_{ij}) + \gamma_{\parallel} (\mathbf{I} - \mathbf{e}_{ij} \otimes \mathbf{e}_{ij}), \quad (2.4)$$

with $\mathbf{e}_{ij} = (\mathbf{r}_i - \mathbf{r}_j) / \|\mathbf{r}_i - \mathbf{r}_j\|$, where r_i, r_j denote the position of the centers (see Fig. 2.2) of cell i and object j (\otimes denotes the dyadic product, \mathbf{I} is the $d \times d$ identity matrix with d the number of spatial dimensions). Further, γ_{\perp} denotes perpendicular and γ_{\parallel} parallel friction. Friction occurring in the perpendicular direction of the movement may be associated with internal friction, in particular if two cells are pushed against each other which leads to deformation and reorganization of the cytoskeleton. Friction in the parallel direction is a description of the dissipative terms when the cell membranes slide along each other. Friction with Extracellular Matrix ($s = ECM$) is usually assumed to be isotropic, meaning that the cell-substrate friction matrix is diagonal.

The linear problem Eq. 2.3 is described by a sparse symmetric matrix, which can be solved efficiently using a Conjugate Gradient method. However, we note that the above system of equations of motion does not conserve total momentum. It basically assumes that momentum is not transferred from the cell to the substrate. This could be an insufficient assumption if communication through elastic force fields between the cells mediated by the ECM would turn out to be important (see chapter 6).

Cell interaction forces: The cells in CBM interact by pairwise potentials having a repulsive and adhesive part, which are characterized by a function of the geometrical overlap δ . A number of different approaches have been used for the interaction force, including linear springs [92, 93, 94], a force derived from Lennard-Jones like potentials [90], and a Hertz force approximating cells by isotropic homogeneous elastic bodies that are moderately deformed if pressed against each other [19, 38]. Here, we explain the latter approach and extensions based upon it. Consider two spherical cells i and j , which are in each others' neighborhood (see Fig. 2.2). If the distance $d_{ij} = \|\mathbf{r}_j - \mathbf{r}_i\|$ between the cells becomes smaller than the sum of their radii, we assume a Hertzian contact force develops:

$$F_i^{rep} = 4/3 \hat{E}_i \sqrt{\hat{R}_i} \delta_{ij}^{3/2}. \quad (2.5)$$

in which $\delta_{ij} = R_i + R_j - d_{ij}$ is the overlap between the cells and \hat{E} and \hat{R} are defined as

$$\hat{E} = \left(\frac{1 - \nu_i^2}{E_i} + \frac{1 - \nu_j^2}{E_j} \right)^{-1} \quad \text{and} \quad \hat{R} = \left(\frac{1}{R_i} + \frac{1}{R_j} \right)^{-1}, \quad (2.6)$$

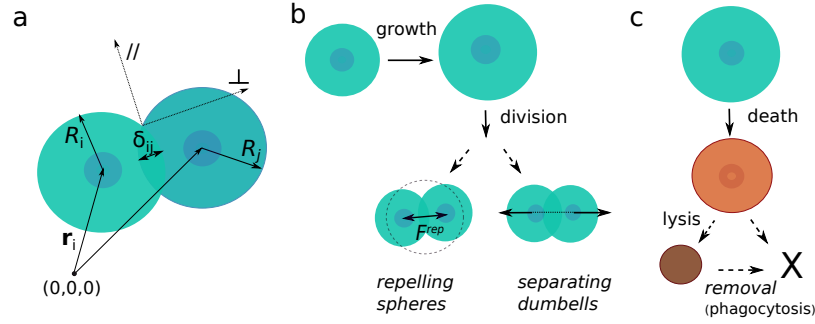


FIGURE 2.2: (a) Cartoon of center based model with cells represented as spheres, defining the basic contact variables. (b) Division of two cells in a CBM. (c) Death and lysis.

with E_i and E_j being the Young's moduli, ν_i and ν_j the Poisson numbers and R_i and R_j the radii of the cells i and j , respectively. Note that the radius of a cell is not constant if growth or necrosis is considered, and must be recomputed from the actual cell volume V_i , see section 2.2.2.

Galle et al. (2005) and Ramis-Conde et al. (2009) [19, 95] considered adhesion of cells to other cells or an underlying substrate by an additive term in the interaction energy which is proportional to the Hertzian contact area, $A_{ij} = \pi \delta_{ij} \hat{R}$ of the cells without adhesion, and the strength of the adhesion formed by bonds W . The magnitude of the adhesion force reads

$$F_i^{adh} = -\pi W \hat{R}, \quad (2.7)$$

The total force $\mathbf{F}^{int} = \mathbf{F}^{rep} + \mathbf{F}^{adh}$ acts in the direction of the vector connection the centers of the spheres. Note that \mathbf{F}^{adh} here does depend not on how much the cells actually overlap. This simplified approach, sometimes called "extended Hertz model", is convenient as it allows to express the force analytically. However, it neglects that adhesion is modifying the contact area, and disregards that the force distribution within the contact area is inhomogeneous. A more realistic adhesive model taking this into account results from the Johnson-Kendal-Roberts (JKR) theory, which includes the hysteresis effect if the cells are separated from each other. JKR is an adhesion theory for solid adhesive soft spheres but can be applied realistically to cells [96]. The JKR force magnitude for soft cells can be approximated by [97, 89]:

$$F_i^{adh} = \frac{4\hat{E}}{3\hat{R}} [a(\delta_{ij})]^3 - \sqrt{8\pi\sigma\hat{E}} [a(\delta_{ij})]^3, \quad (2.8)$$

where the contact radius a in Eq. 2.8 can be obtained from:

$$\delta_{ij} = \frac{a^2}{\hat{R}} - \sqrt{\frac{2\pi\sigma}{\hat{E}}} a. \quad (2.9)$$

We must note here that for high cell densities, neither JKR or Hertz do realistically represent contact forces. As a consequence of considering only pair-wise forces in absence of a notion of cell volume, incompressible cells characterized by a Poisson ratio of $\nu = 0.5$ might in a model simulation become compressed leading to unrealistic multicellular arrangements and thereby to false predictions. Corrections based on Voronoi tessellation have been proposed to circumvent this shortcoming [98, 99], but so far a fully consistent approach for center-based models has been conceptually out of reach. A force correction scheme where the CBM contact forces are inferred from high-resolution models (DCM) has been proposed in [Van Liedekerke et al., 2018a] (see also chapter 4 and Appendix C.1.5).

Another major issue with CBMs is the poor representation of cell shape. As such, it can be difficult, for example, to simulate the Differential Adhesion Hypothesis (DAH) [100], describing the observed segregation process in spheroids with two cell types that have different adhesive properties.

Here cells represented by a CBM have difficulties to overcome the potential energy barriers induced by the pair-wise central forces, and have their the ability of moving past each other decreased (reminiscent to crystalline structures) [101]. In order to alleviate this, some authors have proposed to model the cells as geometries being able to deviate their shape from a sphere (e.g. [102]), thereby effectively increasing the degrees of freedom of motion.

Cell migration and chemotaxis: The migration force \mathbf{F}_i^{mig} is considered as an active force. If no preferred migration direction of the cell is assumed, it is common to write it as a stochastic term with zero mean which is uncorrelated at different points in time, i.e. $\langle \mathbf{F}_i^{mig} \rangle = 0$, $\langle \mathbf{F}_i^{mig}(t) \otimes \mathbf{F}_i^{mig}(t') \rangle = \mathbf{A}_i \delta(t-t')$. Here \mathbf{A}_i is a $d \times d$ autocorrelation amplitude matrix (d : dimension) that may be specific for each individual cell i . However, the mechanisms of cell movement cannot a priori be expected to follow the equipartition theorem of statistical mechanics. Cell migration is active, depending on the local matrix density and orientation, hence we cannot claim that \mathbf{A} is properly described by the aforementioned analogy to colloidal particle movement. As such \mathbf{A} is a parameter phenomenologically describing the cell spreading behavior. Instead, by measuring $\langle ((\mathbf{r}_i(t+\tau) - \mathbf{r}_i(t)) \otimes (\mathbf{r}_i(t+\tau) - \mathbf{r}_i(t))) \rangle = 2\mathbf{D}\tau$, one can estimate the diffusion tensor \mathbf{D} of the cell where again diffusion is not a consequence of collisions with smaller particles, but a parameter phenomenologically describing the cell spreading behavior.

To incorporate persistence in cell motion, we can write \mathbf{F}^{mig} as the vector $F_0^{mig} \mathbf{P}$ where F_0^{mig} is the magnitude of migration, which may depend on cell specific and environment factors, such as e.g. the ECM fiber density. The active migration direction is defined by a polarity vector \mathbf{P} for which the dynamics can be described by a Ornstein-Uhlenbeck process [15] for each cell i described by the equation:

$$\frac{d\mathbf{P}_i}{dt} = \frac{1}{\tau}(\mathbf{P}_{0,i} - \mathbf{P}_i) + \boldsymbol{\eta}_i, \quad (2.10)$$

where τ is the re-polarization time, and $\mathbf{P}_{0,i}$ is the actual preferential direction of the cell. This direction may for instance depend on how the fibers are orientated in the ECM. In some models, one assumes that \mathbf{P} tends to align with the actual velocity component of the cells or it neighboring cells [103, 104, 105]. The random noise component $\boldsymbol{\eta}_i$ reflects the probabilistic character of the movement and satisfies $\langle \boldsymbol{\eta}_i(t) \rangle = \mathbf{0}$.

A more fundamental way would be to consider the individual active force components explicitly that result in the preferential motion of cells. For example, cells can express one or multiple pseudopods to crawl through a medium. A modeling approach of these phenomena is further discussed in this chapter and chapter 6.

Cell growth, division, and death: During the cycle the volume of a mother cell roughly doubles before it splits into two daughter cells. The interphase adding up the G_1 , S and G_2 phase and mitosis phase may be described by an increase of the radius of the cell. However, several studies show that cell growth is not constant throughout the cell cycle [106, 107, 108, 109], with no consensus over a universal growth law. In a basic model assuming constant growth rate during the cell cycle the volume V_i of cell i is updated every timestep Δt as

$$\frac{dV_i}{dt} = \alpha_i(V_i), \quad (2.11)$$

with α_i the growth rate function. If the cell passed a critical volume V_{crit} (doubled volume) or time point T_{div} , the cell undergoes mitosis and two new cells with volume $V_{crit,i}/2$ are created. During the *cytokinesis* process several internal forces develop in the mother cell, involving the formation of an actin contractile ring at the cell equator [110], which is a mechanism that cannot be captured by CBM but can be approximated in several ways.

In a first approach, the system of the two daughter cells is regarded as a rigid dumbbell with the cells gradually distancing each other (see Fig. 2.2b). Because dumbbells lack spherical symmetry, an additional equation of motion for rotation is in principle required, which maybe cumbersome to solve [7]. Alternatively, this rotational motion may be regarded as striving to an energetically most favorable orientation, mimicked by a intermediate Monte-Carlo dynamics using the Metropolis algorithm [8].

In a similar approach to division, cells entering the cell cycle are immediately represented as dumbbells which gradually grow by increasing their distance from zero to twice the radius of the dumbbell spheres, when they separate into two spheres [111, 90]. This algorithm has been found to generate only minor differences on time scales much larger than the cell cycle time, compared to the algorithm distinguishing between a spherical growth and a dumbbell deformation phase.

A drastic simplification of the division algorithm consists of skipping the dumbbell transformation phase and placing directly two smaller daughter cells in the space originally filled by the mother cell at the end of the interphase [99, 19]. This algorithm thus avoids dumbbell rotations but needs to be used with caution. When the two daughter cells are created, the Hertz interaction force will push away the two daughter cells until mechanical equilibrium is reached. If the space filled by the mother cell is small, which is often the case for cells in the interior of a cell population, the local interaction forces occurring after replacing the mother cell by two spherical daughters, can adopt very large (unphysiological) values leading to unrealistic large cell displacements. This might partially be circumvented by intermediately reducing the forces between the daughter cells. Finally, we note that the direction in which the cell divides may be chosen randomly, according to biological principles of the cells' environment, or according to stress principles (see virial stress principle in the following subsection).

During their cycle, cells take several decisions depending on certain external factors. In e.g. contact inhibition, the cell cycle progression is controlled by the presence of other cells. Contact inhibition can be included in the model computing quantities for cell deformation, volume compression, or force and stress thresholds, each of which have proven to qualitatively predict growth limitation in tumor models [112, 38, 19, 99, 113, 8, 111, 114]. However, it is generally accepted that these decisions are not taken continuously over the cell cycle but are restricted by checkpoints (e.g. G_1 , G_2 , M -checkpoint). Cells passing G_1 -checkpoint are committed to pass the entire cell cycle.

If a cell dies, it will gradually loose its volume as a consequence of lysis and/or phagocytosis. In *in vivo* situations, macrophages are present to phagocytose the cell bodies, and the remains of the necrotic cell will be removed relatively quickly. This process may be modeled as a simple stochastic annihilation process with a certain waiting time T_{lys} , after which the cells is completely removed. Contrary, in *in vitro* experiments, there may be no macrophages present and phagocytosis by neighboring cells is much slower [40]. Here we could chose for a gradual decrease of the cell volume according to

$$\frac{dV_i}{dt} = -\beta_i, \quad (2.12)$$

with $\beta_i = 1/T_{lys}$. Depending on the situation, T_{lys} may range from several hours to several days [26]. Modeling of cell lysis is also further treated in chapter 5 and Appendix C.1.3.

Measures for deformation, stress and pressure: There are several possibilities to compute stresses and deformation in CBM. A straightforward quantity for deformation is the overlap function δ (see Eq. 2.5). This definition has been used in e.g. [111] to model contact inhibition effects in tumor spheroids. Alternatively, one can use contact forces and surface (contact) areas to calculate different pressure-related quantities (see [113, 99, 114]). The disadvantages of these measures is that they only give a scalar measure but do not allow to calculate an entire stress tensor as in continuum theories.

An estimation of a full cellular stress tensor can be obtained by introducing the concept of *virial stress*, deduced from theories in molecular dynamics to compute macroscopic stress originating from the interaction of many particles in a box [115]. The general formulation of virial stress let us compute

the average stress¹ in a box of particles due to contact forces \mathbf{F}_{ij}^{int} with other particles. Here, we introduce it (i.e. [Van Liedekerke et al., 2015]) for one cell i :

$$\boldsymbol{\sigma}_i = \frac{1}{V} \sum_j (\mathbf{F}_{ij}^{int} \otimes \mathbf{r}_{ij}), \quad (2.13)$$

where $\mathbf{r}_{ij} = \mathbf{r}_j - \mathbf{r}_i$ and V is the *sampling* volume. In molecular dynamics simulations this volume needs to be large to obtain ensemble averages of particles, yet here we use it as an estimator for individual cell stresses, by taking the sampling volume as the volume of the cell, and taking \mathbf{r}_{ij} as the vector pointing from the center of cell i to the contact plane with cell j , i.e. $\|\mathbf{r}_{ij}\| = (d_{ij} + R_i - R_j)/2$. The hydrostatic pressure p_i on a cell can then be computed by:

$$p_i = \frac{1}{3} \text{tr}(\boldsymbol{\sigma}_i). \quad (2.14)$$

Eq. 2.13 defines a full stress tensor for the cell, which in principle allows extraction of more information than just a pressure. From the stress tensor, we can also derive the principal stress directions $\{n_1, n_2, n_3\}$ and eigenvalues $\{\sigma_1, \sigma_2, \sigma_3\}$ by diagonalization of Eq. 2.13, yielding important information on how stresses on the cells are oriented. The applicability of this formula is discussed in [Van Liedekerke et al., 2015, Van Liedekerke et al., 2018a].

2.2.3 Deformable Cell Models

In recent years, a number of authors has introduced a series of models which can be generally categorized as Deformable Cell Models (DCM). Force-based deformable cell models (DCM) are able to capture the complex shapes of cells and quantify forces in great detail [Van Liedekerke et al., 2015]. In the basic model construction, the cell body is discretized by a number of nodes which are connected by viscoelastic elements, thus creating a scaffolding structure with a large degrees of freedom. Significant research has been conducted for models of multicellular spheroids, invasive tumors as well as normal development of epithelial ductal monolayers [116, 117, 118, 119, 120]. Deformable models of erythrocytes are popular in blood flow simulations [121, 122, 123, 124, 125]. Other topics include cell migration [126, 127, 128], cell rheology [129] or impact dynamics studying damage in cellular tissues [Van Liedekerke et al., 2010b, Van Liedekerke et al., 2011]. Because they in principle can describe cellular mechanics at subcellular detail, it could be argued that deformable cells models provide an ideal tool to investigate mechanotransduction, the mechanism by which cells transduce an external mechanical stimulus into an internal molecular signal. In the section 2.3.2, we give the basic ingredients for our prototype deformable cell model.

2.2.4 Hybrid models

In case one faces to model large multicellular systems or entire tissues, agent-based simulations can become computationally infeasible. One way to alleviate this, is to resort to continuum models. Continuum models are not concerned with individual cells and have no intrinsic scale, hence tissue scale simulations pose in principle no feasibility problems. In recent times however, increasing effort is put into combining strengths of continuum and discrete models. Hybrid models can bring solutions in problems where regions with a “high” and “low” information requirement can be identified. For example, a hybrid mechanical coupling scheme for tumor growth was explored in Kim et al. (2007) [28] who proposed a domain decomposition whereby the active regions (proliferating cells) were represented by agents while the passive tissues (ECM, necrotic zone) were modeled

¹This formula is not complete as the general formula of viral stress includes a kinetic term related to the temperature of the molecular particle system. For a system of cells however, the latter term can be neglected and the stress corresponds to the Cauchy stress of the microscopic system [Ghysels et al., 2009].

by the Finite Element Method discretization of a PDE governing the behavior of an elastic material. Generally, the formulation of hybrid models heavily depends on the conservation laws (mass, momentum, energy) and the key to success of the coupling is an adequate mapping between the constitutive behavior and the averaged discrete variables with respect to growth kinetics, rheology, etc [113, 9, 130, 131, 132, 133, 25, 134]. Here still much research is needed.

Finally, we note that hybrid modeling is not restricted to discrete-continuum systems. It can be applied to any model with sub-model components that are described with a different detail. For example, in chapter 5 we present a working coupling between a CBM and a DCM.

2.3 New model developments and concepts

2.3.1 SPH as a method to model cellular tissues and ECM

The Lagrangian character of SPH allows to naturally capture discrete processes in a continuum material. Being a meshless Lagrangian method, SPH is naturally well suited for situations involving large deformations, impact, fracture and free surfaces [30, 135]. SPH is a robust and suitable method for modeling of fluids and elastic solids (e.g.[136, 137, 138]). It is known to have good conservation properties. Standard SPH formulations may suffer from some notable downsides too. SPH has yet no clear mathematical convergence study so the reliability of method relies mainly on comparison with analytic solutions or empirical tests. Furthermore, imposing correct boundary conditions and avoiding particle clustering in SPH may need special attention [139, 140]. There are several correction mechanisms available and still being developed to cope with these problems, usually at the expense of a higher computational cost. SPH can be computationally more expensive than mesh-based methods such as FEM, although the latter may require re-meshing in order to deal with (very) large deformations or occurring free surfaces, thereby reducing its efficiency.

In this section, I first introduce some basic properties of SPH which are applied in the model of cellular tissues composed of parenchyma cells (see chapter 3). Secondly, I explain a proposed SPH scheme in over-damped form (cfr. the equations of motion for cells) which was meant to speed up the computations in low Reynolds number fluid problems. Thirdly, I demonstrate how we further extended this SPH formulation for viscoelastic solids to explicitly model stress fields in ECM due to cell-extracellular matrix interactions and ECM degradation (see chapter 6).

SPH: equations of motion with extensions

I start with recapitulating the standard SPH formalism; more detailed information can be found elsewhere [141]. In SPH, a body volume is subdivided by particles. The SPH equations of motion for a particle are derived from the approximation of a function variable evaluation $f(\mathbf{x}_i)$ using a set of neighboring particles j :

$$f(\mathbf{x}_i) \approx \sum_j \mathcal{V}_j f(\mathbf{x}_j) W_{ij}, \quad (2.15)$$

where \mathbf{x}_i is the position of the particle, and \mathcal{V}_i is the volume occupied by one particle. The approximation function is a kernel $W_{ij} \equiv W(q, s)$ where $q = r_{ij}/s$, where $r_{ij} = \|\mathbf{r}_{ij}\|$ is the distance to another particle and s is the "smoothing" length, representing the domain over which the particle i has interaction with particles j (see Fig. 2.3). The kernel function should be symmetric, normalized, sufficiently smooth, and have compact support. The choice of the kernel function can influence the accuracy of the results and stability of the simulations (e.g. [142], [Van Liedekerke et al., 2013]). The summation in Eq. 2.15 is over all particles which fall in the influence sphere with radius s_{max} of particle i , including its own contribution. Using the identity $\mathcal{V}_i = m_i/\rho_i$, this definition leads to the relation between the particle masses m_i and the local density ρ_i :

$$\rho_i \approx \sum_j m_j W_{ij}. \quad (2.16)$$

Similarly, the gradient of a function variable can be calculated²:

$$\nabla f(\mathbf{x}_i) \approx \sum_j \mathcal{V}_j f(\mathbf{x}_j) \nabla_i W_{ij}. \quad (2.17)$$

Using the relations Eq. 2.15 and Eq. 2.17, one can derive a basic particle based equation of motion from the continuum momentum Eq. 1.3:

$$m_i \frac{d\mathbf{v}_i}{dt} = -m_i \sum_j m_j \left(\frac{\sigma_i}{\rho_i^2} + \frac{\sigma_j}{\rho_j^2} \right) \nabla_i W_{ij}, \quad (2.18)$$

with σ_i the particle stress tensor expanded as:

$$\sigma_i = -p_i \mathbf{I} + \mathbf{S}_i, \quad (2.19)$$

where p_i is the hydrostatic pressure tensor and \mathbf{S}_i is the deviatoric stress tensor. We can write the equation of motion including external forces for a particle i condensed as

$$m_i \frac{d\mathbf{v}_i}{dt} = \mathbf{F}_i^p + \mathbf{F}_i^v + \mathbf{F}_i^{ext} \quad (2.20)$$

where \mathbf{F}^p , \mathbf{F}^v , and \mathbf{F}^{ext} are the conservative term, the dissipative term, and the external force term on the particle.

For fluids, a particle model can be derived for incompressible or weakly compressible Navier-Stokes equations. In the former, this requires a solution for the pressure Poisson's equation to ensure that $\nabla \cdot \mathbf{v} = 0$ (see [143]). In the weakly compressible SPH method, one uses an equation of state $p = p(\rho)$ to maintain a relation between the pressure and the density, e.g.

$$p = p_0 + c_0^2(\rho - \rho_0), \quad (2.21)$$

or alternatively

$$p = p_0 + K \left[\left(\frac{\rho}{\rho_0} \right)^7 - 1 \right], \quad (2.22)$$

where ρ_0 is a reference density, c_0 is the speed of sound in the fluid, and K is the compression modulus of the fluid. This means that small density fluctuations are allowed and appear as pressure fluctuations. Note that the relation between K and c is given by $c = \sqrt{\left(\frac{\partial p}{\partial \rho} \right)}$.

For Newtonian fluids, we have $\mathbf{S} = \mu \mathbf{D}$ where μ is the viscosity and $\mathbf{D} = \frac{1}{2}(\nabla \mathbf{v} + \nabla \mathbf{v}^T)$ is the strain rate tensor, computed using the SPH approximation of the derivatives:

$$\nabla_i \mathbf{v}_i = \sum_j \frac{m_j}{\rho_j} (\mathbf{v}_i - \mathbf{v}_j) \nabla_i W_{ij}. \quad (2.23)$$

Despite this straightforward formula, authors have introduced other friction formulations giving

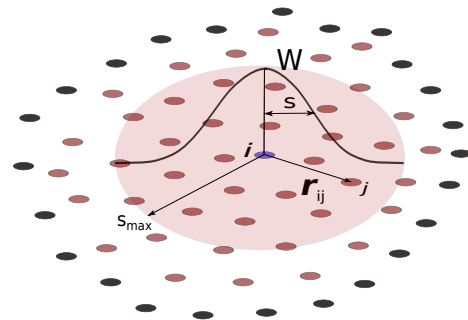


FIGURE 2.3: The SPH Kernel interpolation function (black curve). Field variables for a particle are obtained using the interpolant $W(r_{ij}, s)$. The red particles represent fluid, whereas the black particles represent a boundary.

²Note here that $\nabla_i W_{ii} = 0$.

more stable results. Morris et al. (1997) [142] proposed to use the following friction force

$$\mathbf{F}_i^v = m_i \sum_j m_j \left(\frac{\mu_i + \mu_j}{\rho_i \rho_j} \right) \frac{1}{r_{ij}} \frac{\partial W_{ij}}{\partial r_{ij}} \mathbf{v}_{ij}, \quad (2.24)$$

while Monaghan et al. (2012) [30] used:

$$\mathbf{F}_i^v = m_i \sum_j \chi \frac{m_j}{\rho_i \rho_j} \left(\frac{\mu_i \mu_j}{\mu_i + \mu_j} \right) \frac{1}{r_{ij}} \frac{\partial W_{ij}}{\partial r_{ij}} (\mathbf{v}_{ij} \cdot \mathbf{e}_{ij}) \mathbf{e}_{ij}, \quad (2.25)$$

where $\mathbf{e}_{ij} = \mathbf{r}_{ij}/r_{ij}$ and χ is a fitting constant. A fundamental difference between the two approaches is that the first does not conserve angular momentum of the system, because the friction term $\mathbf{F}_i^v \sim \mathbf{v}_i - \mathbf{v}_j$. Hence, pure rotations of particle pairs are penalized by a friction force. The second formulation does not have this problem, as only the perpendicular term is considered (see Eq. 2.4) and angular momentum is conserved.

In fluid mechanics, the mass conservation of the system is imposed by the continuity equation. The SPH approximation of the continuity equation reads

$$\frac{d\rho_i}{dt} = \sum_j m_j (\mathbf{v}_i - \mathbf{v}_j) \cdot \nabla_i W_{ij}. \quad (2.26)$$

However, the mass of a system is not always preserved. For instance, the fluid mass of the cell is not a priori constant, as water can be transported through so-called aquaporina. Therefore we have extended the continuity equations by introducing an additional source term that reflects fluid mass gain or loss during growth or osmotic effects in cells (see chapter 3). Consider the differentiation of the density formula:

$$\begin{aligned} \frac{d\rho_i}{dt} &= m_i \frac{d}{dt} \left(\frac{1}{\mathcal{V}_i} \right) + \frac{1}{\mathcal{V}_i} \frac{dm_i}{dt} \\ &= \underbrace{\frac{d\rho_i^*}{dt}}_{\text{velocity change}} + \underbrace{\frac{\rho_i}{m_i} \frac{dm_i}{dt}}_{\text{mass change}}. \end{aligned} \quad (2.27)$$

The first term is the change in density due to the deformation of the cell volume, given by Eq. 2.26, while the second term $\sim dm_i/dt$ can be attributed to a change in water content of the cell.

Simulation of over-damped motion with SPH: NSPH

Numerical algorithms for microscopic generally require a small timestep, while the timescale of the evolution of the system may cover several orders of magnitude ($> 10^9$) of this time-step. The normal SPH equations are usually integrated with the well-known second order "Leapfrog" scheme which has excellent energy conservation properties. However, due to the parabolic term in the N-S equations, the viscous diffusion poses restrictions on the timestep:

$$\delta t \leq 0.125 \frac{s^2 \rho}{\mu}, \quad (2.28)$$

where ρ is the density and μ is the dynamic viscosity of the medium. The restriction becomes problematic at small dimension ($s \ll 1$). Let us consider the example of a cell moving in a fluid. If the cell is discretized by particles with a realistic spacing of $\sim 0.1 \mu\text{m}$ in an aqueous medium ($\mu = 5 \text{ mPa} \cdot \text{s}$),

this yields $\Delta t \leq 10^{-9}$ s. This implies a huge number of calculations if the timescale of interest is of the order of 1 h. To circumvent this, some authors have made advances to make algorithms faster (e.g. in [144] a splitting scheme was proposed for SPH). However, [Van Liedekerke et al., 2013] have proposed to rather start from the Stokes equations and formulate them in the SPH formalism (called further NSPH). Let us assume a system that is friction dominated (see also section 2.2.2) so that we can explicitly omit the inertial term in Eq. (1.3). We arrive at the Stokes's equations with external force field \mathbf{F}^{ext} :

$$\nabla p - \mu \nabla^2 \mathbf{v} = \mathbf{F}^{ext}. \quad (2.29)$$

Introducing the volume $\mathcal{V}_i = m_i/\rho_i$ and assuming for simplicity that $m_i = m_j$, the equivalent NSPH creeping flow equations for a particle i read:

$$-\sum_j (\Gamma_{ij}^\perp + \Gamma_{ij}^\parallel) \mathbf{v}_{ij} = \sum_j (p_i \mathcal{V}_i^2 + p_j \mathcal{V}_j^2) \nabla_i W_{ij} + \mathbf{F}_i^{ext}. \quad (2.30)$$

We have introduced a split up of the friction matrix Γ_{ij} in the perpendicular and parallel friction matrices $\Gamma_{ij}^\perp = \gamma_\perp (\mathbf{e}_{ij} \otimes \mathbf{e}_{ij})$, and $\Gamma_{ij}^\parallel = \gamma_\parallel (\mathbf{I} - \mathbf{e}_{ij} \otimes \mathbf{e}_{ij})$ respectively. In this regard, the friction formulation (Eq. 2.25) has $\gamma^\parallel = 0$. This linear system of equations is formally the same as the equations of motion for a center-based cell model (see Eq. 2.3). For instance, if we consider the SPH friction model Eq. 2.24, then the friction matrix can be defined as:

$$\Gamma_{ij} = (\mu_i + \mu_j) \frac{\mathcal{V}_i \mathcal{V}_j}{r_{ij}} \frac{\partial W_{ij}}{\partial r_{ij}} \mathbf{I}. \quad (2.31)$$

The proposed NSPH approach has been shown to reproduce the results of ordinary SPH simulations of Poiseuille flow, Couette flow, and flow past an array of cylinder.

Simulation of viscoelastic extracellular matrix with NSPH

We have further exploited the advantages of (N)SPH proposing a general model for viscoelastic media such as Extracellular Matrix (ECM) [Heck et al., 2017]. Let us regards the ECM as a linear elastic material. To incorporate elastic forces in the SPH equations we define the particle deviatoric elastic stress (Eq. 2.19) according to Hooke's law:

$$\mathbf{S}_i = 2G \left(\frac{1}{2} \boldsymbol{\epsilon}_i - \frac{1}{3} \mathbf{I} \nabla_i \cdot \mathbf{x}_i \right), \quad (2.32)$$

with G the shear modulus and $\boldsymbol{\epsilon}_i = \frac{1}{2} (\nabla \mathbf{x}_i + \nabla \mathbf{x}_i^T)$ the strain tensor. To preserve rotational invariance, one calculates the Jaumann rate of change of the deviatoric stress:

$$\frac{d\mathbf{S}_i}{dt} = 2G \left(\frac{1}{2} (\nabla \mathbf{v}_i + \nabla \mathbf{v}_i^T) - \frac{1}{3} \mathbf{I} \nabla \cdot \mathbf{v}_i \right) + \mathbf{S}_i \boldsymbol{\Omega}_i + \mathbf{S}_i \boldsymbol{\Omega}_i^T, \quad (2.33)$$

with $\boldsymbol{\Omega}_i$ the particle spin tensor defined as:

$$\boldsymbol{\Omega}_i = \frac{1}{2} (\nabla \mathbf{v}_i - \nabla \mathbf{v}_i^T). \quad (2.34)$$

Hence, we need an integration scheme for $d\mathbf{S}_i/dt$ to obtain the actual deviatoric stress. The pressure components and viscous components of the stress tensor are computed as in the SPH formulas for fluids. However, we use the NSPH method to update the positions of the particles which yields a significant speed-up compared to the normal SPH equations.

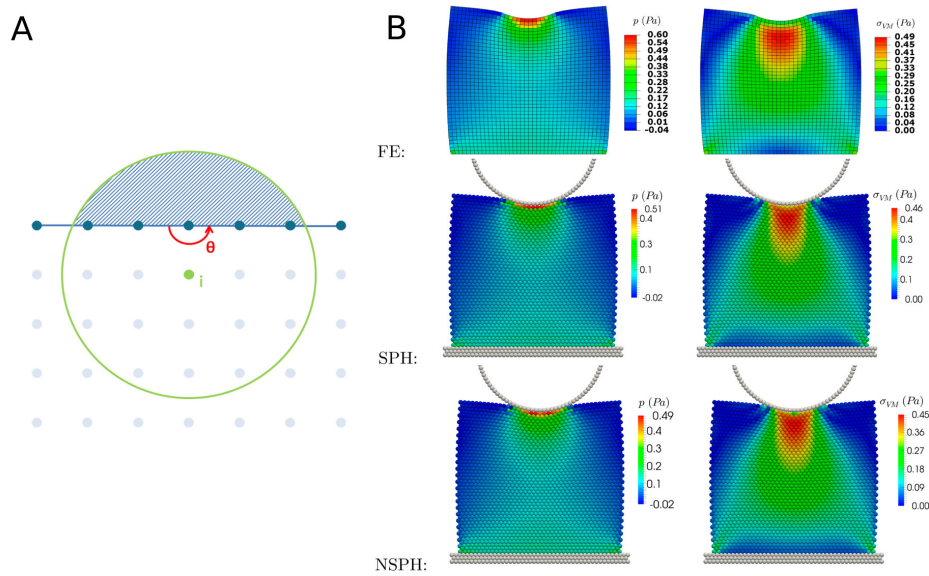


FIGURE 2.4: (A) Illustration of the boundary situation in (N)SPH. The boundary is represented by blue particles and line segments. For a material particle close to the boundary the kernel is not completely filled and information from the hatched area is missing. (B) Comparisons of hydrostatic pressure in Pa (left) and von Mises stress distribution in Pa (right) at steady state for indentation of a circular indenter in a viscoelastic solid modeled by means of FE (top), SPH (middle) and NSPH (bottom). The mutual errors are mostly around 5%.

One of the most challenging parts of (N)SPH is to treat boundary conditions correctly. This difficulty comes from the fact that the SPH formulation is based on the assumption that the smoothing kernel applied is completely occupied by neighboring particles. However, particles close to a rigid boundary miss a part of the kernel support and therefore the error in calculating hydrostatic pressure and deviatoric stress is largest for these particles (see Fig. 2.4A). Since the cell–ECM boundary is an important regulator for cell adhesion and force generation and since the force and displacement fields near the cell–ECM boundary are most interesting from a cellular mechanics point of view, an adequate treatment of these boundary conditions is necessary. We used the boundary condition correction proposed by and Ferrand et al. (2013) [145] and extended it to model the contact between a viscous fluid or a viscoelastic solid and a rigid yet moving object. We successfully tested the method in (N)SPH by comparing the stress field during indentation of body in an elastic medium with FE simulations performed in Abaqus (see Fig. 2.4B). A prototype model for a cell migrating in degradable elastic matrix in further proposed in chapter 6.

2.3.2 Deformable Cell Model: towards high resolution multi-cellular simulations

Our concept of a Deformable Cell Model (DCM) is inspired on an earlier model for parenchyma cells introduced by [Van Liedekerke et al., 2010b], and a red blood cell model for blood flow simulations [123]. In [Odenthal et al., 2013] we further elaborated on the model to simulate single cell spreading dynamics; in [Van Liedekerke et al., 2018b] we have extended it to perform multi-cellular simulations. In our DCM the cell surface is discretized with an arbitrary number of nodes, connected by viscoelastic elements. The nodes at the cell surface form a deformable triangulated structure, accounting for the mechanical response of the membrane and the cortical cytoskeleton (see Fig. 2.5A). We primarily assume that the content of the cell is homogeneous and can be regarded as a compressible fluid. The total force on each node originates from interactions with other cells and intracellular interaction forces, the latter reflecting membrane and cortex mechanical behavior, and cell volumetric

changes. Despite the similarities with a model introduced by Sandersius et al. (2008) [11], we note that our model is different because we clearly distinguish the cell boundary structure (cortex) from the interior of the cell. On the other hand, it also differs from so-called Vertex Models (VM) [2, 146], in which the vertices form a polygonal tessellation (usually Voronoi) which directly represents the common cell-cell interfaces. I will give here a short description of a basic 3D model. Equivalent force components can be formulated for a 2D model as well.

Forces and equation of motion: The equation of motion in DCM has formally the same form as the center-based model (Eq. 2.3) but must now be applied to each node i of a cell³:

$$\Gamma_{ns,i} \mathbf{v}_i + \sum_j \Gamma_{nm,ij} (\mathbf{v}_i - \mathbf{v}_j) = \underbrace{\sum_j \mathbf{F}_{ij}^e}_{\text{in-plane}} + \underbrace{\sum_m \mathbf{F}_i^m}_{\text{bending}} + \underbrace{\mathbf{F}_i^{vol}}_{\text{volume change}} + \underbrace{\sum_T \mathbf{F}_i^T}_{\text{area correction}} + \underbrace{\mathbf{F}_i^{rep} + \mathbf{F}_i^{adh}}_{\text{contact}} + \underbrace{\sum_i \mathbf{F}_i^{mig}}_{\text{migration}} \quad (2.35)$$

with \mathbf{v}_i denoting the velocity of node i , and the matrices Γ_{ns} and Γ_{nm} representing node-substrate friction and node-node friction, respectively (see Eq. 2.4). Importantly, friction between nodes belonging to the same cell and nodes belonging to different cells must be distinguished here. The first and the 2nd term on the rhs (\mathbf{F}^e and \mathbf{F}^m) represent the in-plane viscoelastic forces and bending force associated with the cortex. The third term (\mathbf{F}_i^{vol}) is a volume-change force controlled by the cell compressibility. The fourth force (\mathbf{F}_i^T) term originates from resistance against area expansion of the cell membrane. The force terms (\mathbf{F}_i^{adh} , \mathbf{F}_i^{rep}) describe the adhesion and repulsion contact forces on the local surface element in presence of nearby objects as e.g. another cell (see below). Different from CBMs, the cell bodies in contact do not overlap and therefore triangles belonging to different cells will be repelled upon approaching each other. Finally, the migration force \mathbf{F}^{mig} is an active force which can be modeled in the same way as for a center-based model, as a uniform force equally distributed on all the nodes. The DCM however allows to simulate migration in a highly detailed way, involving complex mechanisms as protrusion formation and cell contractility [126, 147].

Contact model: Maugis-Dugdale theory: In a CBM, the computation of a contact force between two cells is rather straightforward as it is a central force between the cell centers. In a DCM on the other hand, forces for each node-node interaction (\mathbf{F}_i^{adh} , \mathbf{F}_i^{rep}) have to be calculated. Often pairwise potential functions (Van der Waals, Morse) between nodes are used to mimic the effect of short range repulsion and long ranged attraction force [148, 119, 129, 120]. While straightforward to implement, this approach poses problems with respect to the scalability and calibration of the parameters for these potentials.

The approach proposed in our work (i.e. [Odenthal et al., 2013, Smeets et al., 2014]) is different and based on the Maugis-Dugdale theory for adhering bodies which is a generalization of the JKR theory for spheres [149]. This theory captures the full range between the Derjaguin-Muller-Toporov (DMT) zone of long reaching adhesive forces and small adhesive deformations to the Johnson-Kendall-Roberts (JKR) limit of short interaction ranges and comparatively large adhesive deformations in a transition parameter called the Tabor coefficient. Our model is basically a discretization of this continuum theory. For each triangle of the cell, we compute a local curvature and assign it with a circumventing sphere. Two triangles interact by collision of their assigned circumventing spheres. To obtain the interaction forces we compute the Maugis-Dugdale stress for all contacting triangles. The parameters in our model (adhesion energy and interaction range) do not need to be calibrated as they are the same as those in the Maugis-Dugdale formula. Another important advantage of this interaction model is that it permits, in a natural way, to model interactions between a triangulated body and a smooth surface such as a sphere or plane having a fixed curvature. This further permits

³The cell index has been dropped here for clarity.

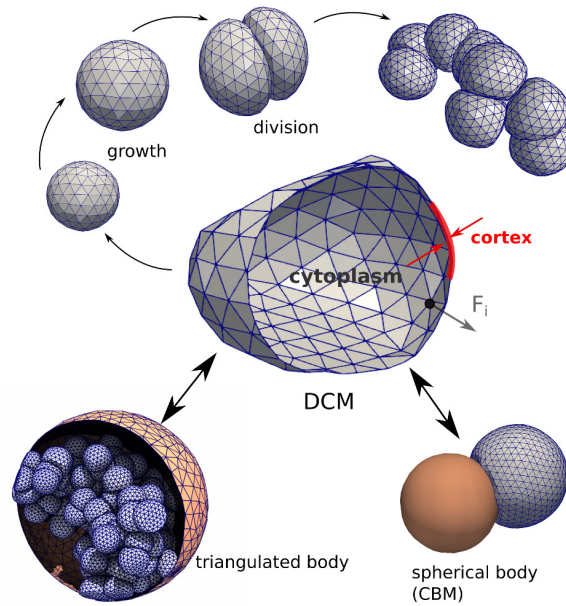


FIGURE 2.5: The force-based Deformable Cell Model (DCM) and its basic components and functionality used in this work. A cell is represented by a viscoelastic triangulated shell (cortex) containing a compressible cytoplasm (center). The cells can grow until they split into two new cells, eventually creating a clump of adhering cells (top). Each nodal point of the cell move according to an equation of motion in response to a force F_i . The cells can interact with other triangulated bodies or simple geometric bodies such as a center-based model (bottom).

development of hybrid models of DCM with a center-based model. We refer to Appendix B.1.2 for more details.

Cell growth, mitosis, and death: During cell division, a process called cytokinesis, the continuous shrinking of the contractile ring, together with the separation of the mitotic spindle, slowly create the new daughter cells. After mitosis the cell has split up in two daughter cells which are adhering to each other.

Division of individual, isolated cells displaying arbitrary cell shape has been modeled by a number of authors (e.g.[120, 150, 151]), whereby in ref. [120, 152] the mechanical processes leading to cytokinesis have been explicitly considered. All of these models are two dimensional. Growth and division in three dimensional triangulated cells turns out to be challenging with regard to both the algorithms and the computational time.

In our new model [Van Liedekerke et al., 2018b] growth is mimicked by adapting the cells' viscoelastic elements to the new intrinsic size and volume so that no artificial stresses are built up in the cell. During division, new nodes must be created so that the total number of nodes per cell remains constant. However, contrary to the aforementioned works, we have chosen to not explicitly model the mechanical force and processes during cytokinesis. Mitosis and cytokinesis together take about 1h compared to the duration of the cell cycle $\sim 24h$ in most mammalian cells, hence are very short events. To increase the computational feasibility, we mimic cell division by a creation of two spherical daughter cells, separated by a division plane, for which the nodes are projected on the surface of the mother cell (see Fig. 2.6). After the cocoon of the mother cell is removed, we obtain a system of two cells that in mechanical equilibrium with their environment. When a cell dies, it can be either removed instantly from the simulation, or gradually shrink (lysis). Algorithm-wise, lysis can be regarded as the inverse of the growth process. We refer to the Appendix, section B.2 for more details

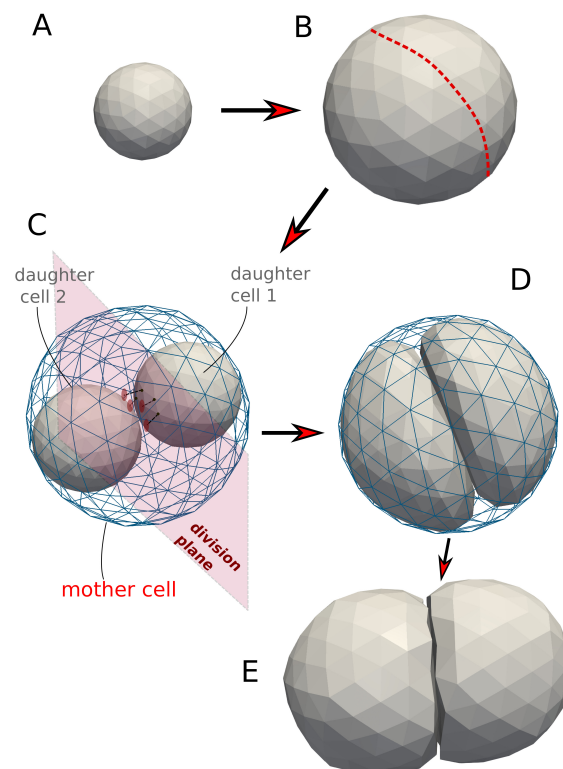


FIGURE 2.6: Model algorithm of the cell cycle for deformable cells: (A-B) Cell growth (double volume by increasing the radius). (B) Choose division direction randomly (assign nodes to one side). (C) Add two default cells as daughter cells to center of masses. Project nodes of the daughter cells to surface of division plane if they intersect it. A sub-simulation is run to come rapidly to situation D. (D) After the sub-simulation, mother envelope is removed. (E) Division stage finished: two mechanically relaxed daughter cells.

of the implementation.

2.3.3 Models for cell migration and invasion in ECM

Cell migration is a complex process, in which cells polarize, elongate, form blebs or express pseudopods that allow it to extend material forward, followed by a backwards retraction resulting in a net motion forward [153, 154, 155]. It occurs during normal cell morphogenesis and wound healing, and also in malignant cells. Migration of cells embedded in 3D extracellular matrix (ECM) requires cells to "invade" this matrix. During invasion cells may undergo very large deformations, or exhibit proteolysis of the extracellular-matrix components.

Single cells actively migrating through a medium can be roughly divided in two modes. In the *amoeboid-like* migration, membrane blebs (balloons) are formed resulting in small protrusions, while other parts of the cells are contracting. A *mesenchymal* phenotype on the other hand, is characterized by an elongated ("spindle-shaped") cell body and longer protrusions or filopodia which work as "arms" that reach out and can pull the cell in a certain direction. They attach to the ECM forming a focal adhesion site that connect the cytoskeleton to transmembrane receptors (integrins) [3]. In this type the cell cytoskeleton is highly organized and exhibits stress fibers. The micro-environment can influence the mode, for instance in cancer cell migration [155].

Cell migration can also be established as a multi-cellular coordinated process, for example in malignant tumors and angiogenesis [156, 157]. Collective cell migration is a complex process which is characterized by groups of cells that hold cell-cell adhesions for long time periods and show a high correlation in directionality between neighboring cells. Cells can move either as narrow linear strands lead by one "leader cell" or as broad, irregularly shaped sheets, which are multiple cells in diameter and lead by several leader cells. Finally, communication between cells may also be established through mechanical signals in the matrix [158].

Modeling the mechanics of cell migration with agent-based models can improve our understanding of the processes. However, simple rigid shaped center-based models in which the migration force is modeled as a body force (section 2.2.2) will not suffice here. Therefore, some authors (e.g. [147, 128, 159, 160]) introduced deformable cell model types for cell migration with a description of protrusion formation and ECM. These have led to a high realism of the simulations, yet they are limited to few cells. Hence, these model types are currently less suited to simulate the effects in e.g. multi-cellular invasion.

In a collaboration with Dr. Habil. D. Drasdo (INRIA), Dr. Andreas Buttenschon (U. British Colombia) and Dr. Magriet Palm (U. Leiden), we propose an "interim" model that aims to overcome the limitations in simulating migration of large cell populations, while maintaining sufficient detail to capture the mechanics of a migrating cell. Our aim here is to eventually simulate invasion patterns in multi-cellular spheroids. Inspired by the observation that invading cells adopt elongated shapes (see Fig. 2.7), the cells in our model are represented as **rods**. The model mimics a mesenchymal behavior of the cell and its shape can vary from a rounded cell to an elongated, polarized cell. As such it can be regarded as an interim model between center-based and a full deformable model. Our model permits to simulate the interactions of a cell with a viscoelastic, heterogeneous ECM. The ECM is represented by a viscoelastic network of springs of which the stiffness and pore size is changeable. The cells can spread small protrusions or filopodia that anchor to the ECM through focal adhesions, and subsequently pull the cell in a certain direction. The cells are able to locally degrade matrix through expression of matrix metalloproteinases (MMPs). As the model is still in a test phase, I will here only describe the key ideas and functionality of the model for a one cell; the model will be extended in the near future to permit interactions with other cells.

Basic cell model, forces and geometry: The cell shapes are described by rods, cylinders of variable length L with spherical caps with radius R on both sides, see Fig. 2.8A. Each cell body also encompasses a spherical nucleus of size R^{nuc} which coincides with the center of the cell. We assume that the

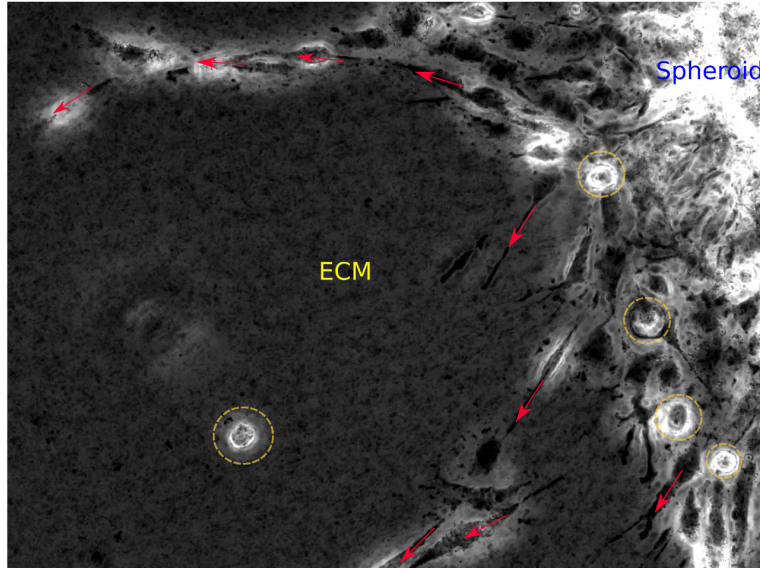


FIGURE 2.7: Live image of an invading spheroid embedded in ECM. The cells with a red arrow are elongated (rod-like) and move in the arrow directions. The cells indicated with a circle have rounded up. Credit: Philippe Chavrier, Institut Curie.

cells approximately conserve their volume. The geometry of the cell depends on the forces exerted on the cell and can change during the course of the simulation. The cell further has a polarization vector \mathbf{P} , which defines the region and angle in which protrusions can be expressed. The orientation of the cells is generally determined by the angles θ and ϕ , however in this work we assume the cells move in a plane (i.e. $\theta = 0$ and $\phi \in [0, 2\pi]$).

Similar as for the center-based model, the change of center-of-mass position of each cell i is obtained by integrating an over-damped Langevin-type equation of motion (see Eq. 2.3). The center-of-mass velocity of a cell i is obtained from following force-balance equation due to interactions with its environment and other cells j :

$$\mathbf{\Gamma}_i^{\text{med}} \mathbf{v}_i + \sum_{k \text{ nn } i} \mathbf{\Gamma}_{ij}^{\text{cn}} (\mathbf{v}_i - \mathbf{w}_k) = \sum_j \mathbf{F}_{ij}^{\text{cyt}} + \sum_j \mathbf{F}_{ij}^{\text{nuc}} + \mathbf{F}_i^{\text{pro}} + \boldsymbol{\eta}_i, \quad (2.36)$$

with on the left hand side three friction terms, respectively cell-medium friction, cell-node friction, cell-cell friction, and on the right hand side the forces acting on the cell. \mathbf{v}_i and \mathbf{w}_i denote the velocities of the cells and nodes respectively. The cell-medium friction matrix $\mathbf{\Gamma}_i^{\text{med}}$ arises from the isotropic viscous interaction of the cell with the gel like material formed by glycosaminoglycans and water (excluding collagen fibres). The second friction term, cell-node friction, accounts for explicit cell-fiber friction. The friction matrices are constructed similarly as for a CBM. The terms on the rhs. summarize the forces between a cell and ECM nodes that consist of the interaction force between a node and the cell cytoplasm \mathbf{F}^{cyt} , which is a relatively soft interaction, and a force \mathbf{F}^{nuc} between a node and the cell nucleus if the node further penetrates into cytoplasm (note that the nuclei of the cell are assume much stiffer than the cytoplasm). The interaction forces are computed using JKR or Hertz' theory for soft adhesive objects. The force between the cell cytoplasm and ECM node consists of an adhesive and a repulsive part and their components are directed along the normal vector of the intersection plane, e.g. $\mathbf{F}_{ij}^{\text{cc}} = \mathbf{n}_{ij} (F_{ij}^{\text{adh}} + F_{ij}^{\text{rep}})$. The interaction force between the cell nucleus and a node can only be repulsive. The exact expressions for F_{ij}^{rep} and F_{ij}^{adh} depend on the local geometry and orientation of the objects that interact.

The cells move because (i) active protrusion forces $\mathbf{F}_i^{\text{pro}}$ develop (see below) and (ii) because of a Brownian motion term $\boldsymbol{\eta}_i$ with zero mean and uncorrelated at different points in time (see section 2.2.2), which reflects the passive, random motion of a small object in a liquid. The cells can also

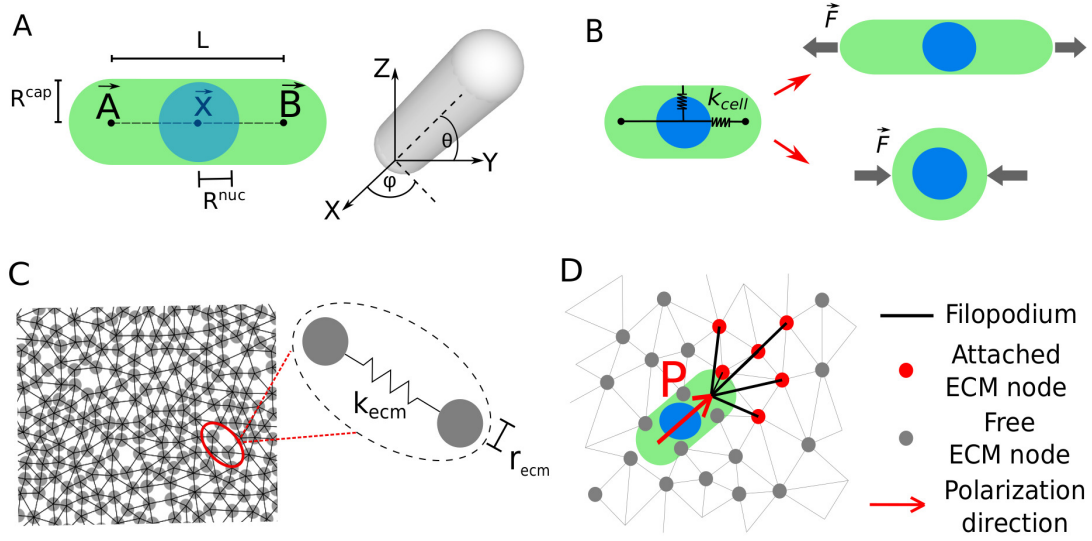


FIGURE 2.8: Overview of model elements. (A) Cells are cylinders with spherical caps with a spherical nucleus in the center. The orientation of the cells is generally determined by the angles θ and ϕ . (B) Cells can deform in response to external forces. In absence of forces they return to a spherical shape. (C) ECM is represented by a network of viscoelastic springs. (D) Cells pull on the ECM with filopodia that are preferentially extended in the polarization direction.

undergo rotational motion, and the orientation of the cell will be obtained by an energy minimizing algorithm [7]. The orientation angle ϕ is changed by considering the potential energy function originating from all the interactions of the cell with nearby obstacles. This energy function is minimized using a Metropolis algorithm.

In our model, a cell can deform in response to the forces that are exerted on it. A free cell in suspension will adopt a spherical shape, yet once this cell expresses protrusion forces with ECM, it can deform into a rod-like shape. To achieve this, we follow the method by Palsson et al. [161, 162] and assume each cell contains two elastic internal elements, one along the radial the other along the axial axis (see Fig. 2.8D). The length of the axis is denote by L while the cell's radius is denoted by R . These are computed by

$$\begin{aligned}\frac{dL}{dt} &= \frac{1}{\mu} (F_z + F_m + k_{cell}L) \\ \frac{dR}{dt} &= \frac{1}{\mu} (F_r + F_m + k_{cell}(R - R_0)),\end{aligned}$$

where F_r and F_z are the total force components on the radial and axial axis respectively, k_{cell} is the spring stiffness (assumed isotropic) and drives the overall contractile restoring mechanism of the cell. The force term F_m is due to keeping the volume of the cell constant. The rest radius R_0 ensures that in the absence of external forces the cell takes of a spherical shape. The above set of equations is solved subject to that the volume of the rod shaped cell

$$V = \frac{4}{3}\pi R^3 + \pi R^2 L,$$

remains constant. For the original idea, see the model by Palsson [162]. A simulation (see Fig. 2.9D) shows that indeed a cell adopts its shape to the obstruction of a rigid ECM.

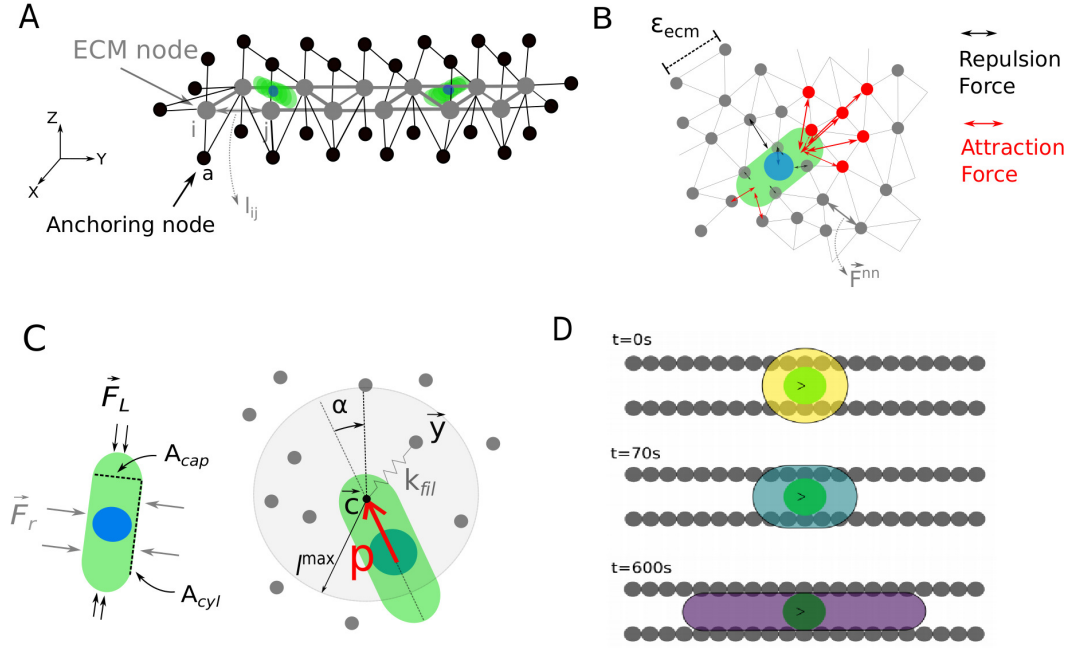


FIGURE 2.9: (A) Model 3D ECM structure with real nodes and anchoring nodes. (B) Forces exerted on a cell in contact with ECM. (C) Definition of radial and axial forces, protrusion range and angle in the cell. (D) Simulation snapshots of a cell being quenched between two ECM "barriers", showing that the cell adopts its shape.

Basic ECM model description: The ECM is represented by a network of nodes that are connected with springs (see 2.9A) resulting in a quasi-3D viscoelastic medium. Each node i is associated to a position \mathbf{y}_i and a list of connected nodes \mathbf{y}_j . We assume cells move in a 2D space. The nodes are generated in a random fashion to avoid lattice artifacts (see [Drasdo et al., 2017]). However, the ECM structure contains also two extra layers of fixed, anchoring nodes (see black nodes in 2.9C). These nodes warrant a 3D elastic behavior of the material. This is certainly needed in the case of matrix degradation by the cells (see below), as a pure 2D structure could fall apart easily. The displacement of a node is described with a force-balance equation:

$$\gamma_m \mathbf{w}_i = \mathbf{F}_i^{nn} - \mathbf{F}_i^{pro}. \quad (2.37)$$

The left hand side of this equation describes the friction force between the ECM node and the medium, with γ_{medium} the friction constant, and \mathbf{w}_i the velocity of ECM node i . We do not incorporate node-node friction in the equation of motion for ECM. The right hand side summarizes the forces acting on the node. The linear elastic force connecting two nodes i and j reads:

$$\mathbf{F}_{ij}^{nn} = -k_{ecm} (\mathbf{l}_{ij} - \mathbf{l}_{ij}^0). \quad (2.38)$$

Here \mathbf{l}_{ij} is the actual connecting vector between the nodes and \mathbf{l}_{ij}^0 the equilibrium vector between nodes i and j . k_{ecm} is the local stiffness of the ECM network. We compute $k_{ecm} = \frac{1}{2}(k_{ecm,i} + k_{ecm,j})$, with $k_{ecm,i}$ and $k_{ecm,j}$ the values of the spring constant assigned to a node i and j respectively. It can be shown that for an isotropic material k_{ecm} can be related to a macroscopic Young's modulus [163].

Cells can degrade matrix in the locality of protrusions (one speaks of "invadopodia"). In our model we permit cells to degrade ECM. When a cell is in the vicinity of a node i , it accomplishes this by decreasing the stiffness value of the node according to:

$$\frac{dk_{ecm,i}(t)}{dt} = -\lambda k_{ecm,i}(t), \quad (2.39)$$

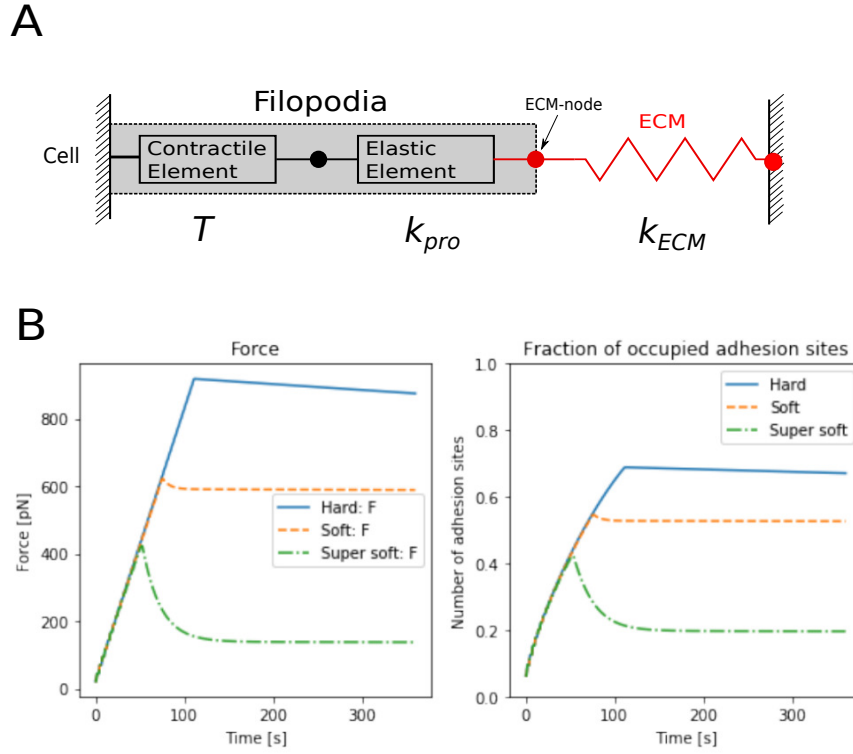


FIGURE 2.10: (A) Schematic representation of the cell protrusion element and anchoring to the ECM node. (B) Simulation of the protrusion element for different ECM stiffness k_{ECM} . Left: force vs. time in the element, right: number of adhesion sites of the protrusion vs. time. The building up of the force stops when $W > W_{max}$.

where λ is the decay rate. Experiments have shown that only membrane tethered MMP's degrade ECM [164, 165, 166, 167] and that ECM degradation is localized at the cell's leading edge [168, 164]. Therefore, we limit ECM degradation to ECM nodes that are in contact with a cell and for which the angle between the polarization vector \mathbf{P} and the vector connecting the ECM node and the cell, is $\pi/4$ or less.

Protrusion forces, mechano-sensing, and cell polarization: The active cell movement is induced by the individual protrusions forces \mathbf{F}^{pro} exerted by the cell to the ECM nodes. Each protrusion starts in one of the end points of the cylinder (points **A** or **B** in Fig. 2.8A) and anchors to an ECM node. Each cell can only extend a limited number of protrusions $N_{pro} < N_{max}$, and can attach to ECM nodes within the distance range l_{max} . The ECM nodes are selected randomly in a region that is formed by a circle with origin **A** or **B** (position of the spherical cap) and radius l_{max} . Protrusion can be formed in all directions when the cell is rounded up, but once a cell becomes polarized, the protrusions are only formed on one side of the cell. The probability of attaching a protrusion to an ECM node depends on the angle α (see Fig. 2.9C) between that protrusion and the polarization vector \mathbf{P} (see below). We assume the probability \mathcal{P}_{attach} is Gaussian distributed:

$$\mathcal{P}_{attach}(\alpha) \sim \frac{1}{\sigma \sqrt{2\pi}} e^{-\frac{\alpha^2}{2\sigma^2}} \text{ with } \sigma = \frac{1}{4}\pi. \quad (2.40)$$

Each protrusion is regarded as a bundle of active microscopic fibers (molecular motors) and is modeled as a unit containing an elastic spring part and a contractile element between the cell and an ECM node (see Fig. 2.10A). The spring element has a specific stiffness k_{pro} . We first let the tension T in the contractile element increased gradually after a protrusion has attached to the ECM. The speed at which the element contracts is a function of a "stall" force F_s : the force at which the fibers can

no longer move [169]. When this stall force is reached in the protrusion, the contraction comes to a halt. After a short resting step, the stalling force is augmented by ΔF_s with $\Delta F_s \sim 20 \text{ pN}$ because the bundles are reinforced [170, 171]. In line with the observations in Wolfenson et al. [170], the resulting protrusion force F^{pro} will be increased by $\sim \Delta F_s$ after every cycle. Every time the force is increased, we need to assume that the number of adhesive integrin bonds in the focal adhesion site increases, otherwise the adhesion complex will get ruptured. Each integrin bond is a receptor-ligand pair for which the formation or annihilation is a stochastic process, which in principle could be simulated by a master equation. The dynamics of a single bond could be naively described by Bell's equation [172], for which the lifetime drops exponentially with the applied force. However, so-called "catch bonds" (see e.g. [173]) seem to yield a more realistic dynamics. Counter-intuitively, a catch bond lifetime initially increases when a force is applied. The bond lifetime of a catch bond is maximal at some finite force, after which it decays again exponentially. Stochastic simulations could in principle yield the accurate growth kinetics of a catch-bond cluster, although they should take into account the whole process of cluster growth and maturation. In addition, the process seems to be greatly influenced by the loading mode (uniform or non-uniform) of the focal adhesion [174]. Mean-field approaches can estimate the number of adhesive bonds as a function of the applied protrusion force [174]. In our initial model, we have used such a mean-field approach (see for example Fig. 2.10B, right), although we still assume the focal adhesion cluster has a fixed lifetime T_{pro} .

The mechano-sensing of the cell with regard to the ECM stiffness is as modeled as follows: we assume for each protrusion only a limited amount of work (energy) can be accomplished by the cell. It can be proven that for the total work W done by a protrusion [174]:

$$W \sim \frac{(F^{pro})^2}{2K_{eff}}. \quad (2.41)$$

Here K_{eff} is the effective system stiffness, i.e. $1/K_{eff} \sim 1/k_{ECM} + 1/k_{pro}$. Hence, if we assume k_{pro} remains constant during the cycle, the work done by the protrusion will increase as k_{ECM} decreases. This has as consequence, that if the total work per protrusion is limited to W_{max} , the process of building up a force in a protrusion will come to a halt earlier on a soft matrix than on a stiff matrix. This is exactly what is observed in experiments [170]. We have performed a simulation of the stepwise force increase in a single protrusion connected to an ECM node. The isolated protrusion is mechanically fixed at the cell end, and at the outer ECM node. In Fig. 2.10A we have plotted the applied force of the protrusion, showing the effect of ECM stiffness. Each curve here represents a ten-fold increase of k_{ECM} . We observe that for stiffer ECM, the force builds up to higher values. Accordingly, the number of bonds in the adhesive complex increases monotonically (see Fig. 2.10B). After W_{max} has been reached, in each simulation relaxation behavior can be observed.

Finally, the polarization direction \mathbf{P} of the cell needs to be updated. While some authors have represented the polarization dynamics in a cell as a balance of spontaneous polarization decay and displacement history of the cell (see e.g. [175]), we here instead propose that \mathbf{P} is determined by the weighted average of the total actual force vectors from each protrusion:

$$\mathbf{P} = \frac{1}{N_{pro}} \sum_i \mathbf{F}_i^{pro}. \quad (2.42)$$

When a cell is polarized but is stuck in the matrix for a certain period T_{max} , for instance due to hindering by ECM nodes, the cell may round up to a spherical shape and chooses a new polarization vector. This could automatically account for experimental observations that cells turn in that way instead of as rigid elongated objects.

Chapter 3

Modeling impact mechanics and bruising of parenchymal tissues: a multi-scale approach

3.1 Introduction

Mechanical stress in plants affect physiological processes, growth development, and gene expression [176]. Research modeling approaches have been developed to understand these processes (e.g. [177, 178]). When exposed to mechanical stress, plant cells, contrary to animal cells, are largely immobilized and therefore have a strong cell wall to protect them from excessive loads. In this work, we aimed to predict the direct response (and damage) when plant tissue is subjected to a sudden mechanical stress (e.g. gravity, wind, impact). This is of major importance in food industries, where bruising and damage of fruits and vegetables represents a significant loss during transport and handling [Van Zeebroeck et al., 2003].

Parenchyma cells in plants are responsible for storage and represent the bulk matter of the organism. Parenchyma cells basically consists of a polymeric cell wall containing a quasi-incompressible liquid kept at a hydrostatic pressure (turgor pressure), which is responsible for the cellular rigidity (cfr. wilting of low hydrated plants). Plant cells adhere through a layer of pectin molecules, which acts as a glue between them.

Our (particle-based) model aimed to incorporate the aforementioned basic features and is meant to be a simulation tool for stress distribution and propagation in tissues, given the mechanical properties of a cell. However, our model is computationally limited to simulations for small spatial scales. A continuum model can handle a much larger spatial scale of tissue and would thus be more appropriate to model behavior of e.g whole plants. Unfortunately, continuum models cannot directly predict the correct mechanical behavior of tissues with a given micro-structure, as the constitutive equation that describes the relation between stress and deformation is not a priori known [179]. To alleviate this, we proposed a multi-scale framework coupling the discrete "micro-model" to a macroscopic FE model. The basic idea behind this *micro-macro* scheme is that the macroscopic stress-strain relation is not provided by a constitutive equation, but by concurrent simulations of the micro-model which are averaged over so-called Representative Volume Elements (RVEs). This approach is similar to techniques proposed for non-homogeneous solid materials (see e.g. [180, 181]), yet here we dealt also with viscous forces which were ignored in the latter.

3.2 Model for parenchyma cells

We considered both 2D models [Van Liedekerke et al., 2010a, Van Liedekerke et al., 2011] and 3D models [Van Liedekerke et al., 2010b]. The 2D model permits simulations of cell aggregates, whereas the 3D model is mechanically more accurate but limited to fewer cells. A parenchyma cell can be regarded as liquid filled flexible vessel [182] which is justified by the fact that parenchymae usually

contain a lot of water (can occupy 80-90 % of the total cell mass) and do not have a dense cytoskeleton such as is the case for animal cells. We can therefore assume that the intracellular fluid can be modeled as a nearly incompressible liquid.

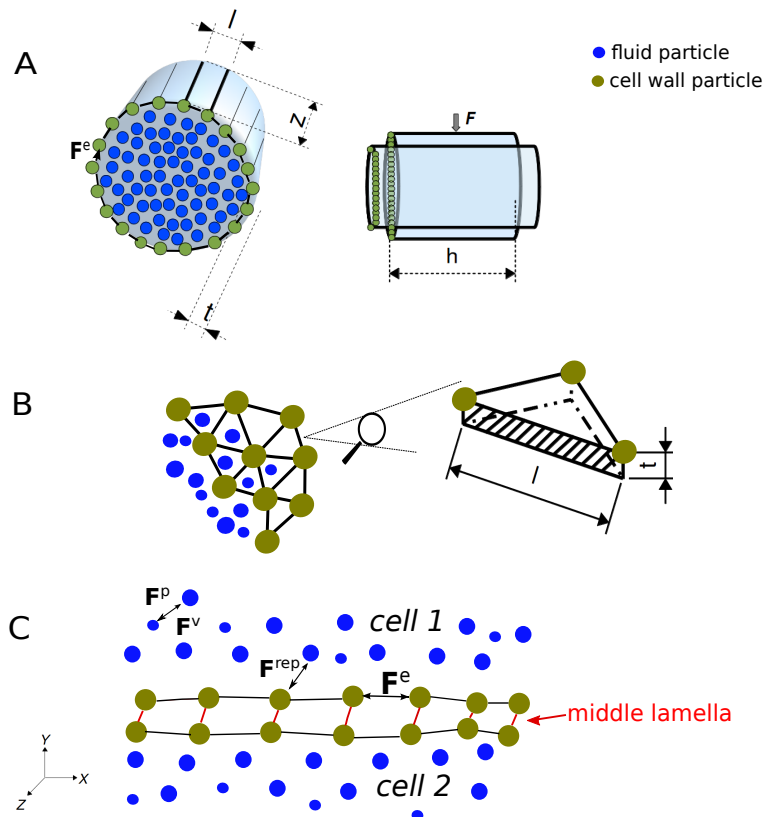


FIGURE 3.1: (A) Representation of the 2D model with wall particles and fluid particles. The cell can be regarded as an extruded 2D object in the Z direction. (B) Detail of the 3D cell wall spring network model. (C) Detail of the middle lamella model gluing two cells together.

Cell fluid model: The content of the cell is represented by SPH particles mimicking a Newtonian liquid. The fluid particles are moving according to the standard SPH approximation (see chapter 2, section 2.3.1). The force balance on a particle i consists of a pressure force \mathbf{F}_i^p , a viscous force \mathbf{F}_i^v and an external force \mathbf{F}_i^{ext} :

$$\mathbf{F}_i = \mathbf{F}_i^p + \mathbf{F}_i^v + \mathbf{F}_i^{ext}. \quad (3.1)$$

The external force can be either a contact force with a wall particle, or a body force (e.g. gravity). We use further Eq. 2.22 as constitutive relation between fluid pressure and density. We chose the compressibility constant such that only small density fluctuations are allowed and appear as pressure fluctuations in the cell. Importantly, the total fluid mass of the cell is not a priori constant, as water can migrate through aquaporins (small channels in the cell wall). These allow plant cells to build up turgor pressure by a change in osmotic balance. A net transport of water through the cell wall will be established as long as the turgor pressure in the cell does not equal the osmotic potential Π ($\Pi < 0$) of the cell content. If the cell fluid mass loss/gain is not too high, Π can be assumed constant. This fluid mass transport through the cell wall can be computed for each particle by the following constitutive

relation [183]:

$$\frac{dm_i}{dt} = -A_c L_p (P_i + \Pi), \quad (3.2)$$

where L_p is the hydraulic conductivity which is assumed to be isotropic over the cell's surface, and A_c is the total cell surface. In the model, we apply this equation directly to the SPH particles. If the cell starts absorbing water, the density will initially increase according to the last term in Eq. 2.27, and hence augment the pressure through Eq. 2.22. This is counter-balanced by the fact that the fluid moves outwards, hence lowering the density. The final density, which differs only slightly from the initial density, will be obtained when the fluid particles cease to move further, i.e. when there is a force balance between the fluid pressure forces and the cell wall forces.

Cell wall model: A plant cell wall consists of polymer-like structures for which stress-strain relationships in case of large deformations cannot be described by simple linear elasticity theory. Mechanically, the cell wall material exhibits elastic and plastic behavior and energy dissipation can be attributed to viscous and structural damping. On short timescales, in which the material composition can be assumed constant, the cell wall can be described by a hyperelastic or elasto-viscoplastic constitutive law [184]. We considered a hyper-elastic incompressible Neo-Hookean law for a material in principal directions k :

$$\sigma_k = G \lambda_k^2 - \sigma_0, \quad (3.3)$$

where G is the shear modulus of the material, λ_k is the extension ratio (in principal directions k) and σ_0 is a hydrostatic constant.

In our model the plant cell wall can be mimicked by a 2D or 3D network structure of springs (see section 2.3.2). In the 2D model, the cell can be regarded as a projection of a cylindrical shaped body in longitudinal (Z) direction, obtaining a 2D deformable structure (Fig. 3.1A). In the original body, the three principal directions are the radial direction (thickness of cell wall), the hoop direction (circumferential direction), and the axial direction (depth of cylinder). We define the corresponding local stretching ratio's for a pair of adjacent particles as $\lambda_t = t/t_0$, $\lambda_l = l/l_0$, and $\lambda_z = z/z_0$. The incompressibility of the material is reflected by the condition $\lambda_t \lambda_l \lambda_z = 1$. In the 2D model the particle properties are integrated over the Z -direction. The stress formula Eq. 3.3 applied to a discrete system leads to an inter-particle force, dependent on the stretching distance between two neighboring particles [Van Liedekerke et al., 2010a]:

$$F^e = \frac{G z_0 t_0}{l_0} \left(\lambda_l - \frac{1}{\alpha^2 \lambda_l^5} \right), \quad (3.4)$$

with the geometry factor α :

$$\alpha = \sqrt{\frac{\beta + \sqrt{\beta^2 - 4(\beta - 1)/\lambda_\theta^6}}{2}}, \quad (3.5)$$

in which $\beta = \sigma_z/\sigma_l$. α is thus determined by the relationship between the axial stress and the hoop stress in a pressurized vessel. For a cylindrical-like cell $\beta = 1/2$, and a cubic shaped cell $\beta = 1$. As default we have used $\beta = 1/2$. In the pure 3D case the cell has initially the geometry of a thin spherical shell, which is modeled as a triangulated spring network (Fig. 3.1B). The initial radius is r_0 . The cell wall has an thickness t , and we can consider the stretch ratios $\lambda = t/t_0$ and $\lambda_l = l/l_0$. The force between the particles reads [Van Liedekerke et al., 2010b]:

$$F^e = \frac{G l_0 t_0}{\sqrt{3}} (\lambda_l - \lambda_l^{-5}). \quad (3.6)$$

Note that for $\lambda \rightarrow 0$, Hooke's law is recovered. The mechanical property of the cell wall is determined by the stiffness factor $K_A = Gt_0$ which is of the order of 100 Nm^{-1} in most cases [185, 186].

A fluid-structure coupling between the fluid particles and wall particles must be defined at the interface of the fluid phase and solid phase. In this work we used the method of repelling boundary particles [30] ensuring that the fluid particles i remain at a certain distance from the wall j . The force between two particles F_{ij}^{ext} takes the form of a Lennard-Jones force [30]:

$$F_{ij}^{ext} = f_0 \left[\left(\frac{r_0}{r_{ij}} \right)^8 - \left(\frac{r_0}{r_{ij}} \right)^4 \right] \frac{1}{r_{ij}^2}, \quad (3.7)$$

with r_{ij} the distance between the fluid particle i and wall particle j , r_0 the equilibrium distance, and F_0 a scaling constant. We must note here that despite this force is effective in keeping the fluid particles inside, it does not a priori guarantee that correct boundary conditions for the fluid velocity at the fluid-wall interface are imposed. This is a well-known problem in standard SPH schemes which can be corrected for (see section 2.3.1 of the previous chapter). However such an algorithm was not been implemented here. In our simple coupling scheme we only warranted that the fluid-wall coupling is sufficiently accurate to give physical insight in the problem, justified by single cell tests (see Appendix A).

In plant tissue, the cells typically form a randomized brick pattern and are glued together by the *middle lamella*, which is a pectin layer between the two cell walls. To incorporate cell adhesion in the model, we propose a one-to-one connection between two particles of adhered cells with linear spring bonds (see Fig. 3.1C). Clearly, this connection mode can only provide rough estimations of stresses between adhered cells. [Van Liedekerke et al., 2010a] proposed a more realistic cell-cell connectivity model which should simulated the shear stresses between cells more accurately.

3.3 Results

3.3.1 Model Initialization and mechanical consistency

For both the 2D and 3D model, we started from an isolated, by default round shaped cell containing the fluid particles that are distributed randomly. At this stage, the system is not in osmotic balance. To achieve this, we first pressurize the cells invoking Eq. 3.2 which will continuously increase the fluid mass particles and build up pressure (Eq. 2.27). When the cell pressure is equal to the prescribed turgor pressure (usually $\sim 200 \text{ kPa}$), osmotic equilibrium is obtained. As mentioned above, the fluid compression modulus K is chosen such that apparent incompressibility of the fluid is warranted. Each cell contained about 100 wall particles and 500 fluid particles in 2D and respectively 2000 and 5000 particles in 3D.

The coupling between the fluid and cell wall model in principle requires that basic laws of the fluid-structure interaction (no slip conditions, tractions at the boundary) are fulfilled. With the simple coupling mechanism with repulsive forces between fluid and wall particles (Eq. 3.2) these are a priori not 100 % warranted. Nevertheless, we verified the static condition that the pressure in the cell which is the average of the SPH particles pressure, together with the tensions in the cell wall, obey Laplace's law. For the 2D as well as the 3D model, we found an acceptable agreement with errors below 6%. Second, we verified whether coupling can reproduce analytic solutions of the dynamics of centro-symmetric oscillations for fluid filled spherical vessels. After modal analysis we found that the model keeps the deviations of eigenfrequencies with the analytical solutions within 10% (see Appendix section A). From this we can conclude that the model should be able to simulate static and dynamical situations with sufficient accuracy to get a physical insight in the system.

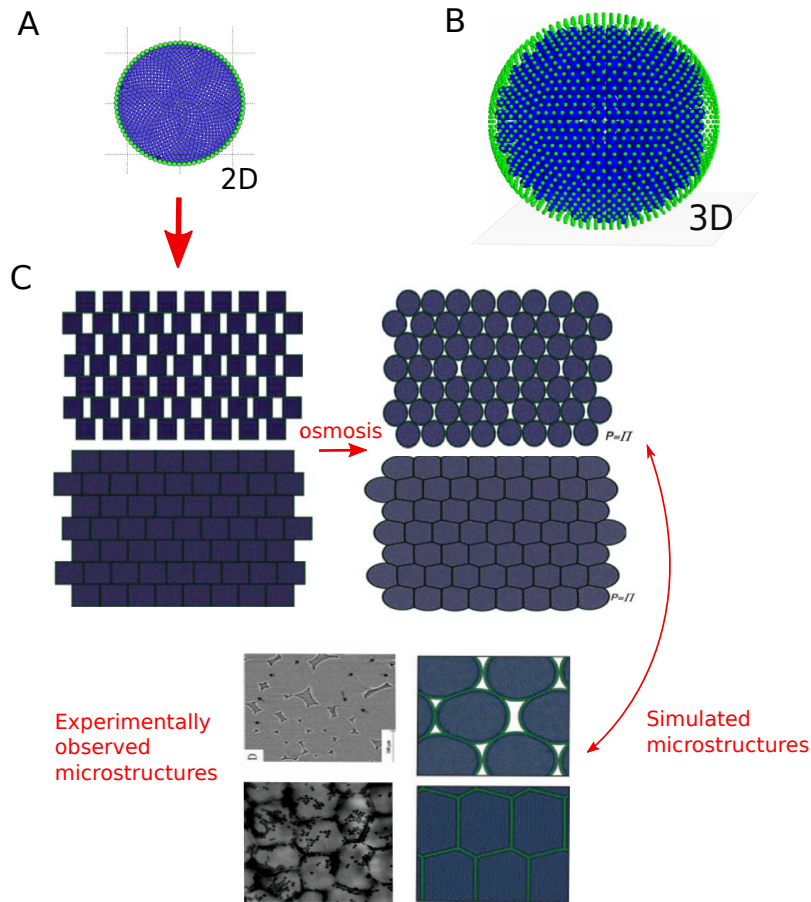


FIGURE 3.2: (A) Snapshot of the 2D cell model. (B) Snapshot of a cell represented in the 3D model. (C) Initial configuration of a small cell aggregate for two different structures (top: sparse, bottom: dense). After osmosis the cells have an internal pressure of $p = \Pi$. At the bottom, a detail of the structure is shown and compared to real experimental structures.

3.3.2 Quasi-static loading of single cells and tissues

Single cell experiment: In this step, we validated the 3D model directly with experimental data. Following the procedure for an *in vitro* experiment on an isolated plant cell [185] in suspension, we simulate the compression of a cell between two flat rigid plates (Fig. 3.3A). The physical properties (cell size, Young modulus of the cell wall, thickness of the cell wall) are known and are directly loaded into the model (no calibration) [Van Liedekerke et al., 2010b]. The force F on the plates as a function of the fractional deformation of the cell $\epsilon = \Delta X/2R$ has been monitored. In Fig. 3.3B, we compare the result of this computer experiment with the experiments and analytical model provided in ref. [185], showing very good agreement for strains below 20%. For higher strains, deviations start to develop between both models and the experiment, which is most likely due the yielding of the cell wall material. Note that the simulations here are not influenced by the fluid viscosity or cell wall permeability.

Cell wall yielding: Cell wall material deforms plastically as a consequence of the cellulose fibrils that begin to slide in the pectin-hemicellulose matrix. The mechanical strain at which this happens is roughly $\lambda = 2\%$ [188]. During stretching, the micro-fibrils embedded in the matrix decrease their

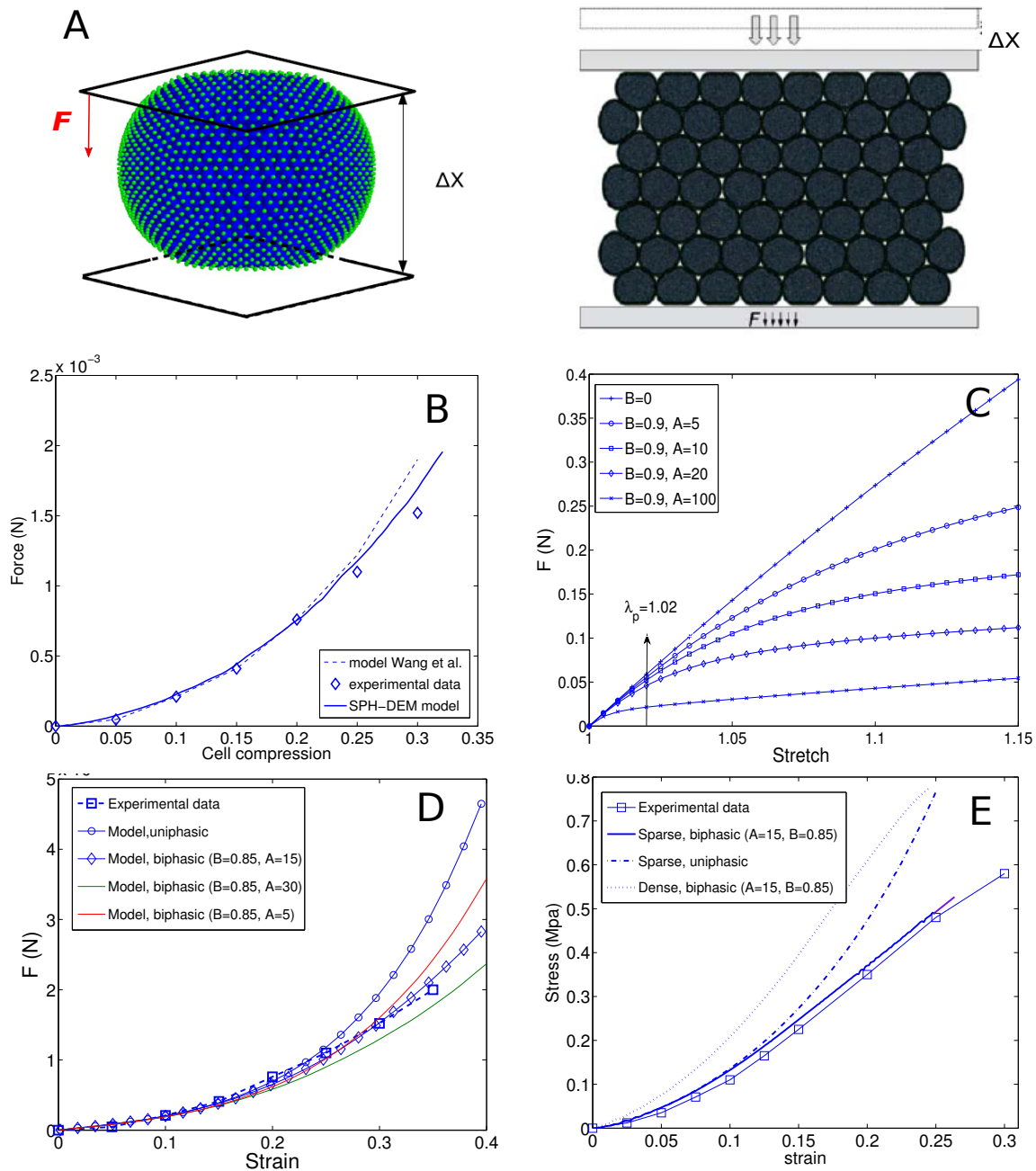


FIGURE 3.3: (A) Left: simulation snapshot of a 3D cell being compressed between two plates. Right: 2D cell aggregate compression. (B) Force-displacement ($F - \Delta x$ curves for 3D simulations (A) and comparison with experimental data [185]. (C) Force-stretch curves simulated with yield model for different parameter settings. (D) 2D single force-displacement ($F - \Delta x$ curves for simulations (with or without cell wall yielding). (E) Simulated stress-strain curves for 2D tissue model and comparison with experimental data from [187].

angle with the direction of the applied strain. At larger strains, the material usually exhibits a lower (but more or less constant) elastic modulus until rupture.

The mechanical wall model can be phenomenologically described as “bi-phasic” with two elastic moduli [Van Liedekerke et al., 2011]. We proposed a shear modulus function depending on the stretch:

$$G(\lambda) = G \left(1 - \frac{2B}{\pi} \tan^{-1}(A(\lambda - 1)) \right). \quad (3.8)$$

This function has the property that $G(\lambda)_{(\lambda \approx 1)} = G$, thus reproducing the initial elastic stiffness of the tissue. One has that $G(\lambda)_{(\lambda \gg 1)} = G(1 - B)$ which states that the elastic modulus at high strains has dropped by a factor $1 - B$. The parameter A determines how fast the stiffness drops from G to $G(1 - B)$ according to λ (the higher A , the sooner this occurs). This enables us to determine the elastic to plastic transition. In Fig. 3.3C, a simulated force-extension curve is shown for a cell wall in uni-axial stretch situation demonstrating the effect of A and B . The cell wall yielding model has been implemented in the 2D model. Fig. 3.3D shows the comparison of the model for the compression of a single cell with experimental data [185] when the uni-phasic and the bi-phasic behavior is invoked or not. In the latter case, an over prediction of the compressive force at larger strains is found. In the yield model we assumed an elastic-to-plastic transition at $\epsilon = 2\%$ ($\lambda_p = 1.02$) and a drop of 90 % in elastic modulus at large strains [188, 189]. This corresponds respectively to the values of $B = 0.9$ and $A = 15$ in the yield model. The other model parameters (cell wall thickness and Young modulus) are kept constant. Fig. 3.3D clearly shows that one has a much better general agreement than the uni-phasic model while it qualitatively also predicts a linearized behavior for large strains ($\epsilon > 20\%$), as can be observed in the *in vitro* experiment.

Tissue modeling: The micro-cellular structure of plant tissues built of turgor-driven cells is static in time and largely depends on the volumetric cell density. Generally, if cells are close to each other, polygonal structures can be observed; if they are only little attached, the cells will acquire a close to spherical shape. Parenchyma tissue consists of billions of cells. Obviously, a simulation of a large macroscopic tissue is prohibitively expensive with the micro-model. Fortunately, the cellular structure is usually repetitive. Therefore, we considered small aggregates of cells (~ 100 cells) which are representative for this tissue structure. The cells are initially rectangularly shaped and have frontal dimensions of $100 \mu\text{m}$, and a depth of $50 \mu\text{m}$. To acquire a certain multi-cellular structure, the cells are first positioned in a slightly randomized brick pattern (see Fig. 3.2C). Although the cells look artificial at this point, bringing them in osmotic equilibrium gives them automatically the honeycomb-like configuration as can be observed in nature [189]. During inflation, Eq. 3.2 is invoked to reach an initial turgor pressure (200 kPa). By positioning the cells further away from each other, a different structure can be obtained (see Fig. 3.2C). The stiffnesses of the pectin connections are chosen so that initially bonded particles from two different cells do not start to diverge from each other during the inflation process. This is equivalent to the statement that the inter-cellular forces are approximately equal in magnitude to the turgor driven forces on the cell wall [190].

The turgid aggregates are simulated to be compressed between two flat plates at low rates. In Fig. 3.3E we compare the results of the simulations run with the sparse structure with experimental data obtained from the compression of a piece of *Jonagored* apple tissue [187] which has as sparse structure with a similar void fraction [191]. The model shows very good agreement with this data, even though the mechanical properties of these cells have not been explicitly determined (we use the same cell wall stiffness values K_A as in the previous test), but perhaps more importantly it shows that the choice of the bi-phasic model is indeed instructive to use. After having performed these validation steps, we assume that the model is accurate enough to predict tissue behavior upon impact.

3.3.3 Dynamic loading and tissue damage

During dynamic loading, inertial effects and viscous stresses come into play in the force balance. With our model we can mimic impact following the same setup as in the previous section, i.e. with a single cell or a cell aggregate squeezed between two horizontal plates, yet now the upper plate moves with a downwards velocity of 5 ms^{-1} , which is a typical impact speed in fruit processing.

There are several candidate model parameters that potentially influence the dynamics at impact: (i) viscosity of the cytoplasm, (ii) stiffness of the cell wall and (iii) the tissue structure. We varied the viscosity in a range up to 1000 times the reference viscosity, considered two cell types: a soft one (reference) and a stiff one (10 times higher cell wall stiffness), and looked at the two tissue structures that were proposed previously: a dense one and a sparse one. To quantify the impact, we focused on stress distribution and transmission from the impact side to the other side of the tissue, and the strain in the cell walls. In summary, our model predicts the following:

- Upon impact, cells deform asymmetrically (Fig. 3.4A,D). The speed of the zone with the highest deformation depends on the global stiffness of the cells: for soft cells the deformation is concentrated near the impact zone, whereas for stiff cells deformation is more symmetric (Fig. 3.4D, right).
- Cells locally deform more when they have a lower cell fluid viscosity. This is caused by the fact that the fluid is more easily pushed away sideways perpendicular to the perturbation direction (lower shear stresses) As a result, stress is deviated towards the cell wall near the impact side (see circle Fig. 3.4C, left). For large cell fluid viscosities, the stress is transformed downwards (see circle Fig. 3.4C, right).
- The transmitted force (defined as the force that is measured on the other side of the impact zone) as a function of strain, further shows a different behavior as the quasi-static curve (see Fig. 3.4B). The former shows an oscillating effect. The influence of viscosity is limited for values up to 100 times the reference value and only becomes significant for values 1000 times the reference value. At this point the viscoelastic body is overdamped and does not exhibit any oscillation any more.

Damage and cellular failure: Mechanical failure in cellular tissue is due to excessive stresses that either cause rupture of the cell wall or the adhesive bonds between the cells. The stress (or strain) at which failure occurs depends largely on the chemical composition of the cell wall material (e.g. cellulose, hemicellulose and pectin content), as well as ambient factors such as relative humidity (RH) or temperature [192]. For instance, an increased RH typically makes the material more ductile and decreases the stiffness. With our model we can simulate tissue failure yet we note hereby that the results of these simulations are difficult to verify because damage at a microscopic level is hard to quantify. At macroscopic level, bruise volumes can be measured but usually only a few days after impact. During this period, the damaged cells, as well as surrounding intact cells, will be prone to oxidation and infections. The eventual bruise volume may thus span a much larger volume than that of the joint damaged cells. As such, we stress that the results presented below are model predictions that have not been validated and must be interpreted qualitatively.

We considered a local failure in the cell wall equivalent to a bond being broken between two particles [193]. This happens when the a critical extension ratio λ_c between two cell wall particles belonging to the same cell is exceeded. First, single 3D cell simulations were performed considering quasi-static compression and impact. Then, we focus on impact of 2D cell aggregates. Here we marked a cell as failed if at least one cell wall bond has ruptured. In summary, the simulations predict the following:

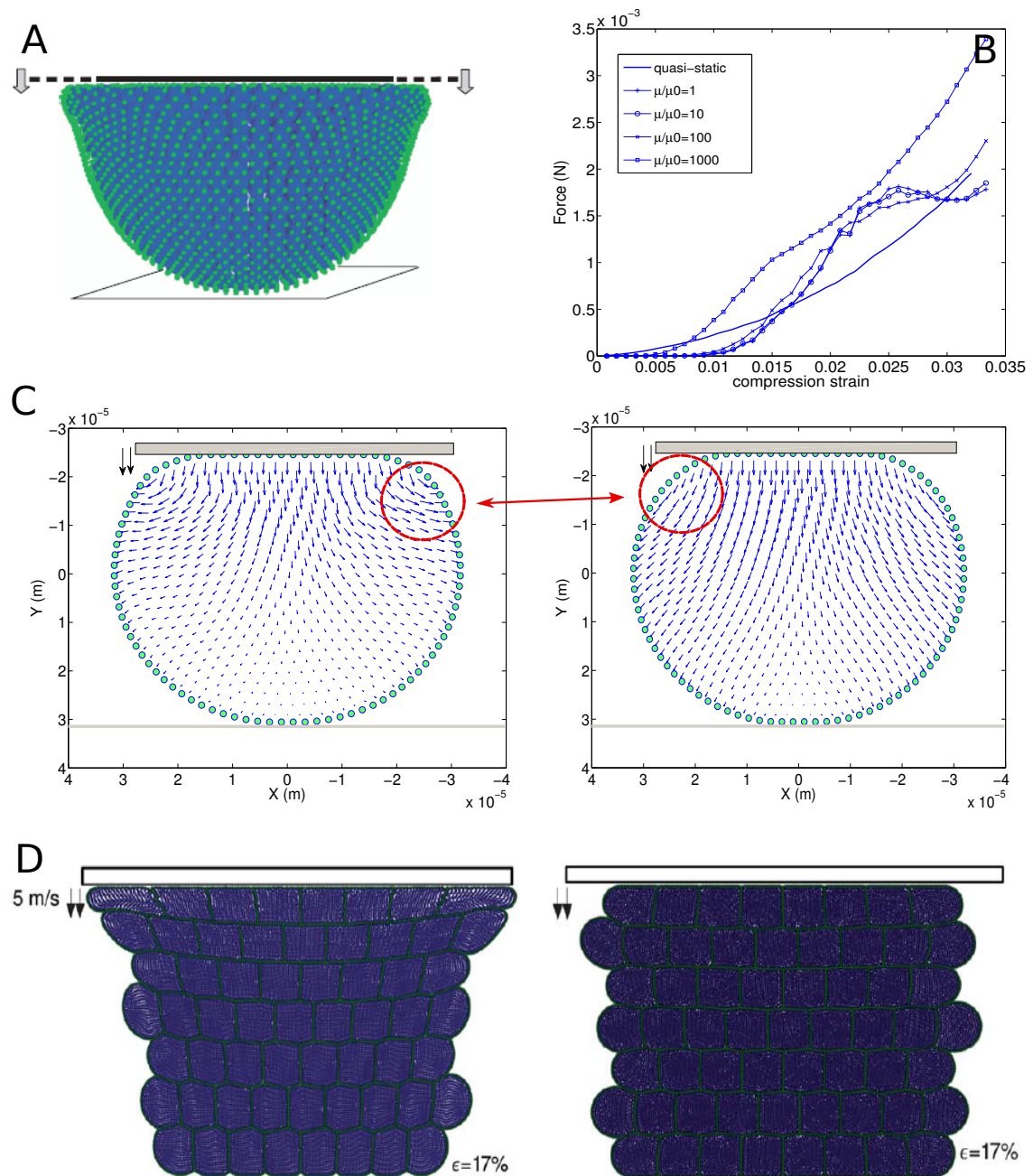


FIGURE 3.4: (A) Simulation snapshot of single 3D cell impacted by a horizontal plate. (B) Force-strain curve during compression (different cell fluid viscosities). (C) Fluid velocity directions during impacts (left: low cell fluid viscosity, right: high fluid viscosity). (D) Simulation snapshot of 2D cell aggregate impacted (left: soft cells, right: stiff cells).

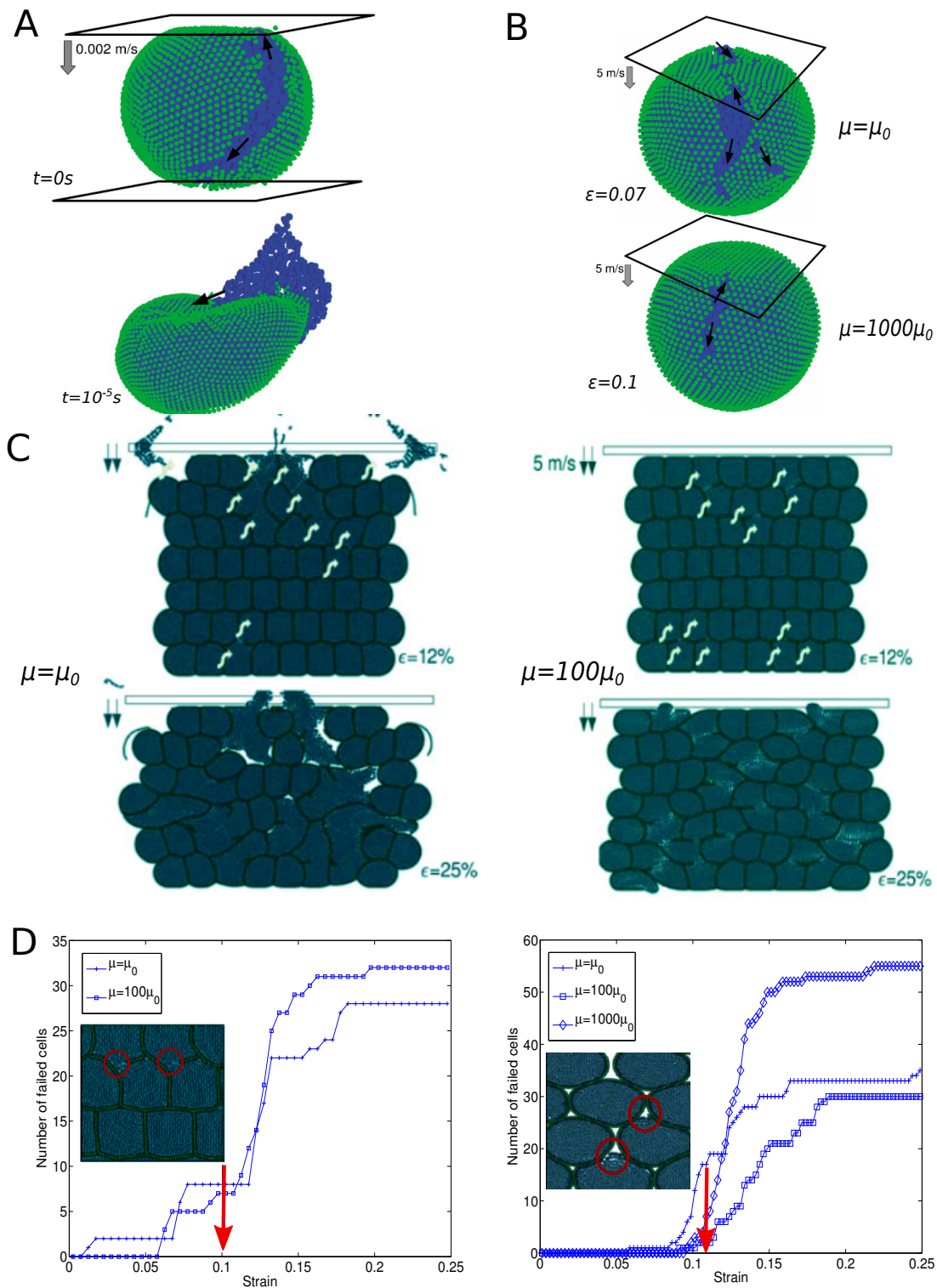


FIGURE 3.5: (A) Simulation snapshot of 3D cell quasi-static compression and failure. (B) 3D cell failure upon impact. (C) Simulations of 2D cell aggregate failure (left: low cell fluid viscosity, right: high cell fluid viscosity). (D) Number of damaged cells as a function of strain during impact (left: dense tissue structure, right: sparse structure).

- In the 3D single cell model during quasi-static compression, a main fracture originating near the equator proceeds towards the poles, where it eventually stops (see Fig. 3.5A). This can indeed be expected as the largest wall stress will be that one in the directions parallel to the equator. As a result of the crack, a jet of fluid escapes from the two partially attached halves. Thanks to the mesh-free approach of SPH, the fluid escape and free surface flow is simulated without numerical problems.
- The behavior during impact in the single cell 3D model shows quite a different picture. Due to the asymmetry in deformation, the fracture originates in the region of the impacting object where the wall is deformed the most and propagates in several directions towards the equator. Also, it occurs earlier in terms of overall compression strain as compared for quasi-static compression. This effect seems to be stronger for a low fluid viscosity, where the cell wall suffers more severe fractures (see Fig. 3.5B). This is in agreement with the observation mentioned in the previous section, i.e. that larger local deformations of the cell shape arise in case of lower fluid viscosities. Thus, although a cell with a high cell fluid viscosity generally suffers higher intracellular stresses and yields higher transmitted forces, its cell wall bears lower stresses leading to less fracture susceptibility during impact.
- In the 2D cell aggregates simulations, we generally find that the number of failing cells progresses as a sigmoid-like function of strain (see Fig. 3.5D). Damage starting earlier in the compression stage as for quasi-static compression. In the case of low viscosities, damage starts earlier and is mainly located at the surface. On the contrary, for large viscosities, damage starts a bit later but occurs also deeper into the tissue. Increased viscosity enhances the energy transfer in the direction of loading and, in this regard, may thus in fact cause more bruising as the forces penetrate deeper into the tissue (see Fig. 3.5C). We note hereby that, fluid viscosity depends on the ambient temperature and thus we predict that temperature may indirectly influence the damage percentages.
- Regarding the influence of tissue structure, we observe that cellular fracturing in the dense arrangement, rupture occurs at the common "point" of three adjoining cells (see Fig. 3.5D, left, red circles). In the sparse structure damage occurs mainly at the common inter-cellular region of three cells (see Fig. 3.5D, right, red circles). The first damage occurs at a lower strain in the dense cell arrangement, which can be addressed to the fact that in the sparse structure the cells have more space to deform while not in the dense structure, and hence stresses will build up quicker in these cells. At the end of impact however, both tissues experience more or less the same damage (i.e. less than 50 % survive) (see Fig. 3.5D).
- Failing of middle lamella occurs mainly at the common point of three cells and then gradually proceeds along the common contact area of two cells (cells are peeled off each other, not shown in figure). Analogously to cell wall rupturing at low strains, a low viscosity causes severe damage especially in the impact region, while a high viscosity causes slightly more penetrating damage at low loading strain. Yet, the overall damage for the former remains significantly higher. This can be attributed to the fact that purely compressive forces between cells contribute little to damage in the middle lamella, in contrast to tensile and shear forces.

3.3.4 Concluding remarks

Within this work, we introduced a high resolution model for parenchymal cellular tissue considering cells as fluid-filled vessels contained by a polymeric cell wall. We used the particle based SPH method to model the fluid inside. The parameters in our model are physically tangible and directly measurable. We showed that the coupling between fluid and cell wall is mechanically sufficiently consistent to get physical insight in the system. We further validated our model with experimental

data for quasi-static compression of cells and tissues, showing that our model gives realistic results with minimal parameters fitting.

Our ultimate goal was to simulate impact of tissues and predict damage on the individual cell level as to be able to understand influence the cell parameters can have. We find that even for heavy deformation of the cells and subsequent failure, the model remains stable and does not exhibit numerical issues. We generally find that cell wall stiffness, viscosity, and cellular structure have potentially a great influence on the damage patterns. However, more (and large scale) tissue simulations would be needed here for further analysis.

3.4 Micro-macro approach to achieve large scale tissue simulations

With our conceived micro-model, real scale tissue simulations are prohibitively expensive. However, simultaneous work was devoted to a computational multi-scale strategy that exploits the relation between the microscopic (cellular) level and the macroscopic (tissue) level to reduce the required simulation time with the microscopic model [Ghysels et al., 2009, Ghysels et al., 2010b]. The proposed method is an extension of the micro-macro coupling strategy based on the concept of Representative Volume Elements (RVEs) [180, 181]. An RVE is a volume element that is statistically representative for the tissue structure. In general, the size of the RVE should be of the order of the characteristic length of the micro-structure.

We derive a dynamical microscopic problem to be solved inside the RVEs, together with a corresponding macroscopic continuum equation. This derivation is based on the framework of generalized mathematical homogenization (GMH) [194, 195, 196]. The macroscopic continuum equation, in which the constitutive stress strain relation is not explicitly known, is discretized on the whole domain using standard Finite Element Methods and integrated in time. In each quadrature point of the finite element, we apply a given deformation on an RVE and perform an appropriate microscopic simulation (see Fig. 3.6). The required stresses are then evaluated on the fly using the stress computed in the micro-model.

In this work we show how these microscopic simulations need to be carried out to recover the viscoelastic deformation behavior at the tissue level. The main contributions of this work are twofold. First, we extend the GMH technique to deal with the velocity dependency of the inter-particle forces, i.e. the viscosity of the material. This leads to a dynamic problem to be solved inside the RVE, in which not only a deformation gradient has to be applied to the RVE, but also a velocity gradient. Second, a computational method is proposed to initialize the RVE consistently with the macroscopic variables and at the same time consistent with the microscopic dynamics. We tested three different approaches, including a simple relaxation to the elastic equilibrium, and a method based on the constrained runs approach [197, 198] which allows internal relaxation of the RVE.

3.4.1 Multiple spatio-temporal scales and rescaled microscopic equations

We first very briefly describe the derivation of a macroscopic continuum equation from the microscopic particle model using generalized mathematical homogenization [194, 195, 196]. We assume a particle system in which the interaction forces depend on their distance and relative velocity (random forces are excluded). The equation of motion for a particle i with position \mathbf{x}_i and velocity \mathbf{v}_i interacting with particles j can be written as (omitting external forces):

$$m_i \frac{d\mathbf{v}_i}{dt} = \sum_j \mathbf{f}_{ij}(\mathbf{x}_{ij}, \mathbf{v}_{ij}), \quad (3.9)$$

where \mathbf{x}_{ij} and \mathbf{v}_{ij} denote $\mathbf{x}_j - \mathbf{x}_i$ and $\mathbf{v}_j - \mathbf{v}_i$, respectively. We introduce a discrete displacement field as follows: if \mathbf{x}_i denotes the current position of an SPH particle and \mathbf{X}_i denotes the original position,

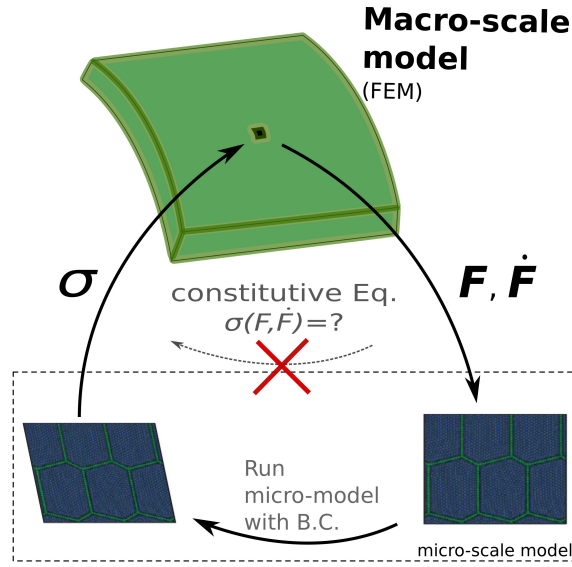


FIGURE 3.6: Micro-macro approach to couple the particle model with a Finite Element Model. The tissue is depicted by the green volume. The macroscopic deformation (rate) tensors \mathbf{F} and $\dot{\mathbf{F}}$ are passed to the micro-model within the RVE. After this step, the RVE becomes deformed. The micro-model is run to obtain the stress in the RVE (virial stress). The stress is passed back to the Finite Element Model which updates the deformation (rates).

i.e. the position at time $t = 0$, then

$$\mathbf{x}_i = \mathbf{X}_i + \mathbf{u}_i, \quad (3.10)$$

with \mathbf{u}_i the displacement of particle i . The displacement field can be written as a function of the original coordinates \mathbf{X}_i , i.e. $\mathbf{u}(\mathbf{X}_i, t)$ (the material description). We then proceed to derive a macroscopic description starting from these equations. The exposition closely follows ref. [196]. However, we extended the derivation to include viscous deformation, which will appear to be important for plant tissue. This viscous term is a direct consequence of the fact that the inter-particle forces depend directly on the particle velocities; the analysis reveals that, on the macroscopic scale, this results in a dependence of the stress tensor on the velocity gradient.

We introduce two distinct material coordinates to describe the continuum scale and the microscopic scale. Let \mathbf{X} coordinates denote the macroscopic scale, at which microscopic features are invisible, and let the microscopic features be captured by the coordinates \mathbf{Y} . The two scales are related by

$$\mathbf{Y} = \frac{\mathbf{X}}{\epsilon} \quad 0 < \epsilon \ll 1. \quad (3.11)$$

The corresponding spatial coordinates are given as \mathbf{x} and $\mathbf{y} = \mathbf{x}/\epsilon$. In the same way, we introduce a fast time variable τ , related to the standard time t by

$$\tau = \frac{t}{\epsilon} \quad 0 < \epsilon \ll 1. \quad (3.12)$$

With these notations, the first two material time derivatives of the displacement field are obtained using the chain rule as

$$\dot{\mathbf{u}}_i(\mathbf{X}_i, \mathbf{Y}_i, t, \tau) = \dot{\mathbf{u}}(\mathbf{X}, \mathbf{Y}_i, t, \tau) = \frac{d\mathbf{u}(\mathbf{X}, \mathbf{Y}_i, t, \tau)}{dt} = \frac{\partial \mathbf{u}}{\partial t} + \epsilon^{-1} \frac{\partial \mathbf{u}}{\partial \tau} \quad (3.13)$$

$$\ddot{\mathbf{u}}_i(\mathbf{X}_i, \mathbf{Y}_i, t, \tau) = \left(\frac{\partial}{\partial t} + \epsilon^{-1} \frac{\partial}{\partial \tau} \right) \left(\frac{\partial \mathbf{u}}{\partial t} + \epsilon^{-1} \frac{\partial \mathbf{u}}{\partial \tau} \right). \quad (3.14)$$

We use the assumption of separation in spatial scales that leads to a multiple scale asymptotic expansion for the displacement field of the form

$$\mathbf{u}(\mathbf{X}, \mathbf{Y}, t, \tau) = \mathbf{u}^0(\mathbf{X}, t) + \epsilon \mathbf{u}^1(\mathbf{X}, \mathbf{Y}, t, \tau) + \dots \quad (3.15)$$

where the term \mathbf{u}^0 represents the macroscopic displacement, independent of the fine scale coordinates \mathbf{Y} and the fast time scale τ . The same expansion can be done for the velocities \mathbf{v} . Since we consider a periodic microstructure, the fine scale perturbations $\mathbf{u}^1(\mathbf{X}, \mathbf{Y}, t, \tau)$ are periodic in \mathbf{Y} . Furthermore, we will also assume \mathbf{u}^1 to be periodic in τ . After an extensive multi-scale asymptotic analysis for Eq. 3.9 [Ghysels et al., 2010b] we collect the terms in equal powers of ϵ . This leads first to the microscopic equation which applies to the particles inside the RVE:

$$\bar{m}_i \frac{\partial^2 \mathbf{u}^1(\mathbf{X}, \mathbf{Y}_i, t, \tau)}{\partial \tau^2} = \sum_j \bar{\mathbf{f}}_{ij}(\mathbf{F}^0(\mathbf{X}, t) \cdot \mathbf{X}_{ij} + \epsilon(\mathbf{u}_j^1 - \mathbf{u}_i^1), \dot{\mathbf{F}}^0(\mathbf{X}, t) \cdot \mathbf{X}_{ij} + \epsilon(\mathbf{v}_j^1 - \mathbf{v}_i^1)) \quad (3.16)$$

This is a rescaled equation of motion where the inter particle force depend on the macroscopic deformation and deformation rate tensors $\mathbf{F}^0(\mathbf{X}, t)$ and $\dot{\mathbf{F}}^0(\mathbf{X}, t)$ respectively, superimposed by a fine scale perturbation $O(\epsilon)$ on the displacements and velocity. The second, macroscopic terms lead to the set of equations (after averaging over RVE):

$$\begin{aligned} \rho \frac{\partial^2 \mathbf{u}^0(\mathbf{x}, t)}{\partial t^2} &= \nabla_{\mathbf{x}} \cdot \langle \boldsymbol{\sigma} \rangle \\ \boldsymbol{\sigma}(\mathbf{x}, t, \tau) &= \frac{1}{2V_{\text{RVE}}} \sum_i \sum_j \mathbf{f}_{ij} \otimes \mathbf{x}_{ij}, \end{aligned} \quad (3.17)$$

with the first equation the continuum equation of motion. The $\langle \cdot \rangle$ denotes the temporal average over a time-interval $[0, \tau_0]$. The second equation reflects the definition of the stress tensor which here corresponds to the mechanical part of the virial stress which can be computed by the micro-scale model.

3.4.2 Initialization of the micro-problem

In our computational multi-scale approach the macroscopic continuum equation is discretized using finite elements [199], and supplemented with a microscopic simulation in an RVE around each quadrature point. In each quadrature point, the Cauchy stress is obtained using the virial stress formula in Eq. 3.17, applied to an appropriately initialized RVE. In a first work [Ghysels et al., 2009] we outlined a strategy to quasi-static elastic deformation of plant tissue without accounting for viscous behavior. The RVE initialization when viscous effects are important needs more care. The problem to be solved inside the RVE, Eq. 3.16, receives displacements and velocities as input from the macroscopic model through $\mathbf{F}^0(\mathbf{X}, t)$ and $\dot{\mathbf{F}}^0(\mathbf{X}, t)$, which will determine the boundary conditions for the unit cell. Solving the microscopic equation means finding a state of the RVE that is consistent with these boundary conditions. However, since there are many more degrees of freedom inside the

RVE, the solution is not unique. The RVE should be consistent not only with the macroscopic input variables, but also with the microscopic system dynamics.

Boundary conditions: The Boundary Conditions (BC) will change the positions of the particles at the boundary of the RVE. The BC can be chosen as Dirichlet or periodic. Here we used periodic boundary conditions, which means that only three corner points of the RVE must be prescribed as $\mathbf{x}_i = \mathbf{F}^0(\mathbf{X}, t) \cdot \mathbf{X}_i$. Periodicity is enforced by letting forces, acting from the interior of the cell on a node on the boundary of the domain, act on the corresponding node of the opposite wall as well (see [Ghysels et al., 2009]). It can be shown that for these conditions the RVE satisfies relations

$$\mathbf{F}^0(\mathbf{X}, t) = \frac{1}{V_{\text{RVE}}} \int_{V_{\text{RVE}}} \mathbf{F}(\mathbf{X}, \mathbf{Y}, t, \tau) dV_{\text{RVE}} \equiv \bar{\mathbf{F}} \quad (3.18)$$

and

$$\dot{\mathbf{F}}^0(\mathbf{X}, t) = \frac{1}{V_{\text{RVE}}} \int_{V_{\text{RVE}}} \dot{\mathbf{F}}(\mathbf{X}, \mathbf{Y}, t, \tau) dV_{\text{RVE}} \equiv \bar{\dot{\mathbf{F}}}, \quad (3.19)$$

where \mathbf{F}^0 , $(\dot{\mathbf{F}}^0)$ are the macroscopic deformation gradient (rate) and $\bar{\mathbf{F}}$, $(\bar{\dot{\mathbf{F}}})$ are the deformation gradient (rate) averaged over the RVE. If the RVE satisfies these relations, it is said to be consistent with the macroscopic variables.

RVE initialization rules: We looked at three different possibilities to reconstruct the microscopic state inside the RVE from the macroscopic state. The first approach called the *Cauchy-Born* rule is used in many multi-scale methods for crystalline structures. If in Eq. 3.16, the problem to be solved inside the RVE, the $O(\epsilon)$ terms are neglected, the particle positions and velocities in the RVE are given by

$$\begin{bmatrix} \mathbf{x}_i \\ \mathbf{v}_i \end{bmatrix} = \begin{bmatrix} \mathbf{F}^0(\mathbf{X}, t) \cdot \mathbf{X}_i \\ \dot{\mathbf{F}}^0(\mathbf{X}, t) \cdot \mathbf{X}_i \end{bmatrix}. \quad (3.20)$$

This is a priori only reasonable approximation for small (linear) deformations. The $\mathbf{u}^1(\mathbf{X}, \mathbf{Y}_i, t, \tau)$ terms can be seen as corrections to the Cauchy-Born rule. Correspondingly, the $\mathbf{v}^1(\mathbf{X}, \mathbf{Y}_i, t, \tau)$ terms can be seen as a correction to a linear velocity profile described by the material velocity gradient $\dot{\mathbf{F}}^0(\mathbf{X}, t)$. We now propose two ways of initializing these corrections.

The second approach is called *Elastic equilibrium*. A possible RVE initialization is the steady-state found by integrating in time until equilibrium. Integration in time, starting from the Cauchy-Born approximation, relaxes the system of particles and reduces its internal energy, hence minimizing the internal forces and the stress. Here we assume the inter-particle forces (and thus the stress) would not depend on the particle velocities. The microscopic problem reduces then to

$$\bar{m}_i \frac{\partial^2 \mathbf{u}^1(\mathbf{X}, \mathbf{Y}_i, t, \tau)}{\partial \tau^2} = \sum_j \bar{\mathbf{f}}_{ij} (\mathbf{F}^0(\mathbf{X}, t) \cdot \mathbf{X}_{ij} + \epsilon(\mathbf{u}_j^1 - \mathbf{u}_i^1)). \quad (3.21)$$

Instead of using (3.20) for the initialization of the microscopic problem, one can use the improved initialization

$$\begin{bmatrix} \mathbf{x}_i \\ \mathbf{v}_i \end{bmatrix} = \begin{bmatrix} \mathbf{x}_i^e \\ \dot{\mathbf{F}}^0(\mathbf{X}, t) \cdot \mathbf{X}_i \end{bmatrix}, \quad (3.22)$$

with \mathbf{x}_i^e the particle positions in the elastic equilibrium. The elastic equilibrium particle positions are thus also used for the determination of the particle velocities. Eq. 3.22 gives a good approximation to the solution of the dynamic microscopic problem (Eq. 3.16), provided the inter-particle forces do not depend too strongly on the velocities. The procedure is illustrated in figure 3.7A (left), where point (a) denotes the first initialization (Eq. 3.20), and point (b), which will be called the elastic equilibrium, denotes the steady-state solution of Eq. 3.21. The surface denoted $\sigma^v(\mathbf{F}, \dot{\mathbf{F}})$ in figure 3.7A is a scalar representation of the (viscoelastic) stress, for different macroscopic \mathbf{F} and $\dot{\mathbf{F}}$, as it would be computed

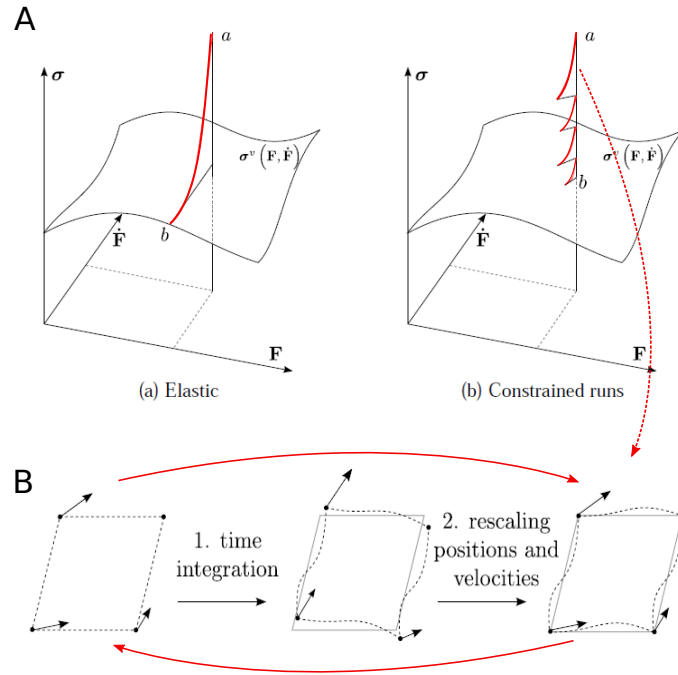


FIGURE 3.7: (A) Real stress manifold function of \mathbf{F} and $\dot{\mathbf{F}}$ and initial configuration. Initializations of the RVE can be done according to a (A-a) Elastic equilibrium, or (A-b) Constrained runs algorithm consisting of time-integration (red lines) followed by rescaling. (B) Illustration of the 2 steps of the constrained runs iteration for an RVE deformed with a shear deformation. The arrows at the corners denote the velocities.

from an RVE embedded in a larger microscopic simulation and consistent with that particular \mathbf{F} and $\dot{\mathbf{F}}$.

In the third approach, called *Constrained Runs*, an initialization scheme is proposed to initialize both particle positions and velocities at the same time by coupling them through the microscopic dynamics. This scheme consists of two steps: first a time integration of the RVE, during which the macroscopic observables are allowed to change, followed by a rescaling in order to restore the consistency with the given macroscopic variables. This is illustrated in Fig. 3.7 (right). The first step, the time integration, uses periodic boundary conditions, but without keeping the corners fixed (see Fig. 3.7B). The goal of this step is to bring the state of the RVE closer to the correct microscopic state as would be found in a full microscopic simulation, i.e., the state is attracted to the $\sigma^v(\mathbf{F}, \dot{\mathbf{F}})$ manifold. After the time integration the macroscopic observables, $\bar{\mathbf{F}}$ and $\bar{\dot{\mathbf{F}}}$, have changed and a rescaling (affine transformation) is necessary to restore the consistency with the imposed values for the macroscopic observables \mathbf{F}^0 and $\dot{\mathbf{F}}^0$. This rescaling is chosen such that it restores the positions and velocities of the corners, while preserving the periodicity of the RVE boundaries, and that it alters the internal configuration of the RVE as little as possible.

3.4.3 Example simulation

As a test case, we considered the dynamics of a square piece of plant tissue fixed on the left side subject to a body (gravity) force \mathbf{g} pointing downwards (see Fig. 3.8B, left). The domain consists of 16×16 individual square parenchyma cells, stacked in a regular grid, see figure 3.7A (left). The same square domain is also discretized using 4×4 bilinear quadrilateral finite elements, see figure 3.8B (right). The FE model has been implemented in the Deal.II package [200]. An explicit time integrator (Runge-Kutta method Dopri [201]) has been opted.

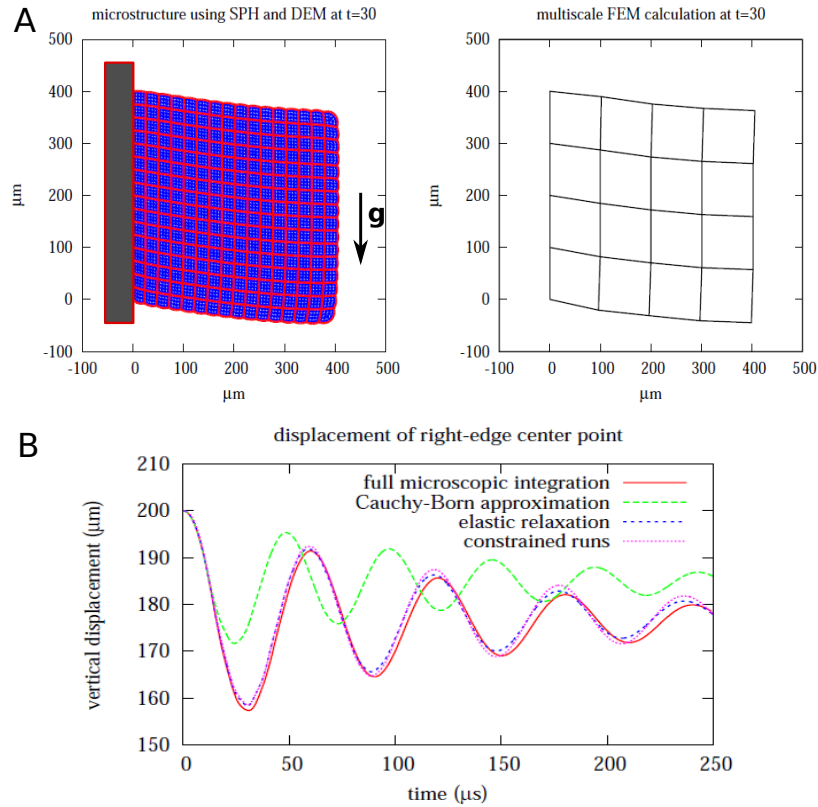


FIGURE 3.8: (A) Left: full micro 16×16 cells. Here the SPH particles are in blue, the cell wall particles in red. Right: coupled multiscale computation. Each finite element uses $4+1$ quadrature points, so in total $4 \times 4 \times 5$ RVEs, one cell each, are kept in memory. (B) The macroscopic evolution, represented by its vertical displacement, of a point in the middle of the right side of the domain is plotted as a function of time. Computation using the full microscopic model is compared to the coupled multiscale method for three different RVE initialization approaches.

Since the microscopic structure is periodic, one period, i.e. one plant cell, is taken as the RVE here. The deformation and velocity gradient at each quadrature point are given as input to an RVE centered around the quadrature point. After initialization of the RVE, the stress tensor is computed using (Eq. 3.17). Fig. 3.8B shows the vertical displacement of a point in the middle of the right boundary of the domain as a function of time for the three different RVE initialization strategies. The Cauchy-Born approximation does not relax the RVE and thus severely underestimates the macroscopic displacements. Since the stresses are overestimated, the material seems stiffer than it actually is. Relaxation to elastic equilibrium, with a linear velocity profile applied afterward, see Eq. 3.22, correctly computes the elastic part of the stress (oscillation around correct steady state). Initialization with the constrained runs iteration gives a similar result, however introduces less damping.

The total speed-up in this example is roughly 2 times for the multi-scale approach as compared to the full microscopic simulations. However, in the coupled multi-scale computations only a fraction of the number of cells is simulated compared to the full microscopic run. For larger domains the number of plant cells has to increase, while the number of finite elements depends only on the desired accuracy, not on the domain size. Thus, a larger separation in spatial scales leads to a larger computational benefit for the multi-scale method. Furthermore, the multi-scale method can also benefit from a possible separation in temporal scales. Faster microscopic dynamics and slower macroscopic emergent behavior lead to larger separation in timescales and greater speedups. A more significant speedup can be achieved if implicit integrators for FEM are used, see [Ghysels et al., 2010a].

3.5 Summary and discussion

In this chapter we showed that particle-based models can be combined with continuum approaches to form a multi-scale framework for tissue mechanics simulations. The micro-model was conceived using a mass-spring model for the solid cell wall, coupled with a Smoothed Particle Hydrodynamics (SPH) model representing the cell fluid. The SPH technique is versatile and can be used to simulate large deformation impact and failure dynamics based on the input of parameters that reflect physical properties of individual cells. Our simulations with the micro-model show how stress propagation and failure of tissue depend on the physical properties of individual cells and the cellular micro-structure. In particular we showed that viscosity of the cell constituents and stiffness of the cell wall change the stress profiles during impact. A low viscosity (close to that one of water) generates flexible cells and external loading will easily introduce shear. As this induces larger deformations, it makes the cells more susceptible to bruising, either by cell wall rupture or middle lamella rupture. In contrast, an increased intracellular viscosity can induce viscous forces that can become comparable to or dominate over pressure forces. Forces are transmitted more in the direction of loading (and thus deeper into the tissue) which is translated into a quicker occurrence of damage there.

Full microscopic simulations for realistic tissue dimensions were not feasible. We instead proposed a continuum macro-model to accomplish this. The coupling of the micro-model with the macro-model is based on the Representative Volume Elements (RVEs) approach in combination with generalized homogenization. On the macro-scale, the continuum equations for momentum hold. The constitutive equation that would normally be required to compute the stress given a deformation, is here replaced by on-the-fly runs of the microscopic model. As a test case for the multi-scale model, we have shown that the proposed micro-macro coupling can effectively be used for simulations of tissue dynamics. However, the accuracy of model heavily depends whether the RVE has been correctly initialized, whereas the performance (speed-up compared to full microscopic model) depends on the separation of spatial and temporal scales.

Chapter 4

Modeling of multi-cellular systems in high resolution in 3D

4.1 Introduction

Driven by the insight that multi-cellular organization cannot be explained by the orchestration of chemical processes at the molecular level alone and flanked by recent development of methods in imaging and probing of physical forces at small scales, the role of mechanics in the interplay of cell and multi-cellular dynamics is moving into the main focus of biological research [202]. Cells respond on mechanical stress passively and actively, hence an understanding of growth and division processes is not possible without properly taking into account the mechanical components underlying these processes. Mathematical models are being established as an additional cornerstone to provide information to clinicians entering in their decisions [203, 204]. This requires high reliability of models and quantitative simulations.

An clinical relevant example is the regeneration of liver after drug induced toxic damage after paracetamol (acetaminophen, APAP or Tetrachloride, CCl₄) overdose. These drugs generate a characteristic central necrotic hepatocyte-depleted lesion in each liver lobule, which is the smallest repetitive functional and anatomical unit of liver. Hoehme et al. (2010) [8] used confocal laser scanning micrographs to set up a realistic spatial-temporal model of a liver lobule. In their model hepatocytes were represented as individual units (agents) parameterized by biophysical and biological quantities and able to move as a consequence of forces on the cell and the cells' own micro-motility. The cells were modeled by a center-based model (CBM, see chapter 2).

For liver, the CBM predicted that active uniform micro-motility forces would not suffice to close the characteristic necrotic tissue lesions generated in the center of each liver lobule but further mechanisms as directed migration and oriented cell division along closest micro-vessels (named hepatocyte-sinusoid alignment, HSA) would be necessary to explain the observed regeneration scenarios [8]. In order to arrive at such a conclusion, the model must for a given set of parameters be able to realistically and quantitatively predict the outcome of the regeneration process. The model can be viewed as a mapping from a set of parameters to a set of typically macroscopic observables such as the size of the necrotic lesion, the cell density in the lobule etc.

Yet as mentioned in chapter 2, center-based models lose the accuracy in dense cell aggregates where the interaction force of a cell with one neighbor changes the interaction force with another neighbor. Such situation can occur during compression of growing cell aggregates, but potentially also in e.g. during liver regeneration where cells enter the cell cycle to close the drug-induced lesion. CBM simulations suffer from poor shape representation, which can lead to inaccurate conclusions if the model assumptions are taken too crude. For instance, a CBM must not be used to analyse local forces in cell-cell junctions that would e.g. trigger a mechano-transduction process.

Our intention is to replace the CBM by the more sophisticated high resolution deformable cell model (DCM) in systems that are critically determined by a correct cell shape, and propose this model as a future tool to perform complex tissue simulations. This chapter is thus devoted to the developments earlier introduced in chapter 2. In [Odenthal et al., 2013] we have shown that the model

parameters can be calibrated with physical and bio-kinetic parameters by performing single cell experiments that give information on how cells deform and adhere. Thanks to the novel cell growth and division algorithm (see chapter 2, section 2.3.2), we can now study the growth and division behavior of the cells in the classical settings of growing monolayer and multicellular spheroids. In addition, the contact algorithm permits to simulate interactions of the cells with smooth objects, such as blood vessels. We illustrate the capability of the model by performing simulations of regeneration dynamics after intoxication in liver with the DCM and compare their results to experimental data and simulation results using a classical center-based model. We analyze the results and basic differences in terms of dynamics and tissue architecture in section 4.4.2. The cell shapes obtained by simulations with the DCM can in principle readily be compared with high resolution confocal microscopy images, which could open up the possibility to infer the stress on the cells in full 3D volume reconstructions from laser scanning confocal micrographs from the cells' shape depending on their constitutive properties.

4.2 Models

Deformable Cell Model (DCM): As outlined in chapter 2, in our DCM the cell surface is triangulated generating viscoelastic elements along each edge of each triangle. This creates a deformable structure with many degrees of freedom for cell surface deformation. Throughout this work, we do not represent the cell organelles, but approximate it as a homogeneous isotropic compressible material.

Center Based Model (CBM): Center-Based Models (CBM) are well established modeling approaches where cells are represented by homogeneous elastic and adhesive spheres (see chapter 2). They lack the accuracy of DCM but are computationally more efficient and can be used to approximate other structures such a blood vessels or they can be used in hybrid simulations.

4.3 Results

4.3.1 Single cell experiments

Classical experiments such as optical stretchers, optical tweezers, and micro-pipetting techniques (e.g. [205, 206, 207]) are used to quantify the mechanical characteristics of the cytoskeleton of the cell and permit here to calibrate the DCM parameters of the cytoskeleton and adhesion models.

Optical stretcher

We have simulated an optical stretcher experiment with a DCM to calibrate the parameters in the viscoelastic network model of our DCM using the experimental data [Van Liedekerke et al., 2018b]. In the experiment, two laser beams in opposite direction and faced to each other trap a cell in suspension (see Fig. 4.1A). The diffracted laser beams exert a surface force on the cell's membrane, deforming it towards the beam direction. Increasing the laser power yields a higher optical stretching force. At the same time the deformation along two perpendicular directions is measured using image analysis, yielding information on cell shape [208, 209, 210].

Data of optical stretcher experiment was generated for MDA-MB-231 breast cancer cells. These cells had an average radius of $8.8 \pm 1.3 \mu\text{m}$ ($N=100$ samples). Actin staining further revealed average approximate cortex thickness of $h_{cor} \sim 500 \mu\text{m}$ (Fig. 4.1C). Ananthakrishnan et al. (2005) [211] has suggested that the cortical actin cytoskeleton is the main component determining the mechanical behavior of the cell.

In each experiment the laser beams are applied during a time interval of a few seconds, in which the cell deforms moderately. Thereafter, the cell relaxation behavior period is monitored for several seconds. The long axis (Z) and short axis (Y) lengths changes over time are derived from analyzing

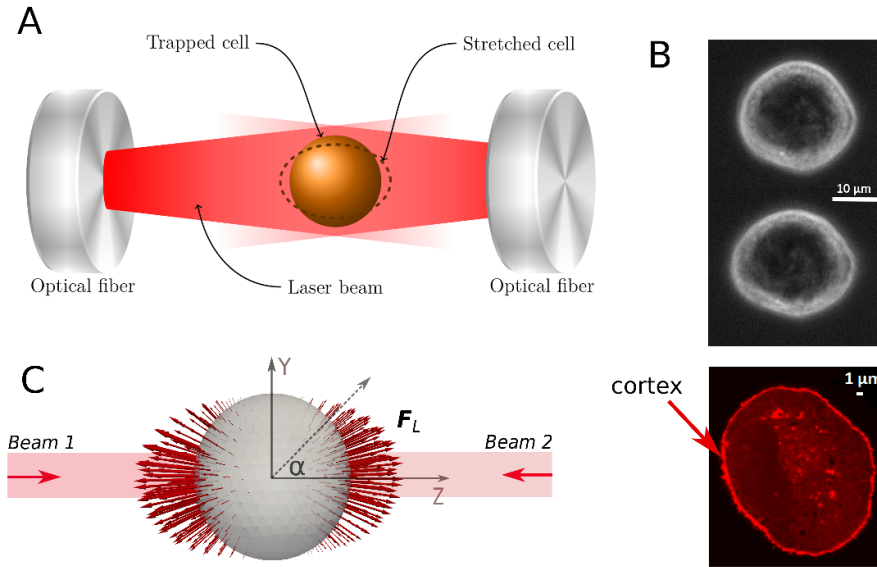


FIGURE 4.1: (A) Sketch of the experimental setup with trapped cell in an optical stretcher. (B) Surface forces profile due to laser is visualized (red arrows) on a triangulated surface of the deformable cell. The Z axis (long axis) is aligned with the laser beam, whereas the Y axis gives the direction of the short axis during deformation. F_L is the nodal force induced by the laser power. (C) Actin stained image of a MDA-MB-231 cell indicating cell cortex actin cytoskeleton.

the images (see data Fig. 4.2). Two laser powers have been considered ($P_0 = 900$ mW and $P_0 = 1100$ mW), with an applied stretching time of 2 seconds and a monitoring of the relaxation behavior of 2 seconds. Because of the large biological variability, for each individual experiment a minimum of about 100 cells were used.

In [Van Liedekerke et al., 2018b] we have first tried to explain the viscoelastic behavior of the MDA-MB-231 cells using Kelvin-Voigt elements (solid-like behavior of the cell cortex). For details about the set up of the simulation, see the Appendix B.3. We have found a parameter set for which an overall reasonable agreement for both laser powers can be obtained (see Fig. 4.2A), if the viscous properties decrease with increasing temperature as a result of the laser beam absorption, i.e. the friction coefficient would scale with temperature T as an Arrhenius law [212]:

$$\frac{\gamma(T)}{\gamma(T_0)} = \exp\left(\frac{E_a}{R}\left(\frac{1}{T} - \frac{1}{T_0}\right)\right), \quad (4.1)$$

with E_a is an activation energy, R the universal gas constant and T_0 a reference temperature. We further note that the calibrated stiffness parameters are in their physiological range (see Appendix B.3). Although the stretching and the relaxation behavior are both qualitatively well captured if thermoelastic effects are accounted for, there is (i) a restoring effect of the cell shape in the simulations (solid like behavior) that is not observed in the time course of the experiment, and (ii) the short axis deformation slightly exceeds the experimental one. This latter deviation (point (i)) might be a consequence of missing out an explicit representation of the internal cytoskeleton in the model, which might here result in a higher resistance to a movement of the cell surface perpendicular to the laser axis, but including an explicit representation of the cytoskeleton is not expected to remove the significant deviations of the model during the relaxation stage (point (i)).

For this reason, we capture a possible contribution from the fluid like behavior of the cortical

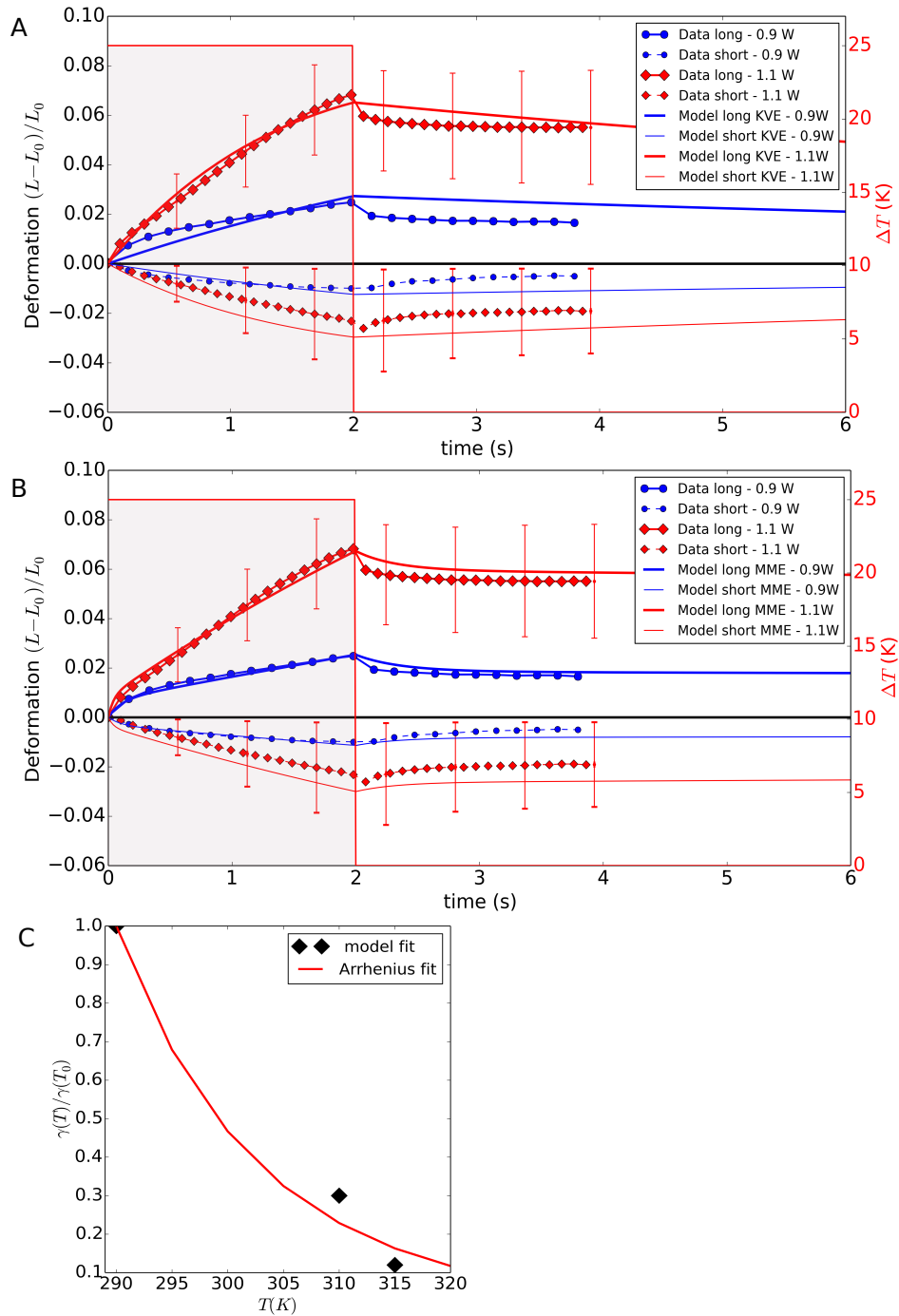


FIGURE 4.2: (A-B) Comparison of the simulated MDA-MB-231 cell deformation with the experimental data in an optical stretcher, using laser powers of 900 mW and 1100 mW. (A) The model was first fitted using a Kelvin-Voigt model (KVE) and assuming temperature dependent friction coefficients for the cytoskeleton. (B) The model then was fitted assuming a modified Maxwell model (MME) but using the same temperature dependence as for KVE. For sake of clarity, the error bars are only shown for some data points, and only for the $P_0 = 1100$ mW case. The errors bars on the data are quite large, indicating a high biological variability. (C) Temperature dependence of damping coefficients, using the model fit for DCM, compared to Arrhenius' law using an activation energy close to the value reported in ref. [212]

cytoskeleton, see e.g. [213], by adding an additional friction element in series with the spring in the Kelvin-Voigt element (with the choice of a small $\gamma(T_0) = 10^{-5}$ Ns/m), resulting in a modified Maxwell model¹ (MME), see Fig. B.1B. The temperature dependence for the friction coefficients was chosen as obtained in the KVE model (Eq. 4.1). The two fits capture the relaxation behavior overall well and much better than the KVE model, with an apparent plastic deformation keeping the cell shape from its original value.

Nevertheless, we could argue that despite the Kelvin-Voigt model results in less optimal fits, may still be useful in simulations, because the behavior of the cells, on longer timescales (minutes to hours) after the experiment is not a priori known and may exhibit active responses, possibly leading to a restoring of the original cell shape [214]. Conform to Ananthakrishnan et al. (2005) we further conclude that the initial sub-model assumption in our DCM, i.e. representing a cell as a deformable shell without internal structure (nucleus, organelles), may be sufficient in simulations where the cells do need not deform excessively.

Red blood cells in an optical tweezer

In [Odenthal et al., 2013] we simulated the cortical cytoskeleton dynamics in a Red Blood Cell (RBC) in preparation to test our cell adhesion model (see next section). An RBC consists of a lipid bilayer attached by cortical cytoskeleton which is built as a spectrin protein network (pentagonal or hexagonal arrangements) linked by short actin filaments (see Fig. 4.3) [215]. RBCs have no nucleus and internal cytoskeleton which makes the more suitable to our model assumptions (see above).

The spectrin network (about 2500 nodes per cell) in our DCM corresponds to a regular coarse-grained effective spectrin cytoskeleton. We here closely follow the modeling work of Fedosov et al. [14, 123]. However, our model assumes over-damped dynamics omitting thermal fluctuations, whereas in their work a Langevin equation was considered (DPD model). In contrast to the optical stretcher experiment, here the cell is attached by two beads glued on opposite sides. During the course of the experiment, the beads are pulled apart by exposing them with laser beams, while the deformation of the RBC is measured continuously (see Fig. 4.3, right). The intensity of the laser determines the force applied on the beads.

In the optical stretcher experiment deformations of the cells are larger than those in the optical tweezer. A significant difference with the cytoskeleton spring model used in the breast cancer cells (previous section) is the need for a nonlinear elastic force type, which accounts for the strain hardening and softening of the filaments in the spectrin cytoskeleton of the RBC. This behavior can be described by a FENE (Finite Extensible Nonlinear Elastic) model. The FENE model expresses that upon stretching, the biopolymers of the cytoskeleton first uncoil, providing relatively little resistance, but when completely stretched out, become practically non-extensible. The node-node FENE spring force can be written as:

$$F_{ij}^e = -k_{FENE} d_{ij} \left[1 - \left(\frac{d_{ij}}{d_{max}} \right)^{-2} \right]^{-1}, \quad (4.2)$$

where k_{FENE} is the stiffness, d_{ij} distance stretch between the nodes, and d^{max} is the maximum distance of the spring at which the force will diverge. FENE springs exert purely attractive forces. In order to account for the limited incompressibility of the spectrin, a simple power law is used for the compressive force F_{ij}^c :

$$F_{ij}^c \sim 1/d_{ij}^2. \quad (4.3)$$

¹Because of the presence of bending elasticity and resistance against area expansion of the plasma membrane, the overall behavior is not purely fluid-like but may rather be regarded as a Standard Linear Solid (SLS). However, these effects only appear on much longer timescales in the simulations.

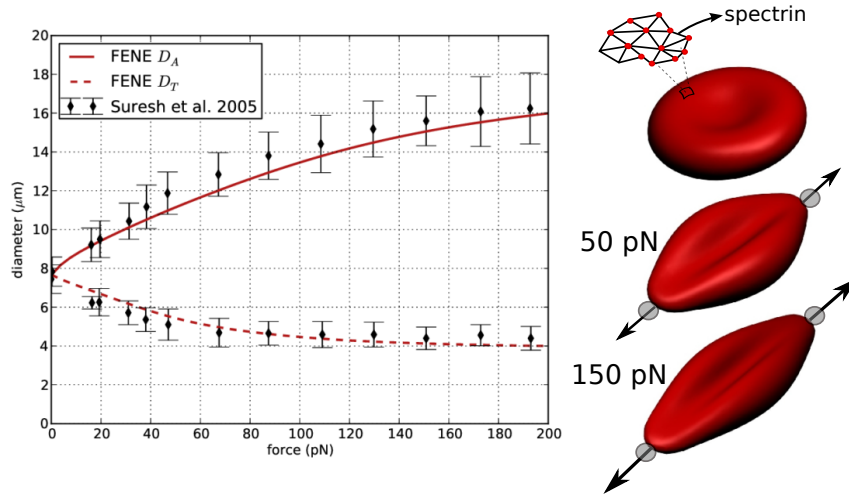


FIGURE 4.3: Results of cell stretching simulations. (Left) shows the change of axial diameter D_A and transversal diameter D_T in function of the stretching force, compared to experimental data from Suresh et al. (2005) [216]. (Right) visualized red blood cells for different stretching forces.

To simulate the RBC behavior, we pull on the outermost 5% of the nodes with the same force, and wait until the system is equilibrated. Despite have we used a different model approach, we have found a very good agreement with the experiments of Suresh et al. (2005) [216], see Fig. 4.3.

Adhesion and initial cell spreading dynamics

Adhesion governs to a large extent the mechanical interaction between a cell and its micro-environment. As initial cell spreading is purely adhesion driven, understanding this phenomenon leads to profound insight in both cell adhesion and cell-substrate interaction. It has been found that across a wide variety of cell types, initial spreading behavior universally follows the same power laws. To understand cell spreading, Cuvelier et al. (2007) [217] have performed experiments in which biotinylated Red Blood Cells were osmotically swollen to become spherical. During contact with streptavidin coated surface, the change of the radius of the contact area with time was measured. In another experiment by Hategan et al. (2004) [218], cells spread on a polylysine coated surface.

We have verified whether our proposed contact model for DCM can predict experimental data on cell spreading using the physical parameters that are known from the experiment [Odenthal et al., 2013]. The majority of the model parameters are physically meaningful, in principle measurable, and can be taken directly from the measurements in the experiment. For example, the adhesion energy values in the experiments are directly adopted in the model. This is different from approaches that model adhesion as potentials between nodes (e.g. [11]) which require extensive parameter tuning. The parameters related the contact friction with the substrate are a priori unknown, but the values used in the simulations are kept in their physiological range (as obtained from literature, e.g. [19]).

Within the model, the contact radius of the RBC with the surface can be calculated easily. Fig. 4.4B shows the power-law behavior of the spreading RBC spreading in double logarithmic representation. The spreading dynamics of the model match the experimentally observed cell spreading very well. Analysis of the initial dynamics of cell spreading with our model reveals that:

1. The “universal” $\sim \sqrt{t}$ power law behavior of initial cell spreading (see [217]) is found consistently in both experiments. Moreover, this behavior is very robust to changes in model parameters, because it is mainly caused by geometrical properties of the spreading cell. From the simulations we observe that this first spreading phase is characterized by the absence of tension

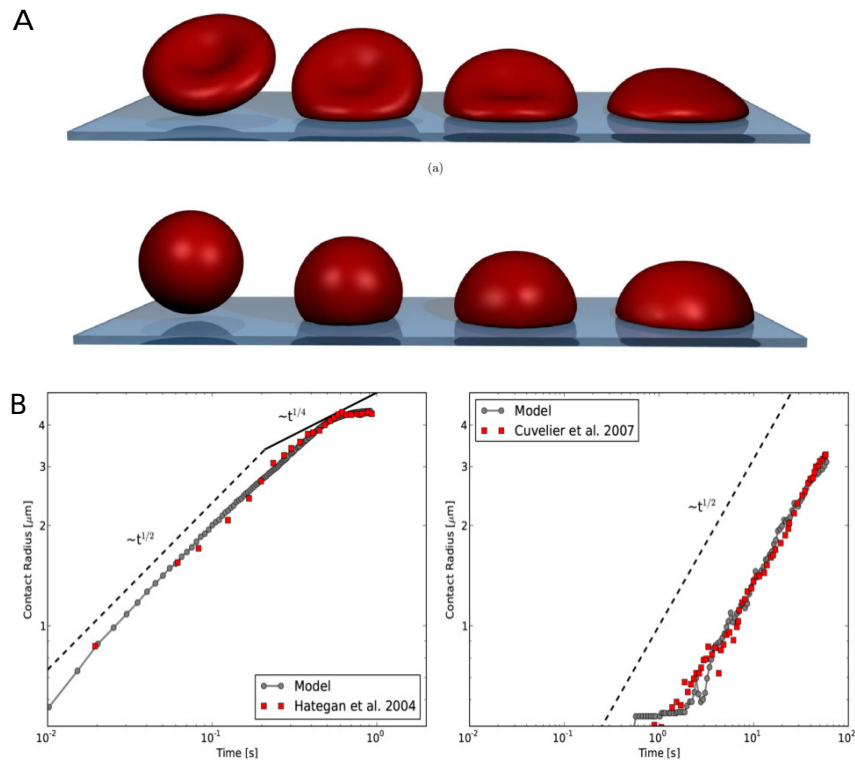


FIGURE 4.4: (A) Simulated cell spreading of the red blood cell at three different time-points. Top: binconcave RBC spreading, bottom: swollen RBC spreading. From left to right: no contact at $t=0s$, early contact at $t=0.1s$, approximately the cross-over between the two regimes at $t=0.3s$ and the fully spread cell at $t=1s$. The binconcave RBC has approximately 40% less volume than the osmotically swollen spherical red blood cell. (B) Contact radius vs. time for cell spreading simulations. comparison with experimental data from (B, left) Hategan et al. [218] for adhesion strength of 1 mJ/m^2 and with data from Cuvelier et al. (B, right) for adhesion strength of $88 \text{ } \mu\text{J/m}^2$.

in the cortical membrane. Since almost no forces are present there, little energy is stored elastically or dissipated in the cortical shell. To understand the $\sim \sqrt{t}$ law for the radius of contact (a), we follow the analysis presented by Cuvelier et al. (2007). We conclude that the energy dissipation rate is mainly affected by contact dissipation due to friction. It is therefore proportional to $\gamma a^2 (\frac{da}{dt})^2$, which can be balanced by the adhesive power. This adhesive power (rate of adhesion-energy gain) is proportional to $W a \frac{da}{dt}$, yielding for the trivial integration (ignoring all constants):

$$a \sim \sqrt{\frac{2W}{\gamma}} t^{1/2} \quad (4.4)$$

which explains (assuming the given approximations) the characteristic $\sim \sqrt{t}$ power law dynamics for the contact radius a . Summarizing, the total energy dissipation per area which is coming into contact with the substrate is constant at this very early stage of cell spreading, yielding the observed dynamics.

2. The first, “fast” slope can only be maintained until the cell’s cortex is under tensile stress: In that case, spreading further dissipates more energy – the stretching deformation causes viscous dissipation in the dashpot-like elements, while some is also stored in the (still weak) FENE-like potential. Cuvelier et al. (2007) show for several cell types, that in this region a second power $\sim t^{1/4}$ can be found, but it is least pronounced in the experimental RBC data (see Fig. 4.4B). From the simulations we observe that there is no clear second power-law regime, but merely a slowing down of the spreading.
3. Most of the energy dissipation during initial cell spreading occurs due to contact dissipation. The simulations indicate that for a red blood cell, no irreversible deformation in the cortical shell is required to reproduce the experimentally observed spreading dynamics. This means that, should we pull back our cell from the substrate, the cell would re-gain its initial shape, as the equilibrium lengths of the FENE connections and the equilibrium angles of the bending connections have not been changed. This is contrary to the simpler, conceptual model proposed by Cuvelier et al. [217], which relies on the dissipative “flow” of the cytoskeleton for energy dissipation.
4. The use of a FENE-like potential is important to consistently obtain these spreading dynamics. The same behavior cannot be captured by simple linear springs since they would be either too stiff to allow the initial “fast” spreading phase, or too soft to keep the cell from spreading out too much when the adhesion driven spreading stops.

Although the model as shown is restricted to RBC spreading dynamics, we expect that these conclusions can be generalized to other cell types: the same key mechanical components are present in other systems as well, and despite the fact that other cells’ cytoskeletons are more complex and the cells can dissipate energy through “active biological processes”, we expect the initial cell spreading phase to be still characterized by contact dissipation.

We note however, that this adhesion model does not represent dynamics of active spreading which are regulated by cellular processes such as actin polymerization, formation of focal adhesion complexes and stress fibers. A similar model incorporating the biological effects occurring during late cell spreading have been described in literature [127] However, they do not directly relate the initial spreading dynamics to material properties such as adhesion strength and contact dissipation.

Adhesion and pull-off force experiments

We have further validated the adhesion model now looking to the adhesive forces between two cells [Van Liedekerke et al., 2018b]. In [96] it was shown that JKR theory can be applied to living cells

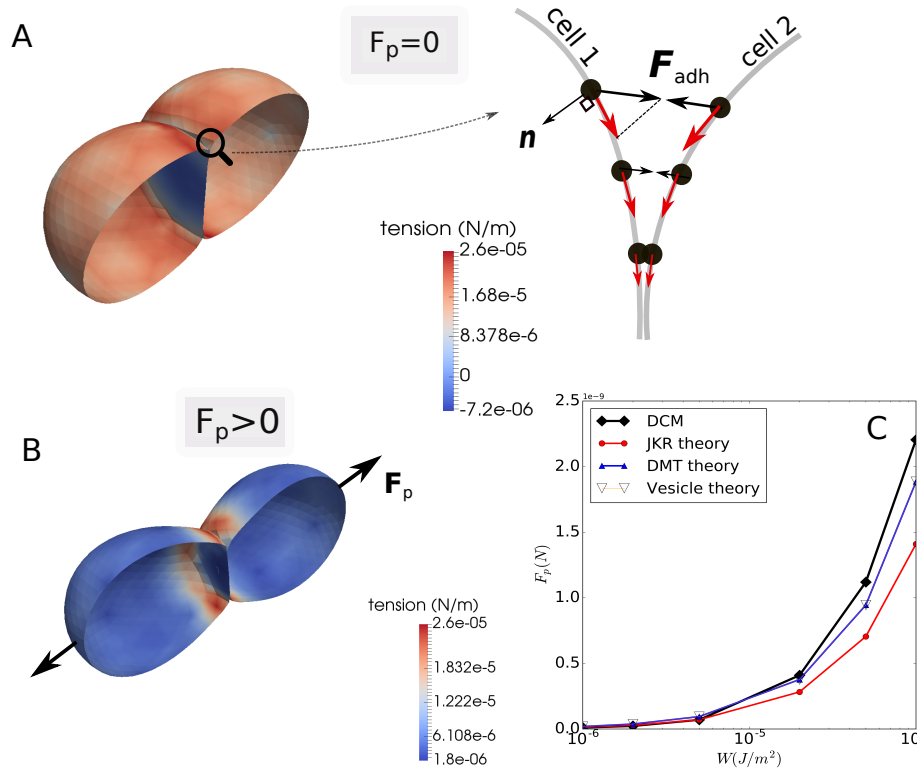


FIGURE 4.5: (A-B) Simulation snapshots of the experiment for determining pull-off force for adhering cells. The color coding is according to membrane stress. Stresses can be negative (compressive) in the common adhesive plane, indicated by the blue coloring (A, left). The 2D cartoon (A, right) shows the forces on the nodes F_{adh} . The resulting nodal force (red arrows) along the cell boundaries point towards the contact center. (B) Cell deformation during the pulling with net force F_p . (C) Pull off forces obtained as function of the adhesion energy: DCM simulations compared to JKR theory, DMT theory, and vesicle theory.

using micro pipette aspiration, providing a technique to determine the adhesion energy between cells experimentally. To verify that the resulting adhesive forces in our discretization are in the correct physical ranges, we have run several test simulations in which two adhered cells (with radius $R_1 = R_2$) are mechanically separated by applying opposite forces to them. The separating force (also called pull-off force) is a well-known quantity in JKR theory for soft adhesive spheres and reads

$$F_p = \frac{3}{2}\pi WR^*, \quad (4.5)$$

where W is the adhesion energy and $\frac{1}{R^*} = \frac{1}{R_1} + \frac{1}{R_2}$. On the other hand, adhesion between stiff spheres is best described by Derjaguin-Muller-Toporov (DMT) theory [219], leading to a pull off force of $F_p = 2\pi WR^*$. For vesicles, a theoretical analysis leads to $F_p = \pi WR^*$ for $R_1 = R_2$ [219].

To measure the cell-cell adhesion force in our simulations, two cells in contact are first brought into contact and relaxed until they are in an equilibrium state. The adhesion energy is a genuine parameter in our model. Then a force equal in magnitude is applied on each node of both cells into the direction perpendicular to the cell-cell contact, whereby the force on one cell is exerted in opposite direction than the force on the other cell. The orientation is chosen such that the contact is under tensile stress (negative load). The cells then move away from each other until a new equilibrium is reached (Fig. 4.5). The force at which the cells just separate defines the pull-off force. By performing several simulations following a binary search algorithm, we estimate the pull-off force. The operation

is done for increasing adhesive forces and depicted in Fig. 4.5C. This shows that the simulated pull-off forces are indeed very close to the theoretical values as calculated from JKR theory, DMT theory, and vesicle theory. Overall, we can assume that the implementation of the adhesion energy and the choice of parameters in the model reproduce realistic magnitudes for the contact force.

A closer analysis of Fig. 4.5 (top) further reveals that local in-plane tensions (Eq. B.5) in the membrane of the adhered cells are largely tensile except in the adhesive plane where they can be compressive. This is a direct consequence of the higher adhesive node-node forces at the boundary of a cell-cell contact, which generate forces (see red arrows in sketch, Fig. 4.5) on the nodes along the cell-cell interface towards the contact zone. This phenomenon is in agreement with experimental observations [220, 221]. A very strong adhesion energy might even result in a buckling of the cell surfaces at the contact zone as we observed in test simulations, and as was suggested in [3].

4.4 Multi-cellular simulations

In the following we illustrate the use and effectiveness of the DCM for monolayers, spheroids, and regenerating liver lobules. The by far largest restriction of the DCM is its computational cost. Therefore, we have endeavored to find down-scaled systems with an equivalent dynamics and/or resort to hybrid modeling, in where we can partially and locally replace the DCM by the ordinary CBM.

4.4.1 Monolayer and spheroid simulations

Multicellular spheroids and monolayers are often used and tested as in-vitro models for tissues [222]. Several authors have investigated the growth dynamics of these systems using agent-based models. In particular, center-based models (see section 2.2.2) have given valuable insights in how cell growth is affected by hypoxia and contact inhibition [38, 114, 99].

Here, we employ our deformable cell model including cell division with regard to the aforementioned systems. In the growth dynamics of multicellular assemblies, important parameters are the strength of cell-cell adhesion responsible for the formation of multiple cell-cell contacts, and viscous cell-cell friction. To determine the cell-cell friction coefficients, we have simulated the relaxation behavior in an experiment whereby a spheroid is first compressed and subsequently released, see Appendix B.4. For long compression times, typical relaxation times of ~ 5 hours have been reported for such experiments [223, 224]. Hence the spheroid relaxation times are much longer than the short relaxation timescales of the cells in the stretcher experiment, indicating that cellular re-organization processes not relevant in the optical stretcher experiments play a major role on the time scale of multicellular spheroid relaxation. E.g., trypsinated cells in suspension round off indicating that on time scales much longer than those probed in optical stretcher experiments, the cell relaxation behavior is governed by processes restoring a spherical cell shape, which is not correctly captured by the modified Maxwell element mimicking short term relaxation (Fig. 4.2B). Instead of further complexifying the viscoelastic elements to capture both the short and long-term relaxation behavior at the expense of elevating the computing time requirement², we here use the simple KV viscoelastic elements for the simulations at the time scale of cell growth and division. This allows to fit the internal friction coefficients and cell-cell friction coefficients such that the spheroid relaxation is approximately 5 hours without prolonging the computing time (see Fig. B.3B).

Both MCSs and monolayer simulations start from a single cell growing and dividing unlimited with a cell cycle time of 24h. Each cell is represented by 162 nodes. For an overview of all the reference parameters, see Table B.1. The simulations are run over several days, in which in total about 1000 cells are created (see time series of simulation snapshots in Fig. 4.6A, B for MCSs and monolayers, respectively). Two cases were simulated, one with the original specific adhesion energy,

²The long-term relaxation into a spherical shape might be mimicked by implementing an additional spring in parallel with small spring constant in the MME element.

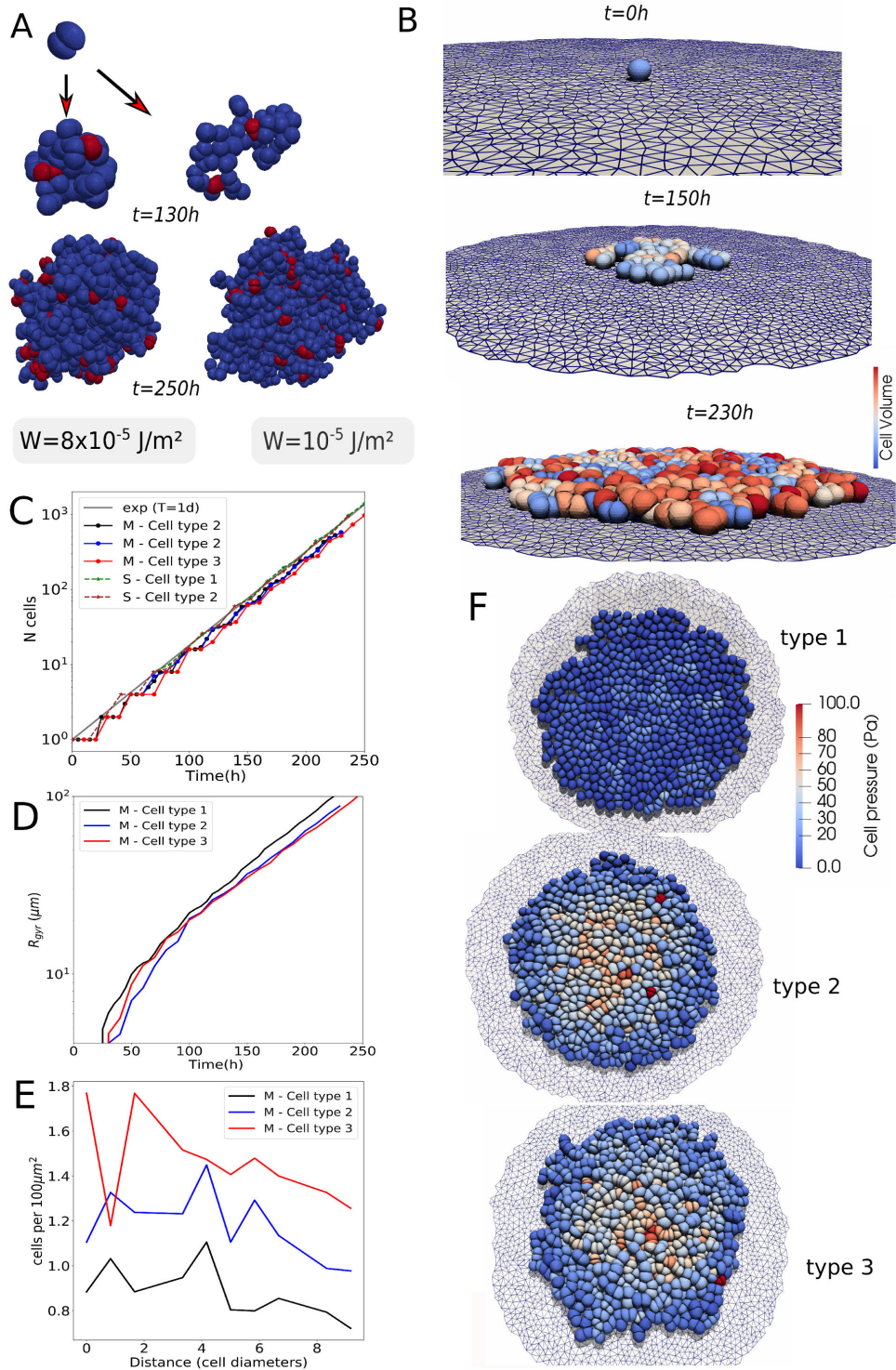


FIGURE 4.6: Simulation snapshots and time series for multicellular spheroid (MCS) and monolayer growth. (A) Spheroid growth with specific cell-cell adhesion energies $W = 1 \cdot 10^{-5} \text{ J/m}^2$ and $W = 8 \cdot 10^{-5} \text{ J/m}^2$. (B) Typical monolayer growth scenario (screenshots). (C-E) Kinetics of the cell population size $N(t)$ (monolayers, MCS), radius of gyration $R_{gyr}(t)$ (monolayers) and area density profile (number of cells per unit of substrate area) $\rho(r, N = 1000)$ (monolayers). (F) Visualization of spatial pressure distribution in multicellular pattern for type 1-3 monolayers (the color encodes internal cell pressure (red: high, blue: low pressure)). Parameters for monolayers: type 1: cell-cell specific adhesion energy $W \approx 0 \text{ J/m}^2$, cell-substrate adhesion energy $W = 10^{-5} \text{ J/m}^2$, $D = 10^{-15} \text{ m}^2/\text{s}$; type 2: cell-cell specific adhesion energy $W = 10^{-5} \text{ J/m}^2$, cell-substrate adhesion energy $W = 10^{-5} \text{ J/m}^2$, $D = 10^{-16} \text{ m}^2/\text{s}$; type 3: cell-cell specific adhesion energy $W = 5 \times 10^{-5} \text{ J/m}^2$, cell-substrate adhesion energy $W = 10^{-5} \text{ J/m}^2$, $D = 10^{-16} \text{ m}^2/\text{s}$.

$W = 10^{-5} \text{ J/m}^2$, one with an increased specific adhesion energy, $W = 8 \cdot 10^{-5} \text{ J/m}^2$. However the cell population sizes were too small to objectify differences in the tumor spheroid shape despite the spheroid with $W = 8 \cdot 10^{-5} \text{ J/m}^2$ looks slightly more compact compared to the other case, where intermittently, small “branches” form (Fig. 4.6A, right). At this cell population size, the number of cells grows exponential in time in both cases (Fig. 4.6C).

In a further step, we test our model for three different cases of monolayer growth. We first constructed a flat fixed adhesive surface, triangulated with a slightly larger mesh size than the one used for the cell surface triangulation. The simulation starts from one cell adhering to the surface (the reference adhesion energy per area is $W = 10^{-5} \text{ J/m}^2$). To study the effect of adhesive strength, we simulated monolayer growth scenarios for three different parameter combinations, denoted as type 1-3, with type 1: specific cell-cell adhesion energy $W = 10^{-16} \text{ J/m}^2$, and relatively large diffusion constant $D = 10^{-15} \text{ m}^2/\text{s}$; type 2: specific cell-cell adhesion energy $W = 10^{-5} \text{ J/m}^2$, and diffusion constant $D = 10^{-16} \text{ m}^2/\text{s}$; type 3: specific cell-cell adhesion energy $W = 5 \times 10^{-5} \text{ J/m}^2$, and diffusion constant $D = 10^{-16} \text{ m}^2/\text{s}$ (Fig. 4.6C-F). Visually no large difference between the spatial pattern for different parameter combinations can be seen. This is objectified by plotting the radius of gyration $R_{gyr}(t)$ for the three different parameter combinations, which is a measure for the spatial cell spread. It is defined as $R_{gyr} = \sqrt{(1/N) \sum_i (\mathbf{x}_i - \mathbf{x}_{com})^2}$, where \mathbf{x}_i and $\mathbf{x}_{com} = (1/N) \sum_i \mathbf{x}_i$ are the center-of-mass positions of the individual cells and the whole multicellular cluster, respectively. There is no significant difference in R_{gyr} for the three different types. All three populations grow exponentially fast during the simulation time period. However, the pressure profile differs: at a population size of 1000 cells, the pressure in the center of the monolayer is largest for type 3, the smallest for type 1 and intermediate for type 2. For type 1, the cell-cell adhesion energy is almost zero while the micro-motility is the largest, which results in a maximum relaxation of compressive stress and lower cell density (Fig. 4.6E). The specific cell-cell adhesion energy for type 3 cells is higher than for type 2 cells while all other parameters are the same, resulting in a higher adhesion and hence a higher compression (highly jammed state) in the interior of type 3 cell populations compared to the interior of type 2 populations (Fig. 4.6E). The spatial profile shows a decrease from the center to the border, in qualitative agreement with earlier observations in center-based model simulations (e.g. [113, 19]) but different from the center-based model. Contrary to the former studies, the cell volume and pressure in DCM simulations can be calculated more precisely.

In summary, these simulations show the potential of the model to analyze in detail forces, shape and pattern formation in monolayers and spheroids. We must emphasize that the aforementioned results are indicative and that much more and much longer simulations maybe required to come to stronger conclusions.

4.4.2 Regeneration of a liver lobule

Finally we come back to the introductory example of the regenerating liver lobule after CCl4-induced peri-central damage, and study whether the regeneration process with the DCM model would lead to different results than obtained with the CBM model [8]. As the smallest repetitive physiological and anatomical unit is a liver lobule, our model simulations focus on this unit. A liver lobule has a central vein located approximately in its center that collects blood from the capillary (sinusoidal) network surrounding the central vein. The blood enters the liver lobule through 3-4 pairs of portal veins and hepatic arteries. Portal veins carry blood from the intestine to the liver contributing about 70% of the blood entering the liver lobule, and hepatic arteries carry oxygen-rich blood from the aorta to the liver. Hepatocytes are arranged around the capillaries. In the cut section perpendicular to the central vein the lobular shape is approximately a hexagon. The distance from the central vein to the lobule border (radius of the lobule) is about 9 cell diameters (Hammad et. al., 2014) [225]. A typical 3D volume data sample obtained by processing of optical sections from confocal micrographs has a height of three cell layers. Between sinusoids and hepatocytes there is an about $0.5 \mu\text{m}$ small space, named "space of Disse" filled with ECM that mechanically stabilizes the sinusoidal network.

The liver lobule micro-architecture ensures a maximum exchange area between hepatocytes and sinusoids for metabolites, thereby promoting metabolism in the hepatocytes. After overdose of the drugs CCl₄ or acetaminophen (paracetamol, APAP) those cells expressing the Cytochrome P450 enzymes CYP2E1 and CYP1A2 metabolize these two drugs to NAPQI, which downstream causes cell death. In healthy liver, CYP-expressing enzymes are localized in hepatocytes within an area fraction of about 40% around the central vein. At sufficiently high doses of CCl₄ (or acetaminophen) the hepatocytes are killed leaving a central lesion with debris with maximal size at about 1-2 days after administration of the drug. About two days after the generation of the lesion, hepatocytes start to divide, reaching closure of the necrotic lesion and regeneration of the hepatocyte mass after about 6 days [8]. The hepatocytes localized at and close to the border of the lesion proliferate by far the most, while proliferation is lower in the layers more distant to the lesion.

The simulations are performed in a statistically representative liver lobules, obtained by sampling of parameters quantifying the lobule architecture in confocal laser scanning micrographs (Hoehme et al., 2010). A statistically representative lobule has a hexagonal structure (Fig. 4.7A-B, XY plane) with a vertically (Z axis) oriented central vein in its center and three portal veins and hepatic arteries in three of its six corners. Earlier simulations with a center-based model revealed that cell proliferation alone, without directed migration of hepatocytes towards the central vein, was insufficient to explain the experimental observations [8]. The mechanical pressure exerted by proliferating cells on their neighbors leading to pushing of cells and squeezing them into the spaces between the sinusoidal network was insufficient to close the lesion within the experimentally observed time period. In center-based models (CBM), cells are by construction usually relatively rigid as only moderate deviations of cell shape from their equilibrium shape in isolation can be captured by that model type. Furthermore, forces in standard center-based models are defined by pairwise lumping compression and deformation forces together. We here study if this rigidity might be responsible for the failure of simulated regeneration in the experimentally observed time period.

As in ref. [8] we used a three-cells-thick lobule architecture representative of a mouse liver. The sinusoids and veins are approximated as a dense network of fixed overlapping spheres, each with radius equal to the vessel radii. The high density of overlapping spheres warrants a smooth interaction with the cells. The hexagonal shape allows for identification of 6 statistically identical "pies" together constituting a full lobule. As a full lobule is currently not amenable to simulations with the DCM because of the large computation times, we simulate regeneration in only one pie, representing 1/6 of a statistically representative liver lobule (Fig. 4.7C) At the outer boundaries of the lobule pie, the cells are pushed back by vertical planes that mimic the presence of the neighboring lobule parts, see Fig. 4.7B. In our model, we assume that vessels can interact with the cells, yet their positions remain static during the simulation [8]. We perform both DCM and CBM simulations of the regeneration and quantitatively compare the differences. Both simulations start from identical initial conditions and configurations, and have the same model parameters (see Table B.1). A maximum equivalence of mechanical parameters for both model types is ensured.

We start from a multi-cellular configuration characteristic for the beginning of the regeneration process after CCl₄ (or acetaminophen)-generated damage, where only hepatocytes localized at distance of at least R_{nec} from the central vein survive (see Fig. 4.7C-D, blue colored cells). Hepatocytes localized at distances smaller than R_{nec} from the central vein are assumed to be killed by the drug and removed from the system as those express the CYP-enzymes metabolizing CCl₄ to NAPQI, which downstream leads to cell death. At $t < 0$, there are about 90 cells positioned in the free spaces between the sinusoids. An initial small radius is assigned to the hepatocytes, so that they initially do not touch the sinusoids. Next, the hepatocytes' size is artificially increased, gradually generating contact with the sinusoids, until the hepatocytes reach a radius of $R_c = 12 \mu\text{m}$ (Hammad et al., 2014) and the system reaches a mechanical equilibrium (Fig. 4.7D). The time at this starting configuration is set to $t = 0$ as we here focus on the regeneration process (which is about 2-2.5 days after drug administration [8]).

During regeneration, those cells that have survived the intoxication enter the cell cycle to grow

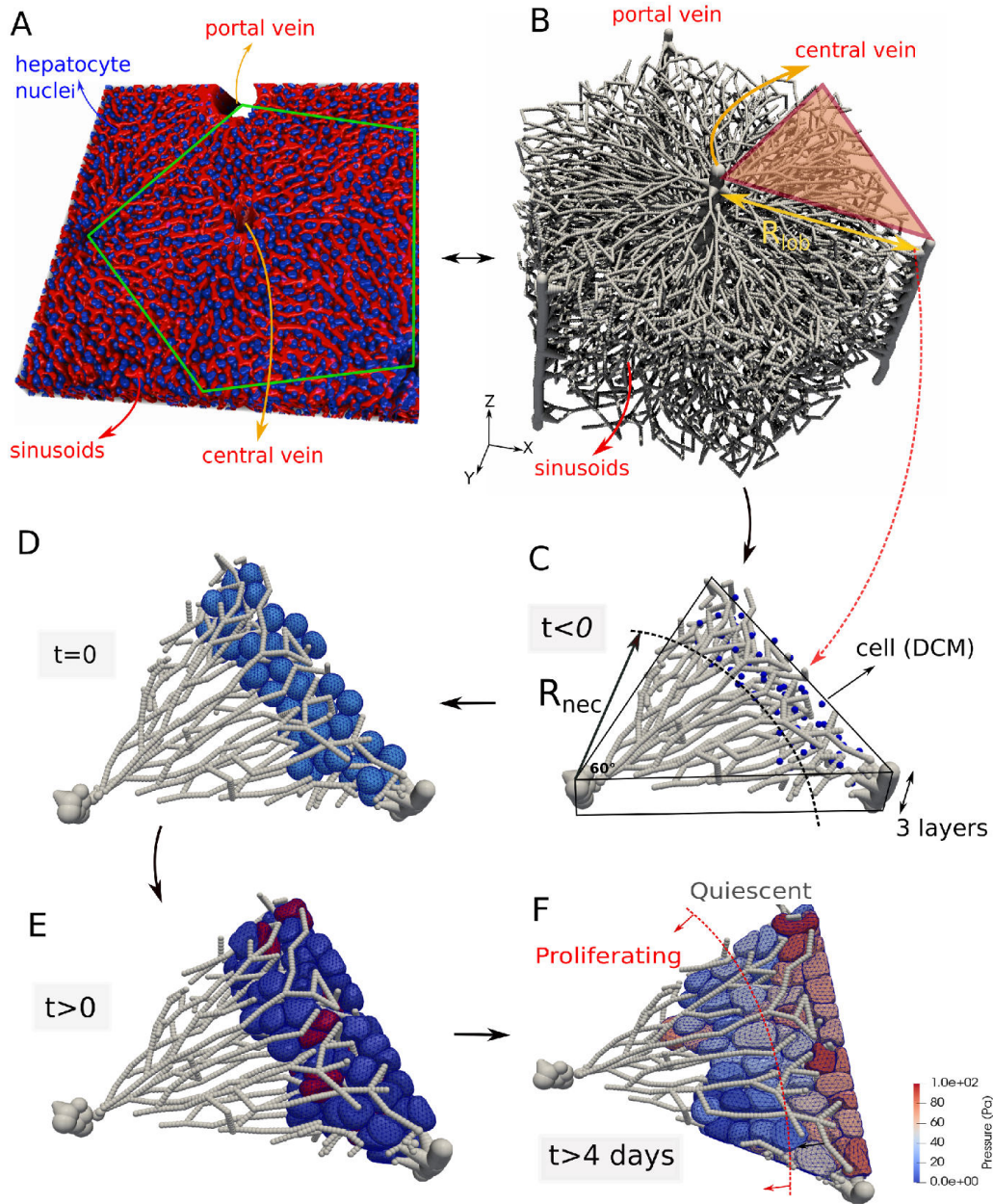


FIGURE 4.7: (A) Segmentation of hepatocyte nuclei (blue) and sinusoidal network (red) in liver tissue of mouse. Green lines outline a liver lobule sub-structure in the tissue. (B) Structure of the blood vessel network of a single lobule within the model. (C) Part of the network used for the simulations with the DCM. (C-D) Cells artificially growing up to realistic cell size (initialization). (E) The spatial-temporal proliferation pattern is imposed. The red cells are dividing. (F) Regeneration process the lobule, cells are colored according to internal pressure.

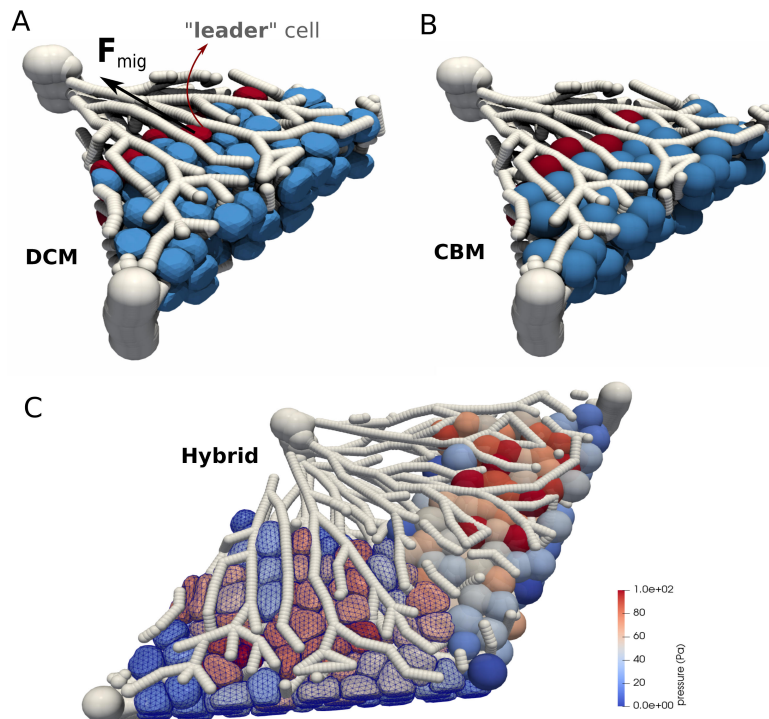


FIGURE 4.8: Simulation snapshots of the liver regeneration performed with the DCM (A) and CBM (B). (C) Simulation of CBM and DCM in hybrid mode. The colorbar here is according to cell pressure.

and divide with a rate depending on their distance from the necrotic lesion. During the regeneration process, they gradually move towards the central part, and eventually close the lesion and restore the lobule hepatocyte mass. Hepatocytes do not enter as individual, isolated cells (like mesenchymal cells) but in a collective movement as a sheet (with epithelial phenotype). In the simulations performed in [8] the spatio-temporal proliferation pattern of the cells during regeneration from an experimental *BrdU* staining pattern was directly imposed to the cells. *BrdU* stains cells in S-phase. Here, we impose a similar but a slightly coarse-grained proliferation pattern (for simplicity and better comparability to CBM-simulations), where cells are proliferating in a certain time window (Fig. 4.9A) and in a region smaller than 4-5 cell layers closest to the necrotic lesion. Outside this window, cells are assumed to be quiescent. Despite we do not simulate the entire lobule, the simulation results can readily be extrapolated to an entire lobule. By extrapolating the ratio of the cells numbers before intoxication and after regeneration with regard to the dimensions [8], the simulation results can be directly compared to that work.

The cells gradually progress towards the central vein to close the lesion with the largest fraction of proliferating cells at the border to the lesion (the front of the expanding tissue) and smallest proliferation activity at the periportal field (Fig. 4.7F). During the simulations, various cell state variables such as pressure, volume, state and tissue properties (cell density, area of the necrotic zone) can be monitored (see Fig. 4.7, Fig. 4.9 and Fig. 4.8)

In a next step we study whether different hypotheses addressing the behavior of individual cells can explain the closure of the pericentral liver lobule lesion generated by toxic concentrations of CCl₄ or acetaminophen. Guided by the choices in ref. [8] we distinguish between three model cases in which the cells differ by certain migratory or proliferation-related properties.

In the basic model (Model I), we assume the cells to be proliferating with daughter cells oriented in a random direction and active movement generated by an unbiased random force (controlled by

the cell diffusion coefficient D)³. With this mechanism, the lesion closure speed⁴ is too small (see Fig. 4.9B), showing that this model is not in agreement with the experimental data for a time window of 10 days after intoxication, for both the DCM and the CBM. This is in line with the conclusion in ref. [8], stating that the pericentral lobule lesion does not completely close within the experimentally observed time period if the driving force for the closure is cell proliferation only. Nevertheless, the DCM simulations exhibit a closer agreement with the experimental data than the CBM. Potentially, this is due to the more realistic contact forces and cell shapes in DCM compared to the CBM, which permit deformable cells to adapt their shape by squeezing in between the sinusoids. The pairwise JKR-based contact force in CBM lumps force contributions originating from cell deformation and compression into one mathematical formula assuming slight cell shape changes only. As a consequence at large compression forces emerging as a result of massive cell proliferation as in liver regeneration after drug-induced pericentral damage, significant overlap among cells, and cells and blood vessels can occur. The overlap might lead to an underestimation of the total volume occupied by the cells and blood vessels and too small repulsion forces between cells, and cells and vessels. This in turn critically slows down cell movement of cells that are pushed by proliferating cells towards the lesion, as the pushing forces result from volume compression. In the DCM simulations, volume is explicitly tracked hence cells are pushed away stronger. At the same time, DCM-cells can automatically adapt their shape and squeeze through the network. Both effects together speed up the cell displacement in DCM compared to CBM.

In the second model (Model II), we assumed that during division the daughter cells align along the closest sinusoid, in Hoehme et al. (2010) [8] named “hepatocyte-sinusoid alignment” (HSA) mechanism and identified as responsible order mechanism for the reconstitution of liver lobule micro-architecture. In ref. [8] healthy liver lobule micro-architecture was shown to be characterized by a maximal hepatocyte-sinusoid contact area, facilitating the molecular exchange area between hepatocytes and blood. However, contrary to the model of Hoehme et al., where cell polarity was introduced as anisotropic adhesive forces, we here do not impose cell polarity; HSA in combination with differential adhesion between hepatocytes and lack of adhesion between hepatocytes and sinusoids already result in a largely columnar order. Moreover, in Hoehme et al. (2010) HSA was combined with a directed migration of hepatocytes towards the central necrotic lesion, which we drop in Model II to test the effect of HSA only. Interestingly, with this “directed division” mechanism, we observe for both the CBM and the DCM a slight “speed-up” of the lesion closure, in line with the reasoning that cells get less obstructed by the sinusoids after division if aligned. Yet, an acceptable quantitative agreement is not obtained (see Fig. 4.9B).

Finally, in the third model (Model III) we assume that cells migrate towards the central vein as a response on a morphogen gradient, whereby the morphogen source is the necrotic lesion. The directed migration manifests itself as an active force \mathbf{F}^{mor} in the equation of motion (Eq. 2.35). Cell migration in liver is mediated by the extracellular matrix (ECM) scaffold, whereby the ECM is localized mainly in the space of Disse [226]. In Hoehme et al. (2010), hepatocytes at the border of the necrotic lesion were observed to stretch filopodia into the necrotic lesion. Consequently, the migration force \mathbf{F}^{mor} is assumed to only act on the outer cells (here referred to as “leader” cells) and directed towards the central vein (Fig. 4.8A).

In Hoehme et al. (2010) adding directed migration forces towards the central vein to Model I was able to ensure complete lesion closure. For the DCM simulations with Model III, we found an excellent agreement with the data if the migration force had a strength of $F^{mor} \sim 0.3$ nN. Contrary, for the CBM simulations with the same model (Model III) a significantly larger force of 1 nN is needed to close the lesion, showing again the significant and important differences between the two model approaches at the quantitative level (Fig. 4.9C). In turn, simulations with DCM with the migration force chosen as the migration force needed in the CBM to close the lesion (i.e. 1 nN) led to a too

³The assumptions in Model I are equivalent to those in Model 1 in ref. [8]

⁴We define here the lesion radius as the average distance from the central vein to the closest cell in every layer whereby we consider the 3 closest layers to the lesion.

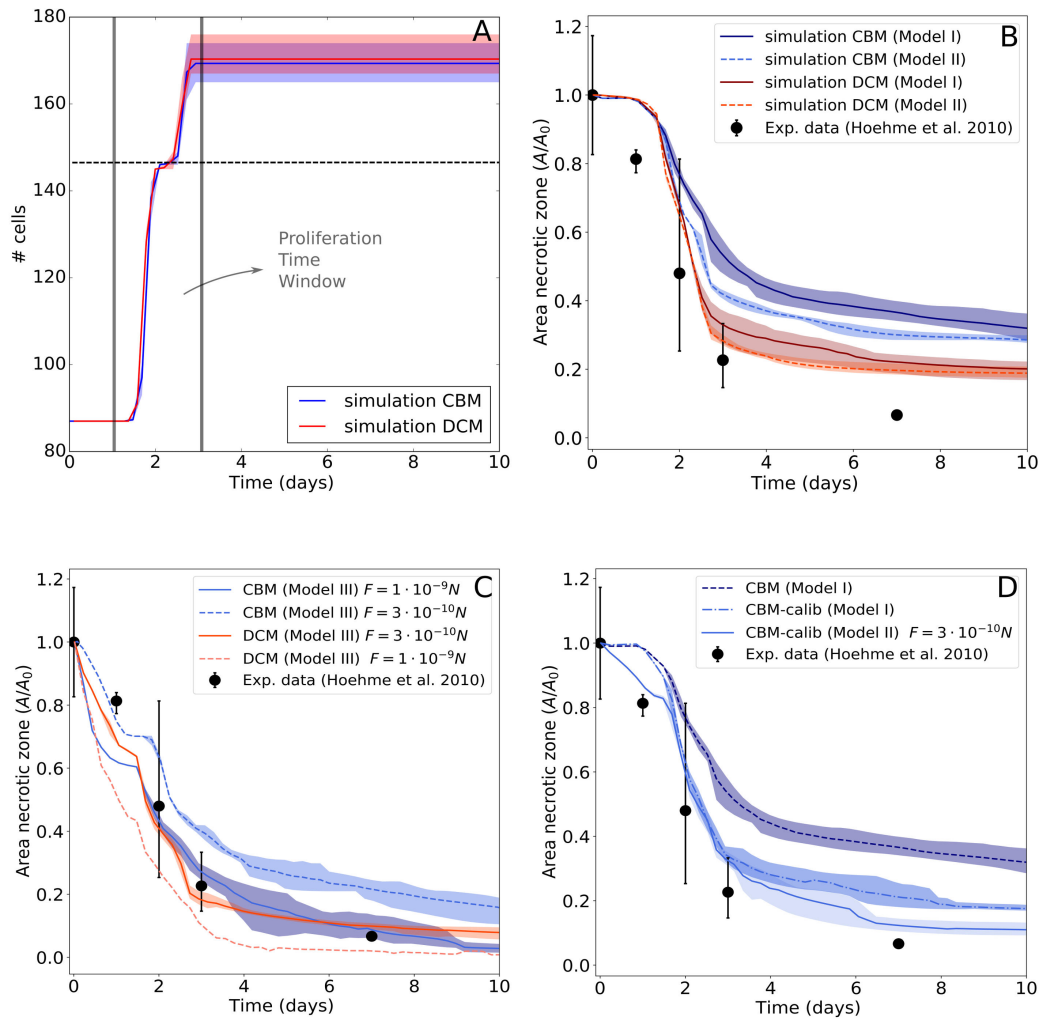


FIGURE 4.9: (A) Simulation (DCM and CBM) of the evolution of cell numbers during the time course of the simulation. (B) Simulated (DCM and CBM) relative area of the necrotic lesion during liver regeneration compared to data from Hoehme et al. (2010), assuming Model I and Model II. (C) Simulated (DCM and CBM) relative area of the necrotic lesion assuming Model III. (D) Simulated (CBM) relative area of the necrotic lesion using the calibration procedure for contact forces, assuming Model I or Model III. Each line is the average of 5 simulations with different random seeds, the shadowed zone indicates maximum and minimum values.

fast motion of the hepatocytes, hence a too fast closure of the lesion (Fig. 4.9C). This again confirms DCM-cells adapt easier to the obstructions imposed by the environment. However, overall the magnitude of the migration force for both approaches is in agreement with experimental observations of migrating cells [227, 228]. Specific measurements for regeneration after drug induced damage have so far not been performed.

The simplified formalism in CBMs thus lead to unadapted cell shapes (Fig. 4.8A-B) and possibly quantitatively incorrect contact forces and cell density. In order to test the influence of the contact forces between the cells on the results, we applied our procedure to re-calibrate the CBM contact forces from the DCM (see Appendix B.4). In the procedure we simulate a spheroid compression experiment. The contact stiffness of every CBM cell is adjusted depending on by how many neighbor cells it is surrounded and by the relative distances between the cell and its neighboring cells, to finally obtain the same contact forces as in the equivalent DCM simulation. As such, we obtain a calibrated CBM that takes the effect of multiple cell contacts into account (see also chapter 5). Using the calibrated CBM, we rerun the simulations for Model I and Model II. For Model I, the lesion is now closing faster and comparable to the DCM simulations. For Model III we now obtained a much better agreement if using the same migration force as in DCM (Fig. 4.9D). This overall shows the significant impact of quantitatively correct contact forces for quantitative simulations of the cell dynamics in the liver lobule. Simulations with center-based models may still be used to give valuable quantitative insight if the cell contact mechanics is corrected. The DCM thus permits to partially correct for inaccuracies of the CBM, and to serve as an instrument for verification simulations for selective parameter sets, whereby parameter sensitivity analysis simulations might now still be performed with the computationally much faster CBM. We conclude that with a more refined cell model as the DCM model, the magnitude of the active migration force needed to close the central necrotic lesion after drug-induced peri-central damage by CCl₄ is smaller than for the center-based model, but over all the same mechanisms i.e., active hepatocyte migration towards the necrotic lesion and oriented cell division are necessary for closure of the lesion. This qualitatively confirms the conclusion made in Hoehme et al. (2010) based on simulations with a CBM. However as we demonstrated, the differences between CBM and DCM simulations become very small if the cell-cell interaction forces in the CBM are calibrated by simulations with the DCM.

In line with this argument, we demonstrate that the two model approaches are capable to work in a hybrid mode. This is particularly useful if one can subdivide the total system in zones with a higher interest where more detail is required (high interest), and others where only approximated dynamics is needed (low interest), see e.g. [28]. Here, a lower computational cost can be obtained if the zone of lower interest can be simulated using CBM. Thanks to the nature of the contact model of the DCM, we can run simulations where parts of the lobule are covered by a DCM while others by a CBM. In Fig. 4.8C we have considered two equal parts of the liver lobule where each part is covered by another model. At the interface, the model ensures that cells from DCM and CBM smoothly interact.

4.5 Summary and conclusions

In this chapter we have introduced an agent-based deformable cell model (DCM) that aims to perform accurate tissue mechanics simulations. An *in silico* cell is primarily constructed by a triangulated network of viscoelastic elements that represent the cortical cytoskeleton, containing a homogeneous compressible cytoplasm. In [Odenthal et al., 2013] we have proven that this model accurately predicts initial spreading behavior of a cell on a surface. We have later extended this single-cell model with algorithms for growth, proliferation, and motility to permit perform multi-cellular simulations [Van Liedekerke et al., 2018b].

Overall, we have shown that the model parameters are physically tangible and can be calibrated with single cell experiments (optical tweezer, optical stretcher, cell adhesion experiments). An adequate choice of the rheological model for the individual subcellular elements (representing the outer

cytoskeleton) and the calibration of parameters hereof, is an essential aspect for acquiring realistic simulations. We have demonstrated how the viscoelastic elements can be chosen to explain data at time scales differing by order of magnitudes, namely optical stretcher experiments to probe cell biomechanics on a time scale of seconds, as well as tissue regeneration occurring at time scales of several days. Performing *in silico* pull-off experiments imposing increasing adhesion energies, we have further verified that the adopted cell contact model consistently reproduces realistic forces in cell-cell adhesive contacts.

The ability in the model for cells to grow and divide currently allows to simulate small *in-vitro* experiments such as monolayers and spheroids. Despite the relatively low cell numbers, we have here illustrated that adhesion energy variations between cells and substrate may have different effects in monolayers as compared to spheroids.

Hoehme et al. (2010) demonstrated that agent-based CBM simulations are capable of giving valuable insights in liver regenerative processes. In particular, their simulations of a liver lobule regeneration showed that after intoxication, cell cycle re-entrance and cell division alone cannot explain the closure of lesions. They concluded that cells need migrative forces in order to acquire a fully regenerated lobule in a realistic time course. However, the center-based model has no explicit notion of shape in case cells are densely packed as this is a case in a regenerating liver lobule. Our simulations with the more sophisticated deformable cell model confirm this hypothesis, yet comparisons between our model and the center-based approach indicates some important quantitative differences, which we could use to identify critical model determinants that must be represented in sufficient detail.

(1) In the DCM, cells adapt to their environment requiring lower migrative forces to close the gap as compared to their center-based counter parts. In the latter, large cell-cell overlaps exists and rigid cell shapes result in a lower closure speed or higher required migrative force to close the lesion.

(2) Cell contact forces play an important role in the dynamics. Replacing the (standard) JKR contact force model in the CBM by new force relations obtained from simulated force probing experiments with the DCM largely removed the difference in the regeneration dynamics between CBM and DCM. However, finding such a force might become almost impossible if, as in diseases such as fibrosis, the spaces between blood vessels and extracellular matrix structures are so narrow, that the cell body has to deform into a long thin object to squeeze through them. Another example where realistic contact forces for a CBM might not be found is in case of fluid-like movement of cells in cell sheets where cells move along each other despite high cell density. In such a type of movement, large deformation of cell shape from spheres might be necessary to permit cells moving, while at the same time, the volume of the cells is largely conserved. This combination -shape change at (almost) conserved volume- is an obstacle for center based models.

(3) DCM simulations result in more accurate cell shapes along the sinusoids as they adapt to the environment (cells do not overlap with sinusoids).

In conclusion, we have argued that this highly detailed model approach may become a requirement to simulate tissue regeneration quantitatively, integrating subcellular information on cell shapes and biomechanics. This is likely to increase the computational cost and require distributed computing. Large population DCM simulations will require code parallelization envisaged for the future. Yet, the approach proposed here also allows to simulate tissues in a hybrid mode. This may open possibilities to accomplish large scale tissue simulations where some parts are modeled at high spatial resolution models, while in other zones approximate models are sufficient. We have demonstrated this by hybrid simulations in a proof of concept.

Chapter 5

Quantitative hybrid modeling of mechanical stress response of growing tumor spheroids

5.1 Introduction

Whereas in chapter 2, I focused on the effects of mechanical stress on cells during impact, here I discuss the results of investigating the long-term effects of stress on cell growth with agent-based models [Van Liedekerke et al., 2018a].

Cell growth in a confined environment such as provided by the stroma and surrounding tissues increases cell density and affects the balance between cell proliferation and death in tissue homeostasis [229, 230]. Avascular Tumor spheroids have long been considered as appropriate in vitro models for tumors [222]. While the dynamics of freely growing spheroids has been extensively studied both experimentally [231] and numerically (e.g. [38, 99]), more recent experiments have also addressed the growth of spheroids under mechanical stress.

Helmlinger et al. (1997) and later Cheng et al. (2009) and Mills et al. (2014) [232, 233, 234] experimentally investigated the growth of spheroids embedded in agarose gel pads at varying agarose concentration as a tunable parameter for the stiffness of the surrounding medium. Other approaches such as the application of an osmotic pressure determined by a dextran polymer solution have also been developed to investigate the impact of external pressure on spheroid growth [235]. In all cases mechanical stress was reported to slow down or inhibit spheroid growth. Delarue et al. [236] suggested that growth stagnation is related to a volume decrease of the cells. However, a quantitative relation between pressure and cell fate has not been reached yet. The works of Helmlinger et al. [232] and their follow-ups have inspired a number of theoretical papers aiming at explaining the observations, either based on continuum approaches considering locally averaged variables [237, 238, 239, 230, 240], or by agent-based models (ABMs) representing each individual cell [114, 241] belonging to the class of models, which are extended and refined in the presented work. For example, the growth kinetics of multicellular spheroids (MCS) embedded in agarose gel as observed by Helmlinger et al. [232] could be largely reproduced, if cell cycle progression was assumed to be inhibited either above a certain threshold pressure or below a certain threshold distance between the cell centers, whereby growth inhibition occurred at different spheroid sizes for different densities of extracellular material [114]. However, the model developed in that reference has no notion of cell shape, hence does not permit definition of cell volume, so pressure and compression cannot be physically correctly related (see section 2.2.2).

In collaboration with the Dr. Pierre Nassoy (U. Bordeaux), we have established a computational model to quantitatively explain the growth kinetics and patterns found for CT26 (mouse colon carcinoma cell line) multi-cellular spheroids constrained by a spherical elastic capsule. A novel experimental technique, called the “cellular capsule technology” [242] allows to measure the average pressure exerted by the cell aggregate onto the calibrated capsule by monitoring the radial expansion

of the shell once confluence is reached. Pressure can be recorded over periods as long as a week and histological data collected and analyzed on fixed and sliced spheroids can provide snapshots of the spatial multicellular pattern.

We refer to this experimental technique as "Experiment I". The thickness, and thus the stiffness of the capsule, was varied to mimic different mechanical resistance conditions.

Delarue et al. (2014) [236] investigated the effect of mechanical stress on MCS growth using the same cell line in a different experimental setting. We exploit these results to challenge our model and determine whether the same computational model designed to match experiment I is capable to quantitatively explain also this experiment (referred to as "experiment II"). In experiment II, mechanical compression was imposed using the osmotic effects induced by a dextran solution. The main difference between those two experiments is that whereas the pressure gradually increases with increasing deformation of the elastic capsule in experiment I, in experiment II a constant stress is applied due to osmotic forces in the absence of any obstructing tissue (see Fig. 5.1A).

We aim to decipher and quantify certain mechanisms of spheroid growth altered by mechanical stress. At this stage, we establish an ABM that can be applied to various systems (cell lines and experimental procedures) and that allows to recapitulate the growth dynamics and the observed cellular patterns. We will show that this can be reached with a minimal number of hypotheses without having to explicitly integrate specific mechano-transduction molecular pathways. Gaining insight in the molecular mechanisms would require additional challenging experiments in which the pathways are selectively inhibited or enhanced in a three-dimensional environment, and would add further parameters to the model. To the best of our knowledge, a specific mechano-transduction molecular pathway has been highlighted once, demonstrating the impact of cell volume change on the expression of the proliferation inhibitor $p27^{Kip1}$ [236].

The agent-based model is a center-based type that circumvents difficulties that earlier CBMs have at large compression, using the hybrid modeling strategy. As such, large cell numbers can be handled, while the (average) mechanics is realistic in spheroids under high compression.

We study this new series of experimental settings in the works [242] and [236] as both utilize a common cell line, and exert stress on growing MCS of that cell line in different experimental settings. The model is then further tested with experiments on other cell lines as provided in the second work.

To unravel the dynamics of MCS subject to external mechanical stress, our modeling strategy is to postulate and implement hypotheses on cell growth, quiescence and death, and iteratively adapt or extend them in case the model simulations are falsified by comparison with the experimental data. Pursuing a similar strategy enabled us to obtain predictions of subsequently validated mechanisms in liver regeneration [243, 8]. Based upon analysis of the relation between pressure, cell density and cell compressibility in the two different experiments, our findings suggest that contact inhibition can be regarded as a robust continuous process imposed by a reduction of cell volume as a consequence of increasing pressure and individual cell compressibility. In addition, the high resolution model shows that potential effects of micro-mechanics at the interface with the capsule may depend on the mechanical properties of the cells.

5.2 Experimental observations

Experiment I: Following microfluidics-assisted encapsulation of CT26 cells into alginate hollow capsules, the growing aggregates of cells were monitored by phase contrast microscopy (see [242] for details). After the tumor cells reached the inner border of the elastic alginate capsule corresponding to a radius of about $100\ \mu\text{m}$ ($t = 0d$ in Fig. 5.1B), they were observed to further induce a dilatation of the capsule, which is an indicator of the exerted pressure. The capsule expansion was measured from the point of confluence over several days, while histological data of the spheroids were collected at the stage of confluence and at $48h$ past confluence. Capsules have been designed to generate shells with two different thicknesses. The thin ones ($H/R_0 \approx 0.08$; $H = 8\ \mu\text{m}$) are the softer while the

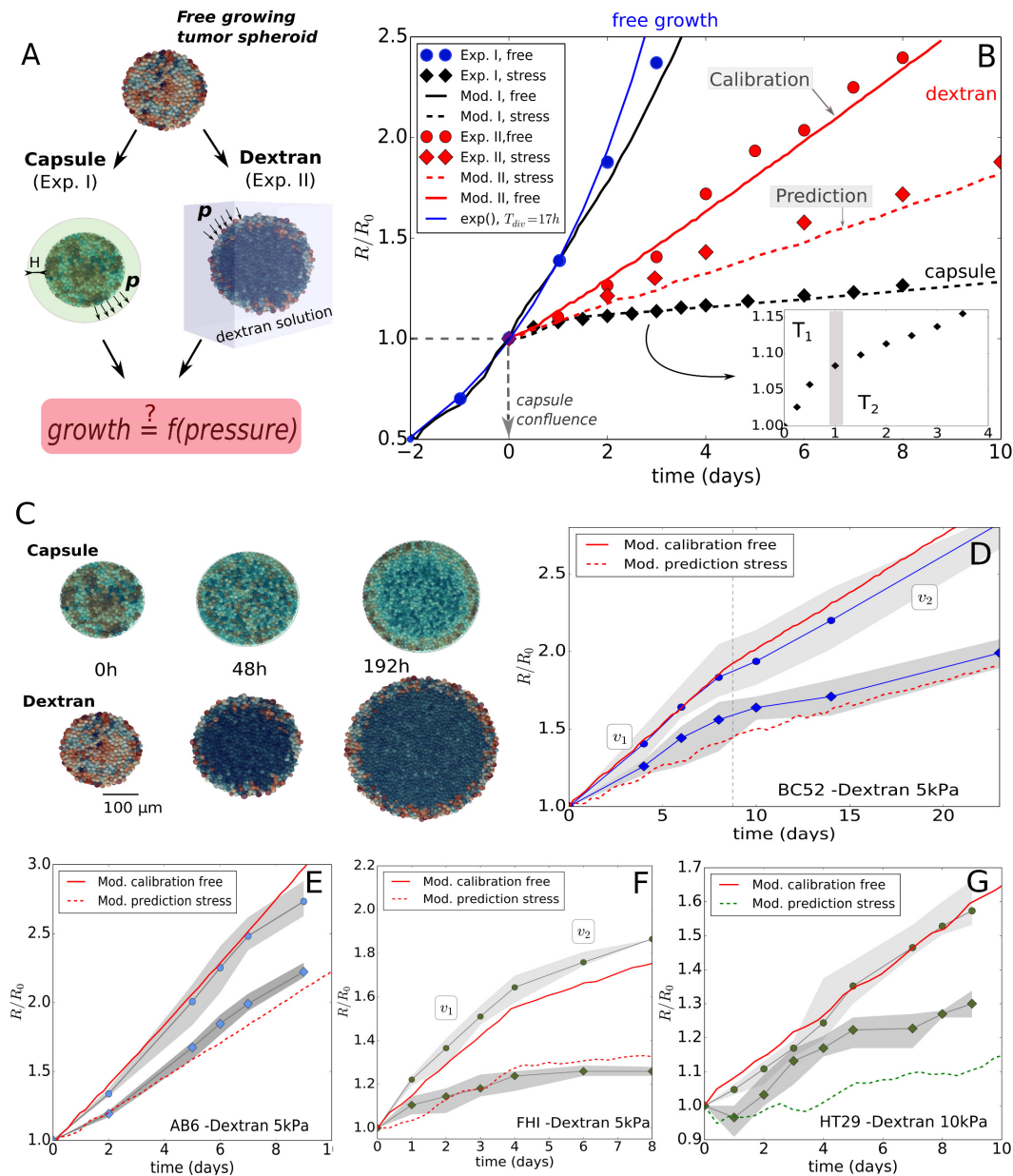


FIGURE 5.1: Summary of key experimental and simulation results. (A) Two experiments setups for growing spheroids considered in this study. In experiment I, the spheroid is in mechanical contact with a capsule, and the mechanical resistance is determined by the wall thickness H . In experiment II, the spheroid is immersed in a dextran polymer solution, and the mechanical resistance originates from the osmotic pressure related to the dextran concentration. (B) Radial growth curves data of the spheroids in units of R_0 ($= 100 \mu m$), for experiment I and II and respective model runs. The blue full circles are the free growth data for CT26, from [242]. The thin blue line indicates theoretical pure exponential growth with doubling time of $17h$. The data starts deviating from an exponential after 2 days. The other lines are simulation results. The black dashed line indicates the optimal parameter set for the stress response in experiment I, performed with final model I. The full black line indicates the same model run for free growth in Exp. I. After re-calibration of one model parameter in model I for the Exp. II conditions in absence of dextran (full red line), the model (referred to as model II to stress the change of the parameter) predicts the stress response in experiment II (red dashed line). (C) Simulation snapshots of both experiments. The cells are colored according to their volume (cells at the border are larger than in the interior). (D-G) Model simulations for Exp. II for the cell lines BC52, AB6, FHI and HT29, respectively. Full red lines represent the same initial calibration procedure, while red dashed lines represent the predicted stress conditions. The stress conditions are $p = 5 \text{ kPa}$ for AB6, FHI and BC52, and $p = 10 \text{ kPa}$ for HT29.

thick ones ($H/R_0 \approx 0.25$; $H = 30\mu\text{m}$) will mimic a larger mechanical resistance against growth. We extract four main observations from these experiments:

(EI.OI) In the absence of a capsule, an initial exponential growth stage was observed with doubling time $T_{cyc} = 17h$ [242]. The growth kinetics however starts to deviate from exponential growth for spheroid size ($R \approx 175\mu\text{m}$, see Fig. 5.1B).

(EI.OII) In the presence of a capsule, the exponential growth is maintained until confluence, i.e. ($R = R_0 \approx 100\mu\text{m}$), which shows that the capsule is permeable to nutrients and allows normal growth. Once confluence is passed, the time evolution of the capsule radius exhibits two regimes: i) an initial “fast” growth stage T_1 ($t < 1\text{day}$), crossing over to ii) a “slow” quasi-linear residual growth stage T_2 ($t > 1\text{day}$) that at least persists as long as the capsules are monitored, i.e. up to one week. The transition happens roughly at a pressure of $\sim 1.5\text{kPa}$, see Fig. 5.5C. The observed long-time growth velocities were $\sim 2\mu\text{m/day}$ for the thin capsules (Fig. 5.5A) and $0.7\mu\text{m/d}$ for the thick capsules (Fig. 5.6).

(EI.OIII) The nuclei density, obtained from cryosections, increases from ~ 1 nucleus / $100\mu\text{m}^2$ before confinement, to roughly 2 nuclei / $100\mu\text{m}^2$ after confluence, with a relatively higher number near the center of the spheroid (1.2 times more compared to the outer regions), and a local increase at the border of the capsule. The distribution and shape of cell nuclei reported in [242] suggests that cells near the capsule border are deformed thus deviating from a spherical shape cells adopt in isolation, while those in the interior look spherically shaped.

(EI.OIV) Most of the cells in the core of the spheroid are necrotic after 48h of confinement, while the cells located in a peripheral viable rim of roughly two cell layers thickness ($\lambda_l \approx 20\mu\text{m}$), show viability and proliferative activity during the whole time course of the experiment, including period T_2 .

Experiment II: in the work of Delarue et al. (2014) [236], CT26 spheroids (initial radius $\sim 100\mu\text{m}$) were grown in a dextran polymer solution. To recover osmotic balance, water expulsion out of the spheroid generates osmotic forces exerted to the outer cells that are transferred as compressive stresses to the interior (bulk) cells. The concentration of dextran regulates the applied pressure.

(EII.OI) The growth rate at $p = 5\text{kPa}$ is significantly lower than in control spheroids where no pressure is exerted.

(EII.OII) The spheroid free growth data does not show an initial exponential phase found in (EI.OI) (Fig. 5.1B). This surprising discrepancy might result from the different culture conditions between both experiments. In experiment I, the medium has repeatedly been refreshed [242], while in experiment II this has not been done so often (private communication), leading to lower concentrations of nutrients and other molecular factors in experiment II. During the whole course of osmotic stress application, an over-expression of the kinase inhibitor $p27^{Kip1}$ together with an increased number of cells arrested in the G1 phase was observed, but no significant change in apoptosis rates after 3 days was reported.

(EII.OIII) Delarue et al. (2014) also considered the stress response for other cell lines (AB6, HT29, BC52, FHI) performing steps EII.OI and EII.OII for each cell line. These data will be used to validate our model despite less information concerning cell size and cycling times is available for these cell lines.

5.3 Models and hypotheses

5.3.1 Hypotheses for growth and death of tumor cells

We propose a number of hypotheses for the growth dynamics common to experiments I and II:

(H.I) In both experiments a linear growth phase was observed after exposing the MCS to external stress. The growth of the cell population that is not constrained by either mechanically-induced growth inhibition, nutrient, oxygen or growth factor limitations is exponential [222]. We assumed

that deviation of growth from an exponential indicates limitation of proliferation to a rim. This may have different reasons, for example necrosis that has been only reported for experiment I (EI.OIV), or of cells being quiescent. Both necrosis and quiescence can result from a lack of nutrients or other factors [38, 40], that may indirectly be promoted by pressure, e.g. in case the compression of the cell layer squeezed between the capsule shell and the inner cell layers leads to the formation of an obstructive barrier for some nutrients (as glucose) to the cells located more deeply in the interior of the tumor. However, cell quiescence or cell death may also be a direct consequence of mechanical pressure, e.g. if cells subject to compression cannot advance in cell cycle for too long and then undergo apoptosis [38, 40]. Yet, simulations of small compressed spheroids performed with the DCM do not indicate large mechanical boundary effects (see 5.4.1).

We do not specify the origin the proliferating rim here, we take it into account through the definition of a thickness λ_k ($k = I, II$ is the experiment index). In Exp. I, λ_I distinguishes the necrotic cells from viable ones, in Exp.II, λ_{II} separates the quiescent cells from the ones that can still proliferate. Necrotic cells as observed in experiment I can undergo lysis, in which they steadily lose a part of their fluid mass. The decrease of mass is limited to about 70% – 90% of the total initial mass of the cell [244, 26].

(H.II) Cell growth rate may be declined or inhibited by pressure [232]. The authors of a recent study [236] hypothesized that the growth rate may be down-regulated if the cell volume is reduced as a consequence of pressure. We here test the hypothesis that growth rate is dependent on the volumetric strain (“true strain”, commonly used in case of large strains),

$$\epsilon_V = -\log(V/V_{ref}), \quad (5.1)$$

where V is the actual compressed volume and V_{ref} is the volume of the cell in free suspension. The volumetric strain can be related with the pressure by integration of the relation $dp = -Kd\epsilon_V$. K is the compression modulus of the cell and depends on the actual volume fraction of water, and the elastic response of the cytoskeleton structure and organelles. It may also be influenced by the permeability of the plasma membrane for water, the presence of caveolae [245], and active cellular responses. As such, the timescale at which K is measured is important.

In our simulations, we regarded K as the long timescale modulus of cell, as growth and divisions are slow processes. We studied constant and a volume-dependent compression moduli (the calculation of growth, volume and pressure for each cell in the model is explained in the Methods section C.1.3, Eq. C.1).

On the molecular level, volume reduction correlates with over expression of $p27^{Kip1}$ which progressively decreases the proliferating potential. Other molecular players such as the transcriptional regulators YAP/TAZ were also reported to be mechano-sensitive [246]. In the scope of the present work, these reports suggest that quiescence, and perhaps also apoptosis, may be controlled by either pressure or cell volume. Experimental studies [106, 107, 108, 109] mainly measured the growth rate of dry mass or size. These indicate that the growth rate α varies within the cell-cycle, yet a unique relationship is difficult to infer.

We propose as general form for growth rate α a Hill-type formula defined as (1 - Hill function):

$$\alpha = \alpha_0 \frac{\epsilon_{V_{ir}}^n}{\epsilon_V^n + \epsilon_{V_{ir}}^n}, \quad (5.2)$$

where α_0 is the growth rate of the unconstrained cell, $\epsilon_{V_{ir}}$ is a threshold value¹, and n is an integer. The parameter $\epsilon_{V_{ir}}$ is the value where the cells have lost 50% of their initial growth rate. Note that for $\epsilon_{V_{ir}} \rightarrow \infty$ we retrieve a constant growth scenario, whereas increasing n from 1 to ∞ modifies the curve from a linear-like decrease to a sharp pressure threshold (see Fig. 5.2A). The use of a Hill

¹We assume $V/V_{ref} \leq 1$ in the experiment meaning the cells are always in a compressive state

function thus makes a variety of growth scenarios possible. Hill formulas have been used in the past to simulate contact inhibition in epithelial tissue and tumors [247, 248, 240].

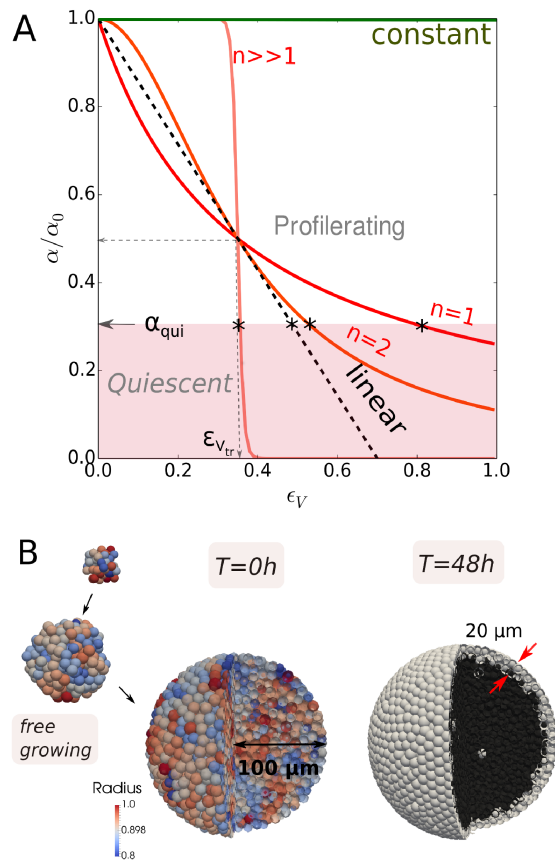


FIGURE 5.2: (A) Plot of Hill-type growth rate function as function of the volumetric strain $\epsilon_V = \epsilon_V(p)$, for $n = 1, 2$ and a large value of n , and for a constant growth scenario ($\epsilon_{V,tr} \rightarrow \infty$). Plot of a linear growth rate function with $\epsilon_{V,tr}$ such that $\alpha/\alpha_0 = 1/2$. Below the pink zone indicated by α_{qui} cells become quiescent and growth stalls. In case of a sharp threshold obtained by the choice of $n \rightarrow \infty$, any cell with $\epsilon_V < \epsilon_{V,tr}$ would proliferate with maximal rate $\alpha = \alpha_0$, while any cell with $\epsilon_V \geq \epsilon_{V,tr}$ would be quiescent. For finite n , there are also proliferating cells for $\alpha < \alpha_0$. The points on the growth rate curves below which the cells go into quiescence are indicated by an (*). In this work we have found that the parameter set $n = 1$, $\epsilon_{V,tr} = 0.35$ and $\alpha_{qui} = 0.3$ results in good fits for all cell lines. (B) simulation snapshots of a CT26 spheroid during the initial free growth, just before confinement (coloring according to cell radius), and at 48h of confinement in capsule (coloring here indicates necrotic cells (dark) and viable cells (white)).

(H.III) It is generally accepted that cells that have passed the G1 checkpoint (also known as restriction point) are committed to divide, else they go into quiescence (G0). In our model we assume this checkpoint is situated after 1/4 of the total cell cycle time [249]. The transition criterion to the quiescence state can be defined as the one at which the growth rate "stalls", i.e. $\alpha/\alpha_0 < \alpha_{qui}$ (see Fig. 5.2A).

"Sizer versus Timer": According to hypothesis H.II growth rate depends on the compression of the cells, hence the volume doubling time can locally vary and is larger than for uncompressed cells. Limiting cases would be that division occurred after volume doubling at a variable time [38] ("sizer"), or after a pre-defined time ("timer") often mentioned in developmental biology [250]. We therefore also compared the effect of constant time vs. doubling of volume criterion in cell division on the cell population behavior. Also mentioned in H.II, the unconstrained growth rate α_0 itself may vary during

the cell cycle. To study the potential effect of these variations we have performed comparative runs considering constant growth rate as well as exponential growth rate during the cell cycle.

5.3.2 Establishment of the Agent-Based Model and its parameterization

For the model development and parameterization we here summarize the multi-step strategy (see Fig. 5.3). The simulations are performed with a center-based model (CBM). As the model is parameterized by measurable physical and bio-kinetic parameters, parameter ranges could readily be determined within narrow limits (see Appendix Table C.2). The cell-cell interaction force in the CBM in this work is calibrated using computer simulations with a deformable cell model (DCM), resulting in an effective stiffness \tilde{E}_i in the CBM at high compression (see Eq. 2.5), that increases with increasing compression, see Appendix section C.1.5. \tilde{E}_i belongs to $\{\mathcal{P}_{C=CT26}\}$ of the CBM. The DCM could not be directly used for the growth simulations, as it is computationally too expensive to run simulations up to the experimentally observed cell population sizes of $\sim 10^4$ cells. The calibration procedure is a more sophisticated variant of the one discussion in chapter 4 (section); whereas here we take the volume change of the cells into account, this is not the case in the previous calibration.

Following, the model parameters for the "model I" to mimic experiment I, $\{\mathcal{P}_{M1}\}$, and "model II" to mimic experiment II, $\{\mathcal{P}_{M2}\}$, are step-wise calibrated from experiments I and II, and in each case first for growth in absence of external mechanical stress on the growing population. They can be categorized by separating between cell line-specific parameters $\{\mathcal{P}_{C=j}\}$, where $j \in \{CT26, AB6, HT29, BC52, FHI\}$, determines the cell line, and experiment-specific parameters $\{\mathcal{P}_{Exp=k}\}$ with $k = I, II$ characterizing the experimental setting (see Appendix C.2 for the detailed procedure).

Almost the entire parameter determination is done by adjusting the model parameters to experiment I for a thin capsule. After this step there is only one fit parameter for each cell line, summarizing the cell-line specific effect of growth conditions of experiment II for the stress-free growth (i.e., the control experiment). The step to simulate population growth subject to external stress, both in the thick capsule for CT26 as well as in experiment II with dextran for the cell lines CT26, AB6, HT29, BC52 and FHI is performed without parameter fitting.

5.4 Results

5.4.1 Simulation of cell deformation and pressure distribution during in a small compressed spheroid with DCM

The DCM simulations of a small spheroid compression experiment show that the cells have a flattened shape at the border of the capsule, see Fig. 5.4. As a consequence of compression forces acting on the cells at the border normal to the capsule border, those cells are observed to extend in the DCM simulation tangentially to the capsule (and shrink along the direction to the capsule border normal vector) elevating the force exerted on their neighbor cells in the same layer. In the CBM simulation, cell shape is not explicitly given hence this effect is missed out²

We further considered whether the apparent boundary effect (EI.OIII) could be attributed purely to mechanical effects. For this, we used a spheroid compression experiment with a scaled capsule system using 400 (quiescent) DCM cells with different cortex properties (i.e. cells that have the reference E_{cor} and cells with 10 times this value). It is shown in Fig. 5.4 that there can be a small mechanical effect in the case for a "high" stiffness of the cortex, as the simulations show that the cells near the boundary acquire higher pressures as compared to the bulk cells and a weak gradient from the

²In the CBM the lack of cell deformation is reflected in the principal stresses (indicated in Fig. C.1A by arrows) that can be computed from the stress tensor Eq. C.4. One observes that the direction of maximal compressive stress points radially to the border cells, while minimal stress direction points tangential to the capsule wall. CBM cells cannot deform to relax the radial stress component hence need to re-arrange in position. In order to balance normal stress from the capsule cells close to the capsule need to rearrange as they cannot deform, while in the DCM they can both deform and re-arrange.

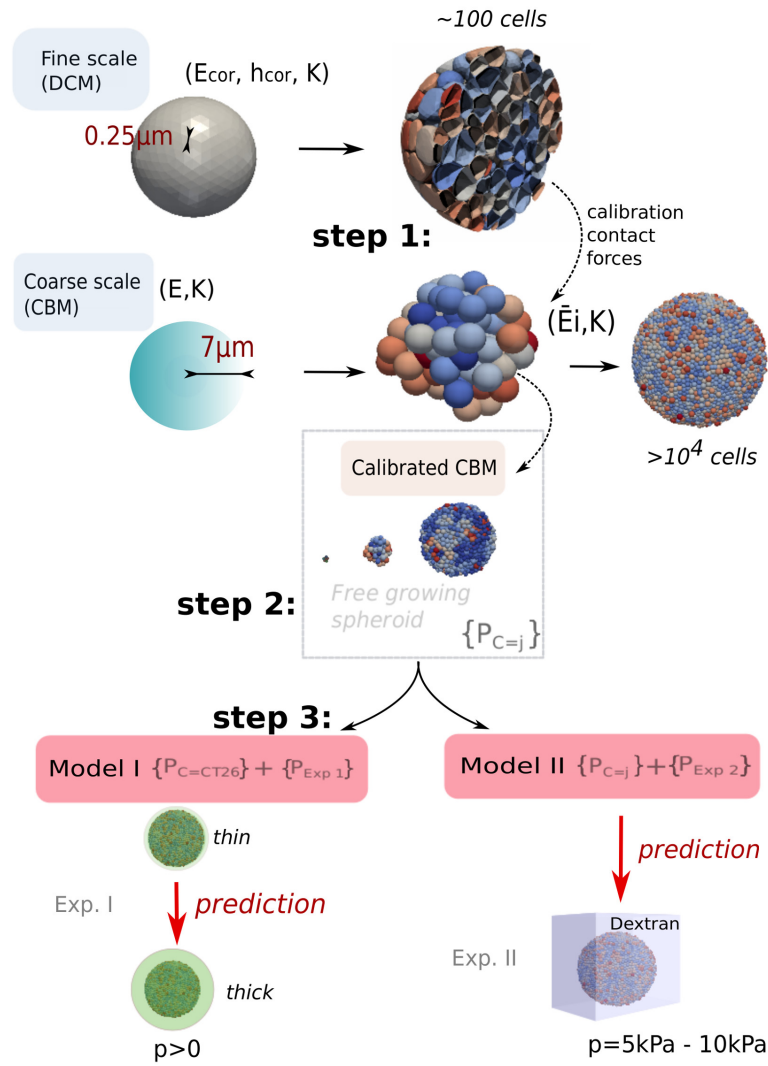


FIGURE 5.3: Model calibration overview. Simulations were performed with a center-based model (CBM). In **step 1**, the contact forces in CBM were calibrated from DCM simulations with parameters (E_{cor}, h_{cor}, K) , yielding a variable effective contact stiffness \tilde{E} of the CBM depending on the compression level. In **step 2** the parameters $\{P_{C=CT26}\}$ of the CBM for cell line CT26 were determined. Comparing simulations of the CBM with stress-free growth of multicellular CT26 spheroids in experiment I determines most parameters of $\{P_{C=CT26}\}$ (Fig. 5.1B, full black line). **step 3**: those cell-line parameters that are affected by the capsule, are specified by comparison with the data from experiment I in presence of the thin capsule. The set of experiment-specific parameters $\{P_{Exp=1}\}$ (Young modulus, Poisson ratio and thickness of the capsule etc.) are given by the experimental setting. For the so specified complete set of parameters the simulation reproduces the experimental data I for the thin capsule (Fig. 5.1B, dashed black line), and, after replacement of the capsule thickness, predicts the experimental data for the thick capsule (Fig. 5.6B). For CT26 cells growing in experiment setting II the cell parameters remain unchanged $\{P_{C=CT26}\}$. The deviation of the growth dynamics of stress-free growth from an exponential in experiment II is taken into account by an experiment-specific parameter, namely the proliferative rim (Fig. 5.1B, full red line). Without any further fit parameter, the model then predicts the correct growth dynamics subject to dextran-mediated stress (Fig. 5.1B, dashed red line). In order to predict the stress-affected growth kinetics of AB6, HT29, BC52 cells, their cell cycle duration is modified to capture the stress-free growth analogously to that of CT26 cells in experimental setting II (Fig. 5.1D-G, full red lines). After determining the parameters, the growth kinetics of these cell lines subject to stress could be predicted (Fig. 5.1D-G, dashed red lines).

center to the spheroid edge can be observed. This can be attributed to *arching* effects (a phenomenon frequently observed in granular mechanics), where outer layers of cells bear more stress and form a shield for the inner layers. The effect increases with increasing cortex stiffness. Contrary, reference parametrized cells spread out more easily, diminishing the pressure differences.

To investigate the boundary mechanics in a more realistic system with dividing cells, the DCM could be extended with the capability to mimic mitosis. In our *simple* compression experiment with cells having estimated cortex properties, the boundary effect appears acceptable.

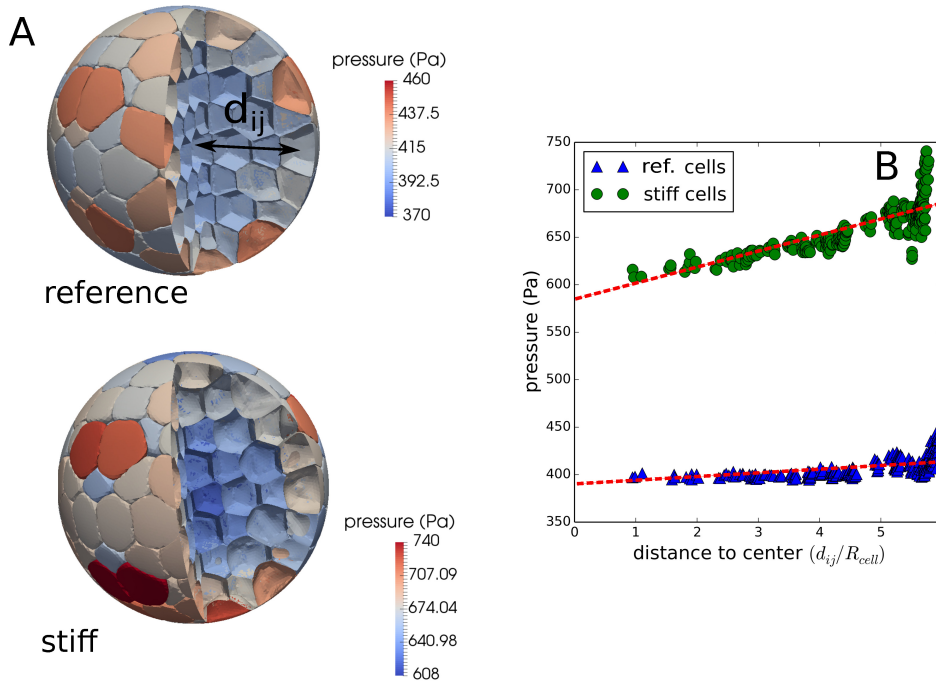


FIGURE 5.4: (A) Simulation snapshots of DCM cells within a scaled capsule model, for the cases of cells with a reference cortex stiffness (top) and a “stiff” cortex stiffness (bottom). The coloring is according to pressure (B) Internal cell pressure for deformable cells in a shrunk capsule for nominal cells and stiff cells, as function of distance to the capsule center. The stiff cell types show a gradient in cell pressure if moving from the spheroid center towards the edge (indicated by dashed red line), while a higher variability as compared to the softer types. Notice that like in the calibration simulations we use cells of equal volume prior to compression but the method can equally be applied to any prior volume distribution.

5.4.2 Model for experiment I with thin capsule

First, we simulate CT26 cells growing freely in the liquid suspension ((EI.OI), Fig. 5.3) for the parameters, see Table C.2). In this situation, CT26 cells grew approximately exponentially indicating absence of growth inhibition.

For a constant cell cycle duration of $T_{cyc} = 17h$ (no inhibition), in the observation period $-2 d \leq t \leq 1 d$, we find a good mutual agreement between the model, the experimental growth curve, and an exponential, see Fig. 5.1B. This determines the intrinsic cell cycle duration T_{cyc} of a growing cell population subject to neither external mechanical stress nor nutrient limitation.

For the simulation we need to specify a subset of parameter set $\{\mathcal{P}_{C=CT26}\}$, namely the division time T_{cyc} , cell radius R , cell Young modulus E and cell compressibility K , characteristic lysis time T_{lys} , the diffusion constant D of the cell as it specifies the micro-motility, the perpendicular and tangential cell-cell friction coefficients $\gamma_{cc,\parallel}$ and $\gamma_{cc,\perp}$, the cell-ECM (extra-cellular matrix) friction coefficient γ_{ECM} , the cell relaxation time T_{rel} , and the growth rate of the cell not subject to mechanical

stress α_0 . For each of these parameters, either estimates from experiment I or literature estimates exist (see Appendix C.2, Table C.2).

In the next step, we use the same model to mimic a growing multicellular spheroid in a thin capsule ($H = 8\mu\text{m}$). In the experiment after confluence, the growth curve crosses over into an approximately linear slope ($t \geq 1d$ in Fig. 5.1B) at a measured pressure of $p_{th} \approx 1.5\text{kPa}$ (EI.OII) with a viable rim of size $\lambda_I \approx 20\mu\text{m}$ (see EI.OIV and H1) enclosing a necrotic zone. Necrosis indicates a lack of nutrients. It is possible that at that pressure, border cells may be so compressed that nutrient diffusion becomes inhibited.

As the experimental data needed to explicitly model the influence of nutrients is not available and would require knowledge on many parameters (see [40]), we do not model nutrient-dependency explicitly but directly implement the experimental observation that the cells further inside the capsule than at distance λ_I die at pressure $p = p_{th}$ (observation EI.OII and Fig. 5.5C).

In our first attempts all cells in the viable rim are assumed to proliferate with a constant rate α_0 . This assumption leads to a too high spheroid growth speed, hence could not explain the growth kinetics in presence of the capsule (see C.2), expressing that λ_I does not determine the growth speed, but only the size of the viable rim.

The constant growth speed for $t > 2d$, despite increasing pressure experienced with increasing size of the MCS, indicates the proliferating rim to be of constant size. This was confirmed by visual observation of the spheroids (personal communication). This argues against an increasing limitation of nutrients with tumor size in the linear growth regime, and in favor of a direct impact of pressure on cell cycle progression.

In our model this is taken into account by replacing the constant growth rate α_0 by a compression-dependent growth rate $\alpha(\epsilon_V)$ Eq. 5.2 expressing, that cells can enter G0 if the relative growth rate α/α_0 falls below a threshold α_{qui} between division and restriction point, see H.III and Fig. 5.2). In our model, cells divide after their volumes have doubled. Consequently, a cell subject to compressive stress has a longer cell cycle duration than an isolated cell.

With this model we find a very good agreement between experimental data and simulation results for $\epsilon_{V_{ir}} \approx 0.35$, $n \in [1, 2]$ and $\alpha_{qui} \leq 0.33$ (Fig. 5.5A, Fig. 5.5B). Values of $n \in [1, 2]$ do hardly discriminate. Choosing $n \geq 4$ results in a faster growth in the beginning as here $\epsilon < \epsilon_{V_{ir}}$, and an experimentally not observed flattening of the residual growth resulting from the sharp decrease of α for $\epsilon_V > \epsilon_{V_{cr}}$. $n \rightarrow \infty$ leads to a plateau. Increasing α_{qui} to 0.5 results in a significant growth stall as cells then already enter quiescence at higher growth rates (Fig. 5.5A). Increasing $\epsilon_{V_{ir}}$ results in a faster capsule dilatation over the whole period as then the growth rate decreases only above a larger pressure (noticing that $d\epsilon_V/dp > 0$). We selected $\epsilon_{V_{ir}} \approx 0.35$ as best fit. The effect of $\epsilon_{V_{ir}}$ is shown in the thick capsule experiment (section 5.4.2, Fig. 5.6A). The Hill function parameters complete parameter set $\{P_{C=CT26}\}$ (Table C.2).

Concluding, using Model I a good agreement with data could be obtained whereby the main underlying assumption is that the cell growth rate and thereby the duration of the cell cycle is controlled by the cells' degree of volumetric compression.

Validation of model for experiment I with thick capsule data

In the first validation step, we consider the thick capsule experiment ($H = 30\mu\text{m}$). A thicker capsule provides a stronger resistance against the spheroid expansion. In simulations with model I and the parameter set ($n \in [1, 2]$, $\epsilon_{V_{ir}} = 0.35$, $\alpha_{qui} = 0.3$) that is able to explain the MCS growth against a thin capsule, we obtain a good agreement also for the thick capsule data without any additional fit parameter (see Fig. 5.6A).

For higher or lower values for the volumetric strain threshold $\epsilon_{V_{ir}}$, respectively, an overestimation or underestimation for the residual growth would be observed consistently with the thin-capsule data. Values $n \geq 2$ result in a clear deviation the end of the observation period and were hence rejected.

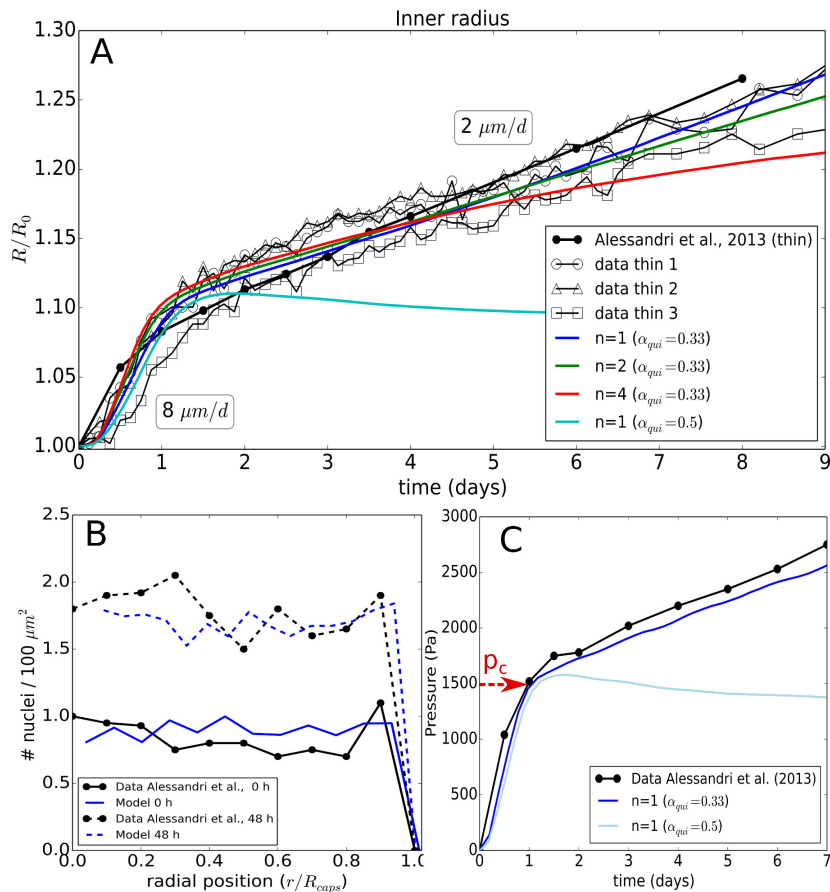


FIGURE 5.5: (A) Time evolution of the radius of the thin capsule for the experimental data and the simulations using Model I showing the effect of a parameter variation for n with $\alpha_{qui} = 0.33$, and $n = 1$ with $\alpha_{qui} = 0.5$. (B) Simulation and experimental values of the radial cell density in the spheroid at $T = 0h$, and $T = 48h$ for the optimal parameters. (C) Pressure curves indicating the pressure at the transition point from free spheroid growth to spheroid growth against the thin capsule in ref. [242] and the simulation.

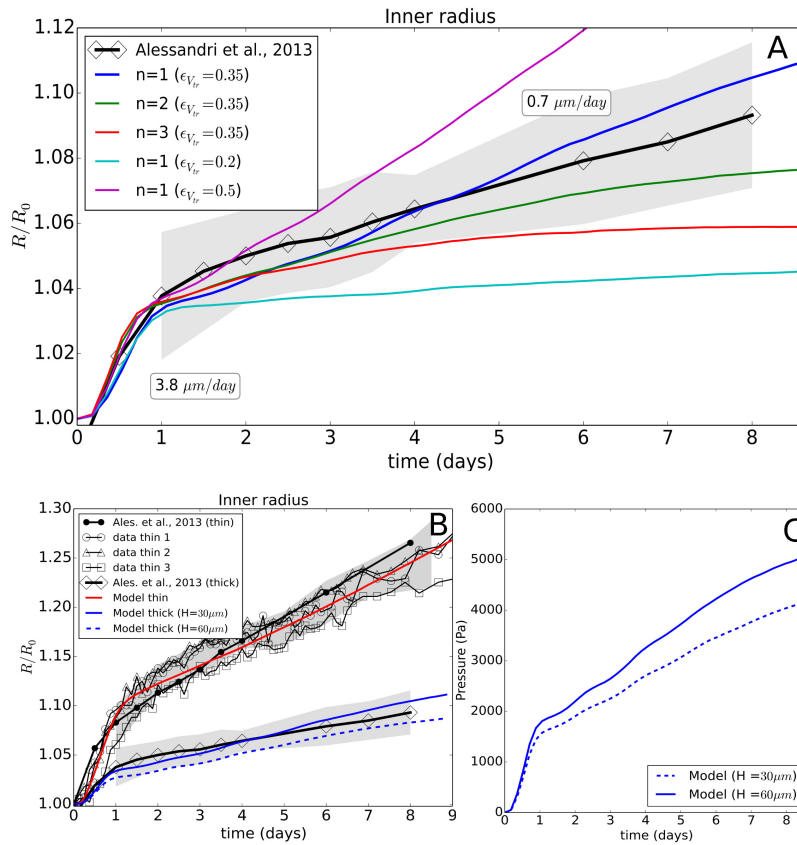


FIGURE 5.6: (top) (A) Time evolution of the thick capsule radius ($H = 30 \mu\text{m}$), shown for the experimental data and the simulation with Model I, indicating the effect of the parameter n and $\epsilon_{V_{ir}}$. As the number of data sets on the thick capsule did not suffice to estimate the experimental error, the errors on the thick capsule data (gray zone) were estimated from the spreading on the thin capsule data, by determining the minimum - maximum intervals for the thin capsule data. These were then rescaled by the ratio of thin - thick capsule dilatations and shifted on to the thick capsule curve. (B) Global view of experiment I and II and respective model runs, including a model prediction for a capsule wall thickness $H = 60 \mu\text{m}$. (C) Simulated evolution of the average pressure in a capsule with $H = 30 \mu\text{m}$ and $H = 60 \mu\text{m}$.

Validation of model for experiment II

We have challenged the model calibrated for experiment I by studying whether it would be able to predict the observed growth of CT26 multicellular spheroids subject to osmotic stress (Experiment II, [236]). The concentration of dextran regulates the applied pressure. The growth rate at $p = 5$ kPa here is also significantly lower than those in control spheroids (freely growing in iso-osmotic conditions). Surprisingly however, the control spheroids in experiment II grow slower than in Experiment I, revealing an overall linear but not exponential growth kinetics. Since the cell line is identical, we associate this difference to varying culturing conditions (e.g. less frequent change of medium).

Growth without external stress: To take the different culture conditions into account within our simulations, we first simulate again the free growing spheroid. Linear growth is characteristic for a proliferative rim of constant size, with the size and spatial distribution of proliferating cells in the rim determining the speed of spheroid expansion [111, 40]. Following the same reasoning as for experiment I, we impose a proliferating rim of size λ_{II} measured from the edge of the spheroids inwards to capture the linear growth. Here, the edge of the spheroid is computed as the average of the radial positions of the most outer cells plus one mean cell radius (see Fig. 5.7A). We find that for $\lambda_{II} = 30 \mu\text{m}$ with cells adopting the same parameter set as in Experiment I, Model I ($n = 1, \epsilon_{V_r} = 0.35, \alpha_{qui} = 0.3$), matches well with the data for freely growing spheroids. As in experiment II no increase in cell death, neither by apoptosis nor by necrosis has been reported, cells outside of the proliferating rim are assumed to rapidly enter a quiescent state without undergoing necrosis i.e., they do not shrink. This is referred to as Model II. Notice that λ is the only parameter value by which Model II differs from Model I, reflecting the response on the growth conditions (therefore attributed to the parameter set \mathcal{P}_{EXPII}).

Growth in presence of external stress: The same parameter values are kept for the growth simulations in the presence of dextran. In another work by Delarue et al. (2014) [251], slight cell elongations were reported towards the tumor center. We neglect here this effect to test whether the experimentally observed response of a growing tumor subject to osmotic stress can already be captured with the model originally developed for the capsule, with the only difference being an adaptation for the free growth conditions.

In accordance with the known pressure-exerting effect of dextran, we apply an external force only to a small boundary of outer cells, directed towards the center of the spheroid, mimicking the osmotic effects which induce depletion-induced adhesion and an increase of the contact area between the cells [96]. The magnitude of the applied force on every outer cell reads:

$$F_{ext} = F_0 \frac{V}{V_{ref}}. \quad (5.3)$$

The magnitude F_0 (fixed parameter) is chosen such that the experimentally observed average cell pressure $\langle p \rangle$ is in the simulation maintained in the bulk of the spheroid during growth. The volume-scaling factor is needed to minimize pressure variations as much as possible. As there is no confining volume of the MCS, we use a *local* calibration approach to compute the contact forces in the agent-based model, see section C.1.5.

Remarkably, the slope of the growth curve obtained from a simulation with the model without any further adjustment matches very well with the data (Fig. 5.1B). This indicates that the response of the CT26 cells on compressive stress is robust and reproducible even if the cells are subject to different environmental conditions. Moreover, the surprisingly good agreement between model prediction and experimental observation suggests that the slight cell elongations observed in [251] might not be a fundamental determinant in the overall response of a growing tumor to external mechanical stress by osmosis. The major contribution to the stress response may be controlled by the proliferating cells that are mainly located close to the border. As proliferating cells, which are on average larger than resting cells, are mainly localized at the border, the nuclei-nuclei distance is larger close to the border

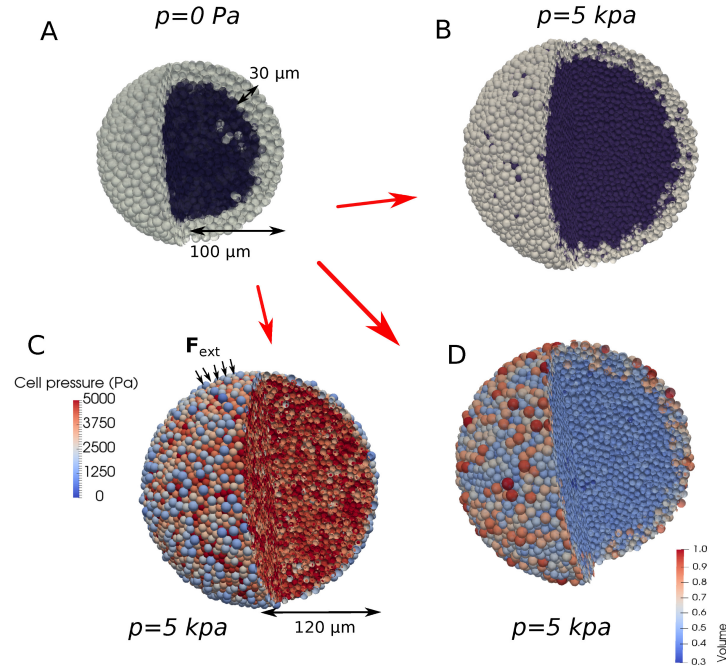


FIGURE 5.7: (A) Simulation snapshot at the beginning of a free growing CT26 spheroid ($R = 100 \mu\text{m}$), indicating quiescent (dark) and proliferating cells (light). (B-D) Simulation snapshots of growing CT26 spheroids at $R = 120 \mu\text{m}$ during dextran application ($p = 5 \text{ kPa}$), indicating quiescent and proliferating cells (B), individual cell pressure (C), and volume for the cells (D).

of the spheroid than inside (see Fig. 5.7D), consistent with reported experimental observations in [236] and in freely growing spheroids [111].

Within our model we find that i) the pressure distribution in the bulk cells is quite homogeneous, and ii) the pressure is locally lower for the most outer cells because some of these cells are experiencing less contact forces from their neighbors (see Fig. 5.7C).

In simulation runs testing parameter sensitivity of the growth kinetics in Experiment II we found for growth parameters $\alpha_{\text{qui}} > 0.33$, $\epsilon_{v_r} < 0.2$ or $n > 2$ a significant underestimation of grow (too many cells go into quiescence), in agreement with our simulations for Experiment I.

In order further challenge our model, we have also simulated the dextran experiments performed with other cell lines, i.e. AB6 (mouse sarcoma), BC52 (human breast cancer), FHI (Mouse Schwann) all at $p = 5 \text{ kPa}$, and the cell line HT29 (human colon carcinoma) at $p = 10 \text{ kPa}$. Since these experiments were less documented, our assumptions are that i) in the simulations the experimental conditions are a priori the same, but ii) cell cycling times are different. These doubling times are estimated by calibration of the growth curves without external stress before predicting the growth curves in presence of external stress without any additional fit parameter following the same strategy as for experiment II above for the CT26 cell line. Doing so, we find that the long-term growth speed was again surprisingly well predicted by the model for all three cell lines. Only transients partially deviate from experimental curves (Fig. 5.1D-G).

We here adjust the cell cycle duration T_{cyc} to capture the growth kinetics of the MCS in absence of externally exerted mechanical stress but we could also have modified, for example, the thickness of the proliferating rim λ_{II} , as the expansion speed v_f of the freely growing MCS is $v_f \propto \lambda_{II}/T_{\text{cyc}}$ [7], so that changing λ_{II} has the same effect as the opposite change in T_{cyc} . We emphasize in this context that λ_{II} does not determine the growth speed v_S under dextran-induced stress, as $v_S \ll v_f$. Thus, our prediction is not dictated by parameter λ_{II} .

For AB6 (Fig. 5.1E), we found a doubling time of $13h$ to make the simulated free growth case

matching well with the experiment (comparing slopes over period of $\sim 9d$; full red line in Fig. 5.1E). We however, did not have any additional information concerning cell size and doubling time on this cell line. Applying the pressure of $5kPa$ in the simulations, one still sees that the simulation agree quite well with the experiment (Fig. 5.1E, dashed red line).

For HT29 (Fig. 5.1G), a pressure of $10kPa$ was applied in the experiment, and hence this puts an extra challenge as the growth model is tested for larger compression. In the simulations, we now have to double the applied forces in the most outer cells to reach the same average pressure. The calibrated doubling time of HT29 for growth in absence of dextran was found to be $46h$, in agreement with values in reported in [252] (full red line in Fig. 5.1G). The cell size is comparable to that of CT26 [236]. The simulation results in presence of dextran indicates a significant differences in the beginning of the experiment, yet overall the growth slope matches quite well with the data (Fig. 5.1G, red dashed line).

Finally, for BC52 (Fig. 5.1D) and FHI (Fig. 5.1F), the experimental results show a more complex behavior, as there seem to be two regimes in the growth. In the case of BC52 the spheroid first grows with $v_1 \sim 0.41\mu m/h$ for the first $9d$, then in the subsequent period the growth slows down to $v_2 \sim 0.29\mu m/h$ (see Fig. 5.1D). We attribute this to a change in growth conditions in the experiment. The model a-priori does take the cross-over effect into account, but we still can test it by imposing ad-hoc changes of experimental conditions after a period of $9d$. To do so, we assume in the simulations for the dextran-free growth that the thickness proliferating rim has decreased during the cross-over by $\lambda_{II} \rightarrow \lambda_{II} \times v_2/v_1 \approx 0.7\lambda_{II}$, which resulted in an overall good calibration curve. The same procedure was applied to the FHI cells, with here the factor $v_2/v_1 \approx 0.35$ for the simulation in absence of dextran. The corresponding simulations in presence of dextran for BC52 (Fig. 5.1D, dashed red line) and FHI (Fig. 5.1F, dashed red line) then shows that the model is again able to predict the experimentally observed slopes in both regimes reasonably well.

We conclude that this model is able to predict the effect of mechanical stress on the expansion speed of the MCS in the elastic capsule experiment (experiment I) and the dextran experiment (experiment II) after calibration of the model parameters with experimental growth data in absence of capsule and dextran i.e., with experimental growth kinetic data in absence of externally exerted mechanical stress.

Robustness of the proposed cell cycle progression function

In our model we have proposed that the cell growth rate decreases according to a general Hill function (Eq. 5.2). From the capsule simulations, we observed that neither a constant growth scenario ($\epsilon_{V_r} \rightarrow \infty$) nor a sharp threshold ($n \rightarrow \infty$) could explain the data. However, in order to justify the choice of the Hill functional shape as compared to a simpler functions, we have performed comparative simulations with a linear progression function. This function has the same boundary value $\alpha = \alpha_0$ at $\epsilon_V = 0$, and $\alpha = 0.5 \times \alpha_0$ at $\epsilon_V = 0.35$, but has a steeper decrease further on (dashed line in Fig. 5.2). We found that with this function the experimental data for small and large capsule thickness could still be reproduced with a fair agreement (see Fig. C.4G, "Linear I" in the Appendix). However using the same function, we could subsequently not match the data of Experiment II, for the CT26 cell lines as well as for the other cell lines. In that case the simulations systematically underestimated the growth indicating the tail of the Hill function is important as it controls the still non-negligible contribution to growth at high strains occurring in the dextran experiment. On the other hand, a linear function (boundary value $\alpha = \alpha_0$ at $\epsilon_V = 0$) calibrated such that the CT26 dextran experiment could be reproduced, resulted in an overestimation of growth in the capsule experiment (see Fig. C.4G, "Linear II" in the Appendix). Concluding, a sufficiently long "tail" in the diagram α versus ϵ_V seems to be necessary to explain the residual growth of the cells. This points towards a nonlinear response of inhibition of growth of the cells upon compression, and further shows that the choice of a nonlinear progression function is necessary so that a Hill growth function, despite it looks complex, seems the

most simple one that is able to explain simultaneously growth of MCS subject to externally applied stress in both experiment types.

5.5 Conclusion and discussion

By establishing a quantitative model of growing multicellular spheroids (MCS) subject to compressive stress calibrated with data on growth in an elastic capsule we are able to demonstrate that the stress response of a growing tumor is quantitatively robust and reproducible even if cells grow under different conditions and if the pressure is exerted by different experimental methods. Given the enormous complexity of intracellular processes involved in the control of MCS growth this is fascinating as it might open the possibility that largely separated robust functional modules may be identified and studied in separation without the need to analyze all interactions of the components of one module with the components of other modules, and without incorporating all interactions at the molecular level. In particular, we have first developed a model to study CT26 cells grown in an elastic thin and thick capsule, and then modified this model in a minimal way by taking into account the remarkably different growth behavior of freely growing tumor spheroids (i.e. not subject to compressive stress) to simulate the tumor growth response of CT26 and other cell lines in a dextran solution. We have shown that the mechanical stress response is quantitatively the same despite significantly different culture and protocol conditions. Without the model, it would have been very difficult to identify this equivalence. The key results of our analysis are:

(R.I) With increasing compression the cell growth rate decreases. This relation could be well captured by a Hill function for the growth rate α that depends on the volumetric strain (Eq. 5.2), and a transition into quiescence if the growth rate dropped below a threshold value. A sharp volume or pressure threshold below which no cell cycle entrance would occur anymore, is not compatible with the data. Together with the strain hardening assumption of cells during compression, this overall points to a nonlinear increasing growth resistance of the cells upon mechanical stress.

(R.II) Cells divide when their dry mass has doubled during the cycle. A "timer" as a decision mechanism for dividing could not explain the data.

A particular point of concern in many studies of spheroids is the appearance of cell death. Our work is based on the observations of Alessandri et al. (2013), who observed necrosis (CT26 cells, using FM4-64) in capsule confined cells, while their free growing spheroids exhibited the normal exponential growth for $R < 150\mu\text{m}$. Helmlinger et al. (1996) [232] observed a decrease in apoptotic (LS174T cells, using TUNEL) events during compression, and reported little necrosis (not quantified) for spheroids with $R < 150\mu\text{m}$. They concluded that the halted growth of the spheroids is mainly due to the increasing compressed state, which can be partially confirmed by our simulations. In the work of Delarue et al. (2014) [236], no increase of apoptosis (HT29 cells, using cleaved-caspase 3) was observed after 3 days for spheroids with $R \sim 100\mu\text{m}$. Contrary, earlier Montel et al. (2012) [235] did report increased apoptosis using cleaved-caspase 3 for CT26 cells, while Cheng et al. (2009) [233] did observe an increase of necrosis (67NR cells, using propidium iodide) even in very small spheroids $R \sim 50\mu\text{m}$, yet mainly for the interior cells. At the periphery, cells were still dividing. Whether necrosis and apoptosis occurs may well be dependent on the cell type and experiment, but overall it seems that the peripheral cells are unaffected.

Another issue that deserves attention is that despite recent significant advances in exploring the relations between the cell mechanical parameters and cell responses during an externally applied mechanical stress, a coherent consensus has not been reached. One issue in this discussion is the cell compression (bulk) modulus. For instance, in Delarue et al. (2014) [236], one concludes that cells are compressible reporting a rapid cell volume reduction at the level of the MCS (Multicellular

Spheroids) under compressive stress. Another work of Delarue et al. (2014) [251] indicates bulk moduli of the order of 10 kPa . Both works consider the long-term effects ($> 1h$) of compression on spheroids.

The work of Lin et al. (2008) [253] seems to concur with this as they measure cell bulk moduli of about 10 kPa with measurements on a timescale of minutes.

On the other hand, the Monnier et al. (2016) [254] report individual cell compression moduli of several orders of magnitude higher (1 MPa) than the ones reported above, also on short time periods of minutes. Yet they state in their paper that on longer timescales, the cell response may become more complex due to intracellular adaptations. We emphasize that in our paper we are considering timescales of larger than one hour as cells are doubling their volume in about a day so that the rate of percentage of the volume increase is about $0.07\%/min$. As such, the compression moduli of the cells that we find should be regarded as long-term values, where the cell can respond differently as compared to short timescales. For instance, the cell may respond by expelling fluid through aquaporins. In the work Tinevez et al. (2009) [255], the cytoplasm bulk modulus is estimated as $\pm 2500\text{ Pa}$. Despite not being the modulus of the whole cell, it indicates that if cells are able to expel water through the aquaporins on longer timescales, their resulting bulk moduli agree with our values.

Our modeling strategy is based on *in silico* experiments i.e., abstracted experiments on the computer, where each individual cell was represented as modeling unit with those properties, actions and interactions that were considered as necessary to quantitatively explain the cellular growth response on mechanical compression. The implementation of cell-cell and cell-environment interaction directly accounts for physical laws with (in principle) measurable physical parameters that permit straightforward limitation of parameter ranges to those physiologically relevant. This made it possible for us to largely confine the parameter values to published or directly observed relatively narrow ranges, and introduce free fit parameters only for the cell cycle progression. A particular challenge was to construct an individual agent-based model that permits stable and robust simulations up to several tens of thousands cells under high compression. Under these conditions cell displacements may have to be minimal, which rules out models operating on lattices unless the lattice size would be chosen a very small fraction of the cell diameter (in which case they would lose their computational advantage). Thus, the requirements of constraining the parameters, and providing realistic simulation trajectories in time favored models operating in lattice-free space implementing a dynamics simulated by equations of motion (as opposed to a Monte Carlo dynamics, which under some condition mimics a master equation). The prototype of lattice free models are center-based models that calculate the forces between cells as forces between cell centers. However, as mentioned above and explained in more detail elsewhere [Van Liedekerke et al., 2015] this model type has significant problems in dealing with cell populations under large compressive stress i.e., with exactly the situation we are faced with in this work. To solve this issue, we have developed a deformable cell model (chapter 4), which represents each individual cell in much greater detail as in center-based models but at the expense of much longer simulation times. As simulations with that model up to several thousands of cells were not feasible, we performed simulations with this model of characteristic MCS configurations under large compressive stress and used the results to establish a new interaction force model within center-based models that permit to mimic large cell populations under large compression.

Furthermore, we mention that despite their limit on cell numbers, simulations with DCM can give valuable information on micro mechanics. In our study, we found that stiffer cells in a scaled capsule model more likely could cause a gradient in cell pressure from the border to the center of the spheroid than soft cells. These potential effects are difficult to investigate with center-based models and prove the necessity of further development of high resolution models, and perhaps running them on high performance computers.

As a final remark, we must emphasize that in our model the interactions of the cells with ECM are not explicitly taken into account. A number of possibilities to overcome this issue are explained in Appendix C.4.

Chapter 6

Modeling of cell motion in fluid and matrix environment

6.1 Introduction

Cells motion comes in a variety of modes. While bacteria simply swim by beating their flagella, mammalian cells' motion is controlled a complex sequence of actin polymerization, actomyosin contractility and cell-matrix adhesion. In the previous chapters, our models have merely simplified cell movement as the result of a net force \mathbf{F}_{mig} acting on them, ignoring a detailed force balance between the cell and its surrounding medium. To understand cell motion from a more fundamental point of view, we need to take the interactions with the medium explicitly into account and hence we also need a model to represent the medium. In the agent-based modeling community, these kind of models are now emerging (e.g. [86, 256, 257, 128, 147]).

In our work (see chapter 2), I presented two possibilities to model a medium in a particle based framework. The first approach is to represent the medium purely as a continuum represented by SPH particles. This is particularly suited if the medium is a fluid or a homogeneous solid (e.g hydrogel). The advantage here is that the equations of motion of the ECM are described by continuum equations which permits accurate results if the constitutive equations of the material are fully known. The second option is to represent it as a network of springs that effectively mimic the fiber-like in the material. This option looks more suited if one wants to model the mechanics of a fibrous material with a significant pore size compared to the cell size. However, the scale at which the fibers are represented is not arbitrary. One can chose here for a coarse-grained model, where the spring network represents the average effect of (aligned) bundles of individual microscopic fibers. The disadvantage here is loss of accuracy. Another method could model each fiber at real scale, which brings greater realism but drastically limits the simulation domain.

In the following, I discuss the results of past and ongoing model development. In section 6.2 I present a particle model for a red blood cell dragged by the plasma flow, represented by the SPH model based on Stokesian dynamics (chapter 2, section 2.3.1). Similar models have been introduced using SPH "standard" equations [258, 122, 259, 260]. In [Van Liedekerke et al., 2013], our purpose was to show the potential and accuracy of the Stokesian SPH approach with regard to standard SPH simulations. In section 6.3, I explain how NSPH can be used to represent a homogeneous viscoelastic medium which is degradable by a cell. In combination with a simple model for cell, we show how the local mechanical stresses around a moving cell can be obtained. This opens opportunities to help in analyzing complex stress-strain relations in ECM-embedded cells based on traction force microscopy (see chapter 7). Finally section 6.4 deals with cell migration in fibrous medium (e.g. ECM). Here the ECM is mimicked by a coarse-grained viscoelastic spring network (discrete model), whereby the distance between the nodes reflects the pore size of the material. The cells in this approach are represented as rods with variable length that can spread protrusions anchoring to the ECM nodes. With this model we are in principle able to simulate systems such as multi-cellular spheroids.

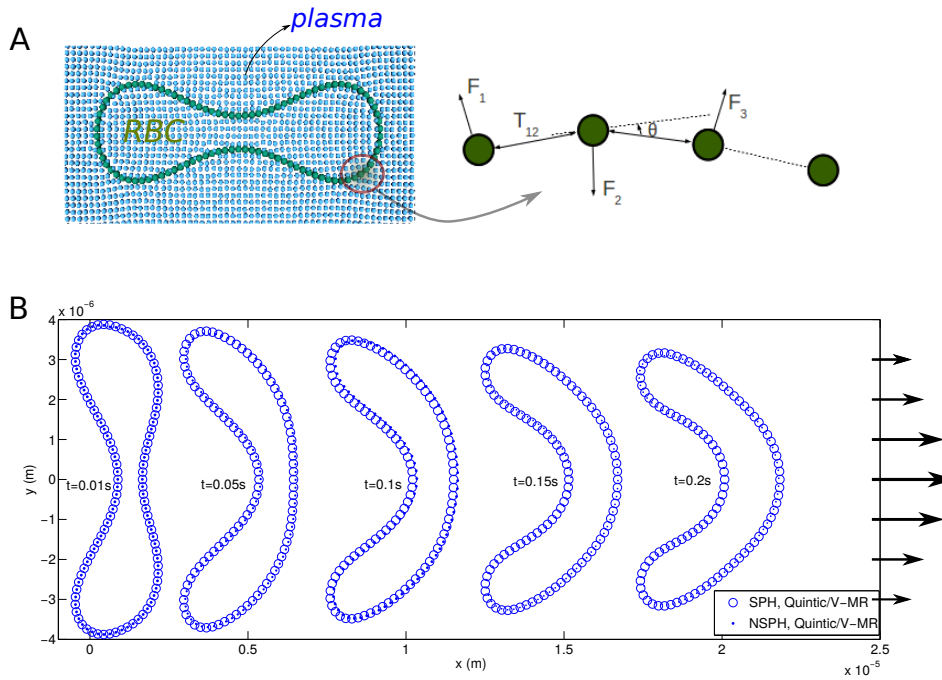


FIGURE 6.1: (A) Deformable cell representation of a erythrocyte in 2D. (B) Comparison of shape and position of an RBC in Poiseuille flow, computed with a standard SPH scheme (circles) and with the proposed NSPH formulation (dots). Images from [Van Liedekerke et al., 2013].

6.2 Modeling of red blood cells through capillaries in Stokes regime

Red blood cells (RBCs) - also called erythrocytes- are mechanically flexible structures with a bi-concave shape, designed to efficiently transport oxygen and flow in the cardiovascular system of mammals. Often the size of the capillaries is lower than that of the RBCs, so the latter need to deform to pass through. The mechanical properties of the cells are critical as e.g. cells with a too low bending stiffness of the cortex will result in an easy deviation from the biconcave shape, while a too high bending stiffness will restrict its motility in small capillaries, causing problems for the organism (e.g. malaria).

The transport properties of blood and the motion of RBCs through small blood vessels has been investigated with agent-based models for several years [258, 261, 14, 124, 262]. The motion of RBC's through capillaries is often represented as a Poiseuille flow system, meaning that the cell is dragged by the plasma flow in a narrow pipe. The flow of blood plasma flow is usually regarded as a Newtonian fluid governed by the Navier-Stokes equations.

We here propose our Stokesian SPH approach [Van Liedekerke et al., 2013], as an alternative to the Navier-Stokes SPH simulations, with as goal to the speed up the computations. The RBCs are modeled by simplified a 2D deformable cell model with a bi-concave shape in which the connected nodes mimic the in plane and bending elasticity of the spectrin cytoskeleton (see Fig. 6.1A).

In [Van Liedekerke et al., 2013] the 2D test problem consists of two parallel plates filled with SPH plasma particles between which the RBC is initially positioned in vertical orientation. The length of the plates is limited but periodic boundary conditions are imposed in the x direction. The system is in total represented by about 12000 particles. The particles are driven by a body force and the plasma flow has a realistic Reynolds number of 10^{-4} . The parabolic velocity field causes the center of the cell to bulge forward and the cell evolves relatively quickly from a biconcave shape to a parachute shape ($t = 0.05$ s) and eventually arrives at a steady state, where the parachute has become smaller and slightly widened in the middle ($t = 0.1$ s, $t = 0.2$ s). We here compare the NSPH solution with

the SPH results, which serve as the reference solution. Fig. 6.1 shows the evolution of the RBC shape in the flow at the beginning and after a longer time, while Fig. 6.1B shows the difference between the two models for the selected times. As can be observed, the shapes obtained with NSPH are in quite good agreement with those obtained from SPH. Additionally, the fluid particle positions show very similar patterns while their velocity profiles match quite well for both methods. The time-step needed in SPH is smaller than 10^{-9} s, whereas in the Stokes formulations, a timestep of 10^{-4} s can be used. The total attained speed-up using NSPH in this example is roughly three orders of magnitude. Obviously the simulations can also be performed with a 3D deformable cell model in a tube.

6.3 Motion of cells in homogeneous degradable viscoelastic matrix

We have further exploited the continuum NSPH model to simulate viscoelastic material (see chapter 2, section 2.3.1). In [Heck et al., 2017], as a proof of principle, simulations of cell migration in a viscoelastic and degradable ECM using the NSPH description for the ECM, have been carried out.

6.3.1 Matrix degradation model

To illustrate the ECM model we resort to a simplification of a real cell and modeled it as a rigid, self-propelling object, embedded in a viscoelastic solid. The cell is represented by particles which are located on a circle. The cell is not deformable although the method is general enough to permit simulations with deformable objects. We do not model the protrusion here. Instead, cell motion is generated by a global migration force with a constant value and a fluctuating direction, representing a biased Brownian motion of the cell (see chapter 2, Eq. 2.10).

ECM degradation is modeled as fluidization of the material in the locality of the cell. We can achieve this by relaxing the deviatoric stress of the ECM particles that have been built up close to the cell, while leaving their hydrostatic pressure unaffected. In a hydrogel this cell-mediated degradation would represent the cleavage of polymers by enzymes (proteinases like matrix metalloproteinases (MMPs)) secreted by the cell. By this cleavage, the connectivity of the polymer network is reduced which allows the cell to move through. Degradation is implemented by introducing a degradation factor f_{deg} which is 1 for an intact viscoelastic solid and 0 for a completely degraded material. We propose an equation that relaxes the stress tensor for each ECM particle (see Eq. 2.33) in the following way:

$$\frac{d\mathbf{S}_i}{dt} = -\Delta f_{deg}(d_i)\mathbf{S}_i \quad (6.1)$$

where $\Delta f_{deg}(d_i)$ is an exponentially decaying function of the distance d_i from the cell center to the ECM particle i :

$$\Delta f_{deg}(d_i) = \frac{1}{\tau_{deg}} \exp\left(-\frac{d_i - R_{cell}}{0.25R_{cell}}\right), \quad (6.2)$$

with τ_{deg} a characteristic degradation time that determines the degradation speed. In this way, particles closest to the cell undergo faster degradation than particles further away. A minimal value of 0 for is enforced for $f_{deg}(d_i)$ in order to prevent negative values. Besides, degradation is limited to particles in front of the cell that are within a certain cut-off distance from the cell and within a certain angle θ_{deg} (see Fig. 6.2A) with respect to the prescribed migration direction. The equation for degradation is arbitrarily chosen and is a simplification of the mechanics that govern degradation kinetics such as proteinase expression, secretion, transport and binding.

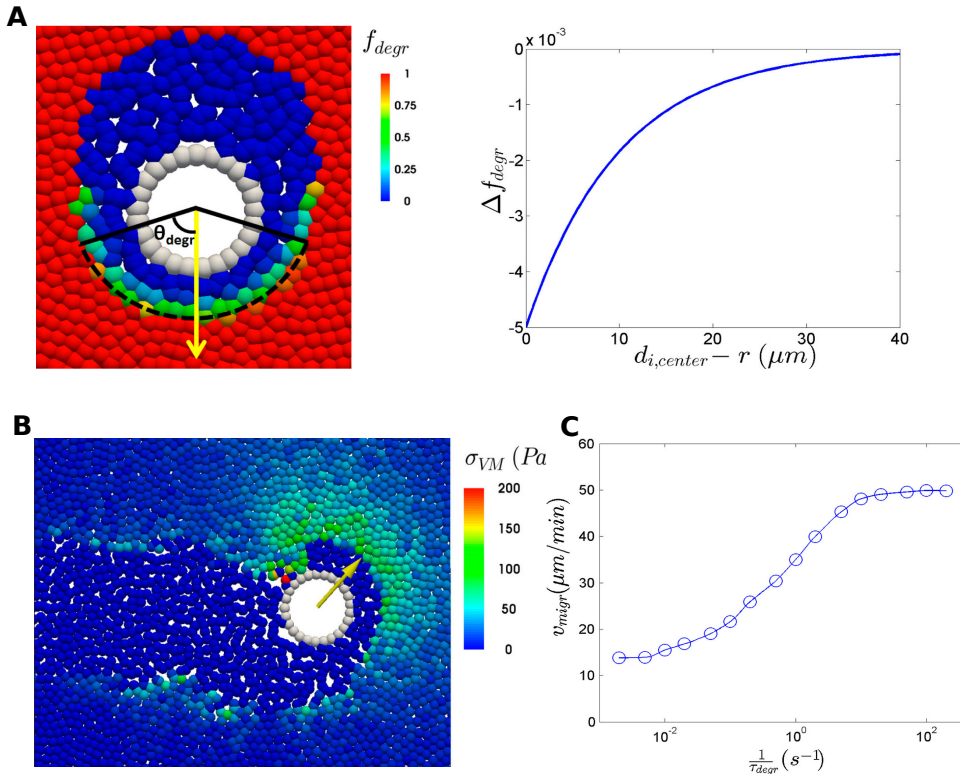


FIGURE 6.2: (A) Left: Illustration of cell migration through the ECM by local ECM degradation. The cell migrates based on a migration force oriented in a certain direction (yellow arrow) and, after an initial degradation around the entire cell, material particles located within a region given by the degradation angle from the migration force direction and within a maximal distance from the cell center are degraded by decreasing the degradation factor. Right: Example of the change in degradation factor for one time step as function of the distance to the cell boundary as described in Eq. 6.3.1. (B) Von Mises stress distribution in the degradable viscoelastic ECM around a migrating cell. The cell degrades the ECM by fluidizing the viscoelastic material and leaves behind a trail of degraded material. The ECM in front of the migrating cell is deformed and builds up deviatoric stress. (C) Cell migration speed in $\mu m/min$ as function of degradation rate τ_{deg} in s^{-1} for migration of a circular cell through a degradable viscoelastic ECM. The migration speed follows a sigmoid curve with a plateau of low cell migration speed for low degradation rate and a plateau of high cell migration speed for high degradation rate. Images from [Heck et al., 2017].

6.3.2 Example: single cell motion in degradable matrix

A cell with a radius of $40 \mu m$ is placed in ECM, modeled as a rectangular domain ($E=2.5$ kPa, $\nu=0.45$, $\mu = 100$ Pa·s and $\rho_0 = 1000$ kg/m³) of $600 \times 800 \mu m$ with an inter-particle distance of $10 \mu m$. The particles are distributed using a method which iteratively uses weighted Voronoi tessellations to get an even distribution of particles in an arbitrary area [263]. In this way, preferred mesh directions are minimized and an even initial distribution around the cell is guaranteed, which is not the case for a cubic or hexagonal lattice. A migration force F_{migr} with a constant value $F_0=10 \mu N$ and a fluctuating direction representing biased Brownian motion is applied to the cell.

A simulation ($Re = 1.0 \times 10^{-7}$) is run for 600 s with a time step of 0.01 s. In Fig. 6.2B it can be seen that the cell has migrated through the ECM, leaving behind a trail of degraded matrix (with low von Mises stress) caused by the local degradation. In front of the cell, the ECM is deformed resulting in a higher deviatoric stress.

In order to demonstrate the effect of degradation rate on cell migration speed, several simulations

are performed with values of reference degradation rates $\frac{1}{\tau_{\text{degr}}}$ ranging from 0.002 to 200 s⁻¹. The migration speed as a function of degradation rate is shown in Fig. 6.2C. It can be seen that the cell migration speed follows a sigmoid curve with a plateau of low migration speed at low degradation rates, an increase in migration rate at intermediate migration speeds and a second plateau of maximal migration at high degradation rates. This is in agreement with our basic understanding that increased ECM degradation can not monotonically augment cell migration. Further in this work, the sensitivity of other migration parameters on the cell migration velocity has been investigated.

Overall, this showed that the method ensures stable and accurate simulations of the degradation process in matrix whereby cells transform a solid like material into a liquid like material, and encourages that the model can be expanded to more accurate presentations of the cell (see chapter 7).

6.4 Migration of cells through non-homogeneous matrix

In chapter 2 (section 2.3.3), I explained the basic components of the rod-shaped cell model with ECM represented as a random network of springs. Contrary to the model in the previous section, here the cells can express protrusion forces on the ECM particles, which in turn can deform the ECM. Degradation of the ECM is mimicked as a local weakening of the spring constants between the nodes (see Eq. 2.39).

In this section we present some preliminary results. First, we illustrate the capabilities of the model by simulating a single non-proliferating cell embedded in matrix and investigate the influence of some mechanical model parameters on the migration speed. This will allow us to identify the key parameters that facilitate invasion. Secondly, we simulate a durotaxis experiment, in which cell migration is guided by rigidity gradients. Durotaxis is believed to play a role in cancer metastasis and liver fibrosis.

Mechanical parameters of the cell as well as those of the ECM can dramatically affect the migration speed. For instance, a study by Haeger et al. (2014) [264] indicates that cell migration is limited by the ECM pore size. To verify this, we have performed simulations of cells migrating in ECM, as function of the ECM pore size. We have construct an ECM lattices with varying pore size, ranging from 0.2 to 1.2 times the initial cell size ($R_{\text{cell}} \sim 6 \mu\text{m}$). The pore size is here the average distance between two lattice nodes. The cells have a default Young modulus of 500 Pa and are positioned initially in the middle of the lattice (see Fig. 6.3). For each lattice pore size, 10 simulations were run with a slightly different initial lattice configuration.

In Fig. 6.3A the paths by the cell are displaced for three pore sizes. Fig. 6.3A clearly shows that for small pore sizes the cells are indeed hindered by the ECM structure, whereas for large pore sizes we observe a similar behavior. Large pore sizes allow the cells to move easier but they limit the number of protrusion and adhesion sites that can be formed drastically, resulting in a net decreased cell speed. For intermediate sizes, an optimal cell migration pattern is established (Fig. 6.3B). To show the importance of cell deformation, we have also performed these simulations with a very rigid cell type that keeps it spherical shape yet expresses protrusions. For these we observe that the distance they can travel is significantly lower than the elongated cells for all pore sizes (see Fig. 6.3B).

We have used the same setup to test the effects of MMP's. Simulations with a non-zero ECM degradation indicate a decrease of the minimum node distance in which migration was possible (Fig. 6.3B), hence our model reproduces the well-known observation [265, 266] that inhibition of MMPs reduces cell migration in small pores. For larger pore sizes however, ECM degradation seems to have a non-significant or even adverse effect.

We have also looked at the effect of nucleus size and overall cell stiffness. The cell nucleus is known to be much less deformable (stiffer) than the cytoplasm and we assume in our model the former remains spherical. An increased nucleus size here slightly impedes the cell migration distance, as is shown in Fig. 6.3C. A too large nucleus size can result in a cell that is trapped, unless MMP's are produced. The same effect can be observed for overall higher cell stiffness (cytoplasm and stiffness).

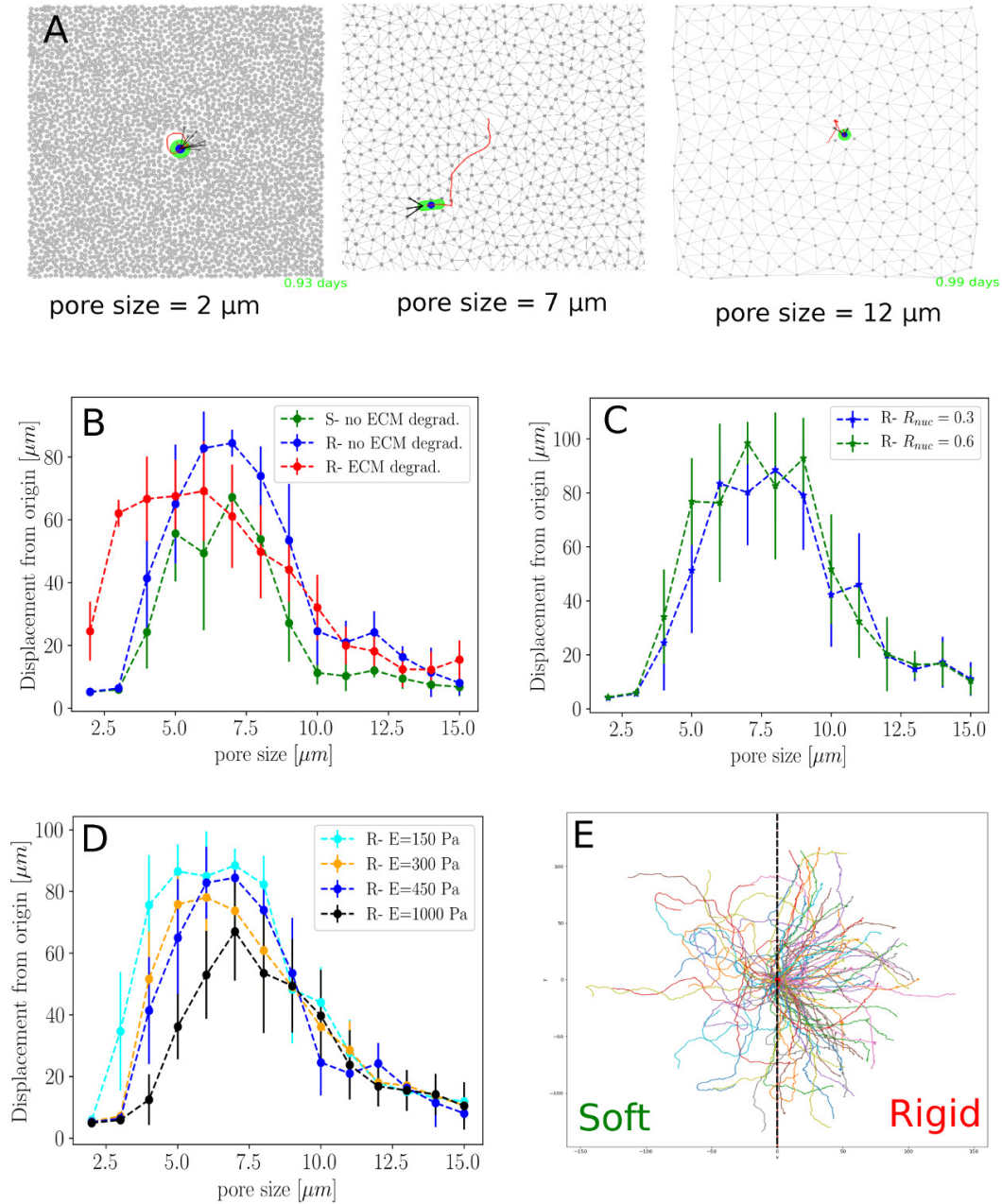


FIGURE 6.3: (A) Simulation snapshots of the migration of a single cell through ECM of varying pore sizes. (B) Effect of ECM pore size on the cell displacement from the initial position (without ECM degradation; with degradation; rigid cell type). (C-D) Effects of nucleus size and cell stiffness on cell displacement. (E) Durotaxis experiment showing the paths of several single cell simulations.

Indeed, Fig. 6.3D clearly shows that stiff cells ($E_{cell} = 1000 Pa, E_{nuc} = 10 kPa$) show a significant decrease in invasion capacity as compared to a cell with ($E = 150 Pa, E_{nuc} = 1500 Pa$). These results in qualitative agreement with observations (i.e. [265, 267]).

Finally, we have tried to simulate durotaxis. Here, we simulate the ECM frame having one soft side (left) and one rigid side (receptively left and right in Fig. 6.3E). The value of k_{ECM} is 10 times higher for the stiff side. Again, a cell is positioned initially in the middle. Because the cell is rounded up initially, it can initially spread protrusions in random directions. During the course of the simulation, the polarization will change according to Eq. 2.42. A total of 100 simulations has run, each with a slightly different random ECM network. The trajectories for the cells in all these simulations are shown in Fig. 6.3E), effectively showing that indeed a majority of the cells prefers to move towards the stiff part of the matrix. This indicates that the assumptions for the protrusion mechano-sensing seem to be conform with durotaxis.

Concluding, this model shows some promising results with regard to the mechanical parameters that guide invasion. Having already performed test simulations with up to 10000 cells, we hope to identify invasion mechanisms in multi-cellular systems.

Chapter 7

Conclusion, outlook and challenges

7.1 Aftermath of the proposed agent-based models

In **chapter 2**, I have given an overview of state-of-the art Agent-Based Models (ABM) used for cell and tissue mechanics. I have discussed the category "lattice-based" types and the category "lattice-free" types herein.

Lattice-based models have a long standing history (since development of cellular automata models) and are nowadays still very popular (i.e. Cellular Potts Models). This can be attributed to their algorithms which are generally easy to implement and to the fact they represent rule-based rather than physics-based dynamics. The major drawback of these models is that they are governed by stochastic processes and hence prevalently deterministic processes are hard to simulate. Cellular Potts models (CPM) allow to mimic complex cell shapes and interesting pattern formations in cellular systems, in the assumption that the Hamiltonian for the configuration space of the cells is correctly defined. However, a CPM yields solutions for equilibrium configurations of cells. They lack a clear timescale, and it is always assumed that cells reach this equilibrium configuration much faster than time scales of other perturbations (e.g. cell division).

Contrary, Lattice-free (particle-based) models are generally formulated with an equation of motion (Langevin type). Here the viscous, stochastic, and conservative forces can be tuned accurately and arbitrary. The equation of motion implies a clear definition of time. However, the algorithms may be intrinsically more complex, computationally more expensive, and may require a greater knowledge of physics and mechanics compared to CPM, which is probably why they are generally less attractive to biologists.

Yet, I hope to have shown that particle-based models are capable of simulating a large variety of mechanical effects in cells and tissues. In **chapter 3** we have shown that we can simulate mechanical impact in parenchyma cells eventually leading to prediction of damage as a function of subcellular properties of the cells. We have shown that the damage in tissue largely depends on the individual cell properties as well as their micro-structure. In **chapter 5** on the other hand, we have addressed the long-term effects of mechanical stress on tumor cells growth, indicating that these are predictable over various cell lines with the same cell cycle progression function. In **chapter 4**, we have elaborated high-detail models in which the various parts of a cell can be discerned. We have shown that most of the parameters in this model can be inferred from standard single-cell experiments. We can simulate monolayers as well as complex tissues including blood vessel networks, at a desired resolution. We argue that these models in the future will more and more replace the old but nowadays still popular center-based model types where cells are regarded as rigid objects. Finally, in **chapter 6** we have presented two modeling solutions for simulating migrating cells embedded in extracellular (ECM) whereby the mechanical and physical aspects of ECM has been explicitly taken into account.

7.2 Ongoing work and future directions

It is likely that future experimental technologies will keep on increasing their accuracy and detail [35]. As such, it should be clear that model development cannot not be a static occupation; instead it needs to co-evolve with the available technologies. Especially the developments of the high resolution model (DCM) open numerous possibilities and applications in biomedical and bio-mechanical sciences. I can only suggest a few here. However, one of the remaining challenges of advanced agent-based models is their computational cost. Indeed, whereas efficiently coded center-based models can handle up to 10^6 cells on a single core machine, simulations with deformable cell models are currently suitable to up to 1000 cells per CPU. One should always keep in mind that computational requirements will keep on increasing, and in the future one should focus to develop algorithms and software with efficient distributed computing.

7.2.1 Mechano-transduction and developmental biology

Mechanical measurements of cells obtained from micro-pipetting or optical stretching give useful mechanical information on their own, e.g. by quantifying differences between distinct experimental conditions. However they usually require a mathematical model to unravel the underlying material properties and forces that characterize the cells. Analytical models (e.g. [268, 269, 270]) provide a fast way to analyze forces but they may lack accuracy as they usually describe the cells as homogeneous solid elastic materials or liquids with surface tension, assuming further the cells maintain a certain symmetry in their shape. The DCM permits to run simulations with high accuracy of cell shape and forces resolved at subcellular level. In combination with microscopic and single-cell techniques (chapter 4), this can become a powerful tool to better understand the influence of mechanics on cellular processes. It is important to mention that the current DCM can be enriched with more details of the cell whenever this becomes necessary. We are currently envisaging to include a cell nucleus and a prototype of cytoskeleton (see Fig. 7.2A).

The DCM permits to calculate force distributions in the cytoskeleton and on the nucleus potentially leading to a better understanding of **mechano-transduction** processes. In chapter 5 we have proposed a generic stress dependent growth function for cells. A cell volume reduction due to mechanical pressure was assumed to correlate with an over expression of p27Kip1 which progressively decreases the proliferating potential. However, other molecular players such as the transcriptional regulators YAP/TAZ that are also reported to be mechano-sensitive may play a role here [246]. YAP and TAZ are involved in the contact inhibition of proliferation and act as sensors and mediators of mechanical cues. Using single cell micro-pipette experiments performed simultaneously in vitro and in silico, one could look more profoundly into the relation between physical forces inside the cell, and Yap/Taz activity.

There are also numerous problems to be addressed in **developmental biology**. Well known phenomena such as inflation of blastula, apical constriction, gastrulation, and formation of lumen by cell apoptosis involve critically important underlying mechanisms for morphogenesis [250]. Agent-based models of the center-based type have been developed (e.g. [92, 78, 271]) to understand such mechanisms, but due to poor shape representation and lack of subcellular detail these are not a priori suitable to investigate these phenomena rigorously. With the DCM, the influence of these phenomena can be quantitatively simulated and identified as to play a key role or to be insignificant¹. For example, the DCM permits in principle to simulate so-called "tight junctions" (which seal the para-cellular pathway and prevent leakage of transported solutes and water) between cells due to e.g. cadherin complexes as localized reinforcements on the cell surface. The DCM is also highly suitable to investigate cell sorting which is observed in nearly all organoid systems. Here, one could investigate balances between

¹We note here that Vertex models (see section 2.3.2) have been proposed for morphogenesis as well [146], but it should be stressed that these models are fundamentally conceived for epithelial sheets and can only represent cell shape as polygonal.

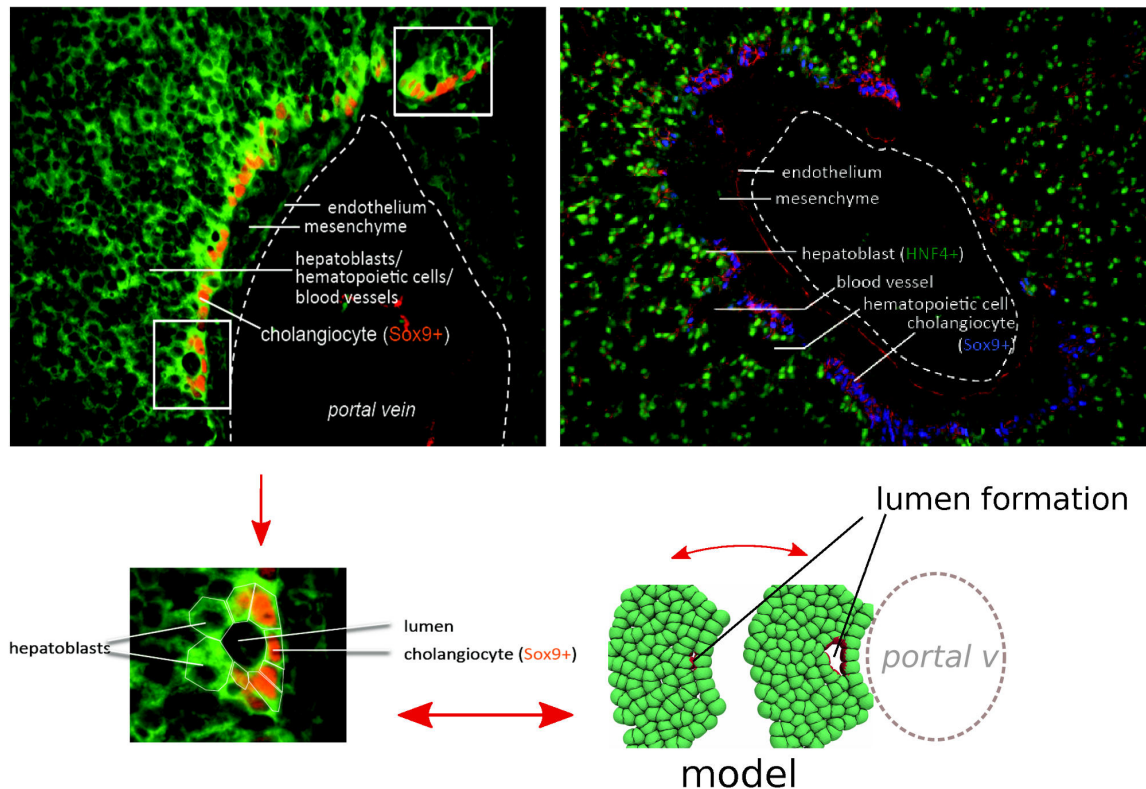


FIGURE 7.1: Top: Images of stained cells from embryonic mice around portal vein (central black area). Right: staining according to E-cadherin expression (red) and Sox9 (blue). Bottom left: zoom of early lumen formation on the left side of the central vein. Right bottom: Simulated formation of lumen with DCM due to local inflation of the extracellular space by hydrostatic pressure as a result of osmosis. In the left simulation, the hydrostatic pressure is not sufficient to push away the surrounding cells and form an opening. Contrary, in the right simulation, this is the case. Credit microscopy images: Frédéric Lemaigre, UCL, Belgium

adhesion-mediated differential interfacial tension (contractility) and persistent cell motility which are responsible for the observed cell segregation at long time periods.

A mechano-biological problem which currently addressed is the formation of bile ducts in embryonic liver (in collaboration with D. Drasdo, INRIA and Prof. Frédéric Lemaigre, UCL, Belgium). Our understanding of duct morphogenesis has recently improved with advanced three-dimensional imaging and computer-assisted analysis. However, the way in which the three-dimensional tissular architecture of the liver develops under influence of which forces in the embryo remains much less explored [272]. Bile duct development is initiated near the hilum of the liver before progressing towards the periphery of the lobes. Despite the experimental imaging techniques at hand, it is difficult to probe the mechanical forces locally hence simulations become mandatory to understand the mechanisms that generate the early cavities of the bile ducts. The initial formation of a duct begins as cholangiocytes (Sox9+) cells close to the endothelial of the portal vein locally begin to separate from hepatoblasts (Sox9-) cells. Polarisation and E-cadherin expression plays a large role herein. The initial gap can be formed by potentially several hypotheses but it is currently unknown which mechanism and which forces are needed for it. In Fig. 7.1 we show some early results of a cavity formation process, simulated with DCM. Here, we have hypothesized that the local cavity is the result of an increased hydrostatic pressure induced by osmosis due to local release of salts by a single cell in the extracellular space [250].

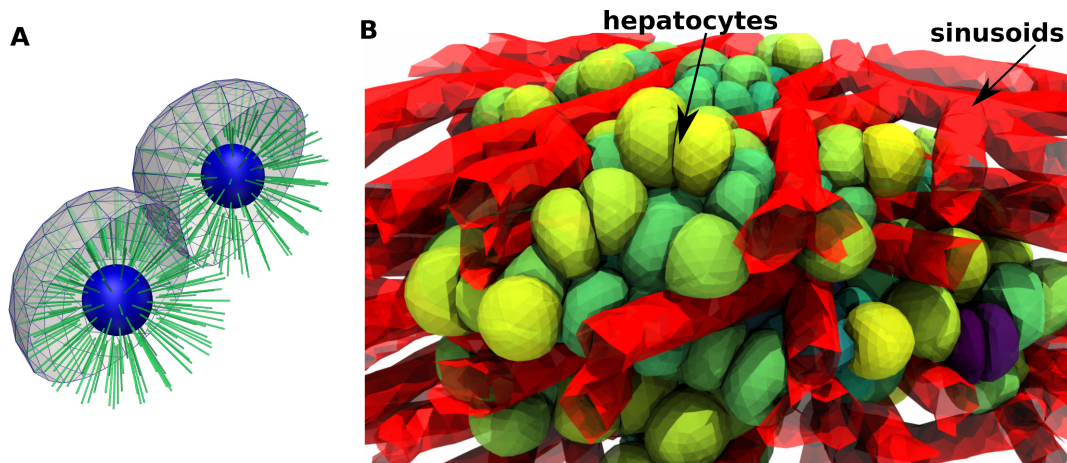


FIGURE 7.2: (A) Prototype of a DCM with internal skeleton (green lines) and nucleus (blue). Each of the cytoskeleton elements connect the nucleus with a node on the cell surface. (B) Snapshot of a liver lobule simulation with DCMs and a triangulated sinusoidal network [Van Liedekerke et al., 2018b] that was obtained from confocal micro-graphs (source: Lab of Dr. Stefan Hoehme, U. Leipzig).

7.2.2 Cell migration mechanics

The developments outlined in chapter 6 have shown that with our models, we have several possibilities in which we can address the mechanics of cell migration by taking into account the interactions with extracellular matrix.

Direction I: The model for a cell embedded in homogeneous (continuum) ECM can be further improved by introducing the deformable cell model instead of a center-based model. A DCM permits here to explicitly simulate phenomena such as the expression of protrusions and the contraction of the cellular cortex.

In collaboration with the research group of Prof. H. Van Oosterwyck (K.U.Leuven), we are developing such a DCM-ECM coupling to simulate **angiogenic sprouting**, or blood vessel formation. The goal is to get a better understanding on how the physical properties of the ECM influence cell migration in the formation of blood vessels. To eventually simulate the motion of the cell, one first needs to obtain good estimations of the force distributions around the angiogenic sprouts, i.e. the forces that are applied by the protrusions of the cell to the ECM.

We primarily have been analyzing experimental Traction Force Microscopy images of human umbilical vein endothelial cells (HUVECs), which yield a displacement field of ECM (Hydrogel) around the cell (see Fig. 7.3A). The cell is modeled as a deformable body capturing the mechanical behavior of the actin cortex (viscoelasticity and bending rigidity). The ECM medium is modeled by SPH (see section 2.3.1). The DCM is here initialized such that its shape is close to the experimental one. Subsequently, forces are applied initially to the ECM points that are close to the boundary of the sprout, in the direction of the local displacement field. These forces mimic the ones that are applied by the protrusion. The forces are optimized iteratively by adapting them based on the difference between the local experimental and computational displacement field. The obtained force estimates in Fig. 7.3A, right) show a large pushing force from the endothelial monolayer and smaller pulling forces at the main protrusions of the sprout. Their magnitudes are of the order of 10 nN .

Single cell migration through a degradable extracellular matrix (ECM) is intended to be modeled as follows (see Fig. 7.3B). Initially, a cell with rounded shape is embedded in ECM. The cell then polarizes and begins to form protrusions by locally weakening the actin cortex and pushing out the actin cortex by a protrusive force representing actin polymerization. The ECM is degraded locally in order to allow the protrusion to form. After a protrusion is formed, a spring-like cell-ECM adhesion is

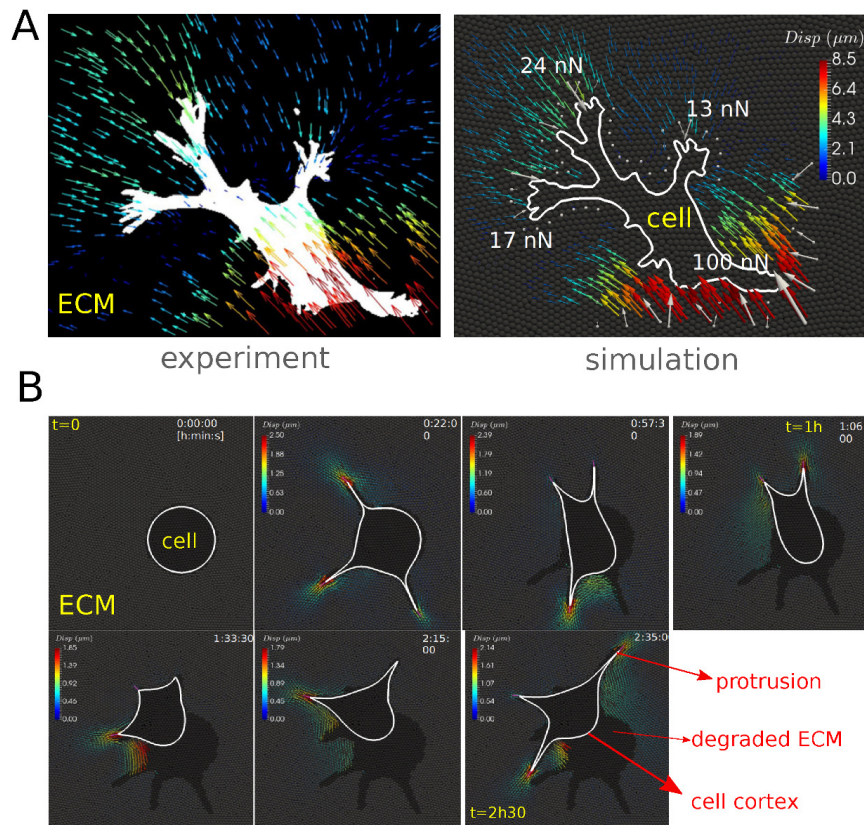


FIGURE 7.3: (A) 2D image of a measured displacement field in Matrigel around an angiogenic sprout of HUVECs (endothelial monolayer located in the bottom right corner -but not clearly visible-, sprout grows towards top left corner) in collagen (left) and force recovery in the DCM by fitting of a computational displacement field to the experimentally obtained displacement field (right). The view field of this sample is $136 \times 113 \mu\text{m}$ (B) Time lapse of the simulated displacement field around a protruding cell. The cell is initially round but then begin to degrade the viscoelastic ECM (solid ECM in light grey, degraded fluid ECM in dark grey) in order to form protrusions. By adhesion of protrusions to ECM particles and contraction of the cell cortex, the cell is able to migrate away. Credit image: Tommy Heck (K.U.Leuven, Belgium).

formed at the tip and the protrusion contracts. The amount of actomyosin contraction is adjusted to the local ECM stiffness (mechanosensing), resulting in stronger actomyosin contraction and cell-ECM adhesion for stiffer ECMs. By forming multiple protrusions that, through the actin cortex, pull on the cell body and other protrusions, we can show (proof of concept) that the cell is able to migrate through the ECM matrix.

Direction II: It is known that the mechanical environment is of key importance to malignant tumors [273]. The second direction in cell migration could continue to focus on invasion in tumors using the rod model presented in chapter 2. Here, we can further test the mechanical cues that regulate a successful invasion. In particular, we should in a first step test the parameter space that controls ECM stiffness, ECM pore size, the mechanical properties of the cells, the role of ECM degrading enzymes (matrix metalloproteinases), and the protrusion forces that are needed for a cell to overcome the resistance of the ECM and invade [274]. Next, we could then study emerging multi-cellular patterns in invasive (in vitro) spheroids (see e.g. [275, 276, 277, 278, 279]). The intermediate model with deformable rods allows to easily simulate over 10^4 cells embedded in a large area of ECM. While this obviously limits us to small tumors, hybrid approaches can bring a solution by replacing the cells in necrotic or quiescent regions in the tumor with a simpler center-based model or even a use continuum approaches. [280].

Direction III: Elaboration on a fine scale ECM model. A more sophisticated way compared to the ECM model as above mentioned, would be to model the ECM as a real fiber network model that accounts for the stretch-dependent formation of weak cross-links between nearby fibers (e.g. Ban et al., 2018 [281]). However, such an approach is expensive both implementation-wise and in terms of computing power and is likely only amendable for tiny dimensions.

7.2.3 Multi-scale modeling approaches

The versatility of our model approach permits to simulate cell mechanics at various scales and details. If one desires to study mechano-transduction phenomena, it will be required that the mechanical parameters in the models are linked to "low level" variables, e.g. concentrations of proteins. The genetic and signaling aspects in cell biology can be captured by the concept of intracellular Gene Regulatory Networks (GRN). Agent-based models are ideal partners to perform "multi-level" simulations as each cell can carry such an intracellular module.

ODE models: Ordinary differential equations allow to compute the time evolution of concentrations of compounds in the cell. For instance, previous work by Ramis-Conde and co-workers [27] concentrated on the problem of cancer cell intravasation introducing biological pathways involving cell adhesion molecules such as VE-cadherin and N-cadherin, and the biophysical properties of the cells. More recently "MecaGen" [282], an integrative modeling platform via GRN, enabling the hypothesis-driven simulation of these dual processes via the coupling between mechanical and chemical variables, has been proposed. Examples here were given for Wnt and Delta-Notch signalling.

Boolean networks : ODEs as representation of gene regulatory network may be confined to small signalling networks. Models with Boolean networks on the other hand are logical networks with computed variables (genes, proteins or specific protein functions) that can acquire only two states: 0 or 1 [283]. Each variable is updated according to the status of its regulating variables, connected by logical connectors AND, OR and NOT. For example, MaBoSS [284] is a tool that uses a Gillespie algorithm to perform stochastic simulations on logical models and obtain model state probabilities, allowing for a semi-quantitative study of the model's phenotypes and perturbations.

In the aforementioned works, agent-based models of the center-based type were used. Here we could significantly improve the mechanical models of the cells by (i) introducing rod-like shaped cells or DCMs, and (ii) the inclusion of ECM material (discrete network or as continuum). In principle here the information feedback loops between mechanics and the intra-cellular pathways can be calculated

with far greater accuracy than in a center-based model. For example, guided by the experimental observations that cells in cancer invasion are largely elongated (personal communication with Phillipe Chavrier, Institut Curie), we could use the rod-shaped cell model that incorporates protrusions explicitly. The research could focus on whether the mechanics of protrusions formation/retraction and the release of MMPs that degrade the matrix, could be both connected to a GRN in the cell that up- or downregulates these enzymes.

7.2.4 Software development

The spreading of software over a community is an essential aspect for the successfulness of the models. To make the models and simulations more accessible to a larger community, there are a number of important steps to be undertaken.

(i) One should aim to develop software with attractive GUI's that allows for users to switch between the models easily.

(iii) For future simulations, one should also strive to run simulations directly starting from microscopic imaging, which would leave less room for speculation on how the tissue architecture is constituted. In-house algorithms and external libraries that perform reconstruction of three-dimensional surfaces of biological systems [285] and converting it to bounded, triangulated structures (representing cells, blood vessels, flexible or stiff structures), should become a part of the software. A proof of concept with a prototype simulation for cells embedded in a blood vessel architecture of liver is shown in Fig. 7.2B (more details on the algorithms in [Van Liedekerke et al., 2018b]).

(iii) Development of parallelized algorithms will be important to simulate increasingly larger cell numbers and at a higher detail of morphology. Alternatively, one can also elaborate on simulations of tissues in a hybrid mode (see Fig. 4.8). This may open possibilities to accomplish larger scale simulations where some parts are modeled at high spatial resolution models, while in other zones approximate models are sufficient.

In collaboration with the Lab of Dr. Stefan Hoehme (U. Leipzig) and D. Drasdo (INRIA) we are developing an efficient, integrated C++ based software "TiSim", that in the future should be able to handle a variety of cell models (center-based, rods, deformable cells) in combination with models for extracellular matrix, diffusion of molecules (nutrients, oxygen), and intracellular modules that can be easily transferred from libraries of pathway modeling (e.g. SBML).

Appendix A

A.1 Fluid-boundary coupling consistency in the parenchyma cell model

We first consider the Laplace equation for a spherical cell. We rewrite it in the form:

$$\sigma t = \langle p_i \rangle \pi R^2, \quad (\text{A.1})$$

where σt is the line tension in the membrane along the equator, R is the radius of the cell and $\langle p_i \rangle$ is the average pressure of the SPH particles in the cell. For the 2D as well as the 3D model, we have evaluated both sides of the Laplace equation and we found an acceptable agreement with mutual deviations below 6%. This quasi ensures that the hydrostatic mechanical coupling between the cell fluid pressure and cell wall tension is accurate.

We further validated the 3D model for dynamic modes by comparing them with analytical solutions for oscillations of a fluid-filled, thin spherical shell with radius R . The analytical equation that yields the frequencies ω of this system is well-known [286]:

$$\frac{j_0(q)}{j_1(q)} - \frac{q\rho_s t}{\rho R} + \frac{4Et}{q\rho c^2 R} = 0, \quad (\text{A.2})$$

where j_k are the spherical Bessel functions of the first kind, with $q = \omega R/c$. Furthermore, $c, \rho \sim 1000 \text{ kg/m}^3$ are the speed of sound in the fluid and its density, and ρ_s, E are the density and the Young modulus of the wall material. We now consider two cases. In a first case, the shell is completely *in vacuo*. This case is obtained by setting $\rho \rightarrow 0$ (no fluid mass) in Eq. A.2. The cell surface will oscillate with a ground frequency:

$$\omega = \frac{1}{R} \sqrt{\frac{4E}{\rho_s}}. \quad (\text{A.3})$$

In the model, an oscillation can be triggered easily by considering a pressurized cell and suddenly remove the enclosed fluid particles. The simulation results determining the period of the radial oscillations of the cell wall are within 1% deviation of these solutions.

Next, we considered the case that the sphere contains a compressible liquid. The analytical solution for the vibrations of this system is somewhat more complicated, as there are more possible frequencies which can be excited. In our model, we excite the system by giving the wall particles an initial inward radial velocity. The cell will then start to oscillate ($\sim \Delta R$) around its initial state. In Fig. A.1 the spectrum of excited frequencies is given for a sound speed of the fluid $c = 50 \text{ ms}^{-1}$ and $c = 250 \text{ ms}^{-1}$ respectively. In addition, the theoretical frequencies are also shown (arrows). The dashed arrows indicate ground frequencies. The SPH model captures the ground mode and at least two higher frequencies reasonably (deviations are between 5% and 10%, due to the discretization errors and the fluid-boundary coupling). For $c = 250 \text{ ms}^{-1}$, a mode shows up which is not close to any analytical solution (indicated by dashed ellipse). However, we argue that in the case of high compression modulus K , the influence of the latter can be minimized because the timescale of the dynamics we are considering here (e.g. impact, relaxation) is much slower, and in addition, the amplitudes of these oscillations are relatively small. The first two frequencies are within 6% deviation from the analytical solution.

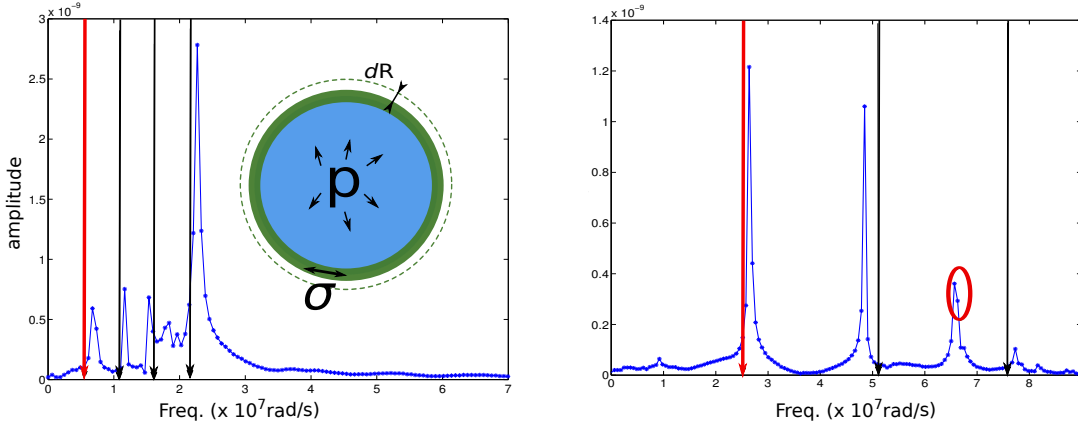


FIGURE A.1: Frequency spectra of the SPH cell model for centro-symmetric oscillations and comparison with analytical solutions. Left: $c = 50 \text{ ms}^{-1}$, right: $c = 250 \text{ ms}^{-1}$ (black arrows, red arrows: ground frequencies).

A.2 Derivation of SPH Euler equations from a coarse-grained MD system

The SPH equations for an inviscid flow at constant entropy (Euler equations) can be derived from the equations of motion of a coarse-grained molecular system with effective many-body interaction potentials \mathcal{U}^e . Let us recall the equation of motion of a conservative system of particles. However, we assume here the "particles" or parcels with positions $\mathbf{r}_1, \mathbf{r}_2, \dots, \mathbf{r}_N$ each representing a finite volume filled with atoms or molecules. The potential energy of the system can be regarded as the internal energy summation $\mathcal{U} = \sum_j \mathcal{U}_j^e(\mathbf{r}_1, \mathbf{r}_2, \dots, \mathbf{r}_N)$. The equation of motion for one of these parcels i in interaction with other parcels j would thus be (recall Eq. 1.1):

$$\begin{aligned} m_i \frac{d\mathbf{v}_i}{dt} &= -\nabla_i \sum_j \mathcal{U}_j^e \\ &= -\sum_{j \neq i} \nabla_i \mathcal{U}_j^e - \nabla_i \mathcal{U}_i^e. \end{aligned} \quad (\text{A.4})$$

We can further write this as:

$$\begin{aligned} m_i \frac{d\mathbf{v}_i}{dt} &= -\sum_{j \neq i} \frac{\partial \mathcal{U}_j^e}{\partial \mathcal{V}_j} \nabla_i \mathcal{V}_j - \frac{\partial \mathcal{U}_i^e}{\partial \mathcal{V}_i} \nabla_i \mathcal{V}_i \\ &= -\sum_{j \neq i} p_j \nabla_i \mathcal{V}_j - p_i \nabla_i \mathcal{V}_i, \end{aligned} \quad (\text{A.5})$$

where we applied that $p = \frac{\partial \mathcal{U}}{\partial \mathcal{V}}$ for our thermodynamic system. Using the identity $\mathcal{V}_i = m_i / \rho_i$ and applying the SPH kernel approximation $\rho_i = \sum_j m_j W_{ij}$, we find that:

$$\nabla_i \mathcal{V}_j = -m_i \frac{m_j}{\rho_j^2} \nabla_i W_{ij} \quad (\text{A.6})$$

and similar,

$$\begin{aligned}
\nabla_i \mathcal{V}_i &= -\frac{m_i}{\rho_i^2} \sum_j m_j \nabla_i W_{ij} \\
&= -\frac{m_i}{\rho_i^2} \sum_{i \neq j} m_j \nabla_i W_{ij}.
\end{aligned}
\tag{A.7}$$

Inserting this in Eq. A.5 yields thus

$$m_i \frac{d\mathbf{v}_i}{dt} = -m_i \sum_j m_j \left(\frac{p_i}{\rho_i^2} + \frac{p_j}{\rho_j^2} \right) \nabla_i W_{ij},
\tag{A.8}$$

which is the conservative part of the standard SPH equation of motion for a fluid particle, see Eq. 2.18. Formally, the SPH kernel function can thus be seen as playing the role of a molecular dynamics pair potential.

Appendix B

Modeling cell and tissue mechanics with high resolution models: model components and parameter calibration

B.1 Deformable Cell Model: forces

B.1.1 Internal forces

We here discuss the force components in Eq. 2.35 in more detail. The CSK in-plane elasticity is controlled by the visco-elastic elements. The elastic forces in the viscoelastic network of a cell are represented by linear springs with spring stiffness k_s , while the friction coefficients are denoted as γ_{int} and might be represented by dashpots. Complex viscoelastic elements can be constructed by combining springs and dashpots.

The combination in which the spring and friction terms are schematically positioned in parallel to each other reflects the Kelvin-Voigt Element (KVE), see Fig. B.1B, representing a solid like behavior in that the elements after release of an external force relaxes back to its original length. Consider for example the internal force F^{int} originating from the Kelvin-Voigt viscoelastic element between node nodes i and j (for simplicity $\gamma_{\parallel} = \gamma_{\perp} = \gamma$).

$$\begin{aligned}\mathbf{F}_{int,ij} &= \mathbf{F}_{e,ij} - \gamma \mathbf{v}_{ij} \\ &= -k_s(\mathbf{r}_{ij} - \mathbf{r}_{0,ij}) - \gamma \mathbf{v}_{ij},\end{aligned}\tag{B.1}$$

where $\mathbf{r}_{0,ij}$ and \mathbf{r}_{ij} are the initial and actual distance vectors, and $\mathbf{v}_{ij} = \mathbf{v}_j - \mathbf{v}_i$ is the relative velocity. The force balance equation with external forces \mathbf{F}_{ext} demands that $\mathbf{F}_{ext} + \mathbf{F}_{int} = 0$, hence:

$$\mathbf{F}_{ext,ij} - k_s(\mathbf{r}_{ij} - \mathbf{r}_{0,ij}) - \gamma \mathbf{v}_{ij} = 0.\tag{B.2}$$

Contrary, a Maxwell element (ME) simulates a fluid like extension of the cortex. In the ME the friction element and spring element are schematically positioned in series (see Fig. B.1B), which is why an external force leading to an extension of the element is damped but removal of the force does not lead to relaxation of the element back to its original length characteristic for a fluid behavior. The equation of the internal force in the element \mathbf{F}_{int} (assuming isotropic constants) involves a differential and reads:

$$\frac{\dot{\mathbf{F}}_{int,ij}}{k_s} + \frac{\mathbf{F}_{int,ij}}{\gamma_{ME}} = \mathbf{v}_{ij}.\tag{B.3}$$

This equation contains a derivative of the force, which can be approximated by $\dot{\mathbf{F}}_{int} = (\mathbf{F}_{int}(t) - \mathbf{F}_{int}(t - \Delta t)) / \Delta t$. From the force balance between external and internal forces (see Eq. B.2) we find now:

$$\mathbf{F}_{ext,ij}(t) + \frac{\mathbf{F}_{int,ij}(t - \Delta t)}{1 + k_s \Delta t / \gamma_{ME}} + \frac{k \Delta t}{1 + k_s \Delta t / \gamma_{ME}} \mathbf{v}_{ij} = 0.\tag{B.4}$$

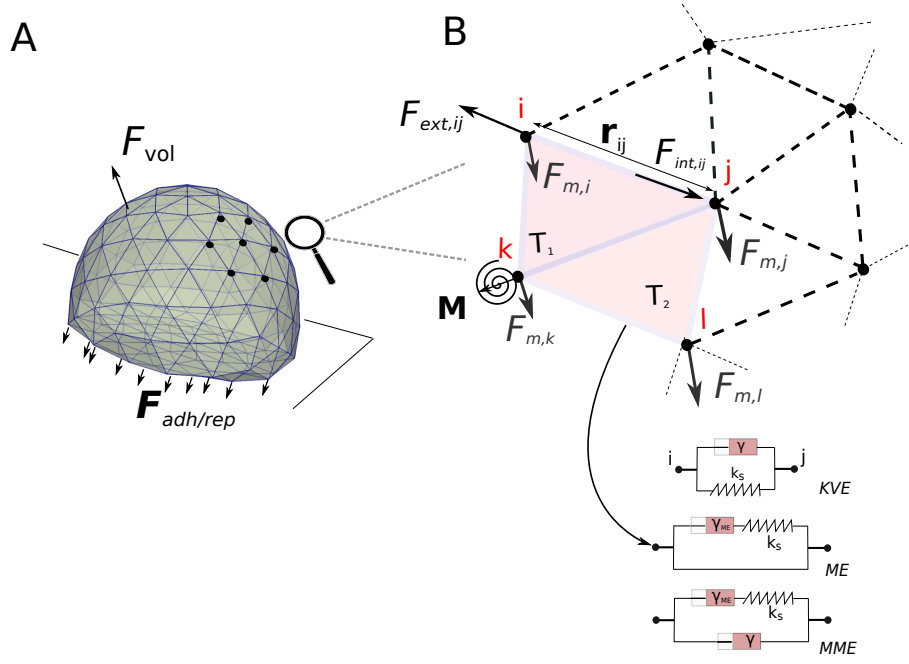


FIGURE B.1: (A-B) left: cartoon of adhering cell and detail of the forces acting on the nodes in the cell surface triangulation (right). Each of the elements between two nodes can be chosen as KVE, ME, or MME.

This equation thus involves the evaluation of the internal force on the previous timestep. Note that the total elastic in-plane forces can be related to a local in-plane stress using the formula [287]:

$$\sigma_i = \frac{\sqrt{3}}{N_i} \sum_{j \in N_i} \frac{F_{int,ij}}{d_{ij}}, \quad (\text{B.5})$$

where N_i is the coordination number of node i , $F_{int,ij}$ is the absolute value of total elastic force between i and j , and d_{ij} is their distance.

Another force component in Eq. 2.35 on the element originate from area and volume constraint forces arise from elastic properties of the membrane and cytoplasm of the cell. A lipid bilayer resists to expansion of its area, but only little to shear forces, which can be expressed by the force magnitude:

$$F_T = k_{mem}(A - A_0). \quad (\text{B.6})$$

Here k_{mem} is the area compression stiffness and A_0 , A are the reference and the current surface areas of the cell, respectively. These can be obtained by summing all the individual triangle areas, i.e. $A = \sum_k a_k$ of the cell surface, where a_k is the surface area of a triangle T_k . Note that A_0 is not necessarily constant as the cell can grow. The direction of the force \mathbf{F}_{T_k} is from the barycenter of each triangle's plane outwards [Odenthal et al., 2013].

The bending resistance force in Eq. 2.35 from the cortex is incorporated by the rotational resistance of the hinges determined by two adjacent triangles $T_1 = \{ijk\}$ and $T_2 = \{ijl\}$, see Fig. B.1B. This permits definition of a bending moment M :

$$M = k_b \sin(\theta - \theta_0) \quad (\text{B.7})$$

where k_b is the bending constant, and θ is determined by the normals to the triangles $\mathbf{n}_\alpha, \mathbf{n}_\beta$ by their scalar product $(\mathbf{n}_\alpha \mathbf{n}_\beta) = \cos(\theta)$. θ_0 is the angle of spontaneous curvature. The moment M can be

transformed to an equivalent force system $\mathbf{F}_{m,z}$ ($z \in \{ijl\}$) for the triangles T_1 and T_2 where here for T_1 we can compute $\mathbf{F}_{m,i} = M/l_1 \mathbf{n}_1$ using l_1 as the distance between the hinge of the triangle pair and the point i , and similar expression for $\mathbf{F}_{m,l}$. The forces working on nodes j, k must fulfill $\mathbf{F}_{m,i} + \mathbf{F}_{m,j} + \mathbf{F}_{m,k} + \mathbf{F}_{m,l} = 0$ to conserve total momentum.

The linear spring constant for a sixfold symmetric triangulated lattice can be related approximately to the cortex Young modulus E_{cor} with thickness h_{cor} by [163]

$$k_{cor} \approx \frac{2}{\sqrt{3}} E_{cor} h_{cor}. \quad (\text{B.8})$$

The bending stiffness of the cortex is in the same way approximated by

$$k_b \approx \frac{E_{cor} h^3}{12(1-\nu^2)}, \quad (\text{B.9})$$

where ν is the Poisson's ratio. The parameter k_{mem} for area conservation forces in the membrane is related to the area compression modulus K_A by

$$k_{mem} \approx K_A / d_0 \quad (\text{B.10})$$

with $d_0 = \|\mathbf{r}_{0,j} - \mathbf{r}_{0,i}\|$ the equilibrium length of triangle edge. For more details on relating the spring force parameters to macroscopic constants, we refer to literature [123, 288].

The volume change forces of the cell in Eq. 2.35 depends on the applied pressure and the cell compressibility K_V . The compressibility of the cell depends on volume fraction of water in the cytosol, the CSK volume fraction and structure, and the compressibility of the organelles. In addition, it may be influenced by the permeability of the plasma membrane for water, the presence of caveolae [245], and active responses in the cell. We calculate the internal pressure in a cell by the logarithmic strain for volume change:

$$p = -K_V \log\left(\frac{V}{V_0}\right), \quad (\text{B.11})$$

whereby V is the actual volume and V_0 is the reference volume i.e., the volume of the cell not subject to compression forces. For small deviations of V from V_0 , $p \approx K_V(V - V_0)/V_0$. Within our model the volume V of the cell is computed summing up the volumes of the individual tetrahedra that build up the cell. The force $F_{vol,i}$ on face i is obtained by multiplying the pressure with the area of the triangle i whereby the orientation of the force is identical with the outwards pointing normal on the triangle if the force is positive, and in opposite direction if the force is negative. The force on a node is calculated by a weighted sum of the forces on the triangles touching that node.

Eq. B.11 expresses isotropic compression only. As $K \gg E_{cor} h_{cor} / R_{cell}$, K controls the overall compressibility of the cell.

In case the internal CSK was explicitly represented by internal structural elements not considered in the simulations of this work, those elements would contribute to both volume compression and shear forces.

B.1.2 Maugis-Dugdale contact model

An interaction between two cells defines several pairwise triangle-triangle interactions (T, T'). We first locally estimate the curvature of every triangle from the location of its neighboring points. For every triangle a circumscribing sphere can be defined. One pair of interacting triangles defines two circumscribing spheres (C_1, C_2) and a common plane to which these triangles are projected (Fig. B.2B, dashed red line). The local stress which depends on the curvature of both spheres and the adhesion energy, can then be computed using the Maugis-Dugdale stress. The total interaction force between a pair of triangles is obtained by integrating this stress on the area common to both projected triangles using standard Gauss quadrature rules [Smeets et al., 2014].

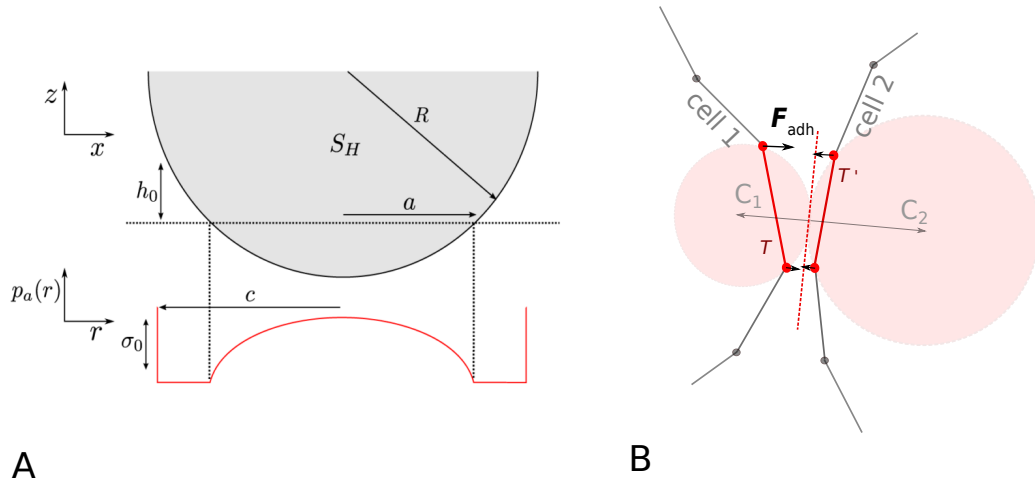


FIGURE B.2: (A) Maugis-Dugdale stress profile in a contact between a sphere and a plane (taken from [Odenthal et al., 2013]). (B) 2D Schematic representation of two triangles from different cells in contact. Each triangle defines a circumscribing sphere.

In the Maugis-Dugdale model, local adhesion tension is assumed to be independent of the overlap until a cut-off distance h_0 . If the asperity is further than h_0 away from the flat surface, the adhesive tension drops to zero. This is illustrated in Fig. B.2A where a sphere with radius R approaches a flat surface. The adhesive stress in a point in the contact zone as a function of the distance r to the contact center is given by:

The local stress which depends on the curvature of both spheres and the adhesion energy, can then be computed using the adhesive Maugis-Dugdale stress formula component:

$$p_a = \begin{cases} -\frac{\sigma_0}{\pi} \arccos\left(\frac{2a^2 - c^2 - r^2}{c^2 - r^2}\right) & \text{if } 0 \leq r \leq a \\ -\sigma_0 & \text{if } a \leq r \leq c \end{cases} \quad (\text{B.12})$$

In this formula, r is the distance from the contact point, a is the effective contact radius (pure Hertz contact) and c is the radius of the adhesive zone (see Fig. B.2A). We first compute the Tabor coefficient [289]:

$$\lambda = \sigma_0 \left(\frac{9\hat{R}}{2\pi W \hat{E}^2} \right)^{1/3} \quad (\text{B.13})$$

where \hat{E} and \hat{R} are the reduced elastic moduli and radii of the two objects in contact¹. The tension σ_0 is the maximum adhesive tension from a Lennard-Jones potential and is related to the adhesion energy W by $W = h_0 \sigma_0$. Here h_0 is the typical effective adhesive range that reflects the attractive cut-off distance between the bodies. We set $h_0 = 2 \cdot 10^{-8} \text{m}$ in all the simulations [219]. Following, the c can be computed from $m = c/a$ with:

¹ \hat{E} is given a large value compared to the cell Young modulus to prevent inter-penetration of triangles

$$\frac{\lambda}{2} \left(\frac{a^3 \hat{E}}{3\pi W \hat{R}} \right)^{2/3} \left[(m^2 - 2) \sec^{-1} m + \sqrt{m^2 - 1} \right] \quad (\text{B.14})$$

$$+ \frac{4\lambda^2}{3} \left(\frac{a^3 \hat{E}}{3\pi W \hat{R}} \right)^{2/3} \left[(m^2 - 2) \sec^{-1} m - m + 1 \right] = 1. \quad (\text{B.15})$$

The repulsive part is given by the Hertz pressure:

$$p_r = \frac{2\hat{E}}{\pi\hat{R}} \sqrt{a^2 - c^2} \quad (\text{B.16})$$

The total stress distribution between the two sphere is thus $p_a + p_r$. The total interaction force $\mathbf{F}_{adh,i} + \mathbf{F}_{rep,i}$ between a pair of triangles is obtained by integrating this stress on the surface area common of the two triangles that are projected on the contact plane using standard Gauss quadrature rules [Smeets et al., 2014]. Once this force is known, it is distributed onto the nodes of both triangles, with the force on the first triangle opposite in sign to the one of the second to conserve the momentum.

B.2 Deformable Cell Model: growth, division, and death

During progression in the cycle, a cell grows by acquires dry mass and water, eventually doubling its volume. The inter-phase adding up the G_1 , S and G_2 phase and mitosis phase may be described by an increase of the radius of the cell. We assume here that for a cell in free suspension during every the growth stage, the reference volume of the cell V_0 gradually increases and is updated according to:

$$V_0(t + \Delta t) = V_0(t) + \alpha \Delta t, \quad (\text{B.17})$$

where α is the growth rate for simplicity assumed to be constant during the cycle, which can be justified if we look at timescales much larger that one cell division. α is chosen such that the volume of a cell doubles in the experimentally observed cell cycle duration.

Cell growth: During cell growth, the volume of the cell is increasing (Fig. 2.6A-B). We model this by a simultaneous update of the reference volume V_0 following Eq. B.17, the reference values of the cell surface area, and those of the spring constants. The reference triangle area A_0 for each triangle, and spring length for each viscoelastic element are recomputed every timestep Δt according to $A_0(V_0(t + \Delta t)/V_0)^{2/3}$ and $l_0(V_0(t + \Delta t)/V_0)^{1/3}$, respectively. The coordinated update of V_0 , A_0 and l_0 is necessary to ensure that no additional volume penalty forces or other artifacts are generated during growth. Note that at this moment, growth inhibition due to excessive external mechanical stress (e.g. [114]) can be easily included in our model, but in the scope of this paper we do not consider it further.

Cell death: When a cell dies, it can be either removed instantly from the simulation, or gradually shrink (lysis). Algorithm-wise, lysis can be regarded as the inverse of the growth process. However, during lysis the mechanical parameters of the cell may change. The process may continue until a certain cell volume has been reached, below which the cell cannot longer shrink. Finally, a lysed cell may be removed completely from the simulation (by e.g. phagocytosis).

Cell division: During cytokinesis, the continuous shrinking of the contractile ring, together with the separation of the mitotic spindle, gradually creates the new daughter cells. After mitosis the cell has split up in two adhering daughter. Such a process of cell division in 2D deformable cells has been previously described (e.g. [120]). In a first attempt we implemented such an algorithm in 3D but it turned out to be prone to numerical instabilities in 3D, as triangles on the side of the contractile ring tended to be extremely stretched while nodes accumulated at the position of the contractile ring. Hence, numerically stable simulation of these processes in DCM would require a complex re-meshing process for the surface in 3D, leaving the local stresses unchanged but avoiding numerical instabilities.

An implementation of these steps turned out to be not only challenging, but also computing time consuming.

As we are merely interested in long term effects (i.e. several hundreds of cell divisions), and as the cytokinesis is a short process compared to the duration of the entire cell cycle, we avoid these particular tedious intermediate steps in our model, and directly create two new adhering cells that are within the shape of the mother cells just before its division as pictured in Fig. 2.6.

First, a division plane is chosen, which determines the direction into which the cells divide. The label of the division plane on the surface of the mother cell can be associated with the position of the contractile ring. The orientation of this plane may be chosen randomly or into a preferred direction, and splits the mother cells into two halves each bounded by part of the surface of the mother cell and the division plane (see Fig. 2.6B-C); note that the mother cell in the figure is spherically shaped, but the algorithm works for arbitrary cell shapes). Then, the centers of the two future daughter cells on both sides of the plane are computed as the two centers of mass of the nodes that form each of the two halves, and each of those two centers of mass is associated with the center of a new spherically shaped daughter cell (Fig. 2.6C). The radii of the daughter cells are chosen such that they are both contained by the mother cell. To ensure the daughter cells are not overlapping at this stage, those nodes that would overlap the division plane are projected back on the division plane. Each of the daughter cells has now as border approximately a half of the mother cell envelop and the division plane that it shares with the other daughter cell. At this stage however, the radii (and volumes) of the daughter cells are not yet those they each should have, i.e. half of the volume of the mother cell.

To achieve this, a *sub-simulation*² is performed where the volume and strut lengths of the viscoelastic network are reset to their reference values for a cell half the size of the mother cell. During the sub-simulation we artificially set all friction coefficients of the daughter cells to very small values. This will “inflate” the two daughter cells rapidly. On the other hand, we momentarily freeze the positions of the nodes of the mother cell. As a consequence, the two cells will rapidly adapt their shapes to the limiting shape of the mother cell “cocoon” and the division plane. The repelling interactions between the triangulated envelop of the mother cell and daughter cells ensure that the latter stay inside. We thus arrive at this step at a system of three triangulated cells: one fixed mother cell, and two encapsulated daughter cells with forming a shape approximately that of mother cell just before cell division.

After the sub-simulation, all the friction coefficients are reset to their normal values, the division plane is discarded and the daughter cells start adhering to each other because the mutual adhesion forces are invoked. The mother cell envelop is removed from the simulation and the daughter cells interact again with their environment. The system can relax slowly towards a mechanical equilibrium Fig. 2.6D over a time span equal to the mitosis phase duration.

B.3 Optical stretcher: DCM parameter determination

In a first consideration we identified some parameter and/or their ranges by comparison to published references. An initial spherical deformable cell was created with a total of $N = 642$ nodes (test runs indicated that further spatial refinement was not required). The cells were immersed in a medium with viscosity μ being close to that one of water. We approximate the cell-medium friction coefficients for each node needed to determine friction term in Eq. (2.35) by $\gamma_{ns} = \gamma_{liq}/N = 6\pi\mu R/N$. This approximation ensures that for a spherical cell of radius R modeled by N nodes at its surface, the friction coefficient is precisely as predicted by the Stokes equation. For viscosity μ the water viscosity has been chosen.

Determination of the elastic force terms in Eq. 2.35 requires that we know the elastic modulus of the cell cortex. Because we did not have information on the elastic properties of the MDA-MB-231

²A sub-simulation means that it runs in parallel and does not add up to the total simulation time (time is kept constant). The duration of a sub-simulation is very short, of the order of 10s.

cells, we adopted a nominal value for the elastic modulus of the cell cortex $E_{cor} \sim 1$ kPa based on different cell types ([255, 213]). Applying Eq. B.8 and Eq. B.9 (see section on Methods), which relate the elastic moduli to the parameters of the coarse grained model of the CSK, the nominal cortical stiffness constants in the model are thus $k_s \sim 4 \cdot 10^{-4}$ N/m, $k_b \sim 1 \cdot 10^{-17}$ Nm (see section B.1, Eq. B.1 and Eq. B.9) To determine the compression force of the cell represented in Eq. (2.35), we assume the cells are compressible with a compression modulus of $K = 2500$ Pa [255]. However, varying this value in the simulations for the optical stretcher, we did not find any significant influence on the results during the time course of the experiment when it was varied within 1000 Pa to 10000 Pa.

The area correction term of Eq. (2.35) represents the effect of the bilayer compression modulus K_A (see Eq. B.6). For pure lipid bilayers about 0.2 N/m have been reported, while in case of a plasma membrane of a cell, much lower values have been measured, likely due to invaginations and inclusions of other molecules in a regular cell membrane. In our model, we chose $K_A = 0.8$ mN/m [213].

In the work of Ananthakrishnan et al. (2005) [211] it was suggested that the cortical actin cytoskeleton is the main component determining the mechanical behavior of the cell. We followed this assumption in this work, yet in order to simulate the experiment, we need know the applied surface force vectors on each node generated by the deflecting laser beams (see Fig. 4.1B). The calculation of this force profile is described in section B.5.

In a second step we identified the type of the viscoelastic elements connecting the surface nodes of the model cells (Fig. 4.2D) by comparing the results of the model simulations with those of the optical stretcher experiments with MDA-MB-231 cells.

In an iterative procedure, elements of increasing complexity have been considered. The characteristic relaxation behavior excludes purely elastic springs (Fig. 4.2). Next we considered Kelvin-Voigt elements (KVE) between the surface nodes (Fig. 4.2D). Kiessling et al. (2013) [212] reported thermoelastic phenomena, whereby an increased laser power causes a transient temperature rise, which in turn modifies the viscoelastic properties of the cell. A thermal analysis of the used setup similar as in [212] indicated an ambient temperature increase from 20 K to 25 K for a laser power from 900 mW to 1100 mW. The temperature rise and fall is very quick ($\sim ms$) in comparison to the duration of the experiment, hence latency effects can be neglected. Because of the thermoelastic effects, we assumed in the model that the viscous properties (i) are changed by the laser power during the stretching stage to (i.e. $\gamma = \gamma(T)$), and (ii) are all restored to their original value during release. A good fit for the $P = 1100$ mW was achieved by the values $k_s = 1.0 \cdot 10^{-4}$ N/m, $k_b = 2 \cdot 10^{-17}$ Nm as cortex elastic constants (close to the nominal values), $\gamma_{||} = \gamma_{\perp} = \gamma(T_0) = 2.3 \cdot 10^{-4}$ Ns/m as nominal friction coefficient (see Fig. 4.2A) and by a temperature dependence of the friction coefficients of $\gamma(310)/\gamma(T_0) = 0.29$ and $\gamma(315)/\gamma(T_0) = 0.11$. The fitted elastic constants for the springs and bending thus correspond well to those obtained from the nominal material properties (see above). We then tested the assumption that the viscosity would scale with temperature as in the Arrhenius law [212]:

$$\frac{\gamma(T)}{\gamma(T_0)} = \exp\left(\frac{E_a}{R} \left(\frac{1}{T} - \frac{1}{T_0}\right)\right), \quad (\text{B.18})$$

where $R = 8.314$ Jmol⁻¹K⁻¹ and $T_0 = 290$ K. Using this equation we got an optimal fit with the model calibrated friction coefficients (see Fig. 4.2C) using the value $E_a = 55$ KJmol⁻¹K⁻¹, which is not too far to $E_a = 74$ KJmol⁻¹K⁻¹ derived in [212]. Neglecting thermoelastic effects, no simultaneous fit of the experimental results for both laser powers could be obtained: if the KVE model is calibrated such that an optimal fit is obtained for $P = 1100$ mW, then using the same constants we get a significant overestimation of the deformation for $P = 900$ mW, and vice versa (result not shown).

An optimal fit for the MME model with $P = 1100$ mW was now achieved using the elastic constants $k_s = 5 \cdot 10^{-4}$ N/m, $k_b = 2 \cdot 10^{-17}$ Nm, but with $\gamma(T_0) = 3 \cdot 10^{-5}$ Ns/m and $\gamma_{ME}(T_0) = 3 \cdot 10^{-3}$ Ns/m as overall damping parameter and for the Maxwell damping respectively (Fig. 4.2B).

B.4 DCM parameters and CBM contact force calibration

A small cell clump is used as *in silico* model to estimate the contact forces and relaxation in a cell aggregate. We note that this method is here conceived for relatively small forces and we don't adapt the volume or radius of the cells during slight compression. For high pressure forces as in the spheroid compressed by a capsule (chapter 5) this needs to be more elaborated (see Appendix C.1.5). We consider a central cell neighbored by several others initially structured as a body centered cubic (Fig. B.3A). The cell clump is then positioned in a imaginary rigid spherical capsule. The radius of the capsule is steadily and step-wise decreased, compressing the cells inside (Fig. B.3A). The average distance between the central cell and its contacting cells is computed as $d_{ij} = 1 - d_{ij}/(R_i + R_j)$ at every timestep. This results in a forces-distance relation during the time course of compression that is used to calibrate the contact forces in the center-based model. In Fig. B.3B we have displayed the average force-distance relation during the experiment. The contact force in the center-based model shows a clear deviation as the distance gets smaller. This clearly shows that JKR or Hertz contact force models do not apply for high cell densities in CBM. To correct this, we keep the original JKR contact law form but modify the apparent modulus $E_i \rightarrow \tilde{E}_i$ of the cell as the cells approach each other, by gradually increasing it in Eq. 2.8 as the cells get more packed. The challenge lies in determining \tilde{E}_i as a function of the compactness of the spheroid. We try to estimate the degree of packing around one cell by using the distances between that cell and its neighbors, introducing a function that depends on the *local* average of the distances $d = \sum_j d_{ij}/N$ (N is the number of contacts) to each of the contacting cells j , noticing that the cell-cell distances differ only very slightly. The simulated force curves of the DCM could well be reproduced with the CBM for the following simple polynomial function of 4th order:

$$\tilde{E}_i(d_i) = a_0 + a_1 \tilde{d}_i^4 \quad (\text{B.19})$$

in where $a_0 = E_i$ and, a_1 is a fitting constant. The best fit to the DCM contact force is shown in Fig. B.3A, with $a_1 = 4 \cdot 10^6$.

The full relaxation behavior of the spheroid is determined by the nodal friction coefficients, the viscous friction of the adherent cells, and the friction with the ECM. To measure relaxation, the cells are suddenly released from the encapsulation. This period for the cells to come back to their original state is a measure for the relaxation time of a spheroid, and is used to calibrate the friction coefficients. The relaxation state is quantified by a strain function measuring again the average distance function d between the cells as a function of time. This is depicted in Fig. B.3C. We choose the optimal friction coefficients so that the cell clump has a relaxation time of $\sim 5h$ as mentioned in [224, 223]. A model run with 5 times higher and 20 times friction is depicted to show a significant increase of relaxation times.

B.5 Estimation of the surface forces on a cell during the optical stretcher experiment

Here, we give explain how the nodal forces on the cell are calculated from the optical laser beam. Therefore, we closely follow the approach detailed in [209]. The cells pass the optical stretcher experimental setup in suspension. The radius of the Gaussian laser beam is $R_{beam} = 8.2 \mu\text{m}$ [210]. We can assume a ray optics approach, since the wavelength of the laser light, $\lambda = 1064\text{nm}$ is much smaller than the diameter of our optical particles ($\approx 17\mu\text{m}$).

Assume first a cube-like object which obstructs in the laser beam path. The laser beam enters the cube at the front side and leaves it at the back side. The incident momentum of the laser $p_i = nE/c$ (E is the energy of the incoming beam, n is the refractive index and c is the speed of light), needs to be conserved at the interfaces of the medium with the cube. The surface picks up the difference of

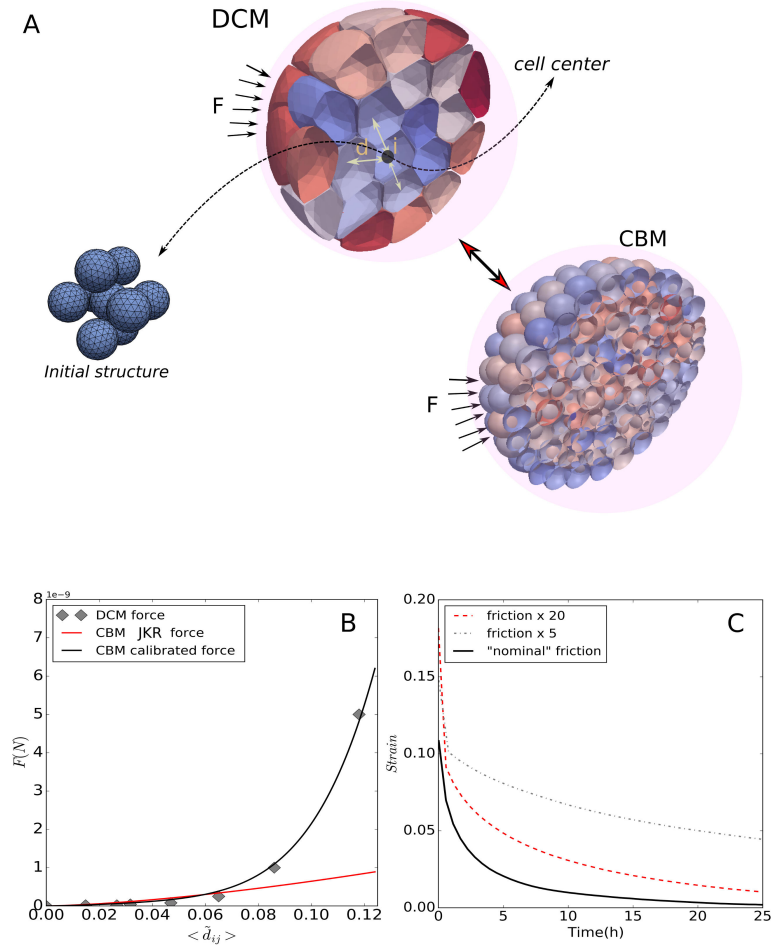


FIGURE B.3: (A) Snapshot of a simulation of a small cell clump of DCM being compressed by isotropic forces. The distance d are computed between the cell centers and averaged. The equivalent CBM simulation is depicted below. (B) Force-distance data for a compression experiment simulated with DCMs, CBMs with using the JKR contact model, and CBMs using the calibrated contact model. (C) Simulated relaxation curves of a small spheroid performed with DCMs assuming different friction coefficients.

momentum $\Delta p = p_{incident} + p_{reflected} - p_{transmitted}$ between the incident ray and the transmitted ray through the cube.

A resulting optical force acting due to momentum transfer for the frontal cube side is calculated using the Fresnel formulas and Newton's second law [209]:

$$F = \frac{\Delta p}{\Delta t} = \frac{n_m \Delta E}{c \Delta t} = \frac{n_m Q P_0}{c}, \quad (\text{B.20})$$

where E is the energy of the photons, c the speed of light, n_m is the refractive index of the medium. The factor Q represents the transferred momentum ($Q = 2$ for total reflection, $Q = 1$ for total absorption) and total P_0 is the incident power. The same formula needs to be applied to the laser beam leaving the cube to the medium. The total force on one side of the cube at the laser axis due to the presence of two lasers in opposite direction can thus be calculated by summing up the transferred

momenta at one side [290, 209]:

$$F_{total} = F_{front} - F_{back} \quad (\text{B.21})$$

$$= \frac{n_m Q_{front} P_0}{c} - \frac{n_c Q_{back} P_0}{c} \quad (\text{B.22})$$

$$= [n_m - (1 - \mathcal{R})n_c + \mathcal{R}n_m] \frac{P_0}{c} - [n_c - (1 - \mathcal{R})n_m + \mathcal{R}n_c] (1 - \mathcal{R}) \frac{P_0}{c}. \quad (\text{B.23})$$

where n_c is the refractive index of the cube. The reflection \mathcal{R} can be neglected for small incident angles, since according to the Fresnel Equation:

$$\mathcal{R} = \frac{(n_c - n_m)^2}{(n_c + n_m)^2} = 1.24 \cdot 10^{-4} \approx 0. \quad (\text{B.24})$$

Hence the total force on the cube interface simplifies to:

$$F_{total} = (n_m - n_c) \frac{2P_0}{c}. \quad (\text{B.25})$$

This force acts always perpendicular to the object opposed to the incoming laser light. The applied stress in the direction of the laser beam on the cube is thus:

$$\sigma_0 = (n_m - n_c) \frac{2P_0}{\pi R_{beam}^2 c}. \quad (\text{B.26})$$

For $n_m = 1.33$, $n_c = 1.36$, $P_0 = 1.1\text{W}$ and $c = 3 \cdot 10^8 \text{ m/s}$, we find $\sigma_0 = 1.05 \text{ Pa}$.

Within our model we need the applied stress for each triangular surface segment. However, the forces due to the laser beam are not equally distributed over the cell, as the cell is not a cube but has a spherical-like shape and the incident angle is not zero anymore but varies along the cell surface. A realistic overall stress profile can be assumed to be approximated by $\sigma(\alpha) = \sigma_0 \cos^n \alpha$ with amplitude σ_0 and fitting parameter n [291]. Here, α is the angle between the laser axes and the nodal position of the cell (see Fig. 4.1C). To determined the parameter n , we evaluate the ratio of the laser beam radius and cell radius:

$$\rho = \frac{R_{beam}}{R_{cell}} = \frac{8.2\mu\text{m}}{8.8\mu\text{m}} = 0.93 \quad (\text{B.27})$$

For a ratio of $\rho \approx 1$, n fits best when set to 2 (see e.g. [290, 209, 291]). As we know how much surface area A_n each node on the cell represents, we can now calculate the forces on the DCM nodes by $F_L(\alpha) = A_n \sigma(\alpha)$, where $F_L(\alpha)$ is oriented perpendicular to the cell surface at that node (Fig. 4.1C).

B.6 Table with model parameters

Parameter	symbol	unit	value	ref
Deformable Cell Model				
Radius (undeformed)	R_c	μm	8.8 – 12	observation, [8]
Cycle time*	τ	h	24	[8]
Cortex Young's modulus	E_{cor}	Pa	1000	[213]
Cortex thickness	h_{cor}	nm	500	observation
Cortex Poisson ratio	ν_{cor}	-	0.5	[255]
Membrane area compression	K_A	N/m	$0.8 \cdot 10^{-3}$	[213]
Cell bulk modulus	K_V	Pa	750 – 2500	[8], [255]
Cell-cell adhesion energy	W	J/m^2	$10^{-5} - 5 \cdot 10^{-5}$	[8],CR
Nodal friction	γ_{int}	Ns/m^3	$1 \cdot 10^{-4}$	CR
Cell-cell friction	γ_{ext}	Ns/m^3	$5 \cdot 10^{10}$	[19, 77],CR
Cell-ECM friction	γ_{ECM}	Ns/m^3	10^8	[19],CR
Cell-liquid friction	γ_{liq}	Ns/m^3	500	CR
Motility	D	m^2/s	10^{-16}	[114, 8]
Center Based Model				
Radius (free suspension)	R_c	μm	12	[8]
Young's modulus*	E	Pa	450	[8]
Poisson's modulus	ν	-	0.47	see K_V , [8]
Cell-cell friction	γ_{ext}	Ns/m^3	10^{10}	[19, 77],CR
Cell-ECM friction	γ_{ECM}	Ns/m^3	$5 \cdot 10^8$	[19],CR
Motility	D	m^2/s	10^{-16}	[114, 8]
Cell-cell adhesion energy	W	J/m^2	$10^{-5} - 5 \cdot 10^{-5}$	CR
Lobule network				
Radius lobule	R_{lob}	μm	280	[8]
Radius portal veins	R_{pv}	μm	15	[8]
Radius central veins	R_{cv}	μm	10	[8]
Radius sinusoids	R_{sin}	μm	4.7	[8]
Sinusoids Young's modulus	E_{sin}	Pa	600	[8]
Sinusoids Poisson's modulus	ν_{sin}	-	0.4	[8]
Cell-sinusoid adhesion energy	W	J/m^2	0	[8]
Radius lesion	R_{nec}	μm	150	[8]

TABLE B.1: Nominal physical parameter values for the model. An (*) denotes parameter variability meaning that the individual cell parameters are picked from a Gaussian distribution with $\pm 10\%$ on their mean value. CR : Calibration Runs.

Appendix C

Modeling stress response spheroids: model components and parameter calibration

This appendix contains the details of the methods that were used in chapter 5.

C.1 Models

C.1.1 CBM volume and compressibility

In our CBM, cells are compressible meaning that cell volume is related to pressure by

$$dp_i = -K_i \frac{dV_i}{V_i} = -\frac{E_i}{3(1-2\nu)} \frac{dV_i}{V_i}, \quad (\text{C.1})$$

in case the cells' properties are largely controlled by the elastic properties of its cytoskeleton and other cytoplasmic constituents. K_i is the bulk modulus of the cell. The observed volume change in general depends on the speed of compression. For slow compression, water can be squeezed out of cells (and tissues), while for fast compression, it would result in nearly incompressible resistance [254]. In case $K_i = K_{0,i}$ is a constant, integration of the above equation yields the cell volume V_i as a function of the pressure on cell i , $\epsilon_{V,i} = (p_i - p_0)/K_{0,i}$ with $p(V_{ref}) = p_0$. Here, $\epsilon_{V,i} = -\log(V_i/V_{ref,i})$ is the logarithmic strain permitting to capture large strains and $V_{ref,i} = 4/3\pi R_{ref,i}^3$ is the uncompressed cell volume the cell would have in isolation, with $R_{ref,i}$ being considered as constant for a quiescent cell. For small deviations $V \approx V_{ref}$ the known relation $\epsilon_V = \log(V/V_{ref}) \approx (V - V_{ref})/V_{ref}$ is recovered.

Several authors have reported strain hardening effects leading to an increased elastic modulus upon mechanical stress [292, 293, 294]. Stiffening of the cells can occur as the cytoskeleton gets denser [163]. In case of strain hardening, K increases with decreasing volume. We mimicked this by [163]:

$$K_i(V_i) = K_{0,i} \frac{V_{ref,i}}{V_i}, \quad (\text{C.2})$$

with $K_{0,i}$ the compression modulus of cell i in absence of stress. In this case, $\epsilon_{V,i} = \log((p_i - p_0)/K_{0,i} + 1)$. The quantity of interest is the volume response on a pressure change $p_i - p_0$, whereby throughout this paper we set $p_i \equiv p_i - p_0$.

Now we assume that as a consequence of internal friction and by remodeling of the cytoskeleton, a cell subject to pressure adapts its volume with a certain delay according to the equation

$$\gamma_{int,i} \frac{d\epsilon_{V,i}}{dt} + K_{0,i} \epsilon_{V,i} = g(p_i), \quad (\text{C.3})$$

where $\gamma_{int,i}$ is a lumped parameter expressing the relaxation behavior after an imposed change of the pressure. It is related to the relaxation time by $\gamma_{int,i} = K_i T_{rel}$ for a single cell (an analogous argument

applies to the whole spheroid). The relaxation period may range from several seconds or minutes up to hours, depending on how long the stress has been applied [295, 223, 236]. This is related to both intracellular and intercellular reorganizations. In our simulations, we assume $T_{rel} \sim O(1h)$ for viable cells motivated by observations of relaxation times in compression experiments [224]. For $K_i = K_{0,i}$ we have $g(p_i) = p_i$, while in case of a dependency as by Eq. C.2 it is $g(p_i) = K_{0,i} \log(p_i/K_{0,i} + 1)$.

C.1.2 CBM Measures for stress and pressure

The external pressure p_i on a cell i is derived from the viral stress and given by:

$$p_i = \frac{1}{3} \text{tr}(\sigma_i) \text{ with } \sigma_i = \frac{1}{\mathcal{V}_i} \sum_j (\mathbf{F}_{ij} \otimes \mathbf{r}_{ij}) \quad (\text{C.4})$$

being the stress tensor quantifying the stresses cell i experiences subject to contact forces \mathbf{F}_{ij} with other cells j [Van Liedekerke et al., 2015]. Here, \mathbf{r}_{ij} is the vector pointing from the center of cell i to the cell j with $\|\mathbf{r}_{ij}\| = d_{ij}/2$ and \mathcal{V}_i is the *sampling* volume which can be taken as the cell volume. The stress tensor can be diagonalized in order to find the principal direction of stress.

C.1.3 CBM Cell growth, mitosis, and lysis

Our basic model assumes constant growth rate during the cell cycle and updates the volume $V_{ref,i}$ of cell i in time as

$$\frac{dV_{ref,i}(t)}{dt} = \alpha_i(t), \quad (\text{C.5})$$

where $\alpha_i(t)$ is the growth rate. We studied both, a constant volume growth rate ($\alpha_i(t) = C_1$) and an exponentially increasing cell volume mimicked by $\alpha_i(t) = C_2 \times V_{ref,i}(t)$ [106, 107, 108, 109]. The cell cycle times in both cases are equal for $C_2 = \log 2 \times C_1 / V_{0,i}$. However, on the time scale (several days) of growth considered here, growth rate variations on time scales of an hour turned out to be negligible. After a cell has doubled its reference volume, it splits into two spherical cells (see the Appendix for more information).

Cells dying either by apoptosis or necrosis eventually undergo lysis. During lysis they gradually shrink. In experiment I the necrotic core appeared very solid like, indicating that the water was drained as a consequence of the high pressure. We mimic the lysing process by setting first $V_{ref,i} \rightarrow \phi V_{ref,i}$ after necrosis, where ϕ is the volumetric solid mass fraction.

The cell volume change rate is mimicked by Eq. C.3 and controlled by γ_{int} . This effectively mimics plastic deformation of the cells during water loss. We assumed that lysis times T_{lys} have a physiological range of 5h to 15 days [26], and we set $\gamma_{int} \sim KT_{lys}$ in Eq. C.3 during lysis.

C.1.4 Elastic Capsule Model

The capsule is made of an quasi-incompressible alginate gel exhibiting a strain hardening behavior. The stress-strains relationship was measured in a stretching experiment of an thin alginate cylinder. Strain hardening behavior was observed for strains $> 15\%$. In case of a thick walled capsule, the expansion strain is low and hence linear elasticity can be applied. We refer to the hollow sphere example as described in [296] to compute the radial displacement of the capsule from the internal pressure. If on the other hand the capsule has a thin wall, strains can become large, and the linear elasticity hypothesis fails. For this case, in line with ref. [242] the original young modulus is modified instead of employing nonlinear elasticity theory. The nonlinear relationship in stress and strain (ϵ_{cap}) was phenomenologically characterized in ref. [242]:

$$E_{cap} = E_{cap,0}(1 + a\epsilon_{cap}) \quad (\text{C.6})$$

where ϵ_{cap} is the strain and $a = 1.5$ to obtain an optimal fit with the experiment.

The capsules have an initial inner and outer radius $R_{in,0}$ and $R_{out,0}$ respectively, whereby typically $H = R_{out,0} - R_{in,0} > 0.2R_{in,0}$ for thick capsules, H being the capsule thickness. The pressure difference along the capsule wall can be related to the change in radii by [242]:

$$p_{cap} = \frac{4}{3}E_{caps}R' \frac{u(R_{in})}{R_{in}} \quad (C.7)$$

Where E_{caps} is the Young modulus of the capsule material, R_{out} is the outer radius, and $u(R_{in}) = R_{in} - R_{in,0}$ is the displacement at the outer radius. Furthermore, $R' = \left(1 + \frac{1}{1 + \Delta R_0^3 / R_{in}^3}\right)$, in which the outer radius is related to the inner radius R_{in} by $\Delta R^3 = R_{out}^3 - R_{in}^3 = R_{out,0}^3 - R_{in,0}^3$, assuming incompressibility of the elastic shell. To simulate the radius evolution of the capsule, one computes pressure p_{cap} by dividing the sum of all contact forces of the cells with the capsule by the actual inner surface area. Taking into account the damping by the alginate material, we arrive at an ODE, formally similar to Eq. C.3:

$$\frac{\gamma_{cap}}{R_{in}(t)} \frac{dR_{in}(t)}{dt} = p_{cap}(t) - \frac{4}{3}E_{caps}R' \frac{u(R_{in}(t))}{R_{in}}, \quad (C.8)$$

with a lumped material damping parameter γ_{cap} . It was shown in [224] that the viscosity of the capsule material is low and does not influence the much slower dynamics of the spheroid. Accordingly, in our model γ_{cap} was chosen low to reflect the material's ability to rapidly adapt to a change in spheroid radius while not affecting the slow growth dynamics.

C.1.5 Calibration of the CBM contact forces using DCM

During the process of compression, cells rearrange and deform to a closer packing. As discussed above, common models to model the interactions between cells (such as Hertz, JKR, extended Hertz, Lennard-Jones, etc.) base on pair-wise interaction force calculations and do not take into account the effect of volume compression emerging from the simultaneous interaction of many cells. In simulations using these interaction force models, the apparent volume (as seen in the simulation) that the spheroid occupies upon strong compression, may become much smaller than consistent with the material parameters; even incompressible cells having Poisson ratio $\nu = 0.5$ reduce their volume [Van Liedekerke et al., 2015, 89]. Simulations of spheroid growth in a capsule performed with an uncalibrated model result in an unrealistic capsule dilatation (see Fig. C.4).

The deformable cell model (DCM) does not suffer from such shortcomings, but is not amenable to the amount of cells observed in experiments I and II in reasonable computing time on standard desktop computers. For this reason we here chose a hybrid strategy: we corrected the interaction force in the CBM based upon numerical compression experiments performed with the DCM, and used the so calibrated CBM to perform simulations reminiscent of virtual computer experiments in the experimental settings I and II (Fig. C.1).

In order to estimate the repulsive contact forces in case of many cell contacts, we have constructed a DCM spheroid computer experiment with ~ 400 cells initially positioned in a closest sphere packing. In this computer experiment, the outer cells were then pushed towards the spheroid center quasi-statically to avoid friction effects, using a shrinking large hollow rigid sphere encompassing the cells (see Fig. C.1A). All cells have the same size but taking into account a moderate variable cells size were found to not affect the results significantly. Interestingly we observed in the calibration simulations, that cell shape of isotropic cells in the calibration compression simulations with the deformable cell model appear distorted near the capsule border in agreement with the shapes one would infer from the position of the cell nuclei in the capsule experiments [242].

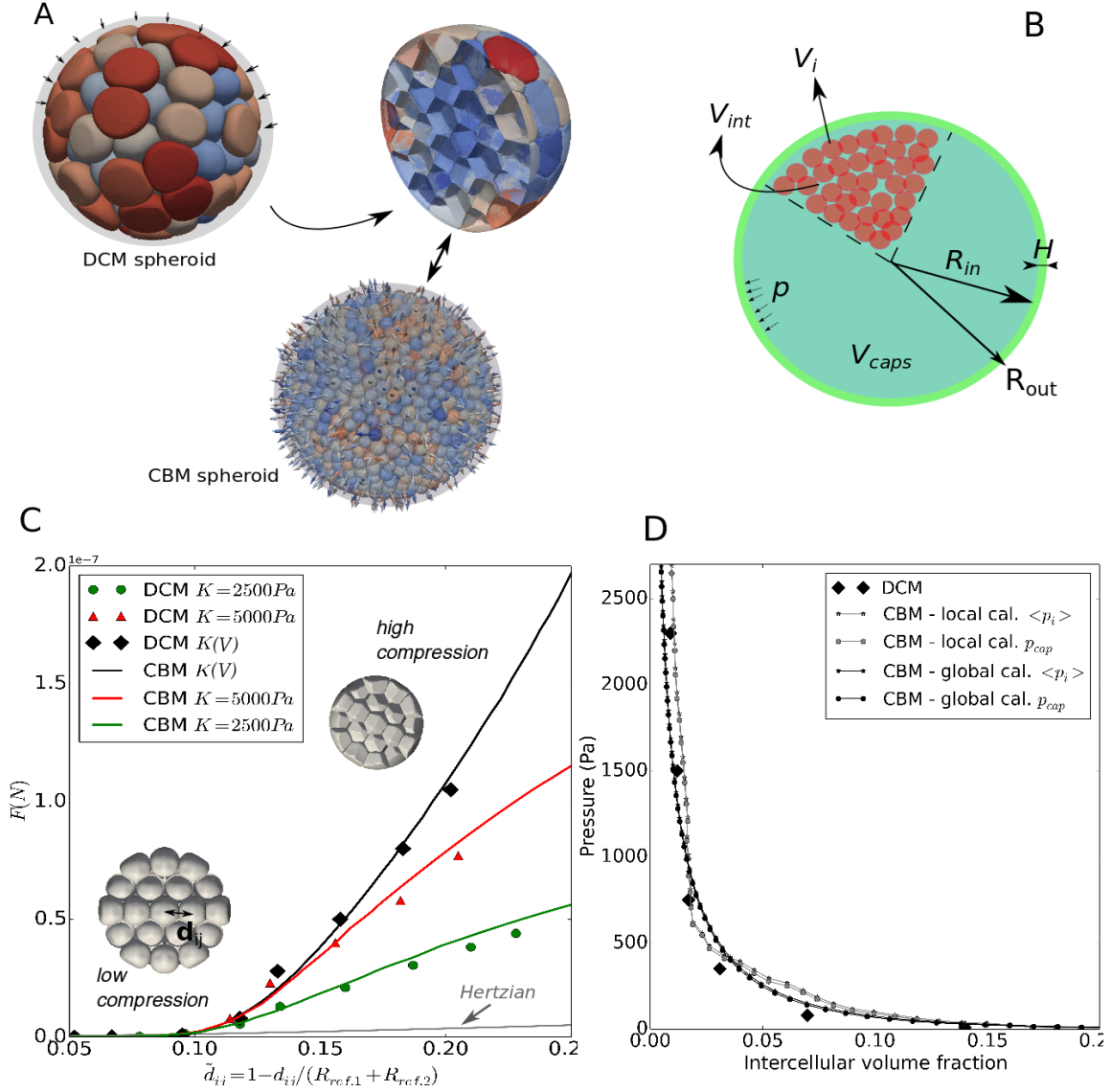


FIGURE C.1: (A) Cartoon illustrating the compression experiment using deformable cells in a capsule to calibrate the center-based model. (A, bottom) Equivalent compression experiment using the center-based model with indication of the maximal principal stress directions of the cells in the capsule during compression using Eq. (C.4). (B) Cartoon showing the volume compartments V_i , V_{int} and V_{caps} in a capsule with thickness H . (C) Average contact force vs. $\tilde{d}_{ij} = 1 - d_{ij} / (R_{ref,i} + R_{ref,j})$ for different K values simulated using DCM (diamonds), and CBM with corrected Hertz contact force (full colored lines) replacing E by \tilde{E} , see Eq. C.9. d_{ij} is the distance between the centers of cells i and j , $R_{ref,k}$ the radius of a free cell $k \in \{i, j\}$. The modified Hertz force shows the same evolution as the force in the DCM, while an uncorrected Hertz force (gray line) strongly underestimates the interaction force for strong volumetric compression. (D) Pressure curves during compression of the spheroid as a function of the inter-cellular volume fraction simulated with the DCM and the CBM with modified Hertz force. The pressure for CBM was computed using both the capsule pressure and average virial stress per cell calculated from Eq. C.4.)

"Local" calibration approach, needed for experiment II

For the DCM simulations we adopted $E_{cor} \approx 2400$ Pa, $h_{cor} \approx 100$ nm and $\nu_{cor} \approx 0.5$ [255] as fixed elastic properties of the cortex. The cortical stiffness $E_{cor}h_{cor} = 0.24$ mN/m, is close to values

deduced from other experiments performed on fibroblasts [297]. As the cell compression modulus K maybe variable and further plays a significant role in this work, we constructed the calibration method such that it works for different values of K .

During the simulated DCM compression experiment (Fig C.1A) we "measure" all the contact forces between a bulk cell i and the surrounding cells j in our simulation, which gives us the force, pressure and volumes change on that cell, as a function of their relative positions, $\tilde{d}_{ij} = 1 - d_{ij}/(R_{ref,i} + R_{ref,j})$. The distance d_{ij} is computed as the length of the vector connecting the two center of masses of the two cells i, j . $R_{ref,k}$ is computed as $(\frac{3}{4\pi}V_{ref,k})^{1/3}$, with $k = i, j$. The average contact force of the central cell i with its neighbors j as a function of the cell-to-cell average distance $\tilde{d}_i = \sum_{j=1}^{N_c} \tilde{d}_{ij}/N_c$ (N_c = number of contacts) is depicted in Fig. C.1C, for $K = 2500$ Pa, 5000 Pa, and a variable $K = K_0(V)$ using $K_0 = 5000$ Pa due to strain hardening. Overall we find that this contact force curve still can be characterized as initial Hertzian contact for $\tilde{d}_i < 0.08$, but is after a transition zone followed by a steep increase ($\tilde{d}_i > 0.12$). The first part in this curve is largely determined by the mechanical properties of the cortex and the changing contact area of the cells, whereas the behavior at larger compression is determined by the bulk modulus of the cells.

We have developed a CBM calibration approach where we keep the original Hertz contact law but replaced the Young modulus E_i by an apparent contact stiffness \tilde{E}_i (i.e., $E_i \rightarrow \tilde{E}_i$) of the cells as they get nearer to each other. In other words, \tilde{E}_i gradually increases in Eq. 2.5 as the cells get more packed, based on the reasoning that indenting a piece of material with another object gets more difficult when confined. The total strain of the cell is composed of a deformation of the cortex largely determined by the apparent stiffness \tilde{E}_i , and the volumetric compression determined by K_i . The volume (and radii) of the cells are adapted using Eq. C.3. It is important to stress here that \tilde{E}_i only reflects the contact stiffness of the cell through Eq. 2.5, while the bulk modulus (Eq. C.1) is determined by the original cell Young's modulus E_i .

To take into account the limited cell volume compressibility in a pairwise cell-cell interaction force, we fitted \tilde{E}_i by a function that depends on the local average distance \tilde{d}_{ij} for a bulk (i.e., interior) cell in the simulated experiment in Fig. C.1A:

$$\tilde{E}_i(\tilde{d}_i, K, E_{cor}, h_{cor}) = \begin{cases} E_i & 0 \leq \tilde{d}_i \leq 0.08, \\ a_0 + a_1\tilde{d}_i + \dots + a_6\tilde{d}_i^6 & 0.08 < \tilde{d}_i. \end{cases} \quad (\text{C.9})$$

Here, the a_k with $k \in [0, 6]$ are fit constants (see section C.3.1). They are calibrated such that the function is monotonically increasing and results in an optimal fit to the average force a cell i experiences upon compression of the cell aggregate (see Fig. C.1A) as function of the distance between the center of cell i and its neighboring cells j in the DCM simulations (see Fig. C.1C). The higher the compression, the higher gets the contact stiffness, so that at strong compression, the contact forces only result in a very small increase of indentation, yet the cell volume decreases (Eq. C.3).

At the point of confluence when outer cells touch the capsule wall, the DCM cells exert a total interaction force $F_{cap} = \sum_i F_{cap,i}$ on the capsule wall. The capsule pressure was then computed by $p_{cap} = F_{cap}/A_{cap}$ where A_{cap} is the inner surface area of the capsule. On the other hand we defined the intercellular volume fraction, as $\epsilon_{int} = V_{int}/V_{cap}$ (see Fig. C.1C). Here $V_{int} = V_{cap} - \sum_i V_{cell,i}$ is the volume of the space in between the cells, V_{cap} is the total capsule volume. We then compared for the DCM simulations and calibrated CBM the resulting pressure versus intercellular volume fractions. These curves do not match exactly, but follow each other closely (Fig. C.1D).

"Global" calibration approach, only valid for confined spheroid

The relationship between forces, inter-cellular volume fraction and pressure established in section C.1.5 can also be computed following a simpler, global approach in case of a confined volume as in experiment I. If compression rates are sufficiently slow as is the case in that experiment, the cells in the spheroid can reorganize, distributing the stress isotropically and homogeneously over the cells in

the spheroid. For the intercellular spaces in the capsule the *global* intercellular volume fraction ϵ_{int} and the cellular fraction ϵ_{cells} are related by $\epsilon_{int} + \epsilon_{cells} = 1$ with $\epsilon_{cells} = V_{cells}/V_{caps}$. We can now use ϵ_{cells} to re-parameterize Eq. C.9 assuming cells are homogeneously distributed over the spheroid during compression (compare Fig. C.1A). The apparent contact stiffness \tilde{E}_i in that case increases for all cells equally with ϵ_{cells} being the equivalent of $1 - \tilde{d}_{ij}$ in the previous approach.

With both different calibration methods, local and global, the CBM simulation results closely follow the DCM curve (Fig. C.1D; Fig. C.4C). However, the curve using the global calibration method is smoother than for the local calibration method as it represents an average over all cells thus disregarding local fluctuations. For high pressures ($p > 2$ kPa), both curves become nearly parallel. On the other hand, as the local approach does not require the existence of an enclosed (capsule) volume it can be used more generally as a cell-cell interaction force upon volumetric compression in many configurations as in experiment II.

We finally point out that no explicit representation of ECM has been considered in the model based on the observations the ECM fraction is rather small (personal communication) and approximately homogeneously and isotropically distributed in the intercellular spaces.

C.2 Model setup and parameter determination

We here explain the determination of the mechanical model parameters starting from the thin capsule experiment. A large fraction of the parameters are fixed from direct observations or published references, see Table C.2 for more details.

Within parameter sensitivity analysis simulations the parameters that could not be fixed by experimental observations, were varied within their physiological ranges to study their impact on the simulation results. Some parameters turned out to only negligibly affect the simulations results, see C.3.

As the simulation time was too long to determine the parameters within their physiological ranges based on a maximization of a likelihood function, or to perform a parameter identifiability analysis, we identified plausible parameters by a two-step procedure.

We first determined those model parameters that determine the simulated growth behavior in case of free growth by comparison to the experimental data for CT26 in experiment I. In the next step the parameters relevant for the specific experiment were fixed. After this, two remaining parameters, namely K and T_{lys} were calibrated by the thin capsule simulations, yielding a model without a growth rate adaptation (see C.2.3).

Each simulation result was compared to the experimentally observed spheroid diameter of the growing spheroid prior to confluence, and the slope of the residual growth curves after 48h, thereby retaining the parameters that are physically plausible and can best explain the data at the same time.

C.2.1 Cell-specific parameters $\{P_{C=j}\}$ to obtain the initial spheroid configuration and free growth

Starting from the calibrated model (step 1), a single run was performed with a small aggregate of 10 CBM cells, all at the beginning of their cell cycle, to grow a spheroid up to the size of $R = 100 \mu m$, which corresponds to the size before confluence, see Fig. 5.2B. A cell cycle time of $T_{cyc} = 17h$ was assigned to each of the cells as this matches the experimental observation. Cells increased their radius from $\sim 6 \mu m$ until their radius reached the division size ($7.5 \mu m$). After each cell division, a new cell cycle time was assigned to each of the daughter cells, randomly chosen from a Gaussian distribution with $\langle T_{cyc} \rangle = 17h$ and standard deviation of $\pm 10/\%$. The intrinsic free growth cell cycle time defines the growth rate $\alpha_0 = 1/T_{cyc}$.

The cell-cell adhesion energy W determines how close the cells approach each other in aggregates not subject to compression by external forces, and has been chosen such that the area density, measured in a cryosection of width $10 \mu m$ of the resulting spheroid with $R = 100 \mu m$, matches that of the

experiments ($\sim 0.85 / 100 \mu\text{m}^2$) [242]. In these simulations the cells have a fixed Young's modulus of $E \sim 450 \text{ Pa}$ and a cell motility coefficient D of $10^{-16} \text{ m}^2/\text{s}$ [114]. The compression modulus was here set to $K = 5 \text{ kPa}$ inferred as an average from values reported in literature, see Table C.2. For MCS grown in absence of external stress, K , if varied in the range of experimentally observed values, had no significant effect on the growth simulation results.

The physical parameters responsible for the inter- and intracellular friction are in the CBM represented by γ_{int} , $\gamma_{cc,\perp}$, $\gamma_{cc,\parallel} \in \{P_{C=j}\}$. Mechanical relaxation time of spheroids compressed over a longer time period indicate relaxation times of 1 to 5 hours in experiments [223, 224]. We have calibrated the friction parameters in the model from a relaxation experiment starting from a compressed spheroid (see Fig. C.1A) such that $T_{rel} \sim 2 \text{ h}$, lying well in the reported range $[1h, 5h]$, was obtained using as observable the spheroid size as function of time. The calibrated coefficients correspond to those found in [19, 77].

The parameter set as determined above resulted in a good agreement for free growth simulation with data from experiment I. The model robustness was finally tested by varying these parameters to see how they affected the simulation results of the thin capsule (see section C.3).

C.2.2 Experiment specific parameters $\{P_{EXP}\}$

Here, we determined the parameters that are exclusively related to the experiments. See Table C.2 for an overview.

Experiment I: From the data for the capsule radius at which the curve is in the transition stage T_1 to T_2 (Fig. C.2, $t = 1d$) and using Eq. C.7, a pressure of $p_{th} \sim 1500 \text{ Pa}$ could be inferred (see Fig. 5.5C), at which bulk (interior) cells further away from the border than λ_I are experimentally observed to become necrotic. To express the variability in the cells' response on pressure we chose p_{th} from a Gaussian distribution with mean 1500 Pa and standard deviation of 150 Pa (10%) in all simulations. A variation of $\pm 300 \text{ Pa}$ on the mean value reduced the agreement with data in all simulations. The rim thickness λ_I within which the cells remain viable is fixed during the simulations as it did not change during the experiment. Notice however, that the value of λ_I does not explain the MCS expansion speed that differs for the thick capsule from that for the thin capsule, as it is demonstrated below (Fig. C.2A). We further assumed that cell-capsule friction coefficients $\gamma_{c,cap}$ are similar to those of cell-cell friction. However, the simulation results are robust with respect to wide variations on friction parameters, see C.3. The elastic properties of the capsule are fixed to the values measured in [242].

Experiment II: In Experiment II, λ_{II} was calibrated to match the growth rate kinetics of the spheroid in the absence of dextran (see EII.OII). Contrary to Experiment I, after adding external mechanical stress via dextran, no increase of necrosis was observed (EII.OII). This was formally captured by setting $p_{th} \rightarrow \infty$ in the model. The magnitude of the osmotic forces to obtain the desired bulk spheroid pressure was computed from Eq. 5.3, fixed for each experiment.

C.2.3 Cell-specific parameters K and T_{lys} during stress conditions

In the next step the compression modulus and the cell specific lysis time have been specified. To acquire the most realistic parameters within their physiological range, we consider the spheroid growth in the capsule, first with the constant growth rate α_0 of the cells as determined from free spheroid growth in Experiment I.

Compression modulus of the cells: The compression modulus of the cells influences the volumetric strain and hence through Eq. C.3 the growth rate α . First we tested the hypothesis that K remains constant during the experiment, varying K in the range $K \in [2.5 \text{ kPa}, 150 \text{ kPa}]$ in simulations

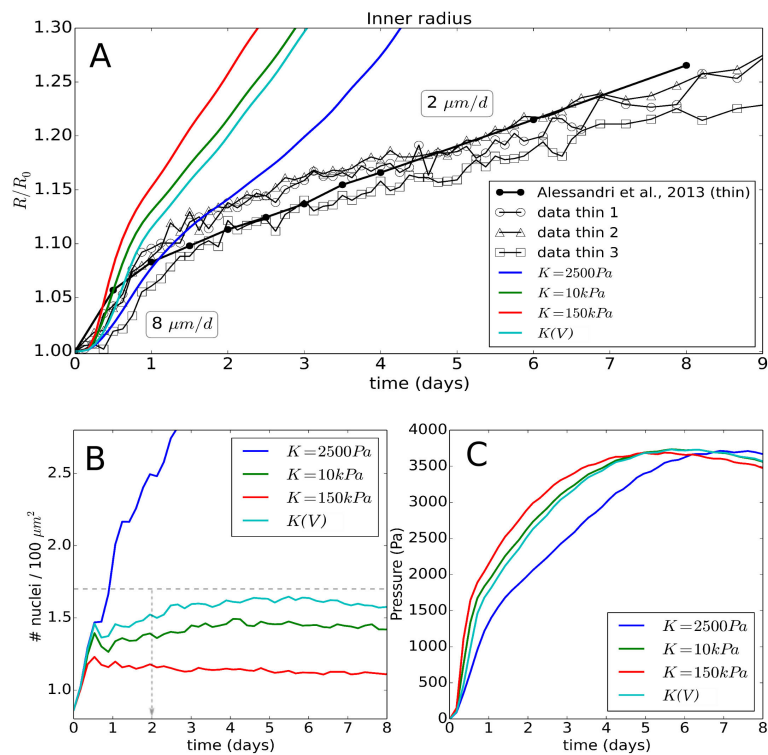


FIGURE C.2: (A) Time evolution of the radius of the thin capsule, shown for the experimental data and the simulation using Model I, with parameter variation on the individual cell compressibility ($K(V)$ means strain hardening). (B) Time evolution of the simulated cell density. The dashed horizontal line indicates the experimentally observed cell density at 48h. (C) Pressure in the capsule versus time.

for Experiment I. $K \sim 2.5$ kPa has been measured for quasi uncompressed L929 fibroblasts [255], $K \sim 10$ kPa for compressed CT26 cells [236].

Simulations with $K = 10$ kPa resulted in a cell density increase at 48h by only a factor of 1.5, while experimentally a factor of two is observed (Fig. C.2B), suggesting that this value of K is too high. Moreover, a significant overestimation of both the initial and the residual radial growth could be observed (Fig. C.2A). We further tested two extremes for K . For $K = 150$ kPa the cell density at 48h is now only 1.3 times the original one (Fig. C.2B), with a largely overestimated initial radial growth. By contrast, for a much smaller value $K \sim 2.5$ kPa, the cell density is strongly overestimated (increase by 3-fold at 48h), hence we reject such low values.

In a next step we tested the consequence of strain hardening (refsec:methods:CBM:compressibility, [292, 293, 294]). $K(V)$ can be initially relatively small, leading to a higher overall cell nuclei density (Fig. C.2B), yet gradually increasing during compression. For an applied pressure of 5 kPa, we find $K(V) = 10$ kPa while for an applied pressure of 10 kPa we have $K(V) = 15$ kPa, comparable to the values reported in [236, 251]. The simulations with strain stiffening show a better estimation of the cell density at 48h.

However, the stiffening alone did not solve the discrepancy between data and model simulation results. It allows a rapid nuclei density increase in a spheroid for low pressure but at the same time leads to higher mechanical resistance with increasing pressure. The capsule pressure generally shows a highly nonlinear behavior with a maximum (Fig. C.2C). This is typical because the mechanical stiffness of a capsule drops at high dilatation [298] as confirmed in the experiment by the observation of cells sometimes breaking through the capsule at later stages [242].

Note further that all the simulations of the capsule radius upon deformation by the growing MCS with time exhibit a short initial lag, in where the capsule dilatation is small (Fig. C.2A). In this stage, the spheroid touches the capsule border but cells are mainly pushed inwards, filling up intercellular spaces. This is less visible in the experiment, yet there the exact point of confluence is difficult to determine. After this period, cells are becoming more and more compressed and the mechanical resistance of the spheroid increases.

Overall, these results demonstrate that the viable rim with $\lambda_I = 20 \mu\text{m}$, constant growth rate and neither constant nor strain-dependent growth rate cannot explain the velocity of the growing spheroid in the linear phase, as it is not possible to simultaneously fit the nuclei density and the long-time radius expansion. For any value that would be capable of fitting the nuclei density, the slope of the radius expansion would be too high.

Lysis time: In a next step we studied whether incorporating the effect of intrinsic volume loss of necrotic cells due to lysis would lower the radius expansion and establish agreement between model and data. Lysis as defined in ref. [26] induces an irreversible water loss and decrease of cell volume limited to the solid volume of the cell. Contrary to *in vivo* experiments, there are no macrophages present to phagocytose the remaining cell bodies, and phagocytosis by neighbor cells is very slow [40]. In line with [26], we studied lysis times $T_{lys} \in [5h, 14d]$ using Model I. We notice that the shorter T_{lys} , the more the curves bend off in the beginning. However, because lysis results in more compression and thus gradually leads to stiffer cells, the numerical growth curves largely fail to reproduce the observed linear behavior (see Fig. C.3). The effect becomes striking at very low lysis times ($T_{lys} = 5h$). Here, the initial behavior of the spheroid is determined by cells quickly loosing their volume (hence a low resistance against pressure). Further in time, a large stiff core develops which will eventually overcome the mechanical resistance of the thin capsule. Nevertheless, adopting $T_{lys} \approx 5d$ yields a good agreement with the cell nuclei density at 48h (Fig. C.3B), which is in line with values found in an *in silico* model for ductal carcinoma *in situ* [26] and is relatively close to the apoptosis time found by fitting phenomenological growth laws for spheroids (\sim few days) [299, 236]. Note that the lysing cells in the bulk tend to move very slowly towards the center of the spheroid.

Non-constant growth rate: Even including lysis it was still not possible to simultaneously fit

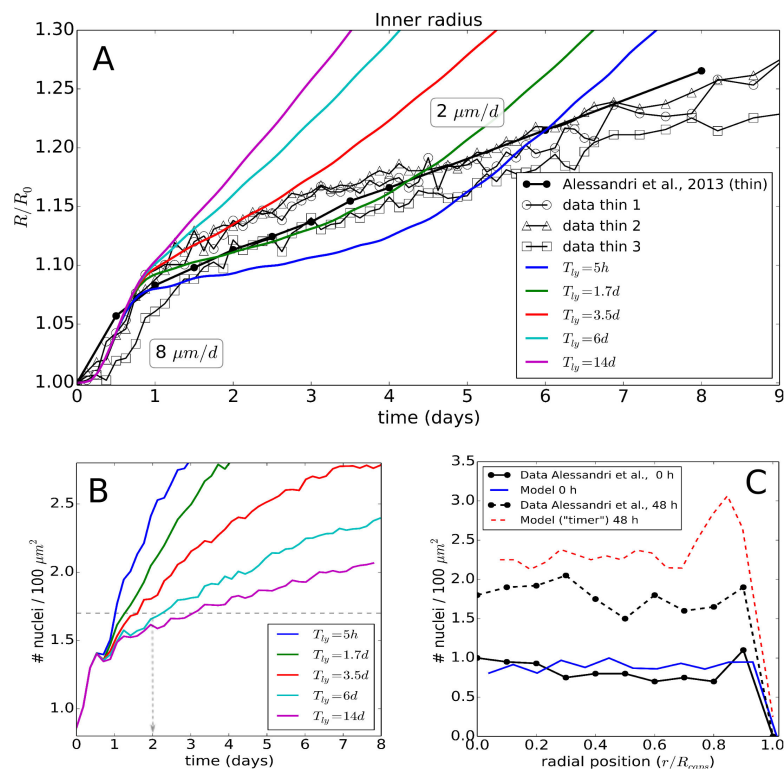


FIGURE C.3: (top) (A) Time evolution of the radius of the thin capsule, shown for the experimental data and simulations using Model I, showing the effect of a parameter variation for the lysis time T_{lys} . (B) Time evolution of the simulated cell density. (C) Cell density at 48h obtained from final model run with optimal parameters, but in which cells divide after a fixed cycle time ("timer") instead of a fixed size.

growth and density curves as improvement of growth kinetics was accompanied by increasing mismatch of density and vice-versa. This prompted us to study non-constant growth rates, decreasing with increasing volumetric strain as explained in the main text.

C.3 Model parameter and algorithm sensitivity

We also studied the potential influence of parameters calibrated for the free growth conditions which could not be directly inferred from the experiments. For the friction terms, the cell-cell friction, cell-ECM friction and cell-capsule friction were varied between 1 % ("low") and 200 % ("high") of their reference values. The effect is shown in Fig. C.4A and indicates that even for low friction coefficients the results remain largely unaffected. For the cell-cell adhesion energy W and cell motility coefficients D , which were varied between 10 % and 500 % [8], we did not observe any significant changes (results not shown). The strength of cell-cell adhesion has been shown to play a role in detachment, but to be of minor importance for multicellular systems under compression (e.g. [76]). Note, that also in MCSs growing in absence of externally applied forces cells are moderately compressed [7].

In conceptual analogy to experimental statistical procedures, we have performed growth expansion simulations in the thin capsule with the optimal parameter set but four different random seeds for the cell-specific cycle time, Young modulus and necrotic pressure threshold to test the effect of stochasticity (see Table C.2, Fig. C.4B). Even after more than 7 days of simulation, only very little mutual differences can be observed, while the slopes of the curves are the same. This can be attributed to self-averaging effects such that the variations on the level of individual cells cancel out at the population level (e.g. ref. [40]).

C.3.1 Comparison of calibration methods

For the local calibration procedure, we used the following constants in Eq. C.9 assuming strain hardening: $a_0 = 0.4454 \cdot 10^5$, $a_1 = 2.347 \cdot 10^5$, $a_2 = -7.918 \cdot 10^6$, $a_3 = 6.615 \cdot 10^8$, $a_4 = -1.206 \cdot 10^9$, $a_5 = -3.091 \cdot 10^9$, $a_6 = 1.1239 \cdot 10^{10}$, yielding a force cell - intercellular distance curve that matches well with the one obtained from the deformable cell simulations experiment (Fig. C.1). The function for $\tilde{E}(\tilde{d}_{ij})$ is monotonically increasing (Fig. C.4D). For the global calibration approach, we obtained a similar curve. In test simulations for the MCS growth in the thin capsule using contact inhibited growth for both local and global calibration, we found only a mutual variation of 5 – 7%, see Fig. C.4C. On the other hand, if no calibration was assumed, a largely unrealistic capsule dilation was obtained (Fig. C.4C), and a consistent relation between pressure and cell density could not be established.

C.3.2 Influence of cell division algorithms

As far as either the volume or the duration of the cell in the cell cycle have passed a threshold value, we replace the mother cell by two daughter cells which are placed very close to each other [19, 99]. This algorithm is different from the approach where cells slowly deform into dumbbells in mitosis phase before splitting into two daughter cells [76, 90]. In our model two daughter cells are created next to each other instantaneously. During the mitosis period (which takes about 1.5h) the daughter cells do not grow. However, the two newly created cells can generate short-time artificial pressure peaks which disappear during the division time course due to small local re-arrangements. To test the impact of the pressure peak formation on our growth simulation results we implemented a smoothing algorithm that reduces these peaks by ensuring that (1) the mother cell divides in the direction of the least stress as derived from the local stress tensor (see Eq. 2.13), and (2) a local energy minimum is sought by varying the distance between the daughter cells and computing the interactions with the other cells. While the smoothing algorithm reduces the short-time pressure peaks, we did not see significant differences in the results compared to simulations where this algorithm had been dropped.

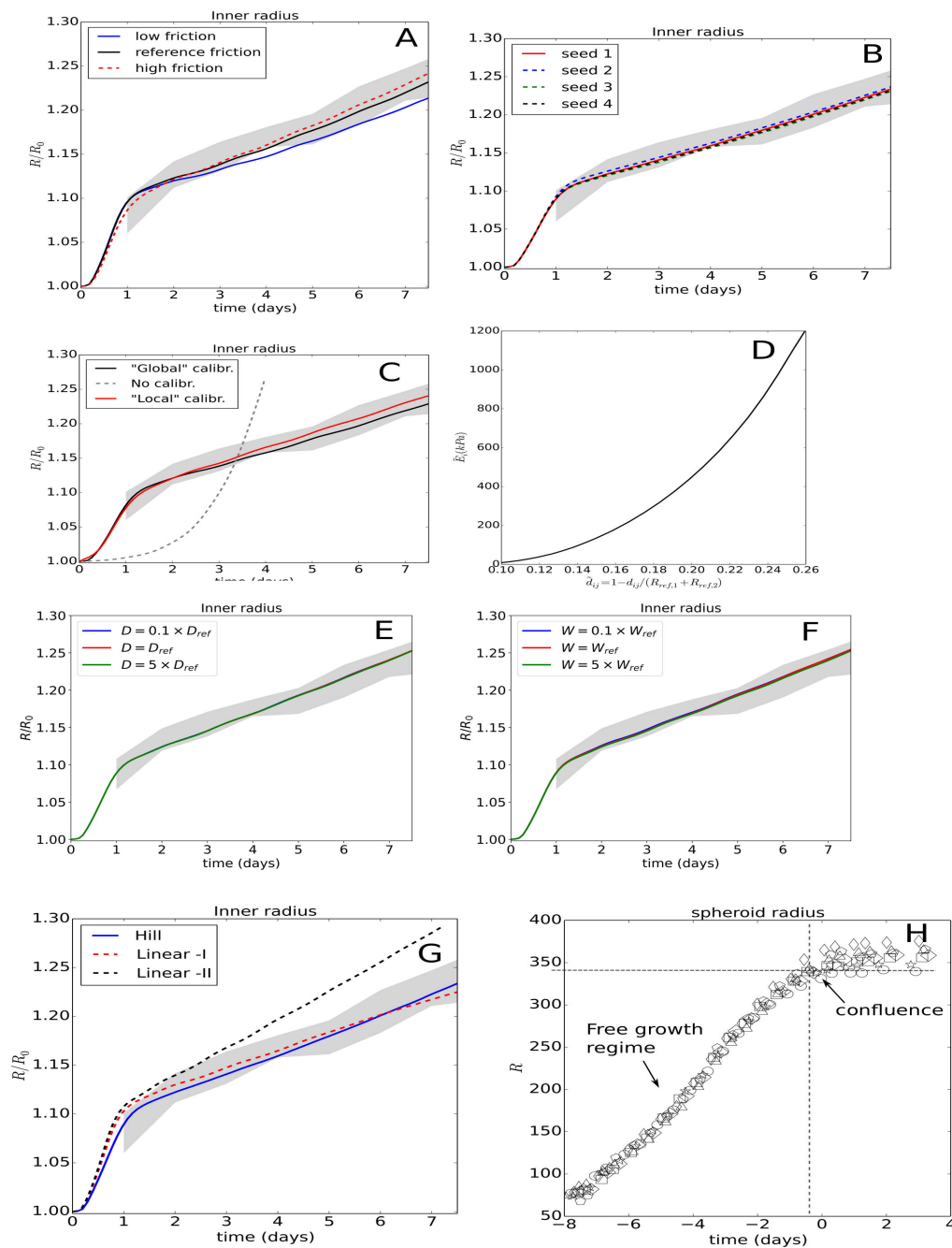


FIGURE C.4: (A) Dependence of simulation results of the thin capsule on a variation on the friction coefficients. (B) Comparison of 4 simulations with different random seed. (C) Comparison of the global and local calibration approach for a growing spheroid in the capsule. (D) Plot of the function $\tilde{E}(\tilde{d}_{ij})$ used for cell contact stiffening upon spheroid compression. (E-F) Comparison of 3 simulations of the thin capsule experiment with different cell-cell adhesion energy W , and cell motility D (G) Simulated thin capsule dilatation using for cell cycle progression: the proposed Hill-type function, the linear function ("Linear -I") as depicted in Fig. 5.2 (which fails to explain the data in experiment II), and a linear function ("Linear -II") optimized to match the CT26 spheroid expansion in Experiment II. (H) Data plots of MCS growth in a thick large capsule ($\sim 400 \mu\text{m}$) growth. The stress-dominated growth regime is too short to identify the stress-response.

C.4 Possible ways to include extracellular matrix in the DCM

An important future extension in the capsule model would be the inclusion of extracellular matrix (ECM), which is why we briefly outline how this can be implemented within the current model framework. There are three approaches with different degree of detail and effort of implementation, one requiring an explicit model of ECM, while two of them might be readily implemented with modest effort.

Approach (i): A sophisticated way would be to model the ECM explicitly e.g., as a network of visco-elastic springs (e.g. Ban et al., 2018 [281]). Such an approach is expensive both implementation-wise and in terms of computing power. Alternatively, the effect of ECM can be estimated within two approximations within the framework of the established model.

Approach (ii): One way is to perform the same simulation and calibration but now assuming that there is an ECM substance present in the capsule. To compute the influence of ECM of compression modulus K_{ecm} , one could assume that the ECM is compressed homogeneously and isotropically (shear elastic effects with cells are neglected). In a next step the volume occupied by the (DCM) cells and ECM within the capsule would be estimated prior to compression of the capsule simulation (see Fig. C.1A) to obtain a corrected relation between cell-cell interaction force and cell-cell distance (Fig. C.1C) that includes the compression and deformation forces of the ECM. For the Dextran experiment, the volume of the MCS could be estimated by the volume inside an elastic membrane enclosing the MCS and touching its surface.

The pressure necessary for ECM compression could be calculated from Eq. C.1 whereby dV then denotes the deviation of the ECM volume from its uncompressed volume as a consequence of compression leading to a relation $p(V)$ for the ECM alone. In the compression simulation used to determine the intercellular forces with cell-cell distance, the reduction of cell-cell distance would now cause both a compression of ECM by reducing its volume, and a deformation of the cells. Both, ECM and cell now resist the compression whereas in neglecting ECM, only the resistance of the cells was traced. As the volume of ECM can be calculated at any time from the difference of capsule volume and total volume of all cells, the pressure generated by compression of ECM during the compression simulations can be calculated, and taken into account in the calculation of the force on the cell by adding a force to each node that is proportional to the area to the node's associated cell surface area. This extends the curves in Fig. C.1C-D by the effect of ECM. For small compression modulus the force would be expected to be small. If at the same time, the compression modulus of the cell would be much larger than order (kPa) (see the discussion of cell compression moduli in the introduction), the repulsive branch of the curves in Fig. C.1 would become steeper. Approach (ii) is a global approximation as it needs information from the entire MCS (the MCS or capsule volume) to estimate the effect of ECM and the simplest approximation.

Approach (iii): The approximation could be based on a composite material approach in which the object that in the main body of the paper mimics the deformable cell, would instead be associated with a tissue unit composed of the cell plus a shell of ECM (for the concept in agent-based models, see Drasdo et. al. (2007) [76]). To determine the relation between force and cell-cell distance in such an approach, the radius of the object now composed of cell and ECM shell would be chosen larger than the cell radius alone to reflect the observed volume percentages of cells and ECM inside the MCS. The Young modulus of the cell cortex in the current approach would be replaced by an effective Young modulus taking into account the Young modulus of the ECM and the Young modulus of the cell cortex. As a simple illustrative example in point mechanics, it is conceptually equivalent to replacing two linear springs of spring constants k_1 (e.g. for the cell cortex) and k_2 (e.g. for the ECM) connected in series by one effective spring with spring constant $k = 1/(1/k_1 + 1/k_2)$ (e.g. for cell cortex plus ECM). Similarly, the compression modulus of the cortex (that emerges from its Young modulus and Poisson ratio) can be replaced by an effective compression modulus, that other

than the spring constants also contain the thicknesses of ECM and the cellular cortex. The effective compression modulus again contains information on compression moduli and volumes. This makes it possible to use the same approach as in the body of this paper by only re-parameterization of the cortex variables and the cell radius. However, in a configuration where cells touch each other, the ECM shell is already under slight compressive stress, which in reality might not be the case. From the definition of the composite material parameters and the geometrical quantities it is possible to track the position of the cell surface (such as its is possible to calculate in the above point mechanics example the contact point between the two springs). In the extreme case where the cell (including cortex) compression and Young moduli would be much larger than the compression modulus of the ECM, the deformation and compression of a cell / ECM unit would basically extend solely on the ECM shell. Approach (iii) would be local and is expected to give reasonable approximations in particular if the compressibility of the ECM is much bigger than that of a cell. Performing simulations with a DCM with composite parameters would lead to a different relationship of interaction force versus distance, which then could again be used within CBM simulations.

C.5 Table with model parameters and algorithm flow chart

Parameter set	symbol	unit	value	ref
Cortex Young's modulus	E_{cor}	Pa	2400	[255]
Cortex thickness	h_{cor}	μm	0.1	[255]
Cell compressibility	K	kPa	[2.5, 10]	CS, [236, 251, 253, 255]

TABLE C.1: Nominal physical parameter values for the DCM to calibrate the CBM.

Parameter set	symbol	unit	value	ref
$\mathcal{P}_{C,CT26}$				
Mean cell cycle time (*)	T_{cyc}	hours	17	CS, [242]
Mean cell radius	R_i	μm	7	Observation [242]
Cell Young's modulus (*)	E	Pa	450	[38]
Cell compressibility (*)	K	kPa	$2.5 - 10$	CS, [255, 236, 251, 253]
Cell motility	D	m^2/s	10^{-16}	CS, [114]
Cell Adhesion energy	W	J/m^2	10^{-4}	CS, [38]
Cell-cell friction	$\gamma_{cc, }$	Ns/m^3	5×10^{10}	CS, [19, 77]
Cell-cell friction, \perp	$\gamma_{cc,\perp}$	Ns/m^3	5×10^{10}	CS, [19, 77]
Cell-ECM friction,	γ_{ECM}	Ns/m^3	5×10^8	CS, [19]
Cell relaxation time	T_{rel}	hours	2	[223, 224]
Cell effective stiffness	\tilde{E}	Pa	$450 - 10^6$	CS
Stall growth rate	α_{qui}	-	0.3	CS
Hill exponent	n	-	1 - 2	CS
Hill threshold (*)	$\epsilon_{v_{tr}}$	-	0.35	CS
Cell lysis time (*)	T_{lys}	days	6	CS,[26]
Cell solid mass fraction	ϕ	-	0.1 - 0.3	[244, 26]
\mathcal{P}_{EXPI}				
Cell-capsule friction	$\gamma_{c,cap}$	Ns/m^3	2×10^{10}	CS
Pressure threshold bulk (necrosis) (*)	p_{th}	kPa	1.5	CS, [242]
Rim thickness (necrosis)	λ_I	μm	20	Observation [242]
Capsule Young modulus	E_{cap}	kPa	68	Observation [242]
Capsule Poisson ratio	ν_{cap}	-	0.5	Observation [242]
Capsule Radius	R_{in}	μm	100	Observation [242]
Capsule Thickness (thin/thick)	H	μm	8/30	Observation [242]
\mathcal{P}_{EXPII}				
Rim thickness (quiescence)	λ_{II}	μm	30	CS
Pressure threshold bulk (necrosis) (*)	p_{th}	kPa	-	Not observed [236]
$\mathcal{P}_{C,AB6} := \mathcal{P}_{C,CT26}$				
Mean cell cycle time (*)	T_{cyc}	hours	12	CS
$\mathcal{P}_{C,HT29} := \mathcal{P}_{C,CT26}$				
Mean cell cycle time (*)	T_{cyc}	hours	30	CS
$\mathcal{P}_{C,BC52} := \mathcal{P}_{C,CT26}$				
Mean cell cycle time (*)	T_{cyc}	hours	31	CS
$\mathcal{P}_{C,FHI} := \mathcal{P}_{C,CT26}$				
Mean cell cycle time (*)	T_{cyc}	hours	20	CS

TABLE C.2: Reference physical parameter values for the model. CS indicates a model choice. If CS shows up with references next to it, the value was chosen from the parameter range in the references. A reference only means the value is fixed from literature. An (*) denotes parameter variability meaning that the individual cell parameters are picked from a Gaussian distribution with $\pm 10\%$ on their mean value. The Gaussian distribution is clamped to 4 times the standard deviation to avoid potentially very low values or very high values. Negative values are excluded.

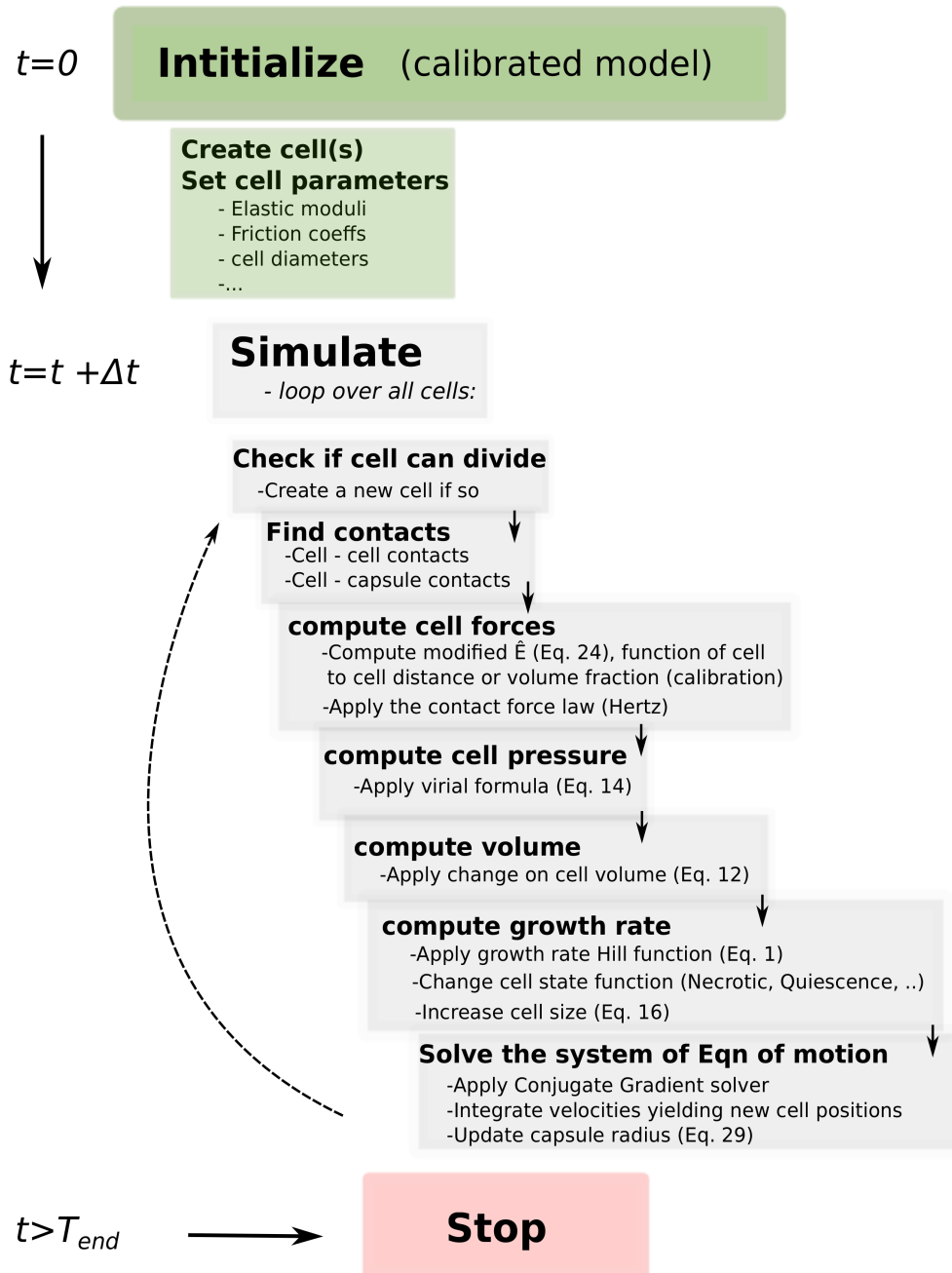


FIGURE C.5: Flow chart of the algorithms executed in the simulations.

References of the author

- [PVLDrasdo et al., 2017] Drasdo, D., Buttenschoen, A., and Liedekerke, P. V. (2017). Agent-based lattice models of multicellular systems: Numerical methods, implementation, and applications. In *Numerical Methods and Advanced Simulation in Biomechanics and Biological Processes*. Miguel Cerrolaza Sandra Shefelbine Diego Garzón-Alvarado.
- [PVLGanzenmüller et al., 2011] Ganzenmüller, G. C., Steinhäuser, M. O., Van Liedekerke, P., and Leuven, K. U. (2011). The implementation of smooth particle hydrodynamics in lammeps.
- [PVLGeris et al., 2010] Geris, L., Van Liedekerke, P., Smeets, B., Tjiskens, E., and Ramon, H. (2010). A cell based modelling framework for skeletal tissue engineering applications. *Journal of biomechanics*, 43(5):887–892.
- [PVLGhysels et al., 2009] Ghysels, P., Samaey, G., Tjiskens, B., Van Liedekerke, P., Ramon, H., and Roose, D. (2009). Multi-scale simulation of plant tissue deformation using a model for individual cell mechanics. *Physical biology*, 6(1):016009.
- [PVLGhysels et al., 2010a] Ghysels, P., Samaey, G., Van Liedekerke, P., Tjiskens, E., Ramon, H., and Roose, D. (2010a). Coarse implicit time integration of a cellular scale particle model for plant tissue deformation. *International Journal for Multiscale Computational Engineering*, 8(4):411–422.
- [PVLGhysels et al., 2010b] Ghysels, P., Samaey, G., Van Liedekerke, P., Tjiskens, E., Ramon, H., and Roose, D. (2010b). Multiscale modeling of viscoelastic plant tissue. *International Journal for Multiscale Computational Engineering*, 8(4):379–396.
- [PVLHeck et al., 2017] Heck, T., Smeets, B., Vanmaercke, S., Bhattacharya, P., Odenthal, T., Ramon, H., Van Oosterwyck, H., and Van Liedekerke, P. (2017). Modeling extracellular matrix viscoelasticity using smoothed particle hydrodynamics with improved boundary treatment. *Computer Methods in Applied Mechanics and Engineering*, 322:515–540.
- [PVLHo et al., 2013] Ho, Q. T., Carmeliet, J., Datta, A. K., Defraeye, T., Delele, M. A., Herremans, E., Opara, L., Ramon, H., Tjiskens, E., van der Sman, R., et al. (2013). Multiscale modeling in food engineering. *Journal of food Engineering*, 114(3):279–291.
- [PVLodenthal et al., 2013] Odenthal, T., Smeets, B., Van Liedekerke, P., Tjiskens, E., Van Oosterwyck, H., and Ramon, H. (2013). Analysis of initial cell spreading using mechanistic contact formulations for a deformable cell model. *PLoS computational biology*, 9(10):e1003267.
- [PVLSmeets et al., 2014] Smeets, B., Odenthal, T., Keresztes, J., Vanmaercke, S., Van Liedekerke, P., Tjiskens, E., Saeys, W., Van Oosterwyck, H., and Ramon, H. (2014). Modeling contact interactions between triangulated rounded bodies for the discrete element method. *Computer Methods in Applied Mechanics and Engineering*, 277:219–238.
- [PVLVan Liedekerke et al., 2017] Van Liedekerke, P., Buttenschoen, A., and Drasdo, D. (2017). Off-lattice agent-based models for cell and tumor growth: Numerical methods, implementation, and applications. In *Numerical Methods and Advanced Simulation in Biomechanics and Biological Processes*. Miguel Cerrolaza Sandra Shefelbine Diego Garzón-Alvarado.
- [PVLVan Liedekerke et al., 2010a] Van Liedekerke, P., Ghysels, P., Tjiskens, E., Samaey, G., Smeets, B., Roose, D., and Ramon, H. (2010a). A particle-based model to simulate the micromechanics of single-plant parenchyma cells and aggregates. *Physical Biology*, 7:26006.

- [PVLVan Liedekerke et al., 2018a] Van Liedekerke, P., Neitsch, J., Johann, T., Alessandri, K., Nassoy, P., and Drasdo, D. (2018a). Quantitative agent-based modeling reveals mechanical stress response of growing tumor spheroids is predictable over various growth conditions and cell lines. *Plos. Comp. Biol.*, page (accepted).
- [PVLVan Liedekerke et al., 2018b] Van Liedekerke, P., Neitsch, J., Johann, T., Warnt, E., Gonzales Valverde, I., Grosser, S., Hoehme, S., Kaes, J., and Drasdo, D. (2018b). Quantifying the mechanics and growth of cells and tissues in 3d using high resolution computational models. *bioRxiv (submitted)*.
- [PVLVan Liedekerke et al., 2015] Van Liedekerke, P., Palm, M. M., Jagiella, N., and Drasdo, D. (2015). Simulating tissue mechanics with agent-based models: concepts, perspectives and some novel results. *Computational Particle Mechanics*, 2(4):401–444.
- [PVLVan Liedekerke et al., 2011] Van Liedekerke, P., Roose, D., Ramon, H., Ghysels, P., Tijskens, E., and Samaey, G. (2011). Mechanisms of soft cellular tissue bruising. A particle based simulation approach. *Soft Matter*, 7(7):3580.
- [PVLVan Liedekerke et al., 2013] Van Liedekerke, P., Smeets, B., Odenthal, T., Tijskens, E., and Ramon, H. (2013). Solving microscopic flow problems using stokes equations in sph. *Computer Physics Communications*, 184(7):1686–1696.
- [PVLVan Liedekerke et al., 2009] Van Liedekerke, P., Tijskens, E., Dintwa, E., Rioual, F., Vangeyte, J., and Ramon, H. (2009). Dem simulations of the particle flow on a centrifugal fertilizer spreader. *Powder technology*, 190(3):348–360.
- [PVLVan Liedekerke et al., 2010b] Van Liedekerke, P., Tijskens, E., Ramon, H., Ghysels, P., Samaey, G., and Roose, D. (2010b). Particle-based model to simulate the micromechanics of biological cells. *Physical Review E*, 81(6, Part 1):61906–61915.
- [PVLVan Zeebroeck et al., 2003] Van Zeebroeck, M., Tijskens, E., Van Liedekerke, P., Deli, V., De Baerdemaeker, J., and Ramon, H. (2003). Determination of the dynamical behaviour of biological materials during impact using a pendulum device. *Journal of sound and vibration*, 266(3):465–480.

Bibliography

- [1] A J Engler, S Sen, H L Sweeney, and D E Discher. Matrix Elasticity Directs Stem Cell Lineage Specification. *Cell*, 126:677–689, 2006.
- [2] Daniel a Fletcher and R Dyche Mullins. Cell mechanics and the cytoskeleton. *Nature*, 463(7280):485–92, jan 2010.
- [3] Ulrich S Schwarz and Samuel A Safran. Physics of adherent cells. *Rev. Mod. Phys.*, 85(3):1327–1381, aug 2013.
- [4] D Lacroix and PJ Prendergast. A mechano-regulation model for tissue differentiation during fracture healing: analysis of gap size and loading. *Journal of biomechanics*, 35(9):1163–1171, 2002.
- [5] Charles A Taylor and CA Figueroa. Patient-specific modeling of cardiovascular mechanics. *Annual review of biomedical engineering*, 11:109–134, 2009.
- [6] *Mathematical biology. II Spatial models and biomedical applications. Interdisciplinary Applied Mathematics V. 18.*
- [7] DIRK DRASDO. Coarse Graining in simulated cell populations. *Advances in Complex Systems*, 08(02n03):319–363, 2005.
- [8] Stefan Hoehme, Marc Brulport, Alexander Bauer, Essam Bedawy, Wiebke Schormann, Matthias Hermes, Verena Puppe, Rolf Gebhardt, Sebastian Zellmer, Michael Schwarz, Ernesto Bockamp, Tobias Timmel, Jan G Hengstler, and Dirk Drasdo. Prediction and validation of cell alignment along microvessels as order principle to restore tissue architecture in liver regeneration. *Proceedings of the National Academy of Sciences*, 107(23):10371–10376, 2010.
- [9] J Galle, L Preziosi, and A Tosin. Contact inhibition of growth described using a multiphase model and an individual cell based model. *Applied Mathematics Letters*, 22:1483–1490, 2009.
- [10] John C. Dallon. Multiscale modeling of cellular systems in biology. *Current Opinion in Colloid & Interface Science*, 15(1-2):24–31, apr 2010.
- [11] S A Sandersius and T J Newman. Modeling cell rheology with the Subcellular Element Model. *Physical Biology*, 5:15002, 2008.
- [12] J A Glazier. Dynamics of Cellular Patterns. *Bussei Kenkyu*, 58:608–612, 1993.
- [13] Paul Macklin, Mary E Edgerton, Alastair M Thompson, and Vittorio Cristini. Patient-calibrated agent-based modelling of ductal carcinoma in situ (DCIS): from microscopic measurements to macroscopic predictions of clinical progression. *Journal of theoretical biology*, 301:122–40, may 2012.
- [14] Dmitry A Fedosov, Huan Lei, Bruce Caswell, Subra Suresh, and George E Karniadakis. Multi-scale Modeling of Red Blood Cell Mechanics and Blood Flow in Malaria. *PLoS Comput. Biol.*, 7(12):e1002270, 2011.
- [15] Néstor Sepúlveda, Laurence Petitjean, Olivier Cochet, Erwan Grasland-Mongrain, Pascal Silberzan, and Vincent Hakim. Collective Cell Motion in an Epithelial Sheet Can Be Quantitatively Described by a Stochastic Interacting Particle Model. *PLoS Comput Biol*, 9(3):e1002944, 2013.
- [16] Olgierd Cecil Zienkiewicz, Robert Leroy Taylor, Olgierd Cecil Zienkiewicz, and Robert Lee Taylor. *The finite element method*, volume 3. McGraw-hill London, 1977.

- [17] Berni J Alder and T E Wainwright. Studies in molecular dynamics. i. general method. *The Journal of Chemical Physics*, 31(2):459–466, 1959.
- [18] Pep Espanol. Dissipative particle dynamics with energy conservation. *EPL (Europhysics Letters)*, 40(6):631, 1997.
- [19] J Galle, M Loeffler, and D Drasdo. Modeling the effect of deregulated proliferation and apoptosis on the growth dynamics of epithelial cell populations in vitro. *Biophysical journal*, 88(1):62–75, 2005.
- [20] M Cristina Marchetti, Jean-François Joanny, Sriram Ramaswamy, Tanniemola B Liverpool, Jacques Prost, Madan Rao, and R Aditi Simha. Hydrodynamics of soft active matter. *Reviews of Modern Physics*, 85(3):1143, 2013.
- [21] Tiina Roose, S. Jonathan Chapman, and Philip K. Maini. Mathematical Models of Avascular Tumor Growth. *SIAM Review*, 49(2):179–208, jan 2007.
- [22] J S Lowengrub, H B Frieboes, F Jin, Y-L Chuang, X Li, P Macklin, S M Wise, and V Cristini. Nonlinear modelling of cancer: bridging the gap between cells and tumours. *Nonlinearity*, 23(1):R1—R9, jan 2010.
- [23] H M Byrne, T Alarcon, M R Owen, S D Webb, and P K Maini. Modelling aspects of cancer dynamics: a review. *Philosophical transactions. Series A, Mathematical, physical, and engineering sciences*, 364(1843):1563–78, jun 2006.
- [24] Julien Barré, Pierre Degond, and Ewelina Zatorska. Kinetic theory of particle interactions mediated by dynamical networks. *Multiscale Modeling & Simulation*, 15(3):1294–1323, 2017.
- [25] Arnaud Chauviere, Haralambos Hatzikirou, Ioannis G Kevrekidis, John S Lowengrub, and Vittorio Cristini. Dynamic density functional theory of solid tumor growth: Preliminary models. *AIP advances*, 2(1):11210, mar 2012.
- [26] Vittorio Cristini and John Lowengrub. *Multiscale Modeling of Cancer: An Integrated Experimental and Mathematical Modeling Approach*. Cambridge University Press, 2010.
- [27] Ignacio Ramis-Conde, Mark A J Chaplain, Alexander R A Anderson, and Dirk Drasdo. Multi-scale modelling of cancer cell intravasation: the role of cadherins in metastasis. *Physical Biology*, 6:16008, 2009.
- [28] YANGJIN Kim, MAGDALENA A. Stolarska, and HANS G. Othmer. A Hybrid model for tumor Spheroid growth in vitro I: Theoretical development and early results. *Mathematical Models and Methods in Applied Sciences*, 17(supp01):1773–1798, nov 2007.
- [29] J J Monaghan. An introduction to SPH. *Computer Physics Communications*, 48(1):89–96, jan 1988.
- [30] J J Monaghan. Smoothed particle hydrodynamics and its diverse applications. *Annual Review of Fluid Mechanics*, 44:323–346, 2012.
- [31] Wm G Hoover. Isomorphism linking smooth particles and embedded atoms. *Physica A: Statistical Mechanics and its Applications*, 260(3-4):244–254, 1998.
- [32] A Vazquez-Quesada, M Ellero, and P Espanol. Consistent scaling of thermal fluctuations in smoothed dissipative particle dynamics. *Journal of Chemical Physics*, 130:34901, 2009.
- [33] Bertrand Maury and Juliette Venel. A discrete contact model for crowd motion. *ESAIM: Mathematical Modelling and Numerical Analysis*, 45(1):145–168, 2011.

- [34] Jeroen Vangindertael, R Camacho, W Sempels, H Mizuno, P Dedecker, and KPF Janssen. An introduction to optical super-resolution microscopy for the adventurous biologist. *Methods and applications in fluorescence*, 6(2):022003, 2018.
- [35] Toshio Ando, Satya Prathyusha Bhamidimarri, Niklas Brending, H Colin-York, Lucy Collinson, Niels De Jonge, PJ De Pablo, Elke Debroye, Christian Eggeling, Christian Franck, et al. The 2018 correlative microscopy techniques roadmap. *Journal of Physics D: Applied Physics*, 51(44):443001, 2018.
- [36] A.B. Bortz, M.H. Kalos, and J.L. Lebowitz. A new algorithm for Monte Carlo simulation of Ising spin systems. *Journal of Computational Physics*, 17(1):10–18, jan 1975.
- [37] Daniel T. Gillespie. Exact stochastic simulation of coupled chemical reactions. *The Journal of Physical Chemistry*, 81(25):2340–2361, dec 1977.
- [38] S Hoehme and D Drasdo. A single-cell-based model of tumor growth in vitro: monolayers and spheroids. *Physical Biology*, 2:133–147, 2005.
- [39] M. Block, E. Schöll, and D. Drasdo. Classifying the expansion kinetics and critical surface dynamics of growing cell populations. *Physical Review Letters*, 99(24), 2007.
- [40] Nick Jagiella, Benedikt Müller, Margareta Müller, Irene E Vignon-Clementel, and Dirk Drasdo. Inferring Growth Control Mechanisms in Growing Multi-cellular Spheroids of NSCLC Cells from Spatial-Temporal Image Data. *PLoS computational biology*, 12(2):e1004412, feb 2016.
- [41] M. Radszuweit, M. Block, J. Hengstler, E. Schöll, and D. Drasdo. Comparing the growth kinetics of cell populations in two and three dimensions. *Physical Review E*, 79(5):051907, may 2009.
- [42] Marco Scianna and Luigi Preziosi. A cellular Potts model for the MMP-dependent and -independent cancer cell migration in matrix microtracks of different dimensions. *Comput. Mech.*, 53(3):485–497, oct 2013.
- [43] René F M van Oers, Elisabeth G Rens, Danielle J LaValley, Cynthia a Reinhart-King, and Roeland M H Merks. Mechanical Cell-Matrix Feedback Explains Pairwise and Collective Endothelial Cell Behavior In Vitro. *PLoS Comput. Biol.*, 10(8):e1003774, aug 2014.
- [44] P J Albert and U S Schwarz. Dynamics of Cell Shape and Forces on Micropatterned Substrates Predicted by a Cellular Potts Model. *Biophys. J.*, 106(11):2340–2352, 2014.
- [45] Emanuele Leoncini. *Applied Mathematics to Biology & Medicine*. PhD thesis, 2010.
- [46] Nicholas J Savill and Paulien Hogeweg. Modelling morphogenesis: from single cells to crawling slugs. *J. Theor. Biol.*, 184(3):229–235, feb 1996.
- [47] Marco Scianna and Luigi Preziosi. A cellular Potts model for the MMP-dependent and -independent cancer cell migration in matrix microtracks of different dimensions, 2013.
- [48] Maciej H Swat, Gilberto L Thomas, Julio M Belmonte, Abbas Shirinifard, Dimitrij Hmeljak, and James A Glazier. Multi-scale modeling of tissues using *compuCell3d*. In *Methods in cell biology*, volume 110, pages 325–366. Elsevier, 2012.
- [49] Sonja E M Boas, Maria I Navarro Jimenez, Roeland M H Merks, and Joke G Blom. A global sensitivity analysis approach for morphogenesis models. *arXiv preprint*, pages 1–29, 2015.

- [50] Margriet M Palm and Roeland M H Merks. Large-scale parameter studies of cell-based models of tissue morphogenesis using CompuCell3D or VirtualLeaf. In Celeste M Nelson, editor, *Tissue Morphogenesis*, volume 1189 of *Methods in Molecular Biology*, pages 301–322. Springer New York, New York, NY, 2015.
- [51] F Graner and J A Glazier. Simulation of Biological Cell Sorting Using a Two-Dimensional Extended Potts Model. *Physical Review Letters*, 69:2013–2016, 1992.
- [52] James A Glazier and François Graner. Simulation of the differential adhesion driven rearrangement of biological cells. *Phys. Rev. E*, 47(3):2128–2154, 1993.
- [53] Stephen Turner and Jonathan A Sherratt. Intercellular adhesion and cancer invasion: a discrete simulation using the extended Potts model. *J. Theor. Biol.*, 216(1):85–100, may 2002.
- [54] Brenda M Rubenstein and Laura J Kaufman. The role of extracellular matrix in glioma invasion: a cellular Potts model approach. *Biophys. J.*, 95(12):5661–5680, dec 2008.
- [55] Abbas Shirinifard, J Scott Gens, Benjamin L Zaitlen, Nikodem J Popławski, Maciej Swat, and James A Glazier. 3D multi-cell simulation of tumor growth and angiogenesis. *PLoS ONE*, 4(10):e7190, 2009.
- [56] Eline Boghaert, Derek C Radisky, and Celeste M Nelson. Lattice-based model of ductal carcinoma in situ suggests rules for breast cancer progression to an invasive state. *PLoS Comput. Biol.*, 10(12):e1003997, dec 2014.
- [57] András Szabó and Roeland M H Merks. Cellular Potts modeling of tumor growth, tumor invasion and tumor evolution. *Front. Oncol.*, 2013.
- [58] Jonathan F Li and John Lowengrub. The effects of cell compressibility, motility and contact inhibition on the growth of tumor cell clusters using the Cellular Potts Model. *J. Theor. Biol.*, 343:79–91, nov 2014.
- [59] Xuefeng Gao, J. Tyson McDonald, Lynn Hlatky, and Heiko Enderling. Acute and fractionated irradiation differentially modulate glioma stem cell division kinetics. *Cancer Research*, 73(5):1481–1490, 2013.
- [60] Roeland M H Merks and James A Glazier. Dynamic mechanisms of blood vessel growth. *Nonlinearity*, 19(1):C1—C10, 2006.
- [61] Roeland M H Merks, Erica D Perryn, Abbas Shirinifard, and James A Glazier. Contact-inhibited chemotaxis in de novo and sprouting blood-vessel growth. *PLoS Comput. Biol.*, 4(9):e1000163, 2008.
- [62] Margriet M Palm and Roeland M H Merks. Vascular networks due to dynamically arrested crystalline ordering of elongated cells. *Phys. Rev. E*, 87(1):12725, 2013.
- [63] Sonja E M Boas and Roeland M H Merks. Synergy of cell–cell repulsion and vacuolation in a computational model of lumen formation. *J. R. Soc. Interface*, 11(92):20131049, 2014.
- [64] Amy L Bauer, Trachette L Jackson, and Yi Jiang. Topography of extracellular matrix mediates vascular morphogenesis and migration speeds in angiogenesis. *PLoS Comput. Biol.*, 5(7):e1000445, jul 2009.
- [65] Amy L Bauer, Trachette L Jackson, and Yi Jiang. A cell-based model exhibiting branching and anastomosis during tumor-induced angiogenesis. *Biophysical journal*, 92(9):3105–3121, may 2007.

- [66] Josephine T Daub and Roeland M H Merks. A Cell-Based Model of Extracellular-Matrix-Guided Endothelial Cell Migration During Angiogenesis. *Bull. Math. Biol.*, pages 1–23, mar 2013.
- [67] U. Frisch, B. Hasslacher, and Y. Pomeau. Lattice-Gas Automata for the Navier-Stokes Equation. *Physical Review Letters*, 56(14):1505–1508, apr 1986.
- [68] Daniel H. Rothman and Stiphane Zaleski. *Lattice-Gas Cellular Automata: Simple Models of Complex Hydrodynamics*. 2004.
- [69] J.-P. Rivet and J. P. Boon. *Lattice Gas Hydrodynamics*. 2005.
- [70] Sabine Dormann and Andreas Deutsch. Modeling of self-organized avascular tumor growth with a hybrid cellular automaton. *In silico biology*, 2(3):393–406, jan 2002.
- [71] Andreas Deutsch and Sabine Dormann. *Cellular Automaton Modeling of Biological Pattern Formation: Characterization, Applications, and Analysis (Modeling and Simulation in Science, Engineering and Technology)*. Birkhaeuser Verlag AG, 2004.
- [72] K. Böttger, H. Hatzikirou, A. Chauviere, and A. Deutsch. Investigation of the Migration/Proliferation Dichotomy and its Impact on Avascular Glioma Invasion. *Mathematical Modelling of Natural Phenomena*, 7(1):105–135, jan 2012.
- [73] Marco Tektonidis, Haralambos Hatzikirou, Arnaud Chauvière, Matthias Simon, Karl Schaller, and Andreas Deutsch. Identification of intrinsic in vitro cellular mechanisms for glioma invasion. *Journal of Theoretical Biology*, 287(1):131–147, 2011.
- [74] Alfons G. Hoekstra, Jiri Kroc, and Peter M.A. Slood. *Simulating Complex Systems by Cellular Automata*. 2010.
- [75] J Galle, G Aust, G Schaller, T Beyer, and D Drasdo. Individual cell-based models of the spatial-temporal organization of multicellular systems—achievements and limitations. *Cytometry. Part A : the journal of the International Society for Analytical Cytology*, 69(7):704–10, jul 2006.
- [76] D Drasdo, S Hoehme, and M Block. On the Role of Physics in the Growth and Pattern Formation of Multi-Cellular Systems: What can we Learn from Individual-Cell Based Models. *Journal of Statistical Physics*, 128:287–345, 2007.
- [77] Peter Buske, Jörg Galle, Nick Barker, Gabriela Aust, Hans Clevers, and Markus Loeffler. A Comprehensive Model of the Spatio-Temporal Stem Cell and Tissue Organisation in the Intestinal Crypt. *PLoS Comput Biol*, 7(1):e1001045, 2011.
- [78] Peter Buske, Jens Przybilla, Markus Loeffler, Norman Sachs, Toshiro Sato, Hans Clevers, and Joerg Galle. On the biomechanics of stem cell niche formation in the gut – modelling growing organoids. *FEBS Journal*, 279(18):3475–3487, 2012.
- [79] Sara Jane Dunn, Inke S Näthke, and James M Osborne. Computational models reveal a passive mechanism for cell migration in the crypt. *PLoS ONE*, 8(11), 2013.
- [80] Richard C van der Wath, Bruce S Gardiner, Antony W Burgess, and David W Smith. Cell organisation in the colonic crypt: a theoretical comparison of the pedigree and niche concepts. *PloS one*, 8(9):e73204, jan 2013.
- [81] Carmen Pin, Aimee Parker, A Patrick Gunning, Yuki Ohta, Ian T Johnson, Simon R Carding, and Toshiro Sato. An individual based computational model of intestinal crypt fission and its application to predicting unrestrictive growth of the intestinal epithelium. *Integrative biology : quantitative biosciences from nano to macro*, 7(2):213–28, feb 2015.

- [82] Ingeborg M M van Leeuwen, Carina M Edwards, Mohammad Ilyas, and Helen M Byrne. Towards a multiscale model of colorectal cancer. *World J Gastroenterol*, 13(9):1399–1407, 2007.
- [83] Gianluca D’Antonio, Paul Macklin, and Luigi Preziosi. An agent-based model for elasto-plastic mechanical interactions between cells, basement membrane and extracellular matrix. *Mathematical biosciences and engineering : MBE*, 10(1):75–101, feb 2013.
- [84] Muhammad H Zaman, Roger D Kamm, Paul Matsudaira, and Douglas A Lauffenburger. Computational model for cell migration in three-dimensional matrices. *Biophysical journal*, 89(2):1389–1397, aug 2005.
- [85] R Rangarajan and M H Zaman. Modeling cell migration in 3D. *Cell Adhesion & Migration*, 2:2:106–109, 2008.
- [86] D. K. Schluter, I Ramis-Conde, and M. A. J. Chaplain. Computational Modeling of Single-Cell Migration: The Leading Role of Extracellular Matrix Fibers. *Biophysical Journal*, 103:1141–1151, sep 2012.
- [87] R Rey and J M García-Aznar. A phenomenological approach to modelling collective cell movement in 2D. *Biomechanics and modeling in mechanobiology*, 12(6):1089–100, nov 2013.
- [88] F J Vermolen and A Gefen. A semi-stochastic cell-based formalism to model the dynamics of migration of cells in colonies. *Biomechanics and modeling in mechanobiology*, 11(1-2):183–95, jan 2012.
- [89] P Pathmanathan, J Cooper, A Fletcher, G Mirams, L Montahan, P Murray, J Osborne, J Pitt-Francis, A Walter, and S J Chapman. A computational study of discrete mechanical tissue models. *Physical Biology*, 6(3):36001, 2009.
- [90] Markus Basan, Jacques Prost, Jean-François Joanny, and Jens Elgeti. Dissipative particle dynamics simulations for biological tissues: rheology and competition. *Physical biology*, 8(2):26014, apr 2011.
- [91] G M Odell, G Oster, P Alberch, and B Burnside. The mechanical basis of morphogenesis. I. Epithelial folding and invagination. *Developmental biology*, 85(2):446–462, 1981.
- [92] Dirk Drasdo and Gabor Forgacs. Modeling the interplay of generic and genetic mechanisms in cleavage, blastulation, and gastrulation. *Developmental Dynamics*, 219(2):182–191, 2000.
- [93] D. Drasdo and M. Loeffler. Individual-based models to growth and folding in one-layered tissues: intestinal crypts and early development. *Nonlinear Analysis: Theory, Methods & Applications*, 47(1):245–256, aug 2001.
- [94] F. A. Meineke, C. S. Potten, and M. Loeffler. Cell migration and organization in the intestinal crypt using a lattice-free model. *Cell Proliferation*, 34(4):253–266, aug 2001.
- [95] Ignacio Ramis-Conde, Dirk Drasdo, Alexander R A Anderson, and Mark A J Chaplain. Modeling the Influence of the E-Cadherin- β -Catenin Pathway in Cancer Cell Invasion: A Multiscale Approach. *Biophysical Journal*, 95(1):155–165, 2008.
- [96] Y S Chu, S Dufour, J P Thiery, E Perez, and F Pincet. Johnson-Kendall-Roberts Theory Applied to Living Cells. *Physical Review Letters*, 94(2):28102, 2005.
- [97] E Barthel. Adhesive elastic contacts: JKR and more. *Journal of Physics D: Applied Physics*, 41(16):163001, 2008.

- [98] Anne-celine Boulanger. Agent-based model -Continuum Model in tumor growth. Technical Report August 2009, 2010.
- [99] Gernot Schaller and Michael Meyer-Hermann. Multicellular tumor spheroid in an off-lattice Voronoi-Delaunay cell model. *Phys. Rev. E*, 71(5):51910, may 2005.
- [100] Steve Pawlizak, Anatol W Fritsch, Steffen Grosser, Dave Ahrens, Tobias Thalheim, Stefanie Riedel, Tobias R Kießling, Linda Oswald, Mareike Zink, M Lisa Manning, et al. Testing the differential adhesion hypothesis across the epithelial- mesenchymal transition. *New Journal of Physics*, 17(8):083049, 2015.
- [101] James M Osborne, Alexander G Fletcher, Joe M Pitt-Francis, Philip K Maini, and David J Gavaghan. Comparing individual-based approaches to modelling the self-organization of multicellular tissues. *PLoS computational biology*, 13(2):e1005387, 2017.
- [102] E. Palsson and H. G. Othmer. A model for individual and collective cell movement in *Dicystostelium discoideum*. *Proceedings of the National Academy of Sciences*, 97(19):10448–10453, sep 2000.
- [103] B. Szabó, G. J. Szöllösi, B. Gönci, Zs. Jurányi, D. Selmeczi, and Tamás Vicsek. Phase transition in the collective migration of tissue cells: Experiment and model. *Phys. Rev. E*, 74:061908, Dec 2006.
- [104] B. A. Camley, Y. Zhang, Y. Zhao, B. Li, E. Ben-Jacob, H. Levine, and W.-J. Rappel. Polarity mechanisms such as contact inhibition of locomotion regulate persistent rotational motion of mammalian cells on micropatterns. *Proceedings of the National Academy of Sciences*, 111(41):14770–14775, oct 2014.
- [105] Juliane Zimmermann, Brian A Camley, Wouter-Jan Rappel, and Herbert Levine. Contact inhibition of locomotion determines cell-cell and cell-substrate forces in tissues. *Proceedings of the National Academy of Sciences of the United States of America*, pages 1522330113–, feb 2016.
- [106] T P Neufeld and B A Edgar. Connections between growth and the cell cycle. *Current Opinion in Cell Biology*, 10:784–790, 1998.
- [107] Amit Tzur, Ran Kafri, Valerie S LeBleu, Galit Lahav, and Marc W Kirschner. Cell Growth and Size Homeostasis in Proliferating Animal Cells. *Science*, 325(5937):167–171, 2009.
- [108] Mustafa Mir, Zhuo Wang, Zhen Shen, Michael Bednarz, Rashid Bashir, Ido Golding, Supriya G Prasanth, and Gabriel Popescu. Optical measurement of cycle-dependent cell growth. *Proceedings of the National Academy of Sciences*, 2011.
- [109] Ran Kafri, Jason Levy, Miriam B Ginzberg, Seungeun Oh, Galit Lahav, and Marc W Kirschner. Dynamics extracted from fixed cells reveal feedback linking cell growth to cell cycle. *Nature*, 494(7438):480–483, 2013.
- [110] Hervé Turlier, Basile Audoly, Jacques Prost, and Jean-François Joanny. Furrow constriction in animal cell cytokinesis. *Biophysical journal*, 106(1):114–23, jan 2014.
- [111] Stefan Hoehme and Dirk Drasdo. Mathematical Population Studies : An International Journal of Mathematical Biomechanical and Nutrient Controls in the Growth of Mammalian Cell Populations. 17(166-187):37–41, 2010.
- [112] D Drasdo, R Kree, and J S McCaskill. Monte Carlo approach to tissue-cell populations. *Physical Review E*, 52(6):6635–6657, dec 1995.

- [113] H Byrne and D Drasdo. Individual-based and continuum models of growing cell populations: a comparison. *Mathematical Biology*, 58:657–680, 2009.
- [114] Dirk Drasdo and Stefan Hoehme. Modeling the impact of granular embedding media, and pulling versus pushing cells on growing cell clones. *New Journal of Physics*, 14(5):55025, 2012.
- [115] JH Irving and John G Kirkwood. The statistical mechanical theory of transport processes. iv. the equations of hydrodynamics. *The Journal of chemical physics*, 18(6):817–829, 1950.
- [116] Katarzyna a Rejniak. An immersed boundary framework for modelling the growth of individual cells: an application to the early tumour development. *Journal of theoretical biology*, 247(1):186–204, jul 2007.
- [117] Katarzyna A. Rejniak and Robert H. Dillon. A single cell-based model of the ductal tumour microarchitecture. *Computational & Mathematical Methods in Medicine*, 8(1):51–69.
- [118] et al. Robert Dillon, Markus Owen. A single-cell-based model of multicellular growth using the immersed boundary method. *AMS Contemporary Mathematics*, 466, 2008.
- [119] Katarzyna A Rejniak and Alexander R A Anderson. A computational study of the development of epithelial acini: I. Sufficient conditions for the formation of a hollow structure. *Bulletin of mathematical biology*, 70(3):677–712, apr 2008.
- [120] Yousef Jamali, Mohammad Azimi, and Mohammad R K Mofrad. A sub-cellular viscoelastic model for cell population mechanics. *PLoS One*, 5(8), 2010.
- [121] I V Pivkin and G E Karniadakis. Accurate Coarse-Grained Modeling of Red Blood Cells. *Physical Review Letters*, 101:118105, 2008.
- [122] M Hosseini and J J Feng. A particle-based model for the transport of erythrocytes in capillaries. *Chemical engineering science*, 64:4488–4497, 2009.
- [123] Dmitry A Fedosov, Bruce Caswell, and George Em Karniadakis. Systematic coarse-graining of spectrin-level red blood cell models. *Computer Methods in Applied Mechanics and Engineering*, 199(29–32):1937–1948, 2010.
- [124] D a Fedosov, B Caswell, S Suresh, and G E Karniadakis. Quantifying the biophysical characteristics of Plasmodium-falciparum-parasitized red blood cells in microcirculation. *Proceedings of the National Academy of Sciences of the United States of America*, 108(1):35–9, jan 2011.
- [125] Zhangli Peng, Xuejin Li, Igor V Pivkin, Ming Dao, George E Karniadakis, and Subra Suresh. Lipid bilayer and cytoskeletal interactions in a red blood cell. *Proceedings of the National Academy of Sciences*, 2013.
- [126] Melda Tozluoğlu, Alexander L Tournier, Robert P Jenkins, Steven Hooper, Paul A Bates, and Erik Sahai. Matrix geometry determines optimal cancer cell migration strategy and modulates response to interventions. *Nature Cell Biology*, 15(7):751–762, 2013.
- [127] Min-Cheol Kim, Devin M Neal, Roger D Kamm, and H Harry Asada. Dynamic modeling of cell migration and spreading behaviors on fibronectin coated planar substrates and micropatterned geometries. *PLOS Computational Biology*, 9(2):e1002926, 2013.
- [128] Jiao Chen, Daphne Weihs, Marcel Van Dijk, and Fred J Vermolen. A phenomenological model for cell and nucleus deformation during cancer metastasis. *Biomechanics and modeling in mechanobiology*, pages 1–22, 2018.

- [129] Sebastian A Sandersius and Timothy J Newman. Modeling cell rheology with the Subcellular Element Model. *Physical biology*, 5(1):15002, jan 2008.
- [130] Philip Murray, Carina Edwards, Marcus Tindall, and Philip Maini. From a discrete to a continuum model of cell dynamics in one dimension. *Physical Review E*, 80(3):031912, sep 2009.
- [131] Hermann B Frieboes, Fang Jin, Yao-Li Chuang, Steven M Wise, John S Lowengrub, and Vittorio Cristini. Three-dimensional multispecies nonlinear tumor growth-II: Tumor invasion and angiogenesis. *Journal of theoretical biology*, 264(4):1254–78, jun 2010.
- [132] L Preziosi, D Ambrosi, and C Verdier. An elasto-visco-plastic model of cell aggregates. *Journal of Theoretical Biology*, 262(1):35–47, 2010.
- [133] Byrne H. M. Osborne J. M. , Walter A., Kershaw S. K., Mirams G R, Fletcher A G, Pathmanathan P , Gavaghan D., Jensen O. E., Maini P. K. A hybrid approach to multi-scale modelling of cancer. *Phil Trans R Soc A*, 368:5013–5028, 2010.
- [134] Ismael González-Valverde and José Manuel García-Aznar. Mechanical modeling of collective cell migration: An agent-based and continuum material approach. *Computer Methods in Applied Mechanics and Engineering*, 337:246–262, 2018.
- [135] MB Liu and GR Liu. Smoothed particle hydrodynamics (sph): an overview and recent developments. *Archives of computational methods in engineering*, 17(1):25–76, 2010.
- [136] Rajarshi Das and PW Cleary. Effect of rock shapes on brittle fracture using smoothed particle hydrodynamics. *Theoretical and Applied Fracture Mechanics*, 53(1):47–60, 2010.
- [137] S E Hieber and P Koumoutsakos. An immersed boundary method for smoothed particle hydrodynamics of self-propelled swimmers. *Journal of Computational Physics*, 227(19):8636–8654, 2008.
- [138] J P Gray, J J Monaghan, and R P Swift. SPH elastic dynamics. *Computer Methods in Applied Mechanics and Engineering*, 190(49–50):6641–6662, 2001.
- [139] MouBin Liu, JiaRu Shao, and JianZhong Chang. On the treatment of solid boundary in smoothed particle hydrodynamics. *Science China Technological Sciences*, 55(1):244–254, 2012.
- [140] S Adami, XY Hu, and NA Adams. A generalized wall boundary condition for smoothed particle hydrodynamics. *Journal of Computational Physics*, 231(21):7057–7075, 2012.
- [141] MB Liu and GR Liu. Smoothed particle hydrodynamics (sph): an overview and recent developments. *Archives of computational methods in engineering*, 17(1):25–76, 2010.
- [142] J P Morris, P J Fox, and Y Zhu. Modeling low Reynolds number incompressible flows using SPH. *Journal of Computational Physics*, 136:214–226, 1997.
- [143] Marco Ellero, Mar Serrano, and Pep Espanol. Incompressible smoothed particle hydrodynamics. *Journal of Computational Physics*, 226(2):1731–1752, 2007.
- [144] S Litvinov, M Ellero, X Y Hu, and N A Adams. A splitting scheme for highly dissipative smoothed particle dynamics. *J. Comput. Phys.*, 229(15):5457–5464, 2010.
- [145] M. Ferrand, D. R. Laurence, B. D. Rogers, D. Violeau, and C. Kassiotis. Unified semi-analytical wall boundary conditions for inviscid, laminar or turbulent flows in the meshless SPH method. *International Journal for Numerical Methods in Fluids*, 71(4):446–472, 2013.

- [146] Silvanus Alt, Poulami Ganguly, and Guillaume Salbreux. Vertex models: from cell mechanics to tissue morphogenesis. *Philosophical Transactions of the Royal Society B: Biological Sciences*, 372(1720), 2017.
- [147] Min-Cheol Kim, Yaron R Silberberg, Rohan Abeyaratne, Roger D Kamm, and H Harry Asada. Computational modeling of three-dimensional ecm-rigidity sensing to guide directed cell migration. *Proceedings of the National Academy of Sciences*, 115(3):E390–E399, 2018.
- [148] K Tamura, S Komura, and T Kato. Adhesion induced buckling of spherical shells. *Journal of Physics: Condensed Matter*, 16(39):L421–L428, oct 2004.
- [149] Daniel Maugis. Adhesion of spheres: The JKR-DMT transition using a Dugdale model. *J. Colloid Interface Sci.*, 150(1):243–269, 1992.
- [150] S Tanaka, D Sichau, and D Iber. LBIBCell: a cell-based simulation environment for morphogenetic problems. *Bioinformatics*, 2015.
- [151] Florian Milde, Gerardo Tauriello, Hannah Haberkern, and Petros Koumoutsakos. SEM++: A particle model of cellular growth, signaling and migration. *Computational Particle Mechanics*, may 2014.
- [152] Ali Nematbakhsh, Wenzhao Sun, Pavel A Brodskiy, Aboutaleb Amiri, Cody Narciso, Zhiliang Xu, Jeremiah J Zartman, and Mark Alber. Multi-scale computational study of the mechanical regulation of cell mitotic rounding in epithelia. *PLoS computational biology*, 13(5):e1005533, 2017.
- [153] Tim Lämmermann and Michael Sixt. Mechanical modes of ‘amoeboid’ cell migration. *Current Opinion in Cell Biology*, 21(5):636 – 644, 2009. Cell-to-cell contact and extracellular matrix.
- [154] Guillaume Charras and Ewa Paluch. Blebs lead the way: how to migrate without lamellipodia. *Nature reviews Molecular cell biology*, 9(9):730, 2008.
- [155] Andrew G Clark and Danijela Matic Vignjevic. Modes of cancer cell invasion and the role of the microenvironment. *Current Opinion in Cell Biology*, 36:13 – 22, 2015. Cell adhesion and migration.
- [156] Peter Friedl and Katarina Wolf. Tumour-cell invasion and migration: diversity and escape mechanisms. *Nature reviews cancer*, 3(5):362, 2003.
- [157] TAM Heck, Marie-Mo Vaeyens, and Hans Van Oosterwyck. Computational models of sprouting angiogenesis and cell migration: towards multiscale mechanochemical models of angiogenesis. *Mathematical Modelling of Natural Phenomena*, 10(1):108–141, 2015.
- [158] René F M van Oers, Elisabeth G Rens, Danielle J LaValley, Cynthia A Reinhart-King, and Roeland M H Merks. Mechanical cell-matrix feedback explains pairwise and collective endothelial cell behavior in vitro. *PLoS computational biology*, 10(8):e1003774, aug 2014.
- [159] Melda Tozluoğlu, Alexander L Tournier, Robert P Jenkins, Steven Hooper, Paul A Bates, and Erik Sahai. Matrix geometry determines optimal cancer cell migration strategy and modulates response to interventions. *Nat. Cell Biol.*, 15(7):751–762, July 2013.
- [160] Jie Zhu and Alex Mogilner. Comparison of cell migration mechanical strategies in three-dimensional matrices: a computational study. *Interface Focus*, 6(5):20160040, 6 October 2016.
- [161] Eirikur Palsson and Hans G Othmer. A model for individual and collective cell movement in Dictyostelium discoideum. *Proceedings of the National Academy of Sciences*, 97(19):10448–10453, 2000.

- [162] E. Palsson. A three-dimensional model of cell movement in multicellular systems. *Future Generation Computer Systems*, 17(7):835–852, may 2001.
- [163] David Boal. *Mechanics of the Cell*. Cambridge University Press, 2 edition, 2012.
- [164] Katarina Wolf, Yi I Wu, Yueying Liu, Jörg Geiger, Eric Tam, Christopher Overall, M Sharon Stack, and Peter Friedl. Multi-step pericellular proteolysis controls the transition from individual to collective cancer cell invasion. *Nat. Cell Biol.*, 9(8):893–904, August 2007.
- [165] Peter Friedl and Katarina Wolf. Proteolytic interstitial cell migration: a five-step process. *Cancer Metastasis Rev.*, 28(1-2):129–135, June 2009.
- [166] Farideh Sabeh, Ichiro Ota, Kenn Holmbeck, Henning Birkedal-Hansen, Paul Soloway, Milagros Balbin, Carlos Lopez-Otin, Steven Shapiro, Masaki Inada, Stephen Krane, Edward Allen, Duane Chung, and Stephen J Weiss. Tumor cell traffic through the extracellular matrix is controlled by the membrane-anchored collagenase MT1-MMP. *J. Cell Biol.*, 167(4):769–781, 22 November 2004.
- [167] Farideh Sabeh, Ryoko Shimizu-Hirota, and Stephen J Weiss. Protease-dependent versus -independent cancer cell invasion programs: three-dimensional amoeboid movement revisited. *J. Cell Biol.*, 185(1):11–19, 6 April 2009.
- [168] Elvira Infante, Pedro Monteiro, Perrine Paul-Gilloteaux, Mélanie Domingues, Mathew Raab, Matthieu Piel, Edgar R Gomes, and Philippe Chavrier. Mechanical stress on the nucleus triggers MT1-MMP digest-on-demand for matrix nuclear tunnel formation.
- [169] Ulrich S Schwarz, Thorsten Erdmann, and Ilka B Bischofs. Focal adhesions as mechanosensors: the two-spring model. *Biosystems*, 83(2-3):225–232, 2006.
- [170] Haguy Wolfenson, Giovanni Meacci, Shuaimin Liu, Matthew R Stachowiak, Thomas Iskratsch, Saba Ghassemi, Pere Roca-Cusachs, Ben O’Shaughnessy, James Hone, and Michael P Sheetz. Tropomyosin controls sarcomere-like contractions for rigidity sensing and suppressing growth on soft matrices. *Nature cell biology*, 18(1):33, 2016.
- [171] Yuriy V Pereverzev, Oleg V Prezhdo, Manu Forero, Evgeni V Sokurenko, and Wendy E Thomas. The two-pathway model for the catch-slip transition in biological adhesion. *Biophysical journal*, 89(3):1446–1454, 2005.
- [172] George I Bell. Models for the specific adhesion of cells to cells. *Science*, 200(4342):618–627, 1978.
- [173] Bérénice Grec, Bertrand Maury, Nicolas Meunier, and Laurent Navoret. A 1d model of leukocyte adhesion coupling bond dynamics with blood velocity. *Journal of theoretical biology*, 452:35–46, 2018.
- [174] Elizaveta A Novikova and Cornelis Storm. Contractile fibers and catch-bond clusters: a biological force sensor? *Biophysical journal*, 105(6):1336–1345, 2013.
- [175] A Szabó and A Czirók. The role of Cell-Cell adhesion in the formation of multicellular sprouts. *Math. Model. Nat. Phenom.*, 5(1):106–122, 3 February 2010.
- [176] Anja Geitmann and Joseph KE Ortega. Mechanics and modeling of plant cell growth. *Trends in plant science*, 14(9):467–478, 2009.
- [177] Roeland MH Merks, Michael Guravage, Dirk Inzé, and Gerrit TS Beemster. Virtualleaf: an open-source framework for cell-based modeling of plant tissue growth and development. *Plant physiology*, 155(2):656–666, 2011.

- [178] Jacques Dumais. Can mechanics control pattern formation in plants? *Current opinion in plant biology*, 10(1):58–62, 2007.
- [179] Gao Qiong, RE Pitt, and JA Bartsch. Elastic-plastic constitutive relations of the cell walls of apple and potato parenchyma. *Journal of Rheology*, 33(2):233–256, 1989.
- [180] V Kouznetsova, WAM Brekelmans, and FPT Baaijens. An approach to micro-macro modeling of heterogeneous materials. *Computational mechanics*, 27(1):37–48, 2001.
- [181] Christian Miehe, Jörg Schröder, and Jan Schotte. Computational homogenization analysis in finite plasticity simulation of texture development in polycrystalline materials. *Computer methods in applied mechanics and engineering*, 171(3-4):387–418, 1999.
- [182] HCP Karunasena, Wijitha Senadeera, Richard J Brown, and YuanTong Gu. A particle based model to simulate microscale morphological changes of plant tissues during drying. *Soft matter*, 10(29):5249–5268, 2014.
- [183] Lincoln Taiz and Eduardo Zeiger. *Plant physiology*. Sinauer associates Sunderland, 2002.
- [184] M.A.J. Chaplain. The strain energy function of an ideal plant cell wall. *Journal of Theoretical Biology*, 163(1):77 – 97, 1993.
- [185] C X Wang, L Wang, and C R Thomas. Modelling the mechanical properties of single suspension-cultured tomato cells. *Annals of botany*, 93(4):443–53, apr 2004.
- [186] Naiqiang Wu and Marvin J Pitts. Development and validation of a finite element model of an apple fruit cell. *Postharvest Biology and Technology*, 16(1):1–8, 1999.
- [187] MC Alamar, Elisabeth Vanstreels, ML Oey, E Moltó, and BM Nicolai. Micromechanical behaviour of apple tissue in tensile and compression tests: Storage conditions and cultivar effect. *Journal of Food Engineering*, 86(3):324–333, 2008.
- [188] Jozef Keckes, Ingo Burgert, Klaus Frühmann, Martin Müller, Klaas Kölln, Myles Hamilton, Manfred Burghammer, Stephan V Roth, Stefanie Stanzl-Tschegg, and Peter Fratzl. Cell-wall recovery after irreversible deformation of wood. *Nature materials*, 2(12):810, 2003.
- [189] Elisabeth Vanstreels, MC Alamar, BE Verlinden, A Enninghorst, JKA Loodts, Engelbert Tjiskens, Herman Ramon, and BM Nicolai. Micromechanical behaviour of onion epidermal tissue. *Postharvest Biology and Technology*, 37(2):163–173, 2005.
- [190] MC Jarvis, SPH Briggs, and JP Knox. Intercellular adhesion and cell separation in plants. *Plant, Cell & Environment*, 26(7):977–989, 2003.
- [191] Pieter Verboven, Greet Kerckhofs, Hibru Kelemu Mebatsion, Quang Tri Ho, Kristiaan Temst, Martine Wevers, Peter Cloetens, and Bart M Nicolai. Three-dimensional gas exchange pathways in pome fruit characterized by synchrotron x-ray computed tomography. *Plant physiology*, 147(2):518–527, 2008.
- [192] Justyna Cybulska, Els Vanstreels, Quang Tri Ho, Christophe M Courtin, Valerie Van Craeyveld, Bart Nicolai, Artur Zdunek, and Krystyna Konstankiewicz. Mechanical characteristics of artificial cell walls. *Journal of food engineering*, 96(2):287–294, 2010.
- [193] F Wittel and F Kun. F. wittel, f. kun, hj herrmann, and bh kröplin, phys. rev. lett. 93, 035504 (2004). *Phys. Rev. Lett.*, 93:035504, 2004.
- [194] Wen Chen and Jacob Fish. A mathematical homogenization perspective of virial stress. *International journal for numerical methods in engineering*, 67(2):189–207, 2006.

- [195] Wen Chen and Jacob Fish. A generalized space–time mathematical homogenization theory for bridging atomistic and continuum scales. *International Journal for Numerical Methods in Engineering*, 67(2):253–271, 2006.
- [196] Jacob Fish, Wen Chen, and Renge Li. Generalized mathematical homogenization of atomistic media at finite temperatures in three dimensions. *Computer methods in applied mechanics and engineering*, 196(4-6):908–922, 2007.
- [197] C William Gear and Ioannis G Kevrekidis. Constraint-defined manifolds: a legacy code approach to low-dimensional computation. *Journal of Scientific Computing*, 25(1):17–28, 2005.
- [198] C William Gear, Tasso J Kaper, Ioannis G Kevrekidis, and Antonios Zagaris. Projecting to a slow manifold: Singularly perturbed systems and legacy codes. *SIAM Journal on Applied Dynamical Systems*, 4(3):711–732, 2005.
- [199] Javier Bonet and Richard D. Wood. *Nonlinear Continuum Mechanics for Finite Element Analysis*. Cambridge University Press, Cambridge, 2008.
- [200] Wolfgang Bangerth, Ralf Hartmann, and Guido Kanschat. deal. ii—a general-purpose object-oriented finite element library. *ACM Transactions on Mathematical Software (TOMS)*, 33(4):24, 2007.
- [201] Ernst Hairer, Syvert P Nørsett, and Gerhard Wanner. Solving ordinary differential equations. i, volume 8 of springer series in computational mathematics, 1993.
- [202] Daniel A Fletcher and R Dyche Mullins. Cell mechanics and the cytoskeleton. *Nature*, 463(7280):485, 2010.
- [203] Marita L Rodriguez, Patrick J McGarry, and Nathan J Sniadecki. Review on cell mechanics: experimental and modeling approaches. *Applied Mechanics Reviews*, 65(6):060801, 2013.
- [204] Aleksandra Karolak, Dmitry A Markov, Lisa J McCawley, and Katarzyna A Rejniak. Towards personalized computational oncology: from spatial models of tumour spheroids, to organoids, to tissues. *Journal of The Royal Society Interface*, 15(138):20170703, 2018.
- [205] J Guck, R Ananthakrishnan, H Mahmood, T J Moon, C C Cunningham, and J Käs. The optical stretcher: a novel laser tool to micromanipulate cells. *Biophysical journal*, 81(2):767–784, 2001.
- [206] Gang Bao and Subra Suresh. Cell and molecular mechanics of biological materials. *Nature materials*, 2(11):715, 2003.
- [207] R M Hochmuth. Micropipette aspiration of living cells. *Journal of Biomechanics*, 33:15–22, 2000.
- [208] Jochen Guck, Stefan Schinkinger, Bryan Lincoln, Falk Wottawah, Susanne Ebert, Maren Romeyke, Dominik Lenz, Harold M Erickson, Revathi Ananthakrishnan, Daniel Mitchell, Josef Käs, Sydney Ulvick, and Curt Bilby. Optical deformability as an inherent cell marker for testing malignant transformation and metastatic competence. *Biophysical journal*, 88(5):3689–3698, may 2005.
- [209] Jochen Guck, Revathi Ananthakrishnan, Hamid Mahmood, Tess J Moon, C Casey Cunningham, and Josef Kaes. The Optical Stretcher: A Novel Laser Tool to Micromanipulate Cells. *Biophysical Journal*, 81:767–784, 2001.
- [210] Steffen Grosser, Anatol W Fritsch, Tobias R Kießling, Roland Stange, and Josef A Käs. The lensing effect of trapped particles in a dual-beam optical trap. *Optics Express*, 23(4):5221–5235, 2015.

- [211] Revathi Ananthakrishnan, Jochen Guck, Falk Wottawah, Stefan Schinkinger, Bryan Lincoln, Maren Romeyke, Tess Moon, and Josef Käs. Quantifying the contribution of actin networks to the elastic strength of fibroblasts. *Journal of Theoretical Biology*, 242(2):502–516, 2006.
- [212] Tobias R Kießling, Roland Stange, Josef A Käs, and Anatol W Fritsch. Thermorheology of living cells—impact of temperature variations on cell mechanics. *New Journal of Physics*, 15:45026, 2013.
- [213] Jan Brugués, Benoit Maugis, Jaume Casademunt, Pierre Nassoy, François Amblard, and Pierre Sens. Dynamical organization of the cytoskeletal cortex probed by micropipette aspiration. *Proceedings of the National Academy of Sciences of the United States of America*, 107(35):15415–15420, 2010.
- [214] Markus Gyger, Roland Stange, Tobias R. Kießling, Anatol Fritsch, Katja B. Kostelnik, Annette G. Beck-Sickinger, Mareike Zink, and Josef A. Käs. Active contractions in single suspended epithelial cells. *European Biophysics Journal*, 43(1):11–23, 2014.
- [215] J Li, M Dao, C T Lim, and S Suresh. Spectrin-Level Modeling of the Cytoskeleton and Optical Tweezers Stretching of the Erythrocyte. *Biophysical Journal*, 88(5):3707–3719, 2005.
- [216] S Suresh, J Spatz, J P Mills, A Micoulet, M Dao, C T Lim, M Beil, and T Seufferlein. Connections between single-cell biomechanics and human disease states: gastrointestinal cancer and malaria. *Acta Biomaterialia*, 1(1):15–30, 2005.
- [217] D Cuvelier, M Thery, Y-S. Chu, S Dufour, J-P. Thiery, M Bornens, P Nassoy, and L Mahadevan. The universal dynamics of cell spreading. *Current Biology*, 17:694–699, 2007.
- [218] Alina Hategan, Kheya Sengupta, Samuel Kahn, Erich Sackmann, and Dennis E Discher. Topographical Pattern Dynamics in Passive Adhesion of Cell Membranes. *Biophysical Journal*, 87(5):3547–3560, 2004.
- [219] D Leckband and J Israelachvili. Intermolecular forces in biology. *Quarterly Reviews of Biophysics*, 34(2):105–267, 2001.
- [220] N Wang, E Ostuni, G M Whitesides, and D E Ingber. Micropatterning Tractional Forces in Living Cells. *Cell Motility and the Cytoskeleton*, 52:97–106, 2002.
- [221] Michael P Murrell, Raphaël Voituriez, Jean-François Joanny, Pierre Nassoy, Cécile Sykes, and Margaret L Gardel. Liposome adhesion generates traction stress. *Nature Physics*, 10(2):163–169, jan 2014.
- [222] R M Sutherland. Cell and environment interactions in tumor microregions: the multicell spheroid model. *Science (New York, N.Y.)*, 240(4849):177–84, apr 1988.
- [223] Philippe Marmottant, Abbas Mgharbel, Jos Käfer, Benjamin Audren, Jean-Paul Rieu, Jean-Claude Vial, Boudewijn van der Sanden, Athanasius F M Marée, François Graner, and Hélène Delanoë-Ayari. The role of fluctuations and stress on the effective viscosity of cell aggregates. *Proceedings of the National Academy of Sciences of the United States of America*, 106(41):17271–5, oct 2009.
- [224] *The Cellular Capsules technology And its applications to investigate model tumor*. PhD thesis, UPMC, 2013.
- [225] Seddik Hammad, Stefan Hoehme, Adrian Friebel, Iris von Recklinghausen, Amnah Othman, Brigitte Begher-Tibbe, Raymond Reif, Patricio Godoy, Tim Johann, Amruta Vartak, Klaus Golka, Petru O Bucur, Eric Vibert, Rosemarie Marchan, Bruno Christ, Steven Dooley, Christoph Meyer,

- Iryna Ilkavets, Uta Dahmen, Olaf Dirsch, Jan Böttger, Rolf Gebhardt, Dirk Drasdo, and Jan G Hengstler. Protocols for staining of bile canalicular and sinusoidal networks of human, mouse and pig livers, three-dimensional reconstruction and quantification of tissue microarchitecture by image processing and analysis. *Archives of toxicology*, 88(5):1161–83, may 2014.
- [226] Giuseppe Mazza, Krista Rombouts, Andrew Rennie Hall, Luca Urbani, Tu Vinh Luong, Walid Al-Akkad, Lisa Longato, David Brown, Panagiotis Maghsoudlou, Amar P Dhillon, et al. Decellularized human liver as a natural 3d-scaffold for liver bioengineering and transplantation. *Scientific reports*, 5:13079, 2015.
- [227] Min-Cheol Kim, Jordan Whisler, Yaron R. Silberberg, Roger D. Kamm, and H. Harry Asada. Cell Invasion Dynamics into a Three Dimensional Extracellular Matrix Fibre Network. *PLoS Computational Biology*, 11(10):e1004535, 2015.
- [228] Guillaume Jacquemet, Hellyeh Hamidi, and Johanna Ivaska. Filopodia in cell adhesion, 3D migration and cancer cell invasion, 2015.
- [229] Darci T Butcher, Tamara Alliston, and Valerie M Weaver. A tense situation: forcing tumour progression. *Nature reviews. Cancer*, 9(2):108–22, 2009.
- [230] Markus Basan, Thomas Risler, Jean F Joanny, Xavier S Garau, and Jacques Prost. Homeostatic competition drives tumor growth and metastasis nucleation. *HFSP Journal*, 3(4):265–272, 2009.
- [231] J P Freyer and R M Sutherland. Regulation of growth saturation and development of necrosis in EMT6/Ro multicellular spheroids by the glucose and oxygen supply. *Cancer research*, 46(7):3504–12, jul 1986.
- [232] G Helmlinger, P A Netti, H C Lichtenbeld, R J Melder, and R K Jain. Solid stress inhibits the growth of multicellular tumor spheroids. *Nature biotechnology*, 15(8):778–83, aug 1997.
- [233] Gang Cheng, Janet Tse, Rakesh K Jain, and Lance L Munn. Micro-environmental mechanical stress controls tumor spheroid size and morphology by suppressing proliferation and inducing apoptosis in cancer cells. *PloS one*, 4(2):e4632, jan 2009.
- [234] K. L. Mills, Ralf Kemkemer, Shiva Rudraraju, and Krishna Garikipati. Elastic free energy drives the shape of prevascular solid tumors. *PLoS ONE*, 9(7), 2014.
- [235] Fabien Montel, Morgan Delarue, Jens Elgeti, Laurent Malaquin, Markus Basan, Thomas Risler, Bernard Cabane, Danijela Vignjevic, Jacques Prost, Giovanni Cappello, and Jean-François Joanny. Stress Clamp Experiments on Multicellular Tumor Spheroids. *Phys. Rev. Lett.*, 107(18):188102, oct 2011.
- [236] Morgan Delarue, Fabien Montel, Danijela Vignjevic, Jacques Prost, Jean-François Joanny, and Giovanni Cappello. Compressive Stress Inhibits Proliferation in Tumor Spheroids through a Volume Limitation. *Biophysical Journal*, 107(8):1821–1828, oct 2014.
- [237] C Y Chen, H M Byrne, and J R King. The influence of growth-induced stress from the surrounding medium on the development of multicell spheroids. *Journal of Mathematical Biology*, 43:191–220, 2001.
- [238] D. Ambrosi and F. Mollica. The role of stress in the growth of a multicell spheroid. *Journal of Mathematical Biology*, 48(5):477–499, 2004.
- [239] M A J Chaplain, L Graziano, and L Preziosi. Mathematical modelling of the loss of tissue compression responsiveness and its role in solid tumour development. *Mathematical Medicine and Biology*, 23(3):197–229.

- [240] Pietro Mascheroni, Cinzia Stigliano, Melania Carfagna, Daniela P. Boso, Luigi Preziosi, Paolo Decuzzi, and Bernhard A. Schrefler. Predicting the growth of glioblastoma multiforme spheroids using a multiphase porous media model, 2016.
- [241] Fabien Montel, Morgan Delarue, Jens Elgeti, Danijela Vignjevic, Giovanni Cappello, and Jacques Prost. Isotropic stress reduces cell proliferation in tumor spheroids. *New Journal of Physics*, 14(5):055008, may 2012.
- [242] Kévin Alessandri, Bibhu Ranjan Sarangi, Vasily Valériévitch Gurchenkov, Bidisha Sinha, Tobias Reinhold Kießling, Luc Fetler, Felix Rico, Simon Scheuring, Christophe Lamaze, Anthony Simon, Sara Geraldo, Danijela Vignjevic, Hugo Doméjean, Leslie Rolland, Anette Funfak, Jérôme Bibette, Nicolas Bremond, and Pierre Nassoy. Cellular capsules as a tool for multicellular spheroid production and for investigating the mechanics of tumor progression in vitro. *Proceedings of the National Academy of Sciences of the United States of America*, 110(37):14843–8, sep 2013.
- [243] Dirk Drasdo, Stefan Hoehme, and Jan G Hengstler. How predictive quantitative modelling of tissue organisation can inform liver disease pathogenesis. *Journal of hepatology*, 61(4):951–6, oct 2014.
- [244] Francisco Feijó Delgado, Nathan Cermak, Vivian C Hecht, Sungmin Son, Yingzhong Li, Scott M Knudsen, Selim Olcum, John M Higgins, Jianzhu Chen, William H Grover, and Scott R Manalis. Intracellular water exchange for measuring the dry mass, water mass and changes in chemical composition of living cells. *PloS one*, 8(7):e67590, jan 2013.
- [245] Bidisha Sinha, Darius Köster, Richard Ruez, Pauline Gonnord, Michele Bastiani, Daniel Abankwa, Radu V. Stan, Gillian Butler-Browne, Benoit Védie, Ludger Johannes, Nobuhiro Morone, Robert G. Parton, Graa Raposo, Pierre Sens, Christophe Lamaze, and Pierre Nassoy. Cells respond to mechanical stress by rapid disassembly of caveolae. *Cell*, 144(3):402–413, 2011.
- [246] Mariaceleste Aragona, Tito Panciera, Andrea Manfrin, Stefano Giullitti, Federica Michielin, Nicola Elvassore, Sirio Dupont, and Stefano Piccolo. A mechanical checkpoint controls multicellular growth through YAP/TAZ regulation by actin-processing factors. *Cell*, 154(5):1047–59, aug 2013.
- [247] Boris I Shraiman. Mechanical feedback as a possible regulator of tissue growth. *Proceedings of the National Academy of Sciences of the United States of America*, 102(9):3318–3323, mar 2005.
- [248] Alberto Puliafito, Lars Hufnagel, Pierre Neveu, Sebastian Streichan, Alex Sigal, D Kuchnir Fygenson, and Boris I Shraiman. Collective and single cell behavior in epithelial contact inhibition. *Proceedings of the National Academy of Sciences of the United States of America*, 109(3):739–44, jan 2012.
- [249] David Owen Morgan. *The Cell Cycle: Principles of Control*. 2007.
- [250] L Wolpert, Cheryll Tickle, and Alfonso Martinez Martinez. *Principles of development*. 2015.
- [251] Morgan Delarue, Jean-François Joanny, Frank Jülicher, and Jacques Prost. Stress distributions and cell flows in a growing cell aggregate. *Interface focus*, 4(6):20140033, 2014.
- [252] Deutsche Sammlung von Mikroorganismen und Zellkulturen. Deutsche sammlung von mikroorganismen und zellkulturen, 2000.

- [253] LAG Lin, AQ Liu, YF Yu, and C Zhang. Cell compressibility studies utilizing noncontact hydrostatic pressure measurements on single living cells in a microchamber. *Applied Physics . . .*, 2008.
- [254] Sylvain Monnier, Morgan Delarue, Benjamin Brunel, Monika E Dolega, Antoine Delon, and Giovanni Cappello. Effect of an osmotic stress on multicellular aggregates. *Methods*, 94:114–119, 2016.
- [255] Jean-Yves Tinevez, Ulrike Schulze, Guillaume Salbreux, Julia Roensch, Jean-François Joanny, and Ewa Paluch. Role of cortical tension in bleb growth. *Proceedings of the National Academy of Sciences of the United States of America*, 106(44):18581–6, nov 2009.
- [256] Marco Scianna and Luigi Preziosi. A cellular potts model for the mmp-dependent and -independent cancer cell migration in matrix microtracks of different dimensions. *Computational Mechanics*, 53(3):485–497, Mar 2014.
- [257] Min-Cheol Kim, Yaron R. Silberberg, Rohan Abeyaratne, Roger D. Kamm, and H. Harry Asada. Computational modeling of three-dimensional ecm-rigidity sensing to guide directed cell migration. *Proceedings of the National Academy of Sciences*, 2018.
- [258] Ken-ichi Tsubota, Shigeo Wada, and Takami Yamaguchi. Particle method for computer simulation of red blood cell motion in blood flow. *Computer methods and programs in biomedicine*, 83(2):139–46, aug 2006.
- [259] S Majid Hosseini and James J Feng. How malaria parasites reduce the deformability of infected red blood cells. *Biophysical journal*, 103(1):1–10, 2012.
- [260] PGH Nayanajith, YT Gu, SC Saha, W Senadeera, and A Oloyede. Numerical simulation of red blood cells' deformation using sph method. In *4th International Conference on Computational Methods, Gold Coast, Australia*, 2012.
- [261] C. Pozrikidis. Numerical simulation of the flow-induced deformation of red blood cells. *Annals of Biomedical Engineering*, 31(10):1194–1205, Nov 2003.
- [262] Ting Ye, Nhan Phan-Thien, and Chwee Teck Lim. Particle-based simulations of red blood cells—a review. *Journal of Biomechanics*, 49(11):2255 – 2266, 2016. Selected Articles from the International Conference on CFD in Medicine and Biology (Albufeira, Portugal – August 30th - September 4th, 2015).
- [263] Steven Diehl, Gabriel Rockefeller, Christopher L Fryer, David Riethmiller, and Thomas S Statler. Generating optimal initial conditions for smoothed particle hydrodynamics simulations. *Publications of the Astronomical Society of Australia*, 32, 2015.
- [264] Anna Haeger, Marina Krause, Katarina Wolf, and Peter Friedl. Cell jamming: collective invasion of mesenchymal tumor cells imposed by tissue confinement. *Biochim. Biophys. Acta*, 1840(8):2386–2395, August 2014.
- [265] Elvira Infante, Pedro Monteiro, Perrine Paul-Gilloteaux, Melanie Domingues, Mathew Raab, Matthieu Piel, Edgar R Gomes, and Philippe" Chavrier. Mechanical stress on the nucleus triggers mt1-mmp digest-on-demand for matrix nuclear tunnel formation".
- [266] Katarina Wolf, Mariska Te Lindert, Marina Krause, Stephanie Alexander, Joost Te Riet, Amanda L Willis, Robert M Hoffman, Carl G Figdor, Stephen J Weiss, and Peter Friedl. Physical limits of cell migration: control by ECM space and nuclear deformation and tuning by proteolysis and traction force. *J. Cell Biol.*, 201(7):1069–1084, 24 June 2013.

- [267] Takamasa Harada, Joe Swift, Jerome Irianto, Jae-Won Shin, Kyle R Spinler, Avathamsa Athirasala, Rocky Diegmiller, P C Dave P Dingal, Irena L Ivanovska, and Dennis E Discher. Nuclear lamin stiffness is a barrier to 3D migration, but softness can limit survival. *J. Cell Biol.*, 204(5):669–682, 3 March 2014.
- [268] J Y Shao and R M Hochmuth. Micropipette suction for measuring piconewton forces of adhesion and tether formation from neutrophil membranes. *Biophysical journal*, 71(5):2892–2901, 1996.
- [269] Sébastien Pierrat, Françoise Brochard-Wyart, and Pierre Nassoy. Enforced detachment of red blood cells adhering to surfaces: statics and dynamics. *Biophysical journal*, 87(4):2855–2869, 2004.
- [270] Stéphane Douezan, Karine Guevorkian, Randa Naouar, Sylvie Dufour, Damien Cuvelier, and Françoise Brochard-Wyart. Spreading dynamics and wetting transition of cellular aggregates. *Proceedings of the National Academy of Sciences*, 108(18):7315–7320, 2011.
- [271] Alexander G. Fletcher, Christopher J W Breward, and S. Jonathan Chapman. Mathematical modeling of monoclonal conversion in the colonic crypt. *Journal of Theoretical Biology*, 300:118–133, 2012.
- [272] Elke A Ober and Frédéric P Lemaigre. Development of the liver: Insights into organ and tissue morphogenesis. *Journal of hepatology*, 2018.
- [273] Matthew J Paszek, Nastaran Zahir, Kandice R Johnson, Johnathon N Lakins, Gabriela I Rozenberg, Amit Gefen, Cynthia A Reinhart-King, Susan S Margulies, Micah Dembo, David Boettiger, Daniel A Hammer, and Valerie M Weaver. Tensional homeostasis and the malignant phenotype. *Cancer cell*, 8(3):241–54, sep 2005.
- [274] Renaud Poincloux, Floria Lizárraga, and Philippe Chavrier. Matrix invasion by tumour cells: a focus on mt1-mmp trafficking to invadopodia. *J Cell Sci*, 122(17):3015–3024, 2009.
- [275] Tânia Rodrigues, Banani Kundu, Joana Silva-Correia, Subhas C Kundu, Joaquim M Oliveira, Rui L Reis, and Vitor M Correlo. Emerging tumor spheroids technologies for 3d in vitro cancer modeling. *Pharmacology & therapeutics*, 184:201–211, 2018.
- [276] Gabriel Benton, Gerald DeGray, Hynda K Kleinman, Jay George, and Irina Arnaoutova. In vitro microtumors provide a physiologically predictive tool for breast cancer therapeutic screening. *PloS one*, 10(4):e0123312, 2015.
- [277] Maria Vinci, Carol Box, and Suzanne A Eccles. Three-dimensional (3d) tumor spheroid invasion assay. *Journal of visualized experiments: JoVE*, (99), 2015.
- [278] Eric B Berens, Jon M Holy, Anna T Riegel, and Anton Wellstein. A cancer cell spheroid assay to assess invasion in a 3d setting. *Journal of visualized experiments: JoVE*, (105), 2015.
- [279] Chun Liu, Daniela Lewin Mejia, Benjamin Chiang, Kathryn E Luker, and Gary D Luker. Hybrid collagen alginate hydrogel as a platform for 3d tumor spheroid invasion. *Acta biomaterialia*, 2018.
- [280] Yangjin Kim, Magdalena A Stolarska, Hans G Othmer, Y Kim, M A Stolarska, and H G Othmer. A HYBRID MODEL FOR TUMOR SPHEROID GROWTH IN VITRO I: THEORETICAL DEVELOPMENT AND EARLY RESULTS, 2007.
- [281] Ehsan Ban, J Matthew Franklin, Sungmin Nam, Lucas R Smith, Hailong Wang, Rebecca G Wells, Ovijit Chaudhuri, Jan T Liphardt, and Vivek B Shenoy. Mechanisms of plastic deformation in collagen networks induced by cellular forces. *Biophysical journal*, 114(2):450–461, 2018.

- [282] Julien Delile, Matthieu Herrmann, Nadine Peyri ras, and Ren  Doursat. A cell-based computational model of early embryogenesis coupling mechanical behaviour and gene regulation. *Nature communications*, 8:13929, 2017.
- [283] Gaelle Letort, Arnau Montagud, Gautier Stoll, Randy Heiland, Emmanuel Barillot, Paul Macklin, Andrei Zinovyev, and Laurence Calzone. Physiboss: a multi-scale agent based modelling framework integrating physical dimension and cell signalling. *bioRxiv*, page 267070, 2018.
- [284] Gautier Stoll, Barth l my Caron, Eric Viara, Aur lien Dugourd, Andrei Zinovyev, Aur lien Naldi, Guido Kroemer, Emmanuel Barillot, and Laurence Calzone. Maboss 2.0: an environment for stochastic boolean modeling. *Bioinformatics*, 33(14):2226–2228, 2017.
- [285] Adrian Friebel, Johannes Neitsch, Tim Johann, Seddik Hammad, Jan G. Hengstler, Dirk Drasdo, and Stefan Hoehme. TiQuant: Software for tissue analysis, quantification and surface reconstruction. *Bioinformatics (accepted)*, oct 2015.
- [286] Philip M Morse and Herman Feshbach. *Methods of theoretical physics*. AAPT, 1953.
- [287] Tim Odenthal, Bart Smeets, Joaquin Christiaens, Kevin Verstrepen, Engelbert Tjiskens, and Herman Ramon. EVOLUTION OF ADHESION PROPERTIES IN YEAST. In *Proceedings of the 10th International Symposium on Computer Methods in Biomechanics and Biomedical Engineering*, pages 431–437. Arup, apr 2012.
- [288] J C Hansen, R Skalak, S Chien, and A Hoger. An elastic network model based on the structure of the red blood cell membrane skeleton. *Biophysical journal*, 70(1):146–66, jan 1996.
- [289] K L Johnson and J A Greenwood. An Adhesion Map for the Contact of Elastic Spheres. *Journal of colloid and interface science*, 192:326–333, 1997.
- [290] J Guck, R Ananthakrishnan, TJ Moon, CC Cunningham, and J K s. Optical deformability of soft biological dielectrics. *Physical review letters*, 84(23):5451, 2000.
- [291] Revathi Ananthakrishnan, Jochen Guck, Falk Wottawah, Stefan Schinkinger, Bryan Lincoln, Maren Romeyke, Tess Moon, and Josef K s. Quantifying the contribution of actin networks to the elastic strength of fibroblasts. *Journal of Theoretical Biology*, 242(2):502–516, 2006.
- [292] Ning Wang, James P Butler, and Donald E Ingber. Mechanotransduction across the cell surface and through the cytoskeleton. *Science*, 260(5111):1124–1127, 1993.
- [293] Dimitrije Stamenovic and Ning Wang. Engineering approaches to cytoskeletal mechanics. *J Appl Physiol*, 89:2085–2090, 2000.
- [294] Jingyuan Xu, Yiider Tseng, and Denis Wirtz. Strain hardening of actin filament networks regulation by the dynamic cross-linking protein α -actinin. *Journal of Biological Chemistry*, 275(46):35886–35892, 2000.
- [295] F Wottawah, S Schinkinger, B Lincoln, R Ananthakrishnan, M Romeyke, J Guck, and J Kas. Optical Rheology of Biological Cells. *Physical Review Letters*, 94:98103, 2005.
- [296] L D Landau, L P Pitaevskii, E M Lifshitz, and A M Kosevich. *Theory of Elasticity, Third Edition: Volume 7 (Theoretical Physics)*. Butterworth-Heinemann, 1986.
- [297] Revathi Ananthakrishnan, Jochen Guck, Falk Wottawah, Stefan Schinkinger, Bryan Lincoln, Maren Romeyke, Tess Moon, and Josef K s. Quantifying the contribution of actin networks to the elastic strength of fibroblasts. *Journal of Theoretical Biology*, 242(2):502–516, 2006.

- [298] Chunfang Wei and Philip M Lintilhac. Loss of Stability: A New Look at the Physics of Cell Wall Behavior during Plant Cell Growth. *Plant Physiology*, 145(3):763–772.
- [299] Morgan Delarue, Fabien Montel, Ouriel Caen, Jens Elgeti, Jean-Michel Siaugue, Danijela Vignjevic, Jacques Prost, Jean-François Joanny, and Giovanni Cappello. Mechanical Control of Cell flow in Multicellular Spheroids. *Phys. Rev. Lett.*, 110(13):138103, mar 2013.